Determination of the Gluon Polarization in the Nucleon

Felix M. Menden

FAKULTÄT FÜR PHYSIK
ALBERT-LUDWIGS-UNIVERSITÄT FREIBURG

Determination of the Gluon Polarization in the Nucleon

INAUGURAL–DISSERTATION
zur
Erlangung des Doktorgrades
der
Fakultät für Physik
der
Albert-Ludwigs-Universität Freiburg im Breisgau

vorgelegt von

Felix M. Menden

aus Hamburg

November 2001

Dekan:	Prof. Dr. Kay Königsmann
Leiter der Arbeit:	Prof. Dr. Kay Königsmann
Referent:	Prof. Dr. Kay Königsmann
Koreferent:	Prof. Dr. Jens Ludwig
Tag der Verkündigung des Prüfungsergebnisses:	18.12.2001

The HERMES Experiment at HERA

Spin Structure of the Nucleon

Deutsches Elektronen-Synchrotron DESY

Contents

1 Introduction

Understanding the fundamental structure of matter is the main goal of high-energy physics. The standard model of particle physics describes matter in terms of elementary fermions which interact by the exchange of bosons. The concept of spin as a fundamental property of elementary particles leads to the common division of particles into two groups: fermions and bosons. While fermions have spins of odd multiples of $\frac{\hbar}{2}$, bosons carry spins of even multiples of $\frac{\hbar}{2}$. The fact that protons and neutrons are fermions, which have to obey the Pauli exclusion principle, explains why nuclear matter as we know it exists at all and does not collapse to one single ground state of nucleons.

Since the discovery of the charged spin-$\frac{1}{2}$ constituents of the nucleon, the quarks, the question of how the spin of the nucleon is composed by its partons remains unresolved. The nucleon spin s_N can be divided into the contributions of its different constituents:

$$\frac{1}{2} = \frac{s_N}{\hbar} = \frac{1}{2}\Delta\Sigma + \Delta G + L_z \quad , \tag{1.1}$$

where $\Delta\Sigma$ is the spin contribution carried by the quarks, ΔG the spin carried by the gluons, and L_z stands for the orbital angular momentum of the quarks and gluons. The first identity of the left hand side of the helicity sum rule formulated in Equation 1.1 is an experimental fact for over 70 years now. In 1927 D.M.Dennison conducted a measurement of the specific heat of molecular hydrogen at low temperatures which only could be explained by the assumption of spin-$\frac{1}{2}$ nuclei in the H_2 molecule [1]. This conclusion was confirmed one year later by W.Kapuscinski and J.G.Eymers through the measurement of transition intensities between rotational states of the H_2 molecule. The ratios of these intensities could again only be explained by spin-$\frac{1}{2}$ nuclei [2].

The disentanglement of the right hand side of Equation 1.1 was approached by deep inelastic scattering experiments in the seventies and eighties of the last century. In these experiments longitudinally polarized (point-like) leptons ($e^{\pm}, \mu^{\pm}, \nu, \bar{\nu}$) were scattered on targets of polarized nuclei to investigate their structure. The first puzzling result by EMC [3] indicated $\Delta\Sigma$ to be small and even consistent with zero after earlier it had been already found that quarks seem to make up only half of the nucleon mass [4]. These findings lead to the so-called *nucleon spin crisis* [5]. An extended perception of the problem reveals that gluons, the field quanta of the strong interaction, themselves can carry a significant fraction of the spin. The observed rate of three jet events in e^+e^- collisions by the experiment TASSO [6] at the collider PETRA (DESY) lead to the discovery of the gluon. The spin-1 nature of the gluon was disclosed by angular correlations of the observed jets. This discovery was followed by the triumphant advance of quantum chromodynamics (QCD), the non-Abelian field theory of the strong interaction [7, 8].

In the following, a next generation of fixed-target experiments at SLAC, CERN and DESY determined the quark contribution to the nucleon spin to be around 30% mitigating the nucleon spin problem. Discrepancies to relativistic quark model calculations which predict about 60% remain but can be clarified by QCD which predicts an anomalous gluon contribution to the quark spins. One of the current experiments is HERMES (HEra MEasurement of Spin) at the Deutsches Elektronen-Synchrotron (DESY) in Hamburg, Germany. HERMES utilizes a polarized dilution free internal gas target and the longitudinally polarized positron beam of the HERA accelerator. The HERMES forward spectrometer comprises a large angular acceptance and particle identification. This allows the detection of the hadronic fragments of deep inelastic scattering which is important to disentangle the contributions of the individual quark flavours to $\Delta\Sigma$. Via dedicated hadron triggers, HERMES also enables the detection of the hadronic final states of photoproduction events. A class of these photoproduction events arises from the direct interaction of the virtual photon from the positron beam with a gluon in the target nucleon (*photon-gluon fusion*). Double spin asymmetries of hadron pairs at large transverse momentum can be linked to photon-gluon fusion events and thus to the gluon polarization. This work exploits this ansatz in order to contribute an important piece towards solving the nucleon spin puzzle.

This work is divided into six main Chapters:
Chapter 2 supplies the theoretical framework needed to interpret the results of deep inelastic scattering and photoproduction. The discussion is extended to perturbative quantum chromodynamics which clarifies the important role of the gluon in the nucleon. Chapter 3 gives an overview of the HERMES experimental apparatus. Since for experimental investigations on the polarized nucleon structure both target and projectile need to be polarized, the measurement of the respective polarizations pose an important prerequisite. In this context, Chapter 4 is dedicated to the determination of the beam polarization by the Longitudinal Polarimeter, which constitutes the hardware contribution of this thesis. The long outstanding calibration of the polarimeter, the best possible analysis of the beam polarization via dedicated programs, and a complete investigation of systematic effects round off the extended efforts.

Chapter 5 covers the dedicated modeling of the hadronization process at the center-of-mass energy of HERMES. The LUND string fragmentation model is adapted to HERMES deep inelastic scattering data. The hadronization modeling is a basic prerequisite for the photoproduction analysis of Chapters 6 and 7. In Chapter 6 a strategy for best possibly tagging the photon-gluon fusion process will be developed using a PYTHIA6 Monte Carlo simulation. Subsequently, the cut scheme is applied to all of the polarized datasets HERMES collected during the years 1996 to 2000. This leads to a measurement of double spin asymmetries of hadron pairs with large transverse momentum. In the subsequent Chapter 7 an extraction of the gluon polarization from the measured asymmetries based on PYTHIA6 Monte Carlo simulations is presented.

2 Theoretical Motivation

2.1 Deep Inelastic Scattering

Deep inelastic lepton nucleon scattering (DIS) is a process for which the four-momentum of the mediating electroweak boson (γ,$W^{\pm}$,Z^0) is so large and therefore the resolved distance so small that the substructure of the nucleon is probed. The following inevitable break-up of the target nucleon manifests the inelasticity of the process.

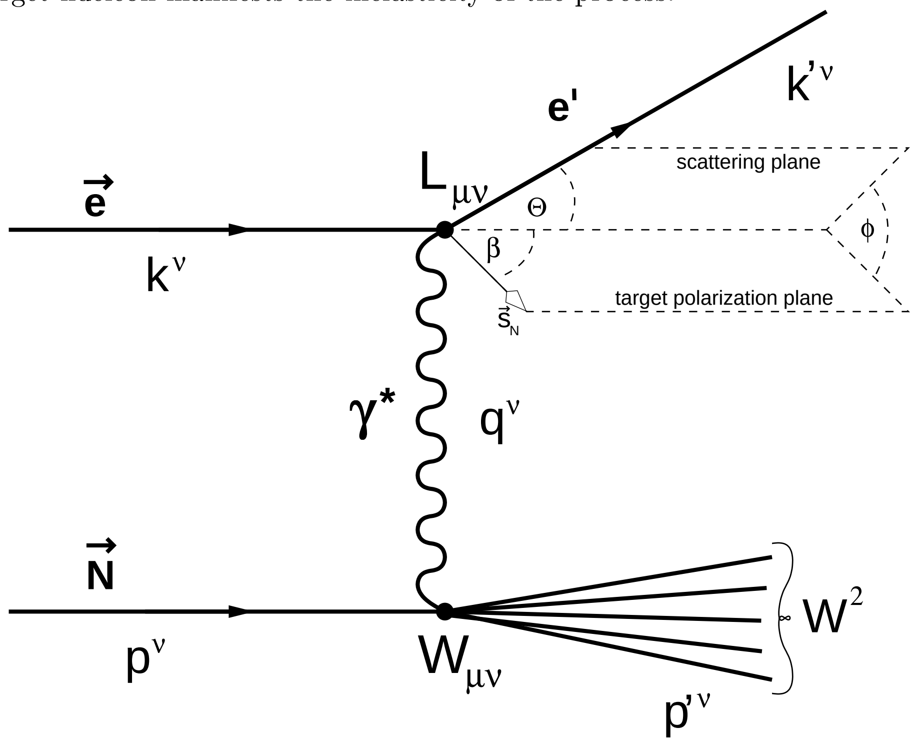

Figure 2.1: The Feynman graph of deep inelastic scattering in the one-photon exchange approximation (bold lines) together with the kinematic quantities defined in the text.

In most DIS experiments, a charged lepton $\ell^{\pm}$ is scattered deep inelastically off a nucleon N to an outgoing lepton $\ell^{\pm\prime}$ and a hadronic final state X:

$$\ell^{\pm} + N \rightarrow \ell^{\pm\prime} + X \quad .$$

In lowest order perturbation theory this process can be described by the exchange of a neutral boson (Z^0, γ) between the two incoming particles. Because at HERMES the center-of-mass energy and the energy transfers of such reactions are well below the masses of the weak gauge bosons, the one-photon exchange is the dominant process (Fig. 2.1). Since the interference of one- and two-photon exchange processes is sensitive to the charge of the lepton beam, the influence of two-photon exchange can be inferred by comparing DIS cross sections with opposite lepton charges. There is no experimental evidence that the DIS cross section at HERMES energies for electrons and positrons differs thus confirming photon exchanges of higher order to be of negligible importance.

In the laboratory frame, the incoming lepton $\ell^{\pm}$ with four-momentum[1] $k^{\nu} = (E, \vec{k})$ scatters under an angle Θ into its outgoing state $k'^{\nu} = (E', \vec{k'})$ by emitting a virtual photon γ^*. The four-momentum squared of the virtual photon is:

$$q^2 = (k - k')^2 \quad . \tag{2.1}$$

By assuming azimuthal symmetry and neglecting the lepton mass ($k^{\nu}_{lab} = (E, E \cdot \vec{u_z})$, the unit vector $\vec{u_z}$ points into the beam direction), the negative four-momentum squared of the virtual photon can be expressed in the lab system as:

$$-q^2 = Q^2 \stackrel{\text{lab}}{=} 4EE' \sin^2 \frac{\Theta}{2} \quad , \tag{2.2}$$

where E (E') is the energy of the incoming (outgoing) lepton. The negative momentum transfer squared Q^2 is positive and is a measure of the scale the photon can resolve ($\lambda \propto \frac{1}{Q}$). The energy transferred by the virtual photon is:

$$\nu = \frac{p \cdot q}{M_N} \stackrel{\text{lab}}{=} E - E' \quad . \tag{2.3}$$

At HERMES, the target nucleon with mass M_N is at rest in the lab frame, thus the four-momentum p of the target nucleon with mass M_N denotes $p^{\nu}_{lab} = (M_N, \vec{0})$. Defining p' to be the sum over the four-momenta of the outgoing hadron fragments X, the invariant mass squared of the hadronic final state W^2 can be expressed as:

$$W^2 = (p + q)^2 = p'^2 \stackrel{\text{lab}}{=} M_N^2 + 2M_N\nu - Q^2 \quad . \tag{2.4}$$

Deep inelastic scattering can be thought of as a scattering process in which $\frac{1}{Q}$ is much smaller than the size of the nucleon so that the lepton scatters off a single constituent. Furthermore, W has to be large enough (> 2 GeV) to ensure the complete break-up of the nucleon instead of the excitation of a hadronic resonance. For a further description, two dimensionless *scaling variables* are introduced:

$$y = \frac{p \cdot q}{p \cdot k} \stackrel{\text{lab}}{=} \frac{\nu}{E} \tag{2.5}$$

$$\text{and} \qquad x = \frac{Q^2}{2\, p \cdot q} \stackrel{\text{lab}}{=} \frac{Q^2}{2M_N\nu} \quad (< 1 \text{ in DIS}) \quad . \tag{2.6}$$

Here, y is the energy fraction of the projectile transferred to the nucleon while x is a measure of the inelasticity of the process. Deep inelastic scattering is formally defined as lepton-nucleon scattering for Q^2, $\nu \to \infty$ at fixed x. All the variables defined in Equations 2.1-2.6 are Lorentz-invariant. For the case of a stationary target these variables can be calculated from the kinematics of the outgoing lepton $\ell^{\pm\prime}$. This enables a structure measurement of the nucleon by detecting just the scattered lepton (*inclusive measurement*).

[1] Throughout this work natural units with $\hbar = 1$ and $c = 1$ are used.

2.1.1 The Unpolarized Cross Section

By evaluating the Feynman graph in Figure 2.1, the inclusive DIS cross section can be written as a matrix product of the leptonic tensor $L_{\mu\nu}$ and the hadronic tensor $W^{\mu\nu}$ (see for instance [9, 10]). The differential DIS cross section in the lab frame for detecting the scattered lepton within the solid angle $d\Omega$ in the energy interval $[\,E', E'+dE'\,]$ is expressed as:

$$\frac{d^2\sigma}{dE'\,d\Omega} = \frac{\alpha^2}{M_N Q^4}\frac{E'}{E}\,L_{\mu\nu}W^{\mu\nu} \quad , \tag{2.7}$$

with the fine structure constant $\alpha \approx \frac{1}{137}$. The tensor $L_{\mu\nu}$ describes the interaction at the leptonic vertex in the one-photon exchange approximation and can be written with the gamma matrices γ_μ and spinor u of the positron (see for instance [11]):

$$L_{\mu\nu} = \sum_{s'_e} \bar{u}(k', s'_e)\gamma_\nu u(k, s_e)\bar{u}(k, s_e)\gamma_\mu u(k', s'_e) \quad . \tag{2.8}$$

The spin four-vector s_e^ν of the incoming positron is defined by:

$$s_e^\nu = \frac{1}{2}\,\bar{u}(k, s_e)\gamma^\nu\gamma^5 u(k, s_e) \quad , \tag{2.9}$$

and set to be $s_e^\nu = (0, \vec{s_e})$ in the rest frame of the particle. Employing trace theorems and summing over the unobserved spin orientations s'_e of the final state, Equation 2.8 leads to:

$$\begin{aligned} L_{\mu\nu} &= Tr[(\not{k}' + m_e)\gamma_\nu(\not{k} + m_e)\frac{m_e + \gamma_5\not{s}_e}{2m_e}\gamma_\mu] & (2.10)\\ &= 2(k_\mu k'_\nu + k_\nu k'_\mu - g_{\mu\nu}(k\cdot k' - m_e^2) - i\epsilon_{\mu\nu\alpha\beta}\, q^\alpha s_e^\beta) & (2.11)\\ &\approx 2(\underbrace{k_\mu k'_\nu + k_\nu k'_\mu - g_{\mu\nu}\; k\cdot k'}_{\frac{1}{2}L_{\mu\nu}^{(S)}} - i\,\underbrace{\epsilon_{\mu\nu\alpha\beta}\; q^\alpha s_e^\beta}_{\frac{1}{2}L_{\mu\nu}^{(A)}}) & (2.12) \end{aligned}$$

The part $L_{\mu\nu}^{(S)}$ is symmetric in $\mu\nu$ and does not depend on the spin of the incident positron while the antisymmetric part $L_{\mu\nu}^{(A)}$ is spin-dependent. Contrary to the lepton tensor, the hadronic tensor $W^{\mu\nu}$ cannot be calculated from first principles. To overcome this difficulty a general ansatz for $W_{\mu\nu}$ can be made using the fact that it can only depend on p^ν, q^ν and s_N^ν, the polarization vector of a spin-$\frac{1}{2}$ target. Using time-reversal invariance and parity conservation of the strong interaction, as well as current conservation at the hadronic vertex, the hadronic tensor can be generally expressed as:

$$W_{\mu\nu} = W_{\mu\nu}^{(S)} + iW_{\mu\nu}^{(A)} \qquad \text{with} \tag{2.13}$$

$$\begin{aligned} W_{\mu\nu}^{(S)} &= F_1\cdot\left(\frac{q_\mu q_\nu}{q^2} - g_{\mu\nu}\right) + F_2\cdot\frac{1}{p\cdot q}\left(p_\mu - \frac{p\cdot q\; q_\mu}{q^2}\right)\left(p_\nu - \frac{p\cdot q\; q_\nu}{q^2}\right) & (2.14)\\ W_{\mu\nu}^{(A)} &= g_1\cdot\frac{1}{p\cdot q}\,\epsilon_{\mu\nu\alpha\beta}\; q^\alpha\; s_N^\beta + g_2\cdot\frac{1}{(p\cdot q)^2}\,\epsilon_{\mu\nu\alpha\beta}\; q^\alpha(p\cdot q\; s_N^\beta - s_N\cdot q\; p^\beta) \quad . & (2.15) \end{aligned}$$

The *structure functions*, $F_1(x,Q^2)$, $F_2(x,Q^2)$, $g_1(x,Q^2)$, and $g_2(x,Q^2)$, appear as coefficients in Equation 2.15 and contain the actual information on the structure of the nucleon. Since all spin-independent terms in Equations 2.12 and 2.15 are symmetric in $\mu\nu$ and all spin-dependent terms are anti-symmetric, non-zero spin-dependent terms in the cross section (Eq. 2.7) will contain only terms with both spins, s_N^ν and s_e^ν, appearing. Therefore, both the projectile and the target must be polarized in an experiment to measure the polarized structure functions g_1 and g_2. The most general ansatz for the hadronic tensor $W_{\mu\nu}$ including the weak interaction [12] leads to one more unpolarized structure function F_3 and three more polarized structure functions g_3, g_4, and g_5.

The unpolarized DIS cross section can be calculated by contracting $L_{\mu\nu}^{(S)}$ with $W^{\mu\nu\,(S)}$, averaging over initial, and summing over all final spin spin states:

$$\frac{d^2\sigma_{unpol}}{dE'\,d\Omega} = \frac{4\alpha^2 E'^2}{Q^4}\left(\frac{2F_1(x,Q^2)}{M_N}\sin^2\frac{\Theta}{2} + \frac{F_2(x,Q^2)}{\nu}\cos^2\frac{\Theta}{2}\right) \quad . \tag{2.16}$$

A series of DIS experiments has mapped the structure function F_2 for the proton and the deuteron in a wide kinematic range of $10^{-6} < x < 0.9$ and $0.1 < Q^2/\mathrm{GeV}^2 < 10^3$. A compilation of world data on F_2^p is displayed in Figure 2.2 [13].

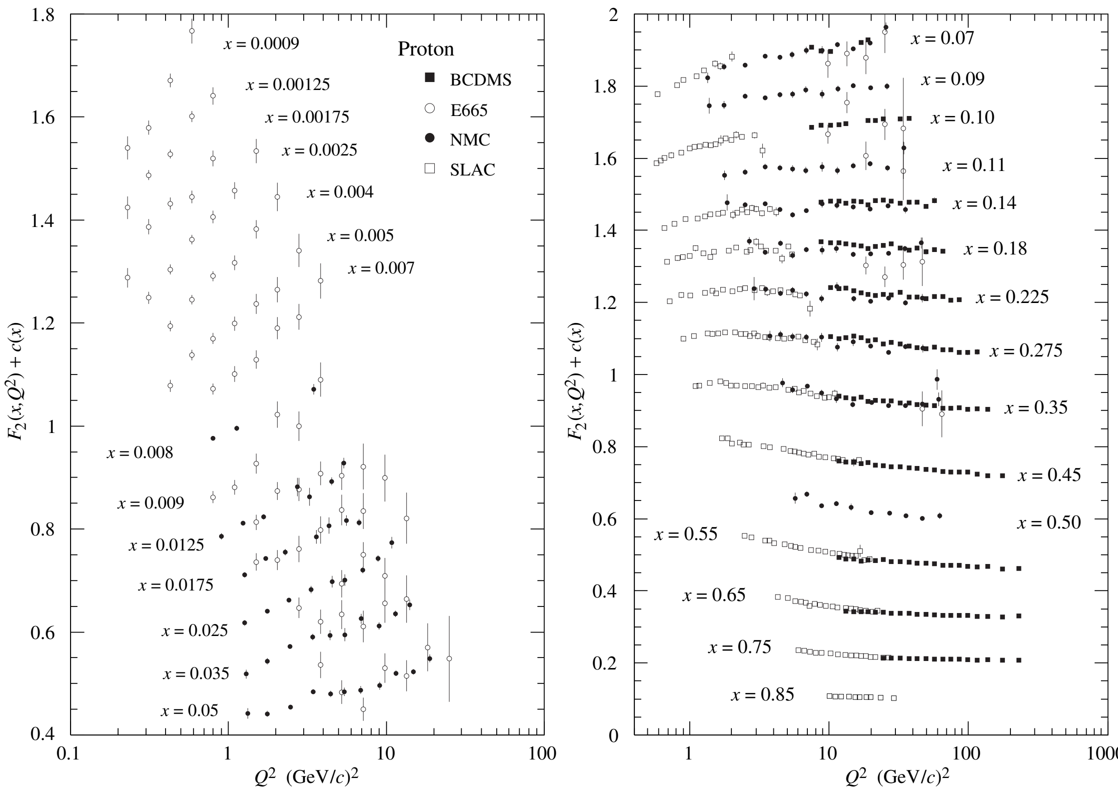

Figure 2.2: The unpolarized structure function F_2^p as a function of Q^2 for different values of x measured at SLAC [14], BCDMS [15], E665 [16], and NMC [17]. For a clear representation a constant $c(x) = j \cdot 0.1$ is added to F_2^p. The counter j ranges from 1 to 14 (15) from higher to lower x-values for the left (right) Figure (according to [13]).

In the Weizsäcker-Williams approach [18, 19] the incoming lepton beam is viewed as a source of virtual photons. The cross section can be factorized into two parts: a virtual photon flux $\Gamma(\nu, Q^2)$ provided by the charged lepton and a virtual photon-nucleon absorption cross section. In this picture, the unpolarized DIS cross section can be expressed by the transverse and longitudinal virtual photon-nucleon (DIS) cross sections $\sigma_T(x, Q^2)$ and $\sigma_L(x, Q^2)$, respectively:

$$\frac{d^2\sigma}{dE'\, d\Omega} = \Gamma(\nu, Q^2) \cdot \left[\sigma_T(x, Q^2) + \varepsilon\, \sigma_L(x, Q^2)\right] \tag{2.17}$$

$$= \frac{\alpha K}{2\pi^2 Q^2} \frac{E'}{E} \frac{1}{1-\varepsilon} \cdot \left[\sigma_T(x, Q^2) + \varepsilon\, \sigma_L(x, Q^2)\right] . \tag{2.18}$$

The choice of the factor K is not unique but is usually set to $K = \nu - \frac{Q^2}{2M_N}$ (Hand convention [20]). The polarization parameter ε of the virtual photon is given for the case of $Q^2 \gg 2m_e^2$ by :

$$\varepsilon = \frac{1 - y - \frac{1}{4}\gamma^2 y^2}{1 - y + \frac{1}{4}y^2(\gamma^2 + 2)} \qquad \text{with} \qquad \gamma^2 = \frac{Q^2}{\nu^2}. \tag{2.19}$$

By comparing Equation 2.17 with Equation 2.16, the ratio of the photoabsorption cross sections σ_L and σ_T can be expressed in terms of the unpolarized structure functions:

$$R_{DIS}(x, Q^2) = \frac{\sigma_L(x, Q^2)}{\sigma_T(x, Q^2)} = (1 + \gamma^2) \frac{F_2(x, Q^2)}{2xF_1(x, Q^2)} - 1 . \tag{2.20}$$

In the limit of high Q^2, the cross section ratio $R_{DIS}(x, Q^2)$ is measured to go to zero [21,22]. In this case Equation 2.20 leads to:

$$\lim_{Q^2 \to \infty} F_2(x) = 2xF_1(x) \qquad \text{(Callan-Gross relation [23])} . \tag{2.21}$$

The underlying reason for this relation is the elastic scattering on a point-like spin-$\frac{1}{2}$ constituent of the nucleon (see Sect. 2.2.1).

2.1.2 The Polarized Cross Section and Asymmetries

For a measurement of the polarized structure functions the antisymmetric parts of the hadronic and leptonic tensor, $W_{\mu\nu}^{(A)}$ and $L_{\mu\nu}^{(A)}$, need to be isolated. In the case of a longitudinally polarized lepton beam this can be done by taking the difference of the cross sections with opposite target spins $\vec{s}_N$ and $-\vec{s}_N$:

$$\begin{aligned} &\frac{d^2\sigma(\beta)}{dE'\, d\Omega} - \frac{d^2\sigma(\beta + \pi)}{dE'\, d\Omega} = \\ &= \frac{4\alpha^2}{Q^2 M_N \nu} \frac{E'}{E} \left[g_1 \cdot (E\cos\beta + E'\cos\vartheta) + g_2 \cdot \frac{2EE'}{\nu}(\cos\vartheta - \cos\beta) \right] , \end{aligned} \tag{2.22}$$

where $\cos\vartheta = \sin\Theta \sin\beta \cos\phi + \cos\Theta \cos\beta$. In this case, the target spin $\vec{s}_N$ is oriented under an angle β relative to the original lepton direction (dashed inset of Fig. 2.1) defining the target polarization plane in the lab frame. The scattered lepton is detected under an azimuthal angle ϕ relative to the target polarization plane. Interesting from the experimental point of view are the cases for $\beta = 0$ and $\beta = \pi/2$. In the first case where target and nucleon spin are aligned ($\overset{\rightarrow}{\Rightarrow}$) and anti-aligned ($\overset{\rightarrow}{\Leftarrow}$), the cross section difference simplifies to ($\cos\Theta = \cos\vartheta$):

$$\frac{d^2\Delta\sigma_{\shortparallel}}{dE'\,d\Omega} = \frac{d^2(\sigma^{\overset{\rightarrow}{\Leftarrow}} - \sigma^{\overset{\rightarrow}{\Rightarrow}})}{dE'\,d\Omega} = \frac{4\alpha^2}{Q^2 M_N \nu}\frac{E'}{E}\left[g_1\cdot(E + E'\cos\Theta) + g_2\cdot\frac{Q^2}{\nu}\right] . \tag{2.23}$$

In the second case the target spin is oriented transversely ($\rightarrow\Downarrow, \rightarrow\Uparrow$) to the longitudinal spin of the projectile ($\cos\vartheta = \sin\Theta\cos\phi$):

$$\frac{d^2\Delta\sigma_{\perp}}{dE'\,d\Omega} = \frac{d^2(\sigma^{\rightarrow\Downarrow} - \sigma^{\rightarrow\Uparrow})}{dE'\,d\Omega} = \frac{4\alpha^2}{Q^2 M_N \nu}\frac{E'^2\sin\Theta\cos\phi}{E}\left[g_1 + g_2\cdot\frac{2E}{\nu}\right] . \tag{2.24}$$

This configuration leads to a dependence of the cross section on the azimuthal angle ϕ. The polarized structure functions can be determined with a longitudinally polarized lepton beam via photon-nucleon cross section asymmetries A_1 and A_2 on longitudinally and transversely polarized targets:

$$A_1(x,Q^2) = \frac{\sigma_T^{\frac{1}{2}} - \sigma_T^{\frac{3}{2}}}{\sigma_T^{\frac{1}{2}} + \sigma_T^{\frac{3}{2}}} = \frac{g_1 - \gamma^2 g_2}{F_1} \tag{2.25}$$

$$A_2(x,Q^2) = \frac{2\sigma_{TL}}{\sigma_T^{\frac{1}{2}} + \sigma_T^{\frac{3}{2}}} = \frac{\gamma(g_1 + g_2)}{F_1} \tag{2.26}$$

Here, ($\sigma^{\frac{1}{2}}$) $\sigma^{\frac{3}{2}}$ denotes the differential cross section with virtual photon spin and target spin (anti-)parallel. The photoabsorption cross section for transverse virtual photons is $\sigma_T = \frac{1}{2}(\sigma_T^{\frac{1}{2}} + \sigma_T^{\frac{3}{2}})$ and σ_{TL} is the interference term between transverse and longitudinal photons. Experimentally, the lepton-nucleon asymmetries $A_{\shortparallel}$ and $A_{\perp}$ are measured:

$$A_{\shortparallel} = \frac{\Delta\sigma_{\shortparallel}}{\sigma^{\overset{\rightarrow}{\Leftarrow}} + \sigma^{\overset{\rightarrow}{\Rightarrow}}} \qquad \text{and} \qquad A_{\perp} = \frac{\Delta\sigma_{\perp}}{\sigma^{\rightarrow\Downarrow} + \sigma^{\rightarrow\Uparrow}} \quad , \tag{2.27}$$

with the short notation of $\Delta\sigma$ instead of $\frac{d^2\Delta\sigma_{\shortparallel(\perp)}}{dE'\,d\Omega}$ for the cross sections from Equation 2.23 (2.24). The experimental asymmetries $A_{\shortparallel}$ and $A_{\perp}$ can be related to the photon-nucleon cross section asymmetries A_1 and A_2 by:

$$A_{\shortparallel} = D\cdot(A_1 + \eta A_2) \qquad \text{and} \qquad A_{\perp} = D\cdot(\xi A_1 + \frac{\eta}{\xi}A_2) \quad . \tag{2.28}$$

The *depolarization factor* D describes the degree of polarization of the virtual photon relative to the incident lepton [24]:

$$D = \frac{1 - \varepsilon\,(1-y)}{1 + \varepsilon\,R_{DIS}(x,Q^2)} \tag{2.29}$$

The quantities η and ξ are trivial kinematic factors which can be expressed as:

$$\eta = \frac{y\,\gamma\,\varepsilon}{1 - \varepsilon\,(1-y)} \qquad \text{and} \qquad \xi = \eta\,\frac{1+\varepsilon}{2\varepsilon} \quad . \tag{2.30}$$

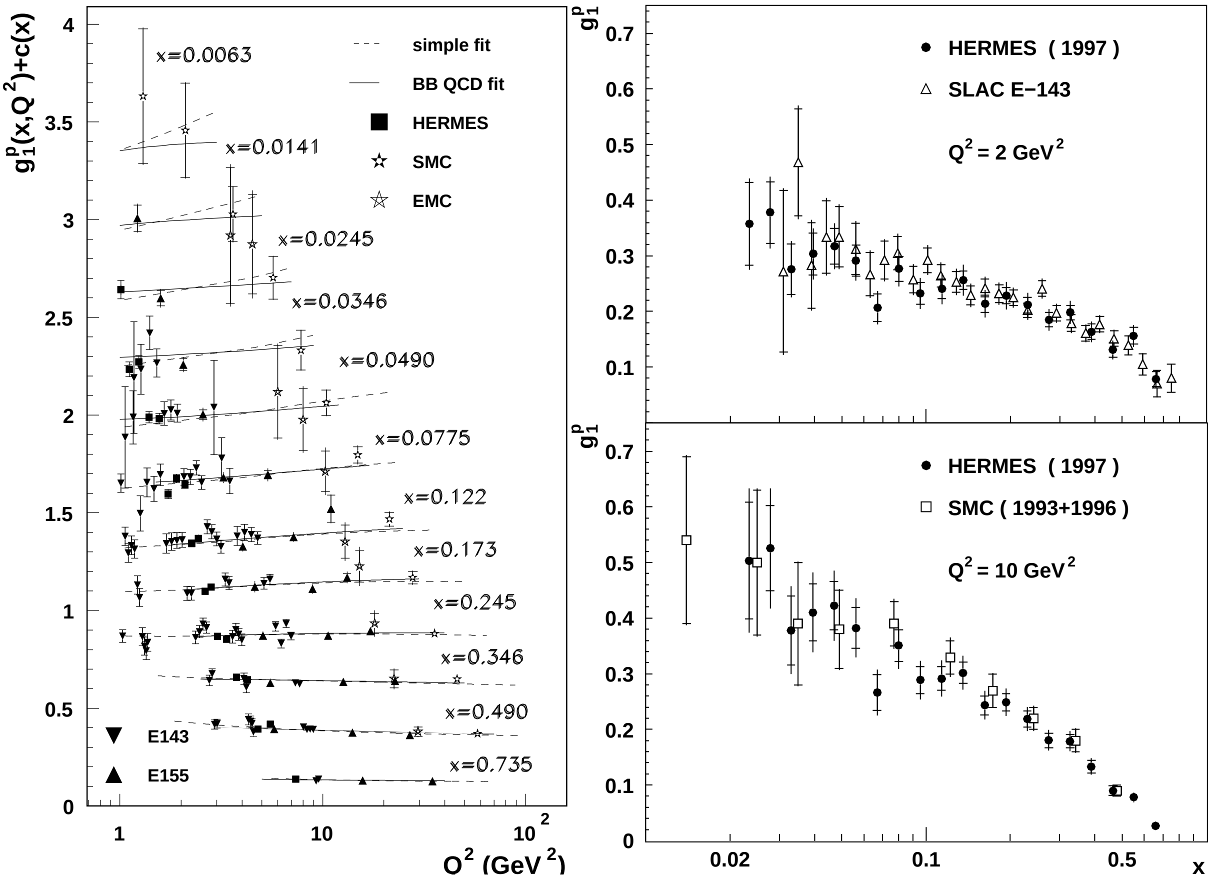

Figure 2.3: Left: World data on g_1^p from recent experiments versus Q^2 for various x bins [26]. The dashed line is a phenomenological fit while the solid line is the QCD fit of reference [27]. **Right**: Recent measurements of g_1^p from HERMES at a scale of $Q^2 = 2$ GeV^2 [25] compared to results from E143 [28] (**top**) and evolved to $Q^2 = 10$ GeV^2 for comparison with SMC data [29](**bottom**).

Measurements from experiments at SLAC, CERN, and DESY determined the structure function g_1^p covering a kinematic range of $0.006 < x < 0.8$ and $1 < Q^2/\text{GeV}^2 < 30$ (Fig. 2.3). The structure function g_2 has been measured on the proton, deuteron and neutron within a kinematic range of $0.01 < x < 0.8$ and $1 < Q^2/\text{GeV}^2 < 30$. The absolute value of $x \cdot g_2$ is found to be smaller than 0.025 and even consistent with zero for $x < 0.3$ [30, 31].

2.2 Quark Parton Model and Quantum Chromodynamics

2.2.1 Parton Distributions

In the limit of high Q^2 and ν, the structure functions F_1 and F_2 become a function of x only. This phenomenon is called *(Bjørken-)scaling*:

$$\lim_{Q^2,\nu\to\infty} F_{1,2}(x, Q^2) = F_{1,2}(x) \quad . \tag{2.31}$$

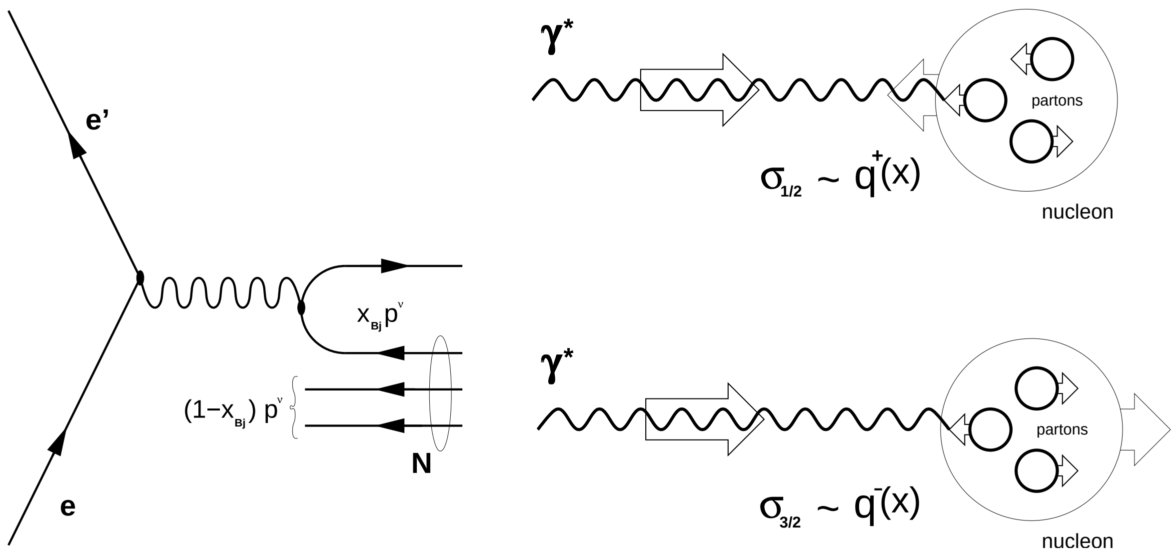

Figure 2.4: Left: DIS in the infinite momentum frame. The quark that carries the fraction x_{Bj} of the nucleon's momentum turns around when hit by the virtual photon. **Right:** Polarized DIS. Depending on the orientation of the target spin the polarized virtual photon hits a parton with spin parallel (top) or anti-parallel (bottom) to the nucleon spin.

The underlying reason is the elastic scattering on a point-like spin-$\frac{1}{2}$ constituent of the nucleon. This can be seen by comparing Equation 2.16 with the e-μ cross section [32] or inserting 'structure functions' for Dirac point particles (charge e_q) into Equation 2.16:

$$\begin{aligned} F_1^{point} &= e_q^2\,\frac{Q^2}{4M_N}\,\delta\left(\nu - \frac{Q^2}{2m_q}\right) = \frac{1}{2}\,e_q^2\,x\,\delta\left(1 - \frac{x}{x_{Bj}}\right) \\ F_2^{point} &= e_q^2\,\nu\,\delta\left(\nu - \frac{Q^2}{2m_q}\right) = e_q^2\,\delta\left(1 - \frac{x}{x_{Bj}}\right) \quad . \end{aligned} \tag{2.32}$$

These *partons* are assumed to carry a fraction x_{Bj} of the four-momentum of the nucleon ($p_q = x_{Bj} p_N$) in the infinite momentum frame (Fig. 2.4, left). The Equations 2.32 automatically yield the Callan-Gross relation (Eq. 2.21) and $x = x_{Bj}$. In this naive *Quark Parton Model* (QPM) [33, 34] the partons are identified with the quarks in the nucleon. Such a parton picture allows the derivation of the four-momentum fraction the struck quark carried in the nucleon from the kinematics of the scattered lepton.

The Quark Parton Model describes deep inelastic scattering on a nucleon as incoherent elastic scattering on non-interacting point-like quarks. The above arguments lead to the definition of parton distribution functions q_f for each (anti)quark flavour f which assemble to F_2 when summed up:

$$F_2(x) = 2\,x\,F_1(x) = \sum_f e_f^2\,x\,q_f(x) \quad , \tag{2.33}$$

where e_f is the respective quark charge. The formalism can be extended to the scattering of a polarized photon on a polarized quark (Fig. 2.4, right). Helicity conservation dictates that the photon can be absorbed only by a quark with its z-component of spin opposite to the direction of the photon spin. Thus, by flipping the spin of the target, either the quarks with spin parallel ($q^+(x)$) or anti-parallel ($q^-(x)$) to the nucleon spin are probed. The structure functions are written as follows in the Quark Parton Model:

$$
\begin{aligned}
F_1(x) &= \frac{1}{2}\sum_f e_f^2\,(q_f^+(x) + q_f^-(x)) = \frac{1}{2}\sum_f e_f^2\, q_f(x) \quad , && (2.34)\\
F_2(x) &= \sum_f e_f^2\, x\,(q_f^+(x) + q_f^-(x)) = \sum_f e_f^2\, x\, q_f(x) \quad , && (2.35)\\
g_1(x) &= \frac{1}{2}\sum_f e_f^2\,(q_f^+(x) - q_f^-(x)) = \frac{1}{2}\sum_f e_f^2\, \Delta q_f(x) \quad , && (2.36)\\
g_2(x) &= 0 \qquad \text{(no transverse spin components in QPM)} \quad . && (2.37)
\end{aligned}
$$

The distributions $q_f(x) = q_f(x)^+ + q_f(x)^-$ and $\Delta q_f(x) = q_f(x)^+ - q_f(x)^-$ are called unpolarized and polarized quark number densities. By integration of the unpolarized distributions over x the correct numbers for the proton have to be retrieved:

$$
\begin{aligned}
\int_0^1 dx\ (u(x) - \bar{u}(x)) &= \int_0^1 dx\ u_v(x) = 2 \quad , && (2.38)\\
\int_0^1 dx\ (d(x) - \bar{d}(x)) &= \int_0^1 dx\ d_v(x) = 1 \quad , && (2.39)\\
\int_0^1 dx\ (s(x) - \bar{s}(x)) &= 0 \quad . && (2.40)
\end{aligned}
$$

The distributions $u_v(x)$ and $d_v(x)$ are the valence quark distributions of the proton. The assumption of isospin symmetry between the proton and the neutron leads to the following relations (the subscript indicates the nucleon):

$$
\begin{aligned}
u(x) \equiv u_p(x) &= d_n(x) \quad , && (2.41)\\
d(x) \equiv d_p(x) &= u_n(x) \quad , && (2.42)\\
s(x) \equiv s_p(x) &= s_n(x) \quad . && (2.43)
\end{aligned}
$$

At HERMES, only the three lightest quark flavours (u, d, and s) are considered. The total nucleon momentum is not carried by the quarks alone:

$$
\int_0^1 dx\ x\ \left[g(x) + \sum_f q_f(x) \right] = 1 \qquad (2.44)
$$

where $g(x) = g^+(x) + g^-(x)$ is the gluon number density in the nucleon, which cannot be measured in DIS since gluons do not interact electromagnetically. Measurements show that the gluons carry about half on the nucleon momentum [4].

The polarized distributions were first determined by global fits to inclusive DIS data from SLAC and CERN Experiments. Recently, SMC [35] and HERMES [36] measured the polarized quark distributions directly by using semi-inclusive deep inelastic scattering (see next Section). The contributions to the spin of the nucleon are obtained if the polarized densities are integrated over x (at $Q^2 = 2.5$ GeV^2):

$$\begin{aligned}
\int_0^1 dx\ (\Delta u(x) - \Delta\bar{u}(x)) &= \Delta u_v \approx\ 0.60 \pm 0.10\ , & (2.45)\\
\int_0^1 dx\ (\Delta d(x) - \Delta\bar{d}(x)) &= \Delta d_v \approx\ -0.25 \pm 0.10\ , & (2.46)\\
\int_0^1 dx\ (2\Delta\bar{u}(x) + 2\Delta\bar{d}(x) + \Delta s(x) + \Delta\bar{s}(x)) &= \Delta q_{sea} \approx\ 0.00 \pm 0.15\ , & (2.47)\\
\int_0^1 dx\ (g^+(x) - g^-(x)) = \int_0^1 dx\ \Delta g(x) &= \Delta G \approx -0.5 \text{ to } 2.0\ . & (2.48)
\end{aligned}$$

If the valence and sea quark distributions as measured in DIS are added, in the QPM all quarks and antiquarks together contribute about 35% to the nucleon spin:

$$\Delta\Sigma_{DIS} = \Delta u_v + \Delta d_v + \Delta q_{sea} \stackrel{QPM}{=} a_0 \approx 0.35\ . \tag{2.49}$$

In the quark parton model $\Delta\Sigma_{DIS}$ equals a_0 which is proportional to the expectation value of the singlet axial-vector current matrix elements in QCD (Eq. 2.59). If $\Delta\Sigma_{DIS} \approx 0.35$ is identified with $\Delta\Sigma$ in the helicity sum rule (Eq. 1.1), other sources are needed to complete the nucleon spin. A sizable gluon contribution ΔG, which is essentially unknown, could give an explanation. Also the axial anomaly (cf. Sect. 2.3.1) or orbital angular momenta of quarks and gluons could explain the unexpectedly small value of $\Delta\Sigma_{DIS}$. Several sum rules were proposed to clarify the situation. The two most important ones relate known quantities from neutron or weak hyperon decays to integrals of the polarized structure functions $g_1^{p,n}$ (Bjørken sum rule [37], Ellis-Jaffe sum rule [38]). Theoretical calculations cannot explain the spin decomposition of the nucleon up to now, motivating further measurements to disclose ΔG in order to take a step towards solving the nucleon spin puzzle.

2.2.2 Fragmentation Functions

In deep inelastic scattering, the detection of a hadron in coincidence with the scattered lepton yields information about the single quark distributions of the target nucleon (*semi-inclusive measurement*). In the quark parton model, the virtual photon transfers all its energy to the struck quark which subsequently emerges from the nucleon. Due to the confinement properties of QCD, the coloured struck quark *hadronizes* into a colour-singlet state consisting of hadrons. The same holds for the coloured target remnant which is left behind. The outgoing hadrons can be found in two kinematic regions: the *current fragmentation region* that consists of hadrons coming from the fragmentation of the struck quark, and the *target fragmentation region* which contains the debris coming from the

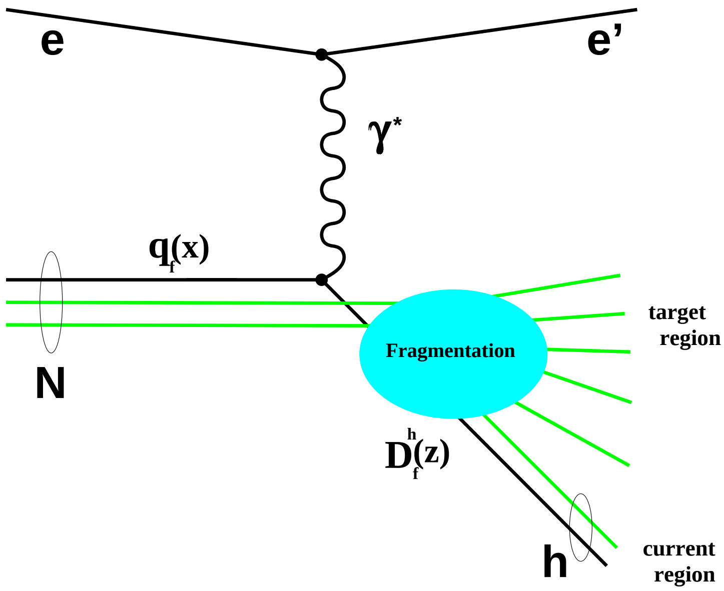

Figure 2.5: Deep inelastic electroproduction of a hadron h. The struck quark q_f hadronizes into a hadron h as described by the fragmentation function D_f^h.

target remnant (Fig. 2.5). The cross section for the DIS reaction with a hadron from the current fragmentation region observed in coincidence, can be expressed in the QPM as:

$$\frac{d^3\sigma^h}{dx\, dQ^2\, dz} = \frac{\sum_f e_f^2 q_f(x,Q^2) D_f^h(z,W^2)}{\sum_f e_f^2 q_f(x,Q^2)} \cdot \frac{d^2\sigma_{unpol}}{dx\, dQ^2} \quad , \tag{2.50}$$

where σ_{unpol} is the unpolarized DIS cross section (Eq. 2.16) and $z = E_h/\nu$ is the fraction of the energy of the virtual photon that is carried away by the hadron. The *fragmentation functions* $D_f^h(z, W^2)$ parameterize the structure of the *hadronization* process and are proportional to the probability that a struck quark of flavour f fragments into a hadron h (Fig. 2.5). The fragmentation functions fulfill energy conservation:

$$\sum_h \int_0^1 z\, D_f^h(z,W^2)\, dz = 1 \quad , \tag{2.51}$$

and are normalized to the total average hadron multiplicity $\langle n_h(W^2)\rangle$:

$$\sum_f \int_{z_0}^1 D_f^h(z,W^2)\, dz = \langle n_h(W^2)\rangle \quad , \tag{2.52}$$

for all quark and antiquark flavours f and the threshold z_0 of the process. In Equation 2.50 it is assumed that the fragmentation functions only depend on z and W^2 and the quark distribution functions only depend on x and Q^2. In this simple QPM picture the fragmentation into the hadronic final state is independent of the absorption of the virtual photon by the quark (*factorization*). However, implicit correlations are visible already in the simple QPM approach: the fragmentation functions depend on W^2 since the hadron multiplicity usually rises logarithmically with W^2 (see Fig. 5.16 for instance). Therefore, $D_f^h(z, W^2)$ seems to depend on the kinematics of the scattered lepton because x and Q^2 determine the measured W^2. Besides this trivial argument, higher order QCD corrections at the virtual photon-quark vertex cause factorization violations which can be calculated and are in agreement with experimental results [40].

To be sensitive to the flavour of the struck quark, it is necessary to detect a hadron from the current region at high enough z and x_F. The quantity x_F (*x-Feynman*) is defined in the photon-nucleon center-of-mass frame in terms of the longitudinal momentum of the hadron with respect to the virtual photon:

$$x_F = \frac{2\, p_{cm}^{\parallel}}{W} \quad . \tag{2.53}$$

If the x_F variable is positive, then the hadron is in the forward hemisphere of the virtual photon frame and hence very likely in the current region. The higher z and x_F, the more probable it is that the hadron contains the struck quark [39]. Consequently, a cut on these quantities is necessary for the interpretation of a semi-inclusive measurement. The ansatz formulated in Equation 2.50 can then be utilized in polarized DIS to disentangle the different polarized quark distribution functions according to the quark flavours.

For charged pions the number of fragmentation functions can be reduced using isospin symmetry and charge conjugation:

$$\begin{aligned} D_1(z) &= D_u^{\pi^+}(z) = D_{\bar{u}}^{\pi^-}(z) = D_d^{\pi^-}(z) = D_{\bar{d}}^{\pi^+}(z) \\ D_2(z) &= D_u^{\pi^-}(z) = D_{\bar{u}}^{\pi^+}(z) = D_d^{\pi^+}(z) = D_{\bar{d}}^{\pi^-}(z) \\ D_s(z) &= D_s^{\pi^+}(z) = D_s^{\pi^-}(z) = D_{\bar{s}}^{\pi^+}(z) = D_{\bar{s}}^{\pi^-}(z) \quad . \end{aligned} \tag{2.54}$$

D_1 is called the *favoured*, D_2 the *unfavoured*, and D_s the *strange* fragmentation function. Observations show that $D_1 > D_2$ since the fragmentation into a hadron is favoured if the hadron contains the struck quark. Using the simplifications of Equations 2.54 the fragmentation functions can be measured at HERMES by analyzing semi-inclusive hadron production on different targets [41]. Since the calculation of the fragmentation functions is not possible in QCD, models have to be employed to calculate the hadronic final state. This is described in more detail in Chapter 5. Moreover, fragmentation functions are proven to be *universal* no matter whether the hadronization process was triggered by a (virtual) photon-nucleon interaction or an e^+e^- annihilation [42, 43].

2.2.3 QCD Evolution of Structure Functions

The scaling of parton distributions (Eq. 2.31) as motivated by the simple QPM is only approximately true. As visible in Figure 2.2, the structure function F_2 varies slowly with Q^2. These *scaling violations* can be explained in quantum chromodynamics (QCD) by the

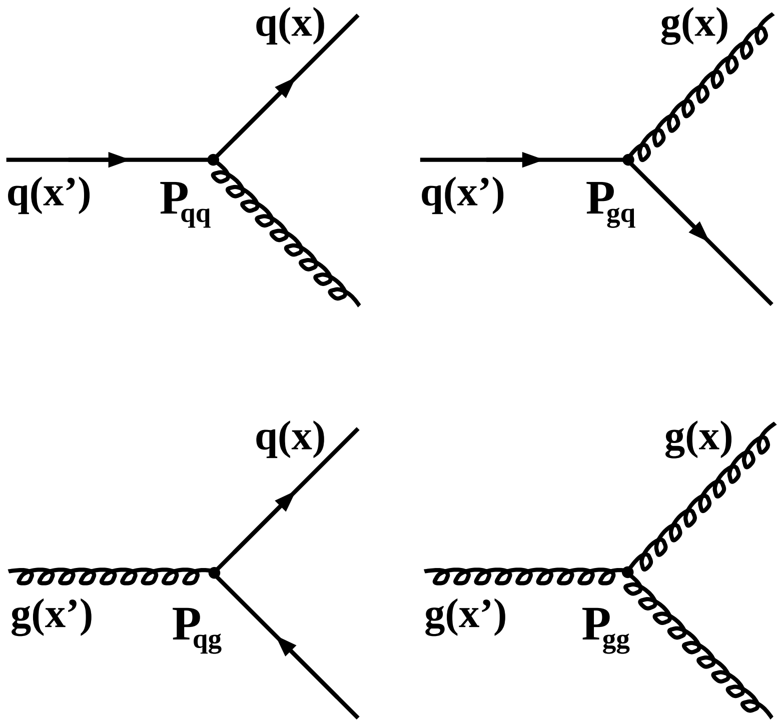

Figure 2.6: Symbolic representation of the QCD processes corresponding to the four splitting functions P_{qq}, P_{gq}, P_{qg} and P_{gg}. In each process a parton with momentum fraction x emerges from a parton with a larger momentum fraction x'.

interaction of quarks and gluons. The gluons are the field quanta of the strong interaction which can interact with themselves resulting in a scale dependent coupling strength:

$$\alpha_s(\mu^2) = \frac{4\pi}{(11 - \frac{2}{3}n_f)\ln(\mu^2/\Lambda^2_{QCD})} \qquad \text{with the number of quark flavours} \quad n_f \ , \tag{2.55}$$

to first order in QCD. The parameter $\Lambda_{QCD} \approx 0.3$ GeV sets the scale for the possibility of carrying out perturbative QCD calculations. The coupling strength $\alpha_s(\mu^2)$ decreases with rising scale μ^2 ($= Q^2$ in DIS) resulting in the *asymptotic freedom* of the quarks in the high energy limit.

In this picture, the quarks in the nucleon are surrounded by a cloud of gluons and quark-antiquark pairs. The cloud becomes more and more detailed as the resolution (i.e. Q^2) is increased. If a parton is probed at a certain value of Q^2, at some higher Q^2 this parton most likely carries a lower momentum fraction than before since it radiated off other partons. Consequently, the parton distributions depend on Q^2 and are coupled among each other.

The *evolution* of the parton densities can be described by the coupled integro-differential Dokshitzer-Gribov-Lipatov-Altarelli-Parisi Equations (DGLAP) [44–46]:

$$\frac{d\,q_i(x,Q^2)}{d\,\ln Q^2} = \frac{\alpha_s(Q^2)}{2\pi}\int_x^1 \frac{dx'}{x'}\,\left[\,q_i(x',Q^2)\cdot\,P_{qq}\left(x/x'\right) + g(x',Q^2)\cdot\,P_{qg}\left(x/x'\right)\right] \quad (2.56)$$

$$\frac{d\,g(x,Q^2)}{d\,\ln Q^2} = \frac{\alpha_s(Q^2)}{2\pi}\int_x^1 \frac{dx'}{x'}\left[g(x',Q^2)\cdot\,P_{gg}\left(x/x'\right) + \sum_i q_i(x',Q^2)\,P_{gq}\left(x/x'\right)\right]. \quad (2.57)$$

The *splitting functions* $P_{ij}(x/x')$ have an intuitive meaning: they correspond to the probability that a parton i with momentum fraction x was radiated off by a parton j with momentum fraction $x' > x$. For example the integral of Equation 2.56 can be understood to collect all possibilities of a quark with momentum fraction x that could have come from another quark or gluon with momentum fraction between x an 1. The several splitting processes considered are depicted in Figure 2.6. The splitting functions in Equations 2.56 and 2.57 are known algebraic expressions which beyond leading order depend on the factorization scheme used (see for instance [47, 48]). Although the DGLAP Equations can describe the interconnection of the parton distributions, they cannot provide an ab initio statement on the actual distributions for a given Q^2 and x without the knowledge on their shape at some other scale Q_0^2.

2.3 The Gluon in the Nucleon

The structure of the nucleon cannot be explained without understanding the role of the gluon. The details of how the strong field quanta, exchanged between the confined quarks, carry momentum and spin of the nucleon lead to deep insights of the mechanisms of the strong interaction. Experimental results in that respect will also be a test for quantum chromodynamics which, up to now, always turned out to be the correct field theory to describe strong interactions.

2.3.1 Aspects of Perturbative QCD

Scaling Violations (unpolarized)

Since the gluon density $g(x,Q^2)$ is woven via splitting processes into the evolution of the quarks densities, it will also influence the evolution of F_2 (Eq. 2.35). With an ansatz for the shape of the parton distributions, the splitting functions P_{ij} at hand, and data measured over a broad range of x an Q^2 (Fig. 2.2), the gluon number density $g(x,Q^2)$ can be implicitly fit and retrieved via Equation 2.57. Usually, the parton distributions are fixed at some arbitrary input scale Q_0^2 and then evolved to any given $Q^2 > Q_0^2$. It is found that the DGLAP evolution indeed matches the scaling violations observed thereby confirming QCD to be the correct theory to use. Results from a variety of fits are shown in Figure 2.7 (top). The gluon density increases with higher Q^2 since more and more splittings in the parton cloud are resolved. Equivalently, $g(x,Q^2)$ grows extremely with falling x since more and more quark-antiquark pairs (*sea quarks*) arise from emitted gluons as the momentum fraction becomes less and less. Nonetheless, the accuracy of the gluon density obtained from fits to F_2 is limited due to the precision of the data and the systematic bias of the evolution analysis. The latter arises from the assumptions on the parton density shapes and higher order corrections.

Scaling Violations (polarized)

Equivalently to the unpolarized parton densities the polarized distributions evolve with $\ln Q^2$. The polarized DGLAP Equations read identically to Equations 2.56 and 2.57 with the replacements $q \to \Delta q$, $g \to \Delta g$ and $P_{ij} \to \Delta P_{ij}$. The splitting functions ΔP_{ij} describe the case of a helicity flip of the parton j while it radiates off a parton i in the processes depicted in Figure 2.6. The polarized splitting functions are known to next-to-leading order [49–51] and also depend on the factorization scheme. Consequently and from arguments given below, all statements on the helicity sum rule (Eq. 1.1) depend on Q^2 and the factorization scheme applied.

In analogy to the extraction of the unpolarized gluon density, the polarized gluon density can in principle be derived from the scaling violations of g_1. Since a significant variation with Q^2 of the experimentally measured quantity $A_1 \approx g_1/F_1$ has not been observed yet, g_1 basically evolves like F_1 giving very few additional information for a polarized DGLAP fit. Also the mapped Q^2 and x range is quite limited (see Fig. 2.3, left) and since the evolution predicts variations with $\ln Q^2$, the polarized gluon density $\Delta g(x, Q^2)$ is hardly constrained at all as can be seen from polarized DGLAP fits (Fig. 2.7, bottom).

The Axial Currents

If in a perturbative QCD ansatz for g_1 the quark fields $\psi_i = (\psi_u, \psi_d, \psi_s, \dots)$ are treated as *free quark fields*, the integral of the structure function g_1^p can be calculated [12]:

$$\Gamma_1^p = \int_0^1 dx\ g_1^p(x) = \frac{1}{12}\left(\frac{4}{3}a_0 + a_3 + \frac{1}{\sqrt{3}}a_8\right)\ . \tag{2.58}$$

The Lorentz scalars a_k are proportional to the expectation values of the axial-vector currents J_5 of the proton:

$$a_k = \frac{\langle p, s_N | J_5^{k\,\mu} | p, s_N \rangle}{(1+\delta_{0i}) s_N^\mu M_N}\ , \tag{2.59}$$

for a proton with four-vector p^ν and covariant spin vector s_N^ν. Assuming $SU(3)_f$ flavour symmetry (u, d, s quarks only), the axial-vector current operators J_5 can be written as:

$$J_5^{k\,\mu} = \frac{1}{2}\bar{\psi}_i \gamma^\mu \gamma^5 \lambda_k^{ij} \psi_j \qquad k = 0, \dots, 8\ , \tag{2.60}$$

with the $SU(3)_f$ generator matrices $\lambda_{1,\dots,8}$ in the Gell-Mann representation and the singlet matrix $\lambda_0^{ij} = \delta^{ij}/\sqrt{6}$. The definition 2.60 describes the spin of the quark field ψ_j in analogy to QED (see Eq. 2.9). The expectation value a_0 of the flavour singlet axial-vector current J_5^0 corresponds to the expectation value of the z-component of all quark spins in the naive parton model: $s_{quarks,z} = a_0/2$. Among the octet currents $J_5^{1,\dots,8}$ the coefficients a_3 and

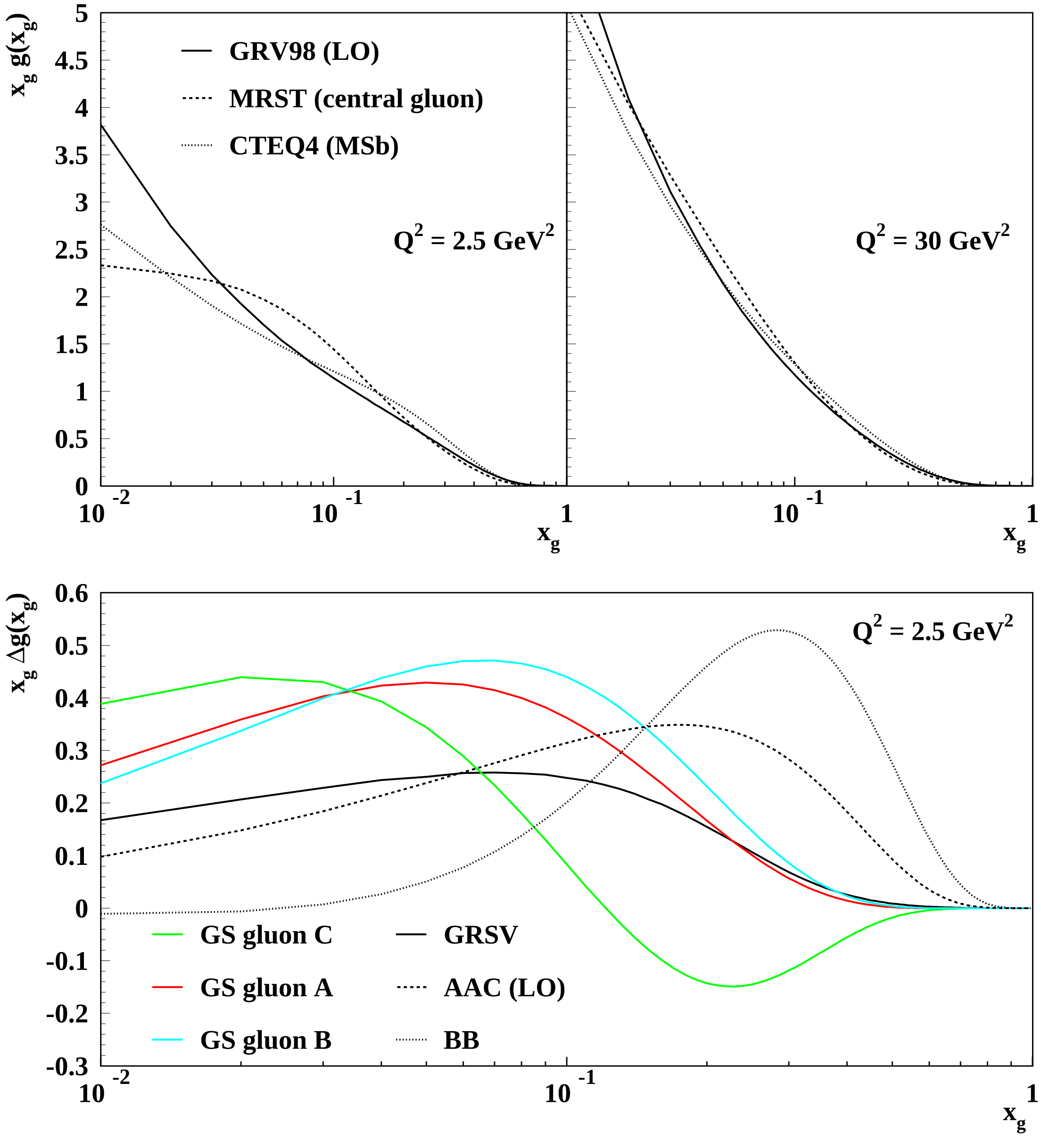

Figure 2.7: Top: The unpolarized gluon density (times x_g) for $Q^2 = 2.5$ GeV^2 and $Q^2 = 30$ GeV^2 inferred from scaling violations of F_2 by three different QCD fits (GRV98 [52], MRST [53], CTEQ4 [54]). **Bottom:** The polarized gluon density (times x_g) from various QCD fits to $A_1(x, Q^2)$ or $g_1(x, Q^2)$ (GS [55], AAC [56], BB [27], GRSV [57]).

a_8, for which λ_k^{ij} is diagonal, are of particular interest since they can be related to the weak decay constants F and D which are known from hyperon decays [59]:

$$a_3 = F + D \approx 1.2 \qquad \text{and} \qquad a_8 = 3F - D \approx -1.8 \; . \tag{2.61}$$

To get a QCD prediction for Γ_1^p the values for a_3 and a_8 can be inserted together with $a_0 \approx 0.35$ into Equation 2.58. Then, $\Gamma_{1\,QCD}^p \approx 0.13$ is obtained which agrees with inclusive measurements of g_1^p (see for instance [25]).

The Axial Anomaly

While the spin structure of the proton as reflected by g_1 can be understood in terms of the axial currents, the identification of a_0 with $\Delta\Sigma$ is complicated by the so-called *axial anomaly* originally found in quantum electrodynamic calculations by Adler, Bell and Jackiw [60, 61]. In the limit of massless quarks the axial currents J_5 are not conserved as would be expected from the free Dirac Equation [12]:

$$\lim_{m_q \to 0} \partial^\mu J^k_{5\,\mu} = \frac{\alpha_s(Q^2)}{8\pi} G^{a\,\mu\nu} \epsilon_{\mu\nu\rho\sigma} G_a^{\rho\sigma} \neq 0 \; , \tag{2.62}$$

with the strong field tensor G and the colour index a. If in a calculation of a_0 all gluons are assumed off the mass shell $k^2 \neq 0$ (gluon momentum four vector k^μ), the singlet axial current a_0 picks up an extra contribution for each quark flavour with $m_q \ll k^2$ [62–64]:

$$\Delta\Sigma_{DIS} \equiv a_0 = \Delta\Sigma - \frac{n_f \alpha_s(Q^2)}{2\pi} \Delta G(Q^2) \tag{2.63}$$

with the number of massless quark flavours n_f. In this picture a_0 is modified by an anomalous gluon contribution which is proportional to ΔG. Thus, the smallness of the measured value of $\Delta\Sigma_{DIS}$ could be explained by a positive value for ΔG. Equation 2.63 is not independent of the factorization scheme and is given here in the Adler-Bardeen scheme [65]. For instance, in the $\overline{\text{MS}}$ scheme [66] the gluon anomaly disappears showing that all statements on single terms of the helicity sum rule are scheme dependent. For the AB scheme the axial anomaly remains unchanged if higher order α_s corrections or loop diagrams are included [60, 65, 67].

The axial anomaly can be treated in a more direct and elegant way if the gluons are introduced directly into a modified singlet axial current:

$$\tilde{J}_5^{0\,\mu} = J_5^{0\,\mu} - \frac{n_f \alpha_s(Q^2)}{2\pi} K^\mu \quad \Rightarrow \quad \partial_\mu \tilde{J}_5^{0\,\mu} = 0 \;\; , \tag{2.64}$$

where K^μ is the axial gluon current. The operator $\tilde{J}_5^{0\,\mu}$ is scale independent, i.e. does not depend on Q^2. The gauge of the gluon field can be chosen such that the proton expectation value of K^μ is proportional to ΔG:

$$\Delta G = -\frac{\langle p, s_N | K^\mu | p, s_N \rangle}{2 s_N^\mu M_N} \; . \tag{2.65}$$

Corresponding to Equation 2.59, the modified axial current $\tilde{a_0}$ equals the spin contribution carried by the quarks in the proton:

$$\begin{aligned}
\tilde{a_0} &= \frac{\langle p, s_N | \tilde{J}_5^{0\,\mu} | p, s_N \rangle}{2 s_N^\mu M_N} \\
&= \frac{1}{2 s_N^\mu M_N} (\langle p, s_N | J_5^{0\,\mu} | p, s_N \rangle - \langle p, s_N | K^\mu | p, s_N \rangle) \\
&= a_0 + \frac{n_f \alpha_s(Q^2)}{2\pi} \Delta G \underset{\mathrm{Eq.\,2.63}}{=} \Delta\Sigma \ .
\end{aligned} \tag{2.66}$$

Thus, $\Delta\Sigma$ is scale independent in this framework. The stunning consequence is that:

$$\lim_{Q^2 \to \infty} \alpha_s(Q^2) \Delta G(Q^2) = \text{const.} \ , \tag{2.67}$$

to first order. Therefore with rising Q^2, $\Delta G(Q^2)$ grows monotonically in the way $\alpha_s(Q^2)$ decreases. More precisely, it can be shown that [63, 64]:

$$\frac{d\, \alpha_s(Q^2) \Delta G(Q^2)}{d\, \ln Q^2} = 0 + \mathcal{O}(\alpha_s^2(Q^2)) \ . \tag{2.68}$$

For rising values of Q^2 at constant $\Delta\Sigma$, the helicity conservation formulated in Equation 1.1 only stays valid if the increasing polarized gluon density is compensated by a change in orbital angular momentum L_z. It can be shown that during the quark evolution processes (Fig. 2.6) indeed gluons in preferred helicity states are produced. This leads to an opposite orbital angular momentum of the participating qg-pair and hence a contribution to L_z [68].

To come to a conclusion, perturbative QCD is needed to define the tools to understand the role of quarks and gluons in the nucleon. However, up to now quantum chromodynamics can only serve the relevant interconnections but not give predictions for $\Delta\Sigma$, ΔG and L_z which have to be measured to get deeper insight.

2.3.2 Photon-Gluon Fusion

A direct way to measure ΔG is to isolate the *photon-gluon fusion* (PGF) process (Fig. 2.8, left) in polarized lepton-nucleon interactions. Photon-gluon fusion was first suggested by Babcock, Sivers, and Wolfram [69] to explain charm production cross sections by a QCD effect. In the PGF process the photon interacts with a gluon from the target nucleon by exchanging a virtual quark. The result is a quark-antiquark pair which is produced back-to-back in the photon-gluon center-of-mass system. The Mandelstam variables for this subprocess are:

$$\hat{s} = (q + p_g)^2 \quad , \quad \hat{t} = (q - p_q)^2 \quad , \quad \hat{u} = (q - p_{\bar{q}})^2 \ , \tag{2.69}$$

where q is the momentum four-vector of the virtual photon, p_g the four-vector of the gluon and p_q ($p_{\bar{q}}$) the four-vector of the produced quark (antiquark). The Mandelstam variables are connected to Q^2 and the mass m_q of the produced quarks ($m_{gluon} \to 0$):

$$\hat{s} + \hat{t} + \hat{u} = 2m_q^2 - Q^2 \ . \tag{2.70}$$

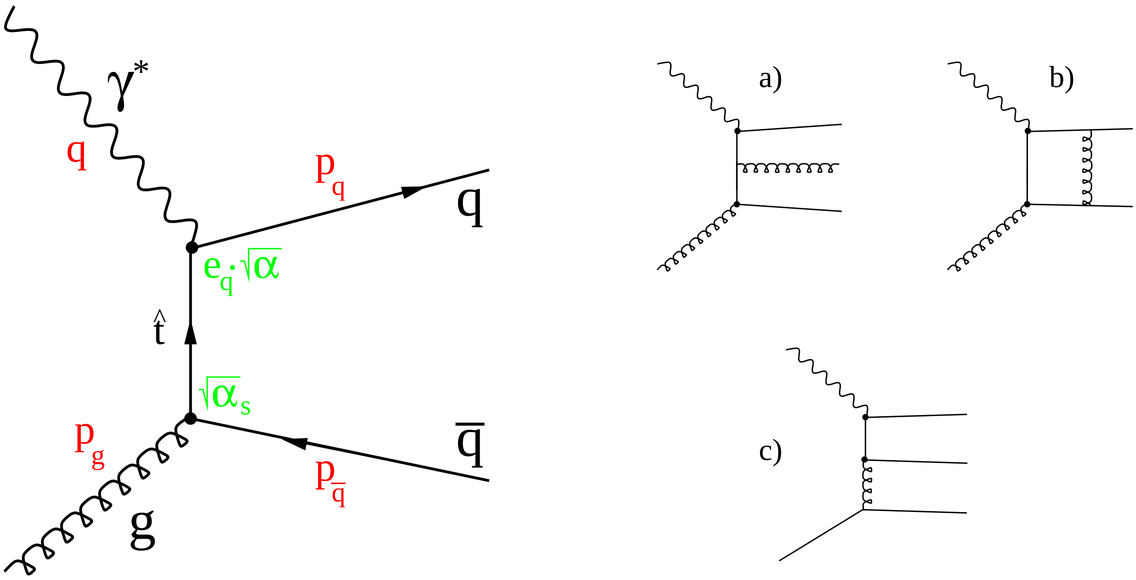

Figure 2.8: Left: The leading order Feynman graph of the photon-gluon fusion process. **Right**: Next-to-leading order radiative corrections. The graph a) is the dominant correction term in charm production. The process b) interferes with leading order PGF because of their same final state resulting in an $\mathcal{O}(\alpha\alpha_s^2)$ contribution to the cross section. Graph c) contributes directly to $\mathcal{O}(\alpha\alpha_s^2)$.

Charm Production

The theoretically and experimentally cleanest way to isolate PGF is to look at reactions in which a charm quark and an anti-charm quark are produced. The cross section can be factorized according to the Weizsäcker-Williams approach [18, 19] (see also treatment in Equation 2.17):

$$\frac{d\sigma^{\ell N\to c\bar{c}}}{d\hat{s}} = \Gamma(\nu, Q^2) \cdot \frac{d\sigma^{\gamma^* g\to c\bar{c}}}{d\,\hat{s}} \cdot g(x_g, \mu^2) \ . \tag{2.71}$$

The cross section is proportional to the gluon density where the gluon momentum fraction is for $\nu \gg M_N$ fixed by the kinematic relation $x_g = \hat{s}/2M_N\nu$. The scale at which the gluon distribution is probed is usually set to $\mu^2 = \hat{s}$. Since the mass of the charm quark is about $m_c \approx 1.1-1.4$ GeV and $\sqrt{\hat{s}} > 2m_c$, the scale μ^2 always is large enough compared to Λ^2_{QCD} to carry out perturbative calculations of $d\sigma^{\gamma^* g\to c\bar{c}}$. If the experiment is carried out with a polarized beam and target, the polarized cross section $\Delta\sigma^{\ell N\to c\bar{c}} = \sigma_+^{\ell N\to c\bar{c}} - \sigma_-^{\ell N\to c\bar{c}}$ is proportional to $\Delta g(x_g, \mu^2)$:

$$\frac{d\,\Delta\sigma^{\ell N\to c\bar{c}}}{d\hat{s}} = \frac{1}{D} \cdot \frac{d\,\Delta\sigma^{\gamma^* g\to c\bar{c}}}{d\,\hat{s}} \cdot \Delta g(x_g, \mu^2) \ . \tag{2.72}$$

Thus, a double spin asymmetry $A_{\shortparallel}^{c\bar{c}}$ from counting photoproduction charm events is sensitive to $\Delta G/G$:

$$A_{\shortparallel}^{c\bar{c}} \sim \frac{\Delta\sigma^{\ell N \to c\bar{c}}}{\sigma^{\ell N \to c\bar{c}}} \sim \frac{\Delta\sigma^{\gamma g^* \to c\bar{c}}}{\sigma^{\gamma g^* \to c\bar{c}}} \cdot \frac{\Delta G}{G} \,, \tag{2.73}$$

with the integration over the applicable Q^2, ν and x_g ranges. The cross sections $\sigma^{\gamma g \to c\bar{c}}$ and $\Delta\sigma^{\gamma g \to c\bar{c}}$ have been explicitely calculated in the photoproduction limit $Q^2 \to 0$ [70,71].

Contributions from higher-order processes to the PGF charm cross section (Fig. 2.8, right) have been calculated for real [72] and for virtual photons [73]. Radiative corrections on the cross section of up to 60% compared to the leading-order expression are expected to come from order $\mathcal{O}(\alpha\alpha_s^2)$. The kinematic shape of the corrections is found to be similar to the leading-order cross section so that radiative corrections can be accommodated for by a a simple scale factor K to the leading-order cross section [64].

Photon-gluon fusion can be tagged by detecting a $D \to K\pi$ meson which came from the fragmentation of one of the charm quarks (*open charm*). The main background arises from non-resonant $K\pi$ production which can be suppressed by requiring an additional soft pion from the decay $D^* \to D\pi_{soft}$ among the final state hadrons. Open charm production of D^* mesons in DIS and photoproduction has been used to extract the unpolarized gluon density [75]. Measurements of photoproduced D^* mesons at HERMES have been attempted [76, 77] but did not yield enough events for a double spin asymmetry since the HERMES center-of-mass energy is just little above the charm production threshold. Future experiments like COMPASS [78] and E161 [79] are proposed to measure $\Delta G/G$ via charm production from photon-gluon fusion events.

In the production of *hidden charm* the quark-antiquark pair produced in the PGF process recombines to a J/ψ meson. In this case an additional soft gluon needs to be exchanged after the hard reaction to give a colour singlet J/ψ. Such production mechanisms are covered by the colour singlet model [80] and the colour octet model [81]. Both models find $\Delta G/G$ to be proportional to a double spin asymmetry in J/ψ production but differ in the predicted analyzing powers. Experimentally, the clear identification of hidden charm events is complicated by the background from diffractive J/ψ production. First attempts to measure double spin asymmetries at HERMES in J/ψ production can be found in [82]. Similarly, the unpolarized gluon density was extracted by NMC [83] and EMC [84] from measurements of J/ψ production.

Jets with Large Transverse Momenta

Another possible approach to measure the (polarized) gluon density is to tag photon-gluon fusion events which resulted in the production of light quarks ($m_q \to 0$). The unpolarized and polarized PGF cross sections for light quarks in the final state can be calculated in QCD for the parton subprocess [85,86]:

$$\frac{d\,\sigma^{\gamma g \to q\bar{q}}}{d\,\hat{t}} = \frac{\pi\alpha\alpha_s e_q^2}{\hat{s}^2}\left(\frac{\hat{u}}{\hat{t}} + \frac{\hat{t}}{\hat{u}}\right) \quad \text{and} \quad \frac{d\,\Delta\sigma^{\gamma g \to q\bar{q}}}{d\,\hat{t}} = -\,\frac{\pi\alpha\alpha_s e_q^2}{\hat{s}^2}\left(\frac{\hat{u}}{\hat{t}} + \frac{\hat{t}}{\hat{u}}\right) \,, \tag{2.74}$$

in the photoproduction limit $Q^2 \to 0$. In contrast to PGF charm production, the parton level cross section is colinearily divergent (i.e. for $\hat{u} \to 0$ or $\hat{t} \to 0$) and the contributions of higher-order processes are not determined for low energies like at HERMES. At very high energies the influence on a measured spin asymmetry is found to be less than 30% [88] ($\hat{s} > 200$ GeV^2). Radiative corrections at low energies are believed to scale the unpolarized cross section with a factor K, equivalently to charm production. Because of the colinear divergence, the expressions 2.74 are only valid if the quarks are emitted with a sizable $\hat{p}_T^2 = \hat{t}\hat{u}/\hat{s}$. The factorization and renormalization scale is usually chosen to be $\mu^2 = \hat{p}_T^2$ which has to be larger than 1 GeV^2 to ensure the validity of this approach. Thus, photon-gluon fusion can be tagged by measuring a quark and antiquark jet at large transverse momenta relative to the virtual photon. The electroproduction cross section for two large-p_T jets and a jet from the target remnant (2+1 jets) can be written as:

$$\frac{d\,\sigma^{\ell N \to (2+1) jets}}{d\hat{t}} = \Gamma(\nu, Q^2) \cdot \sum_{q=u,d,s} \frac{d\,\sigma^{\gamma^* g \to q\bar{q}}}{d\,\hat{t}} \cdot g(x_g, \hat{p}_T) \;, \tag{2.75}$$

and is largest for $Q^2 \to Q^2_{min} = \frac{m_e y^2}{1-y}$ when the photon flux becomes maximal. Thus the best chance of tagging PGF are given in the limit of quasi-real photons which for simplicity will be called photoproduction in the following. The gluon density is probed at the momentum fraction:

$$x_g = \frac{\hat{s} + Q^2}{2M_N \nu} = x_{Bj}(1 + \hat{s}/Q^2) \qquad \text{for} \qquad \nu \gg M_N \;. \tag{2.76}$$

Equation 2.75 can be used to extract the gluon density from a direct measurement from the production of large-p_T jets (Fig. 2.9). This was done for instance at the E665 experiment by studying the energy correlations between jets [89]. Recently, the H1 experiment determined the gluon density by measuring 2+1 jet configurations [90] and found agreement with the predictions from scaling violations and measurements from charm production (Fig. 2.10).

The same idea can be utilized to measure Δg with jet production in polarized $\vec{\ell}\vec{N}$ collisions. The parton level analyzing power $\hat{a}_{PGF}$ is then defined by the cross section asymmetry:

$$\hat{a}_{PGF} = \frac{\Delta\sigma^{\gamma^* g \to q\bar{q}}}{\sigma^{\gamma^* g \to q\bar{q}}} \underset{Q^2 \to 0}{=} -1 \;. \tag{2.77}$$

The parton level cross sections have also been calculated for virtual photons (see for instance [87]), causing the analyzing power to rise slightly with Q^2 ($\hat{a}_{PGF} \approx Q^2/\hat{s} - 1$ for $y \to 1$) and the cross section to fall with $1/(\hat{s} + Q^2)^2$. The transverse momenta of the quarks relative to the virtual photon are given by $\hat{p}_T^2 = \hat{s}\hat{t}\hat{u}/(\hat{s} + Q^2)^2$ in this case. A measured double spin asymmetry $A_\parallel$ on PGF events can be related to $\Delta g/g$:

$$A_\parallel^{q\bar{q}}(x_g, \hat{p}_T^2, Q^2, \nu) = \frac{\Delta\sigma^{\ell N \to q\bar{q}}}{\sigma^{\ell N \to q\bar{q}}} = \hat{a}_{PGF} \cdot \frac{1}{D(\nu, Q^2)} \cdot \frac{\Delta g(x_g, \hat{p}_T^2)}{g(x_g, \hat{p}_T^2)} \;, \tag{2.78}$$

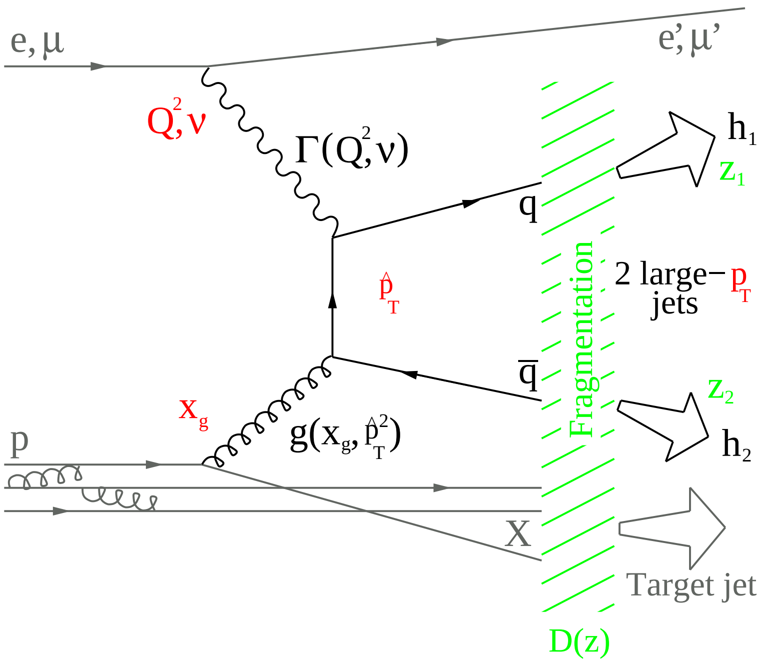

Figure 2.9: Illustration of photon-gluon fusion in an ep or μp reaction. The emerging quark-antiquark pair fragments into two large-p_T jets (or hadrons h_1 and h_2) while the proton remnant forms a target jet.

with the depolarization factor of the virtual photon $D(\nu, Q^2)$. In case of the lower energies at fixed target experiments compared to colliders the observation of correlated hadron pairs at large transverse momenta serves to tag PGF instead of jets. This ansatz was firstly motivated by Bravar, Harrach, and Kotzinian [93] together with a cut strategy for the COMPASS experiment [78] derived by the Monte Carlo program POLDIS [87]. This was confirmed by several cross section calculations for large-p_T hadron pair production for COMPASS and HERMES kinematics [94,95]. Regarding the fact that the produced quark and antiquark each end up in a hadron, the polarized electroproduction cross section is:

$$\frac{d^3\,\Delta\sigma^{\ell N\to h_1 h_2}}{dQ^2\,d\nu\,d\hat{t}} = \Delta\Gamma(\nu, Q^2) \sum_{q=u,d,s} \frac{d\sigma^{\gamma^* g\to q\bar{q}}}{d\,\hat{t}}\ \Delta g(x_g, p_T^2)\ \left[\mathrm{D}_q^{h_1}(z_1)\mathrm{D}_{\bar{q}}^{h_2}(z_2) + \mathrm{D}_{\bar{q}}^{h_1}(z_1)\mathrm{D}_q^{h_2}(z_2)\right]\ . \tag{2.79}$$

The detection of a h^+h^- pair is preferable because the product of two favoured fragmentation functions will enter Equation 2.79. The clear identification of large-p_T hadron pairs is complicated by other sources of transverse momentum like intrinsic k_T, p_T acquired in the fragmentation, or multiple soft gluon radiation of the outgoing quarks. Also background events from hard QCD processes and vector meson production have to be regarded.

Background processes to the photon-gluon fusion process are depicted in Figure 2.11. The competing QCD process to PGF is the QCD Compton process (QCDC) where the

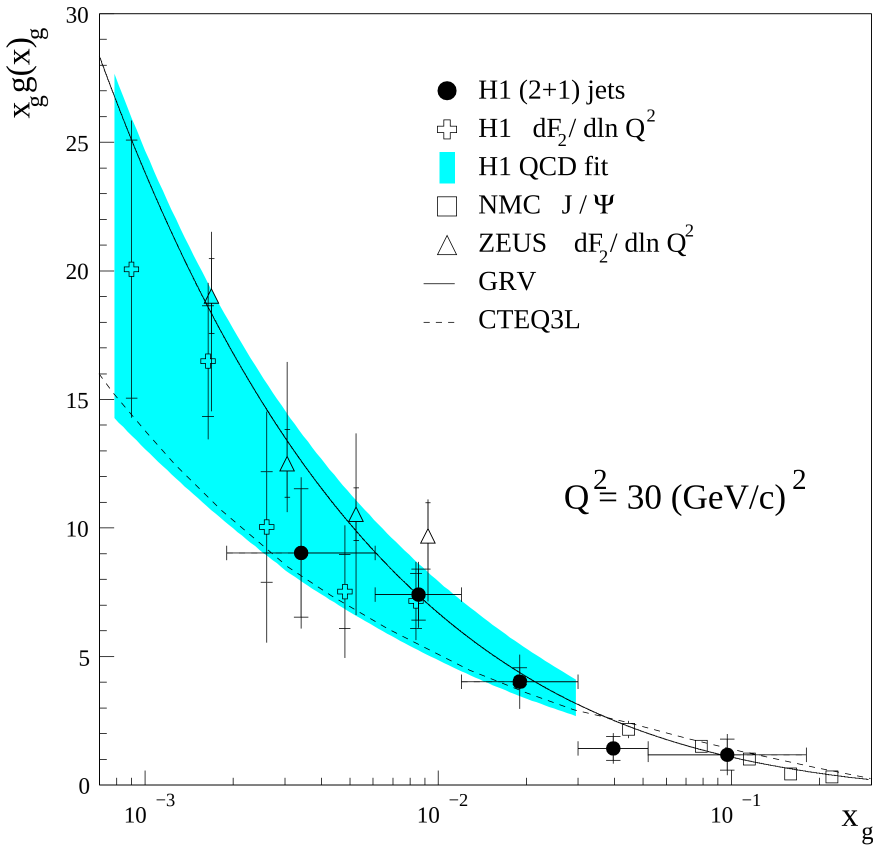

Figure 2.10: The measured gluon density by a (2+1) jet analysis (solid circles) by H1 [90]. The results are compared with indirect determinations by H1 [91] and ZEUS [92] as well as a measurement by NMC from J/ψ production (evolved to $Q^2 = 30\ \mathrm{GeV}^2$) [83]. QCD fits exploiting the scaling violation of F_2 are superimposed (H1 QCD fit, GRV, CTEQ3L).

quark which absorbed the virtual photon radiates off a hard gluon. The parton level cross sections for QCDC are known from QCD [85, 86]:

$$\frac{d\,\sigma^{\gamma q\to qg}}{d\,\hat{t}} = \frac{8\pi\alpha\alpha_s e_q^2}{3\hat{s}^2}\left(-\frac{\hat{s}}{\hat{u}} - \frac{\hat{u}}{\hat{s}}\right) \quad \text{and} \quad \frac{d\,\Delta\sigma^{\gamma q\to qg}}{d\,\hat{t}} = \frac{8\pi\alpha\alpha_s e_q^2}{3\hat{s}^2}\left(-\frac{\hat{s}}{\hat{u}} + \frac{\hat{u}}{\hat{s}}\right)\,, \tag{2.80}$$

From these expressions the parton level analyzing power for the QCD Compton process can be inferred:

$$\hat{a}_{QCDC} \;=\; \frac{\hat{s}^2 - \hat{u}^2}{\hat{s}^2 + \hat{u}^2} \underset{\hat{u}\to -\hat{s}/2}{=} \frac{3}{5}\ . \tag{2.81}$$

The analyzing power is positive and amounts to $\frac{3}{5}$ for the case of the largest possible $\hat{p}_T$. Since both DIS and QCDC probe the quarks in the nucleon, their double spin asymmetries are approximately proportional to A_1. Contributions from vector meson production and anomalous photon processes are expected to have a zero double spin asymmetry. A measured double spin asymmetry will result from a composite of all processes involved at large transverse momenta. This complex situation with a variety of competing processes is best evaluated by the modeling of a Monte Carlo simulation which can be used to optimize the cut strategy (see Chapter 6) and to find the contributing fractions of PGF and the background processes (Chapter 7). HERMES has recently attempted a model-based extraction of $\Delta g/g$ from a measured negative double spin asymmetry for the production of hadron pairs at large transverse momenta from data on polarized ^{1}H [96]. From all the processes mentioned above only PGF in connection with a positive gluon polarization may cause such a result ($\hat{a}_{PGF} = -1$) since all other processes have positive or zero asymmetry.

This work extends the analysis of the publication [96] to all polarized HERMES datasets from the running year 1996 to 2000. The analysis ansatz is supported by investigations on the modeling of the fragmentation process and on the definition of a consistent cut strategy. The latter uses the PYTHIA6 Monte Carlo simulation [165] which will also be employed to extract a value for the gluon polarization.

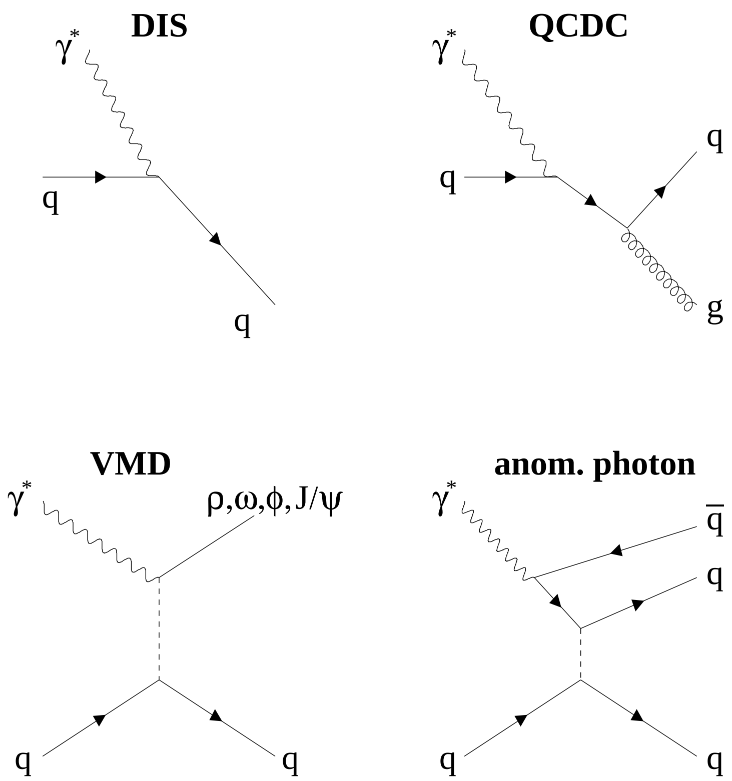

Figure 2.11: Processes which contribute to the production of two hadrons at large transverse momenta and pose a background for photon-gluon fusion events. The description of the single processes can be found in Section 7.1.1 of Chapter 7.

2.3.3 Measurements in pp-Collisions

The gluon polarization can also be accessed through prompt photon production in polarized proton-proton or proton-antiproton scattering [97]. The two underlying subprocesses are $q\bar{q} \to \gamma g$ (quark-antiquark annihilation) and $qg \to \gamma q$ (inverse QCD Compton process) shown in Figure 2.12. In $\vec{p}\vec{p}$ collisions the quark-antiquark annihilation contributes only 10% to the leading order cross section (at $\sqrt{s} = 200$ GeV) since the antiquark density in the nucleon is small compared to the gluon density at that scale. If in a $\vec{p}\vec{p} \to \gamma + jet + X$ reaction the inverse QCD Compton process dominates, a measured double spin asymmetry is proportional to $\Delta g/g$:

$$A_{\parallel} \sim \hat{a}(qg \to \gamma q) \cdot \frac{\Delta g}{g} \cdot \frac{\sum_i e_i^2 \Delta q_i}{\sum_i e_i^2 q_i} \,. \tag{2.82}$$

Such a measurement is proposed as part of the RHIC spin program [98, 99] with the detectors STAR and PHENIX. In case of the STAR experiment the expected partonic asymmetry $\hat{a}$ varies from 0.05 to 0.2 as x_g goes from 0.03 to 0.3. Main sources of background like photons from π^0 or η decays in the fragmenting jets are hoped to be suppressed by cuts which kinematically isolate the photon [100].

An additional possibility offers the study of the single or di-jet cross section asymmetries in polarized proton-proton collisions [101]. Single jet production at large transverse energy flow in $\vec{p}\vec{p}$ collisions is sensitive to Δg. In intermediate regions of transverse energy flow di-jets could be used to determine Δg [102].

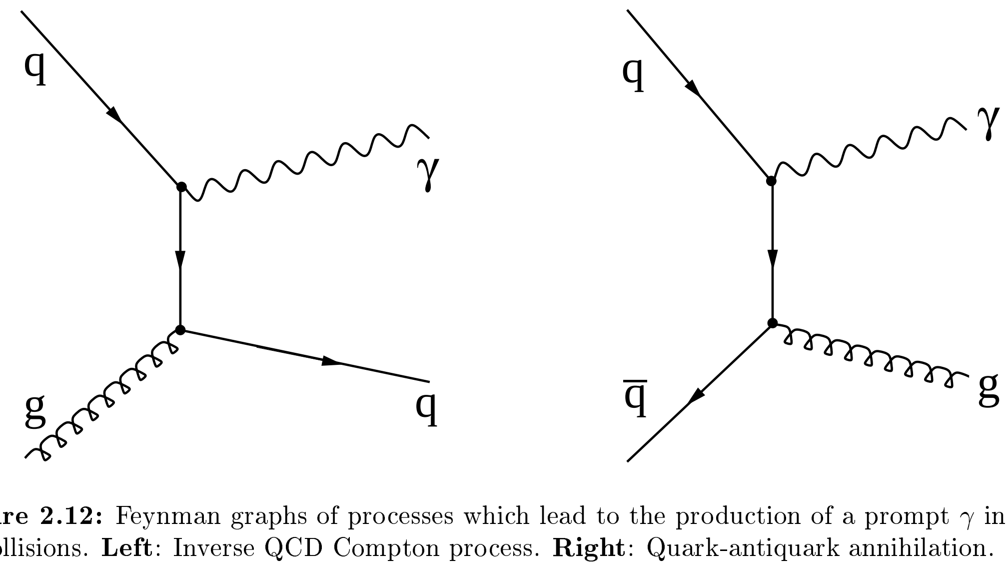

Figure 2.12: Feynman graphs of processes which lead to the production of a prompt γ in pp or $p\bar{p}$ collisions. **Left**: Inverse QCD Compton process. **Right**: Quark-antiquark annihilation.

3 The HERMES Experiment

The 6.3 km long storage ring HERA at DESY consists of a 920 GeV proton beam and a 27.5 GeV positron beam[2] and hosts four high-energy physics experiments: H1, ZEUS, HERMES, and HERA-B (Fig. 3.1). The HERMES experiment is located at the east area and utilizes the polarized positron beam only. Two spin rotators are installed up- and downstream of the HERMES interaction region. Each spin rotator is an arrangement of three horizontally and three vertically deflecting magnets, which turn the transverse polarization of the positron beam into the longitudinal direction and back, respectively [103] . In order to reduce systematic uncertainties for spin-dependent measurements, the spin rotators can also be arranged to reverse the orientation of the longitudinal beam polarization. At HERMES, the polarized beam is scattered off polarized or unpolarized target gas which is injected into a ring-internal storage cell. Downstream of the storage cell follows the HERMES forward spectrometer which detects the products of the initiated positron-nucleon reactions.

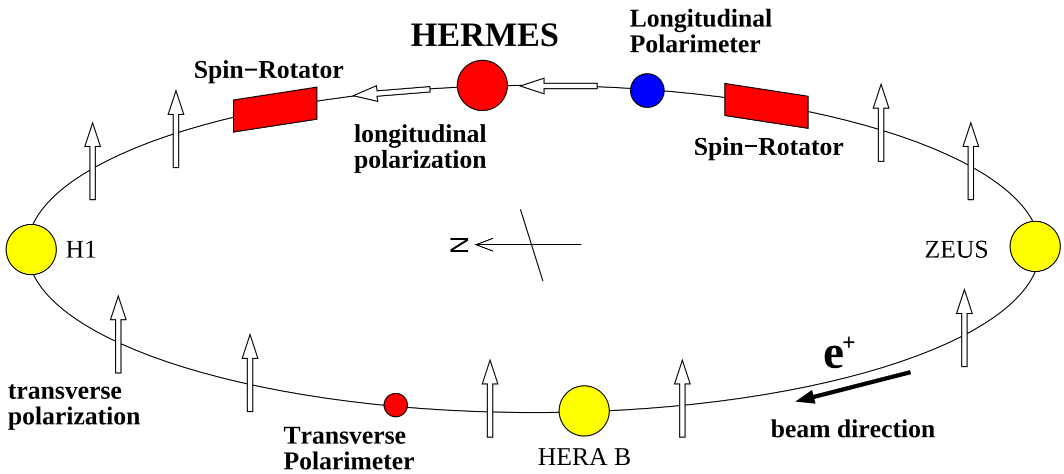

Figure 3.1: Sketch of the HERA positron ring at DESY in Hamburg, Germany. The open arrows indicate the direction of the beam polarization.

3.1 The Polarized Positron Beam

The positron beam becomes transversely polarized by the Sokolov-Ternov mechanism [104] . By emission of synchrotron radiation in the arcs of the storage ring, positrons can flip their spin direction. Since the spin-flip amplitude involves a small asymmetry, the spin state parallel to the magnetic guiding field of the ring becomes slowly populated [105]. The polarization builds up with time according to:

$$P(t) = P_\infty(1 - e^{-t/\tau}) \;, \tag{3.1}$$

where P_∞ is the asymptotic polarization and τ the characteristic rise-time. For an ideal

[2]Except for the year 1998, HERA operated from 1995 to 2000 with positrons instead of electrons.

synchrotron without vertically deflecting magnets (i.e. without spin-rotators) the theoretical maximum asymptotic polarization can be calculated to be $P_{opt} = 92.4\%$. The rise-time depends on the beam energy and the bending radius of the ring giving $\tau_{opt} = 36.5$ min in the case of HERA.

However, depolarizing effects in a real storage-ring can change the rise-time and substantially reduce the maximum achievable polarization. The main contribution to these effects comes from non-vertical magnetic fields which tip the positron spin. In the semi-classical picture this can be seen by employing the Thomas-Bargman-Michel-Telegdi (T-BMT) Equation [106] . So, slightly misaligned magnets in the HERA lattice or deviations of the orbit from its design course resulting in non-zero field components in quadrupole magnets can disturb the positron spins. But also oscillations of positrons within a bunch caused by synchrotron radiation or Coulomb interaction with the colliding proton bunches limit the achievable polarization ([107, 108] and references therein). The number of rotations of the classical spin vector of the positron during a revolution in the synchrotron is called the *spin tune* ν_s and is given by:

$$\nu_s = \left(\frac{g}{2} - 1\right)\gamma\,, \tag{3.2}$$

where g is the gyromagnetic ratio of the positron and $\gamma = 5.4 \cdot 10^4$ is the positron Lorentz factor at HERA. All depolarizing effects can be incorporated into a time constant τ_{dep} which then modifies the rise-time τ and the asymptotic polarization P_∞:

$$\frac{1}{\tau} = \frac{1}{\tau_{opt}} + \frac{1}{\tau_{dep}}, \qquad \text{and} \tag{3.3}$$

$$P_\infty = P_{opt}\,\frac{\tau_{dep}}{\tau_{opt} + \tau_{dep}} \qquad . \tag{3.4}$$

On one hand depolarizing effects reduce the maximum asymptotic polarization, on the other hand they shorten the rise-time. Depolarization can be minimized by tuning the positron orbit using the method of *harmonic bumps* [109] and setting the spin tune off the betatron- and synchrotron tunes of the accelerator by changing the beam energy at the order of a few MeV. At HERA a spin tune of $\nu_s = 62.5$ is chosen corresponding to a beam energy of 27.56 GeV. Apart from the points mentioned above this setting has the advantage of qualitatively compensating disturbances of the spins after two turns.

If Equation 3.4 is used to eliminate τ_{dep} in Equation 3.3, for a synchrotron without spin rotators:

$$\tau = P_\infty \left(\frac{\tau_{opt}}{P_{opt}}\right), \tag{3.5}$$

is obtained. Thus, typical beam polarizations of 50-60% reached at HERA correspond to rise-times of 20 to 24 minutes. In principle, the scale of a beam polarimeter can be calibrated using Equation 3.5 if the exponential rise and the asymptotic settlement of the polarization is measured (*rise-time calibration*).

3.2 The Internal Gas Target

The 40 cm long storage cell is embedded in the target vacuum chamber (Fig. 3.2) which is built into the HERA positron ring. The cell, with an elliptical cross section[3] of $9.8 \times 29.0\,\mathrm{mm}^2$, is made out of 75 μm thin ultra-pure aluminum in order to reduce multiple scattering of outgoing particles. The cell is cooled to about 70-100 K and coated with Drifilm and a layer of ice to conserve the polarization of the bouncing atoms within. Upstream, a set of collimators shields the target region against synchrotron light and particles from the beam halo. Downstream, a 0.3 mm thin exit window and a beam pipe of similar thickness ensure minimal interaction between the material and the produced particles. Thin titanium meshes at the ends of the storage cell provide a smooth conductive transition from the circular beam pipe to the elliptical target cell. Thus, wake fields that would heat up the cell are prevented. The polarized gas is injected in the middle of the cell and differentially pumped away at its open ends. In order to define a spin quantization axis along the beam direction and to avoid spin relaxation, the electron and nuclear spins are decoupled by a longitudinal magnetic holding field (0.34 T for ^{1}H and ^{2}H).

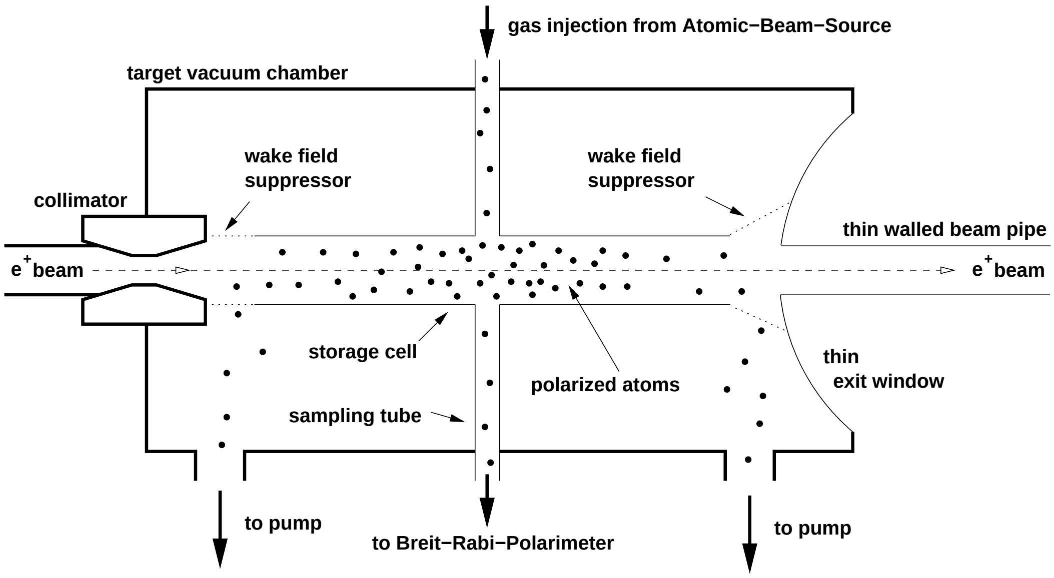

Figure 3.2: Schematic view of the HERMES target vacuum chamber.

3.2.1 Polarized ^{1}H and ^{2}H Targets

The polarized target consists of an atomic beam source (ABS), a Breit-Rabi polarimeter (BRP), and a Target Gas Analyzer (TGA); all of them connected to the storage cell (Fig. 3.3). The ABS supplies the target cell with polarized hydrogen or deuterium atoms, while the BRP measures the polarization of the gas sampled off the cell by a sampling tube. Additionally, the TGA measures the degree of dissociation of the target gas with a quadrupole mass spectrometer.

[3]In 2000 a smaller cell with the measures $8.9 \times 21.0\,\mathrm{mm}^2$ was installed.

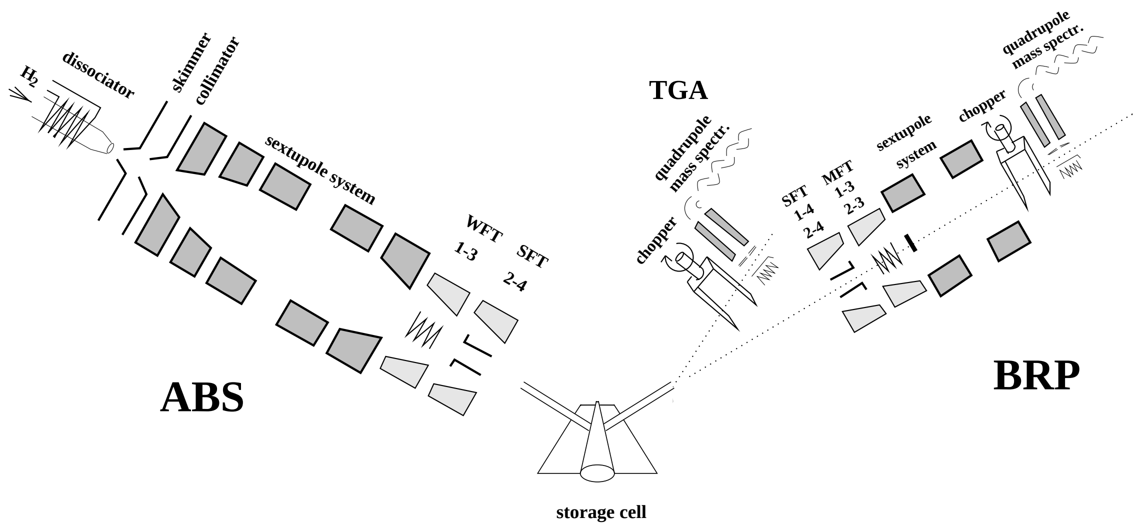

Figure 3.3: Schematic picture of the polarized hydrogen target with Atomic Beam Source (ABS) and its transition units (WFT, SFT), Breit-Rabi Polarimeter (BRP), and Target Gas Analyzer (TGA). For polarized deuterium operation, an additional field transition unit (MFT) was installed into the ABS.

The Atomic Beam Source

The ABS [110–112] uses a radio frequency (or microwave) dissociator [113] to atomize molecular hydrogen/deuterium before injecting the atoms through a cooled nozzle into a sextupole magnet system. The preparation of nuclearly polarized gas is achieved by the principle of a Stern-Gerlach separation, explained for hydrogen in the following. The sextupole magnets select the hyperfine states $|1>$ and $|2>$ with electron spin orientation $m_s = +\frac{1}{2}$ and nuclear spin orientations $m_I = +\frac{1}{2}$ and $-\frac{1}{2}$, respectively (Fig. 3.4, left). All other states are deflected and pumped away. Adiabatic high frequency transitions can now transfer the electron spin polarization to the nuclear spin. This is realized either by the weak field transition unit (WFT) which interchanges the occupation numbers of the hyperfine states $|1>$ and $|3>$ ($m_s = -\frac{1}{2}$, $m_I = -\frac{1}{2}$). Or the strong field transition unit (SFT) is activated to flip the occupation of the states $|2>$ and $|4>$ ($m_s = -\frac{1}{2}$, $m_I = +\frac{1}{2}$). Thus, the nuclear spin direction can be chosen by employing either the WFT or the SFT resulting in a highly polarized ensemble of nuclei which are injected into the storage cell. Moreover, the electron polarization of the two selected states is zero on average. The supply of a polarized deuterium beam is reached similarily by a different set of field transition units. Because deuterium is a spin-1 nucleus, there are six hyperfine states (Fig. 3.4, right) so the ABS needs an additiononal transition unit (MFT, Medium Field Transition Unit).

In the storage cell, densities of 6.4×10^{16} (5.2×10^{16}) $\frac{\text{nucleons}}{\text{cm}^2}$ can be achieved for polarized hydrogen (deuterium). Nuclear polarizations of up to 90% are realized for both gases. To

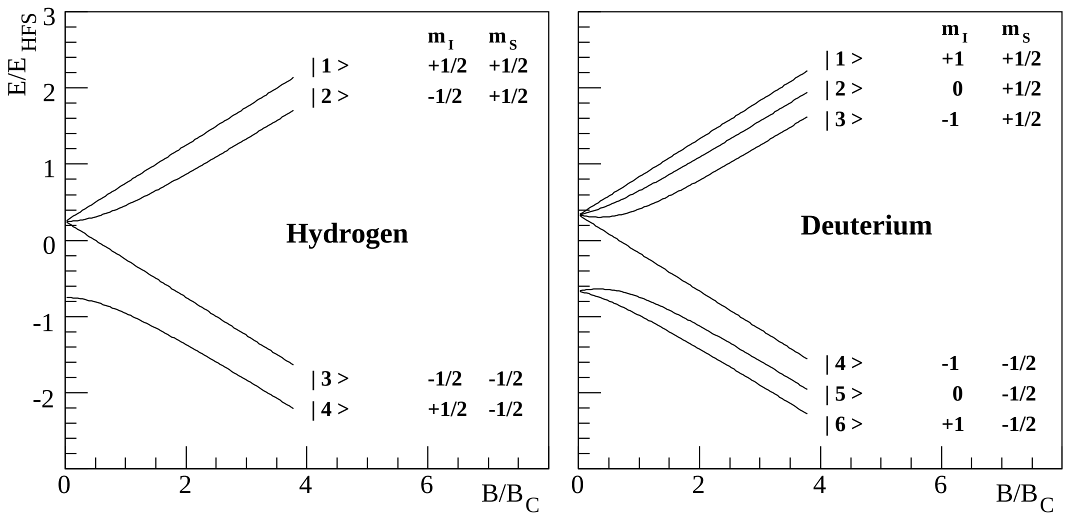

Figure 3.4: The hyperfine states of hydrogen (**left**) and deuterium (**right**). The ratio of the evergy level E relative to the hyperfine splitting energy E_{HFS} is shown as function of the ratio of the external magnetic field B and the critical magnetic field B_C.

minimize systematic effects, the sign of the target polarization was randomly chosen every 45, 90 or 140 seconds depending on the running year.

The Breit-Rabi Polarimeter

The polarimetry of the target is realized by a structure that is in principle the reverse of the ABS: the Breit-Rabi polarimeter (BRP) [114, 115]. It focuses a desired set of hyperfine states into a quadrupole mass spectrometer and deflects the other states. The measurement of the relative population of different hyperfine state combinations yields the information to compute the electron and nuclear polarization of the target gas. The target polarization P_T in the storage cell can be calculated by:

$$P_T = P_{BRP}\,\alpha_0\,(\,\alpha_r\,+\,\beta\,(1-\alpha_r)\,) \quad , \tag{3.6}$$

where P_{BRP} is the polarization of the atoms as measured by the BRP and $\alpha_0 = 0.99 \pm 0.01$ is the degree of dissociation of the gas leaving the ABS. The fraction of atoms that recombine to molecules within the storage cell is $1 - \alpha_r$, while β describes the remaining polarization of a nucleon in a recombined molecule relative to the nucleon polarization in an atom. The degree of recombination α_r can be deduced from TGA measurements (α_r^{TGA}) and a sampling correction: $\alpha_r = c_s\alpha_r^{TGA}$. The sampling correction c_s is needed since the gas sample taken through the sampling tube is not entirely representative for the whole cell as Monte-Carlo simulations show. Typical mean values of α_r are 0.97 ± 0.04 for the 1997, or 0.99 ± 0.01 for the 2000 running, for example. The quantity β could be constrained to lie between 0.2 and 1.0 by analyzing dedicated studies at low and high α_r values [116].

3.2.2 Other Targets

In the commissioning year 1995, HERMES ran with a polarized ^{3}He Target [117]. The corresponding dataset was not used for analysis in this thesis and is therefore not described in detail.

Another interesting alternative for physics measurements as well as for target calibration poses the Unpolarized Gas Feed System (UGFS). It allows to inject a variety of unpolarized gases into the storage cell. Over the entire HERMES running 1995-2000 samples of unpolarized $^1H_2$, $^2H_2$, ^{3}He, $^{14}N_2$, ^{20}Ne and ^{84}Kr have been used. This yielded measurements of unpolarized DIS (see Section 5.2.1, for example) at high statistics, the flavour asymmetry of the light sea quark distributions [118], nuclear effects on vector meson production [119] and hadronization [120], and spin transfer in Λ^0-production [121].

3.3 The Spectrometer

The HERMES forward spectrometer [122] consists of two identically constructed halves, one above and one below the HERA beam pipes (Fig. 3.5). Both, the positron and the proton beam pass through the central plane of the spectrometer and are shielded from the HERMES magnetic field by a steel plate. Each spectrometer half consists of a set of tracking chambers, (trigger) hodoscopes and four particle identification detectors. A

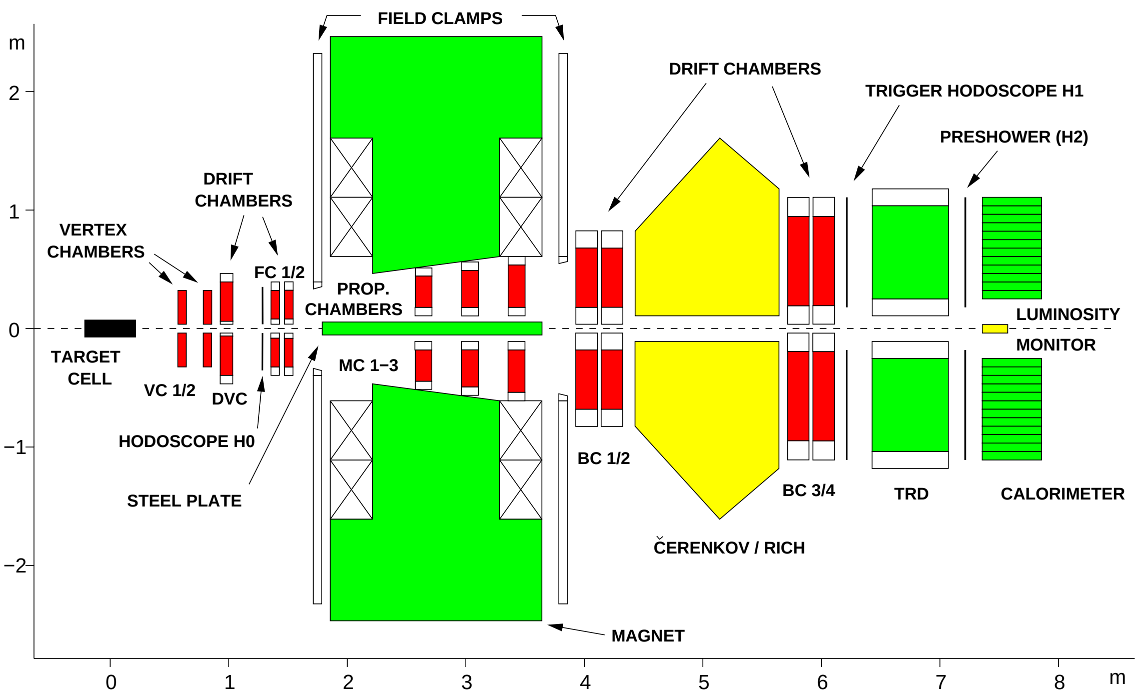

Figure 3.5: Schematic side view of the HERMES spectrometer.

luminosity monitor is installed at the rear of the spectrometer. The acceptance of the spectrometer extends vertically from 40 to 140 mrad and horizontally to ±170 mrad. The resulting total angular acceptance from 40 to 220 mrad covers a large kinematic region.

3.3.1 Magnet and Tracking

The normal-conducting HERMES spectrometer magnet deflects charged particles to analyze their momenta. For this purpose, the dipole magnet provides a vertical field with a deflecting power of $\int B\,dl = 1.3$ T·m. Field clamps in front and back of the magnet protect the adjacent detectors from fringe fields. To shield the HERA beam pipes, they are embedded in a 11 cm thick steel plate. The influence of the magnetic field on the positron beam is compensated additionally by a correction coil.

The HERMES detector contains a series of tracking chambers: two microstrip vertex chambers (VC 1/2), a set of drift vertex chambers (DVC), and two drift chambers (*Front Chambers*: FC 1/2) in front of the magnet; three proportional chambers (*Magnet Chambers*: MC 1-3) in the magnet; and two pairs of drift chambers (*Back Chambers* BC 1/2, BC 3/4) behind the magnet. Each chamber hosts several planes with wires oriented vertically (x-plane) or tilted by ±30° (u,v-planes) with respect to vertical axis. A precise drift-time measurement leads to a spatial resolution of 0.2 -0.3 mm for the drift chambers. The VCs were fully operational only in 1997 and later dismounted due to technical problems. Therefore, only the FCs and the DVC are used to define the partial front track in all data sets used in this thesis. Hits in the BCs determine partial back tracks and allow to link the tracks to the responses of the particle identification detectors. The Magnet Chambers are only used to reconstruct tracks of particles which do not reach the rear of the spectrometer.

The event reconstruction is done by the HERMES Reconstruction Code (HRC) [123]. It reconstructs the partial front and back tracks from the drift chamber hits by a pattern recognition algorithm (*tree-search algorithm*). To increase the precision for the front tracks, an additional artificial point in the middle of the magnet (where the partial back track points) is added (*forced bridging technique*). The momenta of the particles are measured by the slope differences between front and back tracks using a fast lookup-table. This way a relative momentum resolution of (0.7 - 1.3)% is achieved with the HERMES setup. Also *short tracks* which do not reach the rear of the spectrometer are determined using hits in the magnet chambers. Moreover, an iterative fitting algorithm in HRC involving all front tracks finds primary and secondary vertices in the target region.

3.3.2 Particle Identification Detectors

Particle identification (PID) at HERMES is provided by a Čerenkov counter, a transition radiation detector (TRD), a preshower counter, and a lead glass calorimeter. The main task of the PID detectors is to separate reliably positrons from hadrons. After the end of the 1997 running period, the Čerenkov counter was replaced by a dual radiator ring imaging Čerenkov detector (RICH) which is capable of identifying all hadron types over a broad momentum range.

Čerenkov Counter

The threshold Čerenkov counter (Fig. 3.6) was installed between the two back-tracking chamber pairs BC 1/2 and BC 3/4. Particles faster than the speed of light in the detector gas radiate Čerenkov photons ($\beta_{thres} = 1/n_{med}$, n_{med} : refractive index of the radiator). As radiator gas a mixture of 30% C_4F_{10} and 70% N_2 was used in 1996 and 1997. Produced photons are reflected by two rows of 10 mirrors each into 20 corresponding photo-multiplier tubes (for each detector half). The thin entrance and exit windows (0.1 mm Mylar and 0.03 mm Tedlar) minimize multiple scattering of the traversing particles.

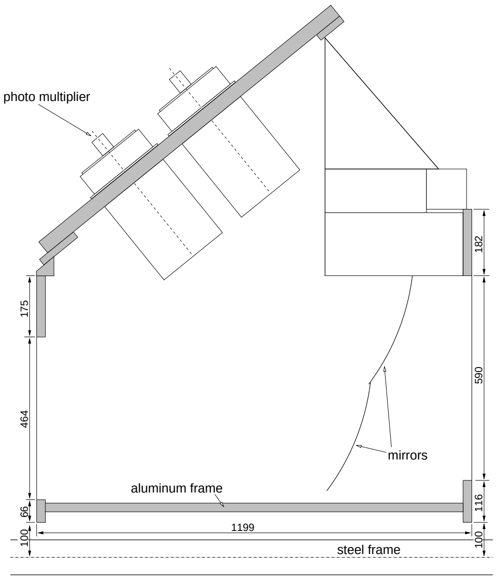

Figure 3.6: Cut view of the upper threshold Čerenkov counter.

Table 3.1: Properties of the threshold Čerenkov counter.

radiator gas	C_4F_{10}/N_2
n_{med}	1.000629
e threshold	0.014 GeV
π threshold	3.9 GeV
K threshold	13.9 GeV
p threshold	26.4 GeV

From the size of the photo-multiplier signals the number of photoelectrons produced by the Čerenkov photons is deduced. Figure 3.8(left) shows that the majority of the hadrons do not leave a signal in the counter while positrons yield about four photoelectrons on average. So, the Čerenkov counter helps to separate positrons and electrons from hadrons. Furthermore, the Čerenkov detector can be used to separate pions from other hadrons between the momenta of the pion and kaon threshold. The momentum threshold for each particle type is given in Table 3.1.

Ring-Imaging Čerenkov Detector (RICH)

In 1998 the threshold Čerenkov detector was replaced by a dual-radiator RICH [124]. Each detector half of the RICH is equipped with two radiator materials: a wall of 5×17 silica aerogel stacks made of five tiles each and a gas volume filled with pure C_4F_{10}. The setup

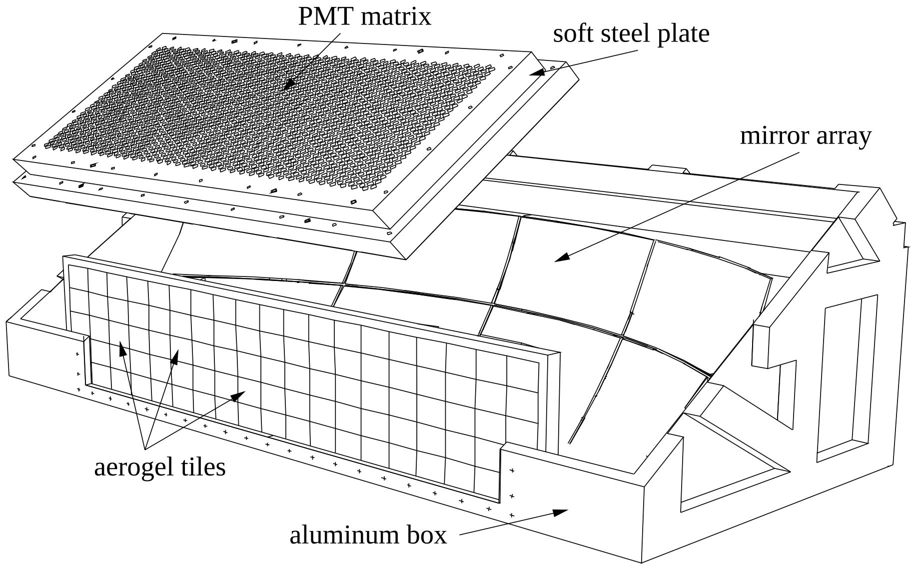

Figure 3.7: A perspective view of the upper RICH detector setup.

is completed by an 2×8 array of spherical mirrors made of aluminized graphite fiber composite coated with epoxy. The mirrors reflect the produced Čerenkov photons on a hexagonal matrix of $74 \times 26/27$ photo-multipliers which is read out by a LeCroy PCOS4 system (Fig. 3.7).

A particle with velocity β above β_{thres} radiates Čerenkov photons on a cone with an opening angle of $\theta_c = \arccos(\,1/(n_{med}\beta)\,)$. The spherical mirrors project the photons on the planar photo-multiplier matrix where they appear as elliptical rings. The emission angle θ_c can be calculated since the position of the track is known from the track reconstruction. The result can be viewed versus particle momentum and can be compared with the theoretical anticipation (Fig. 3.8, right). The refractive indices of the aerogel ($n = 1.0304$) and the gas ($n = 1.00137$) were chosen such that a clean identification of pions, kaons, and protons is ensured over almost the entire HERMES momentum range.

For particle identification with the RICH two different concepts are employed: the *Indirect Ray-Tracing* Method (IRT) and the *Direct Ray-Tracing* Method (DRT) [125]. If the IRT Method is employed, the angular spectrum of the emitted photons is calculated. A window is imposed on the spectrum under the expected angle for each particle type hypothesis. The number of photons found in these ring-shaped areas is then used for a probability analysis to determine the particle type. The advantages of this method lie in its fast and robust calculation. In contrast to this approach, the DRT Method calculates a hit probability for each photo-multiplier of the matrix by a full Monte-Carlo simulation. This is done specifically for the track configuration of every event under all particle hypotheses possible. The particle type is deduced from the actual hits and their simulated probabilities.

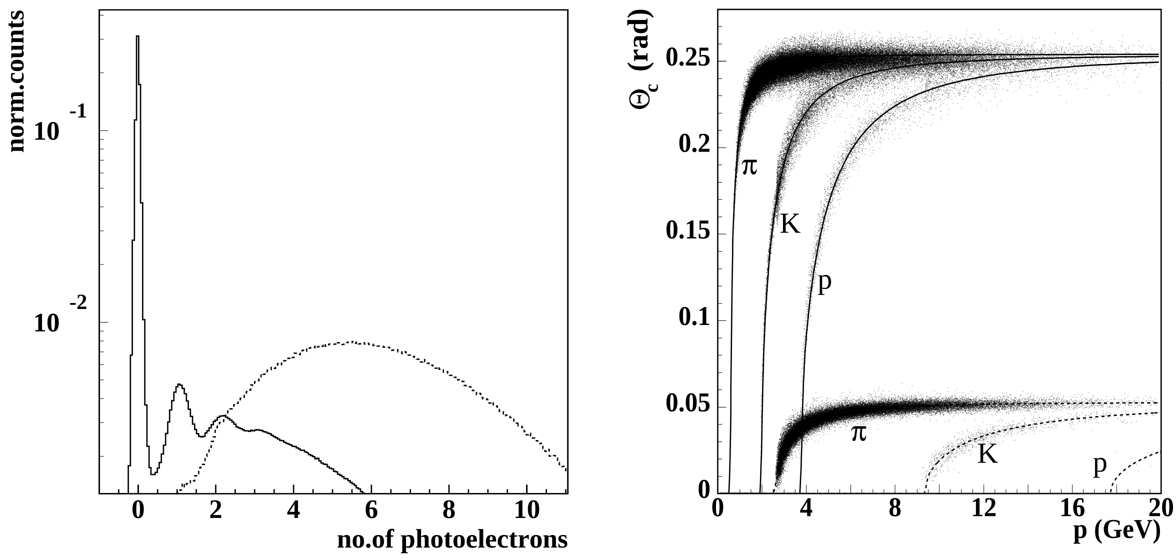

Figure 3.8: The responses of the Čerenkov detectors. **Left**: response of the threshold Čerenkov for hadrons (solid line) and positrons (dashed line) from 1997 data integrated over all momenta. **Right**: the photon emission angle θ_c as measured by the RICH detector versus particle momentum [126]. The theoretical expectations for the silica aerogel (solid line) and the C_4F_{10} gas radiator (dashed line) are superimposed for each particle type.

Compared to the IRT Method, DRT needs orders of magnitude more computing time but for instance identifies events with more tracks in one detector half more reliably. During the processing of HERMES events, a program, the *RICH PID-Scheduler* [127], decides event-wise which method is best to be employed.

Transition Radiation Detector (TRD)

The two halves (top and bottom) of the HERMES TRD are located between the two hodoscopes H1 and H2. Each half consists of six identically constructed modules in a row (Fig. 3.9). A single module contains a 6.35 cm thick matrix of polypropylene/polyethylene fibers as radiator in front of a 2.54 cm thick multi-wire proportional chamber (MWPC). The MWPC is filled with a mixture of 90% Xenon and 10% CH_4 and detects the generated transition radiation photons as well as the energy lost by the charged particle through ionization ($\frac{dE}{dx}$). The anode wires of the MWPC are strung vertically every 1.27 cm enabling a horizontal resolution of the signals, making it possible to link the single wire responses to the partial back tracks of the particles in an event. The large active area of $2 \times 72.4 \times 325\,\mathrm{cm}^2$ of both TRD halves covers the entire HERMES acceptance.

When a highly relativistic point charge traverses a dielectric boundary, it emits electromagnetic radiation. This can be explained by the necessity to add an additional transition radiation field to satisfy Maxwell Equations at the boundary (see for instance [128,129]).

The additional transition radiation field can appear in form of X-ray photons. For a particle with Lorentz factor γ, the photons are mostly emitted under a typical angle of $\varphi \propto \frac{1}{\gamma}$ relative to the track. Because of reabsorption and interference effects, transition radiation photons appear above a threshold proportional to $\gamma\omega_p$ where ω_p is the plasma frequency of the medium. The power radiated above a threshold is also proportional to γ [130]. This enables the identification of highly relativistic ($\beta \approx 1$) particles where conventional, velocity dependent methods (Čerenkov radiation, ionization) fail. Because transition radiation is a relatively small effect, many dielectric surfaces are required for a practical detector.

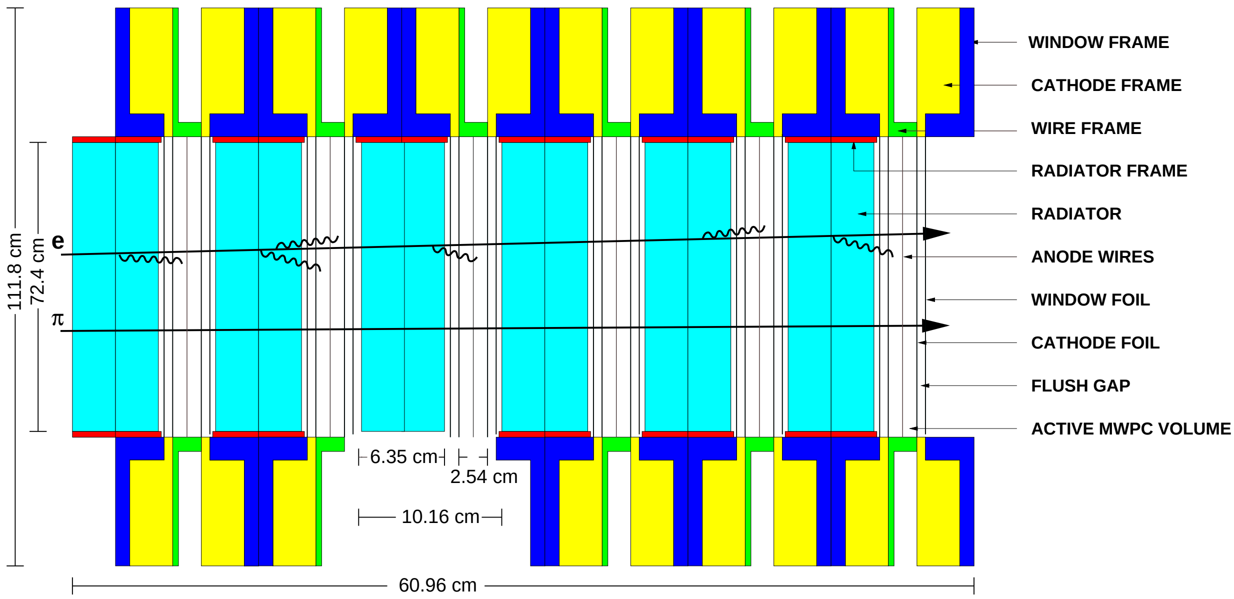

Figure 3.9: One half of the HERMES Transition Radiation Detector. The opening angles of the transition radiation photons emitted by the electron/positron are exaggerated.

The HERMES TRD achieves an equivalent of about 250 surfaces with its radiator. The effective threshold is found to be around $\gamma = 500$ [131]. So, in contrast to a 5 GeV pion ($\gamma = 36$), a positron with the same momentum ($\gamma = 9800$) leaves a larger signal in the MWPC than hadrons because in addition to the higher ionization energy loss, transition radiation photons contribute to the deposited energy. To suppress the Landau tail arising from delta electrons, the *truncated mean* of the six modules is calculated; the mean of all signals without the largest of the six responses (Fig. 3.10, left). At 90% efficiency a pion rejection factor of about 100 is reached. This can be improved by a factor of three using a probability analysis of the responses of the single modules [132](Fig. 3.10, right).

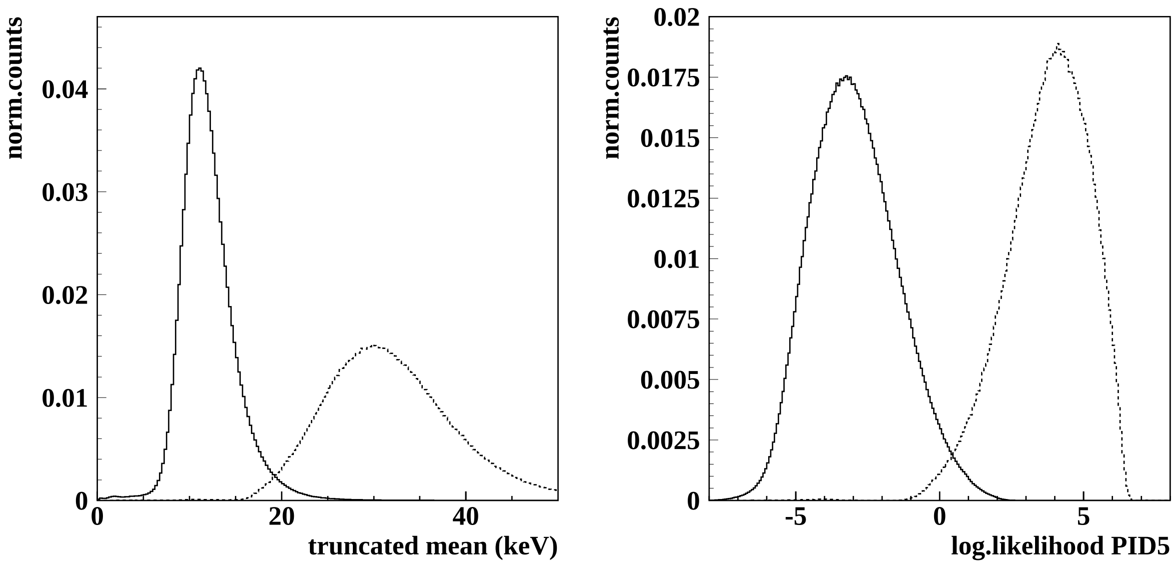

Figure 3.10: The truncated mean of the six TRD module responses (**left**) and the result of the TRD probability analysis (**right**) for hadrons (solid line) and positrons (dashed line).

Preshower Detector

Located behind the TRD, the hodoscope wall H2 with a 11mm lead curtain in front is used as preshower detector. The hodoscope H2 consist of 42 vertical plastic scintillator paddles with photomultipliers mounted on the end away from the beam pipe (Fig. 3.11). The thickness of the lead corresponds to two radiation lengths so positrons have a relatively high probability of starting an electromagnetic shower which can be detected in the scintillators. The resulting light is captured by the photo-multipliers. Since the nuclear interaction length is much larger than a radiation length, hadrons have a much lower probability of showering than positrons. Hadrons will give only a minimum ionizing signal in hodoscope H2 and can be separated from positrons (Fig. 3.12, left).

Calorimeter

The lead glass calorimeter [133] follows downstream of the preshower detector. The calorimeter serves to separate positrons and electrons from hadrons as well as to detect energetic photons. The upper and lower half of the calorimeter can be moved 50 cm away from the beam during injection to avoid radiation damage. Each half consists of 42×10 lead glass blocks of 9×9 cm^2 (Fig. 3.11). Each block is 50 cm long corresponding to 18 radiation lengths. The light is collected in photo-multiplier tubes mounted at the rear of each block. Most particles leave signals in a cluster of blocks. The resolution for a 3×3 cluster is $5\%/\sqrt{E_{CALO}\,[GeV]} \oplus 1.5\%$. By weighting the energies in each block of a cluster, a position resolution of about 1 - 2 cm for photons is achieved.

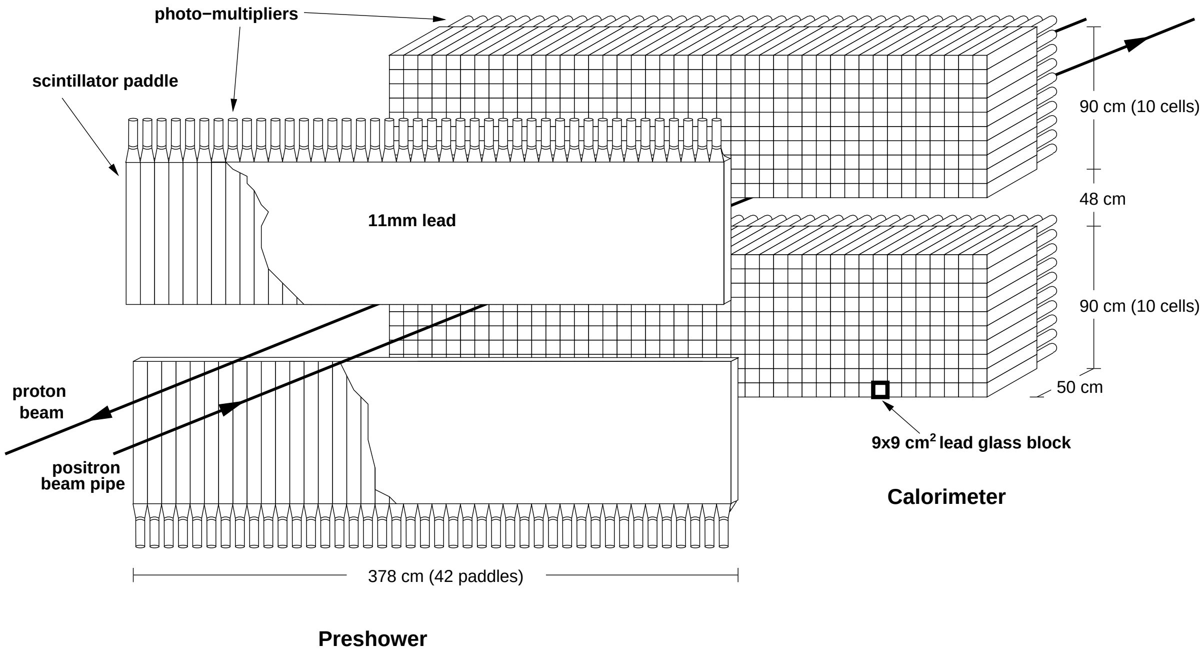

Figure 3.11: Perspective view of preshower detector and calorimeter.

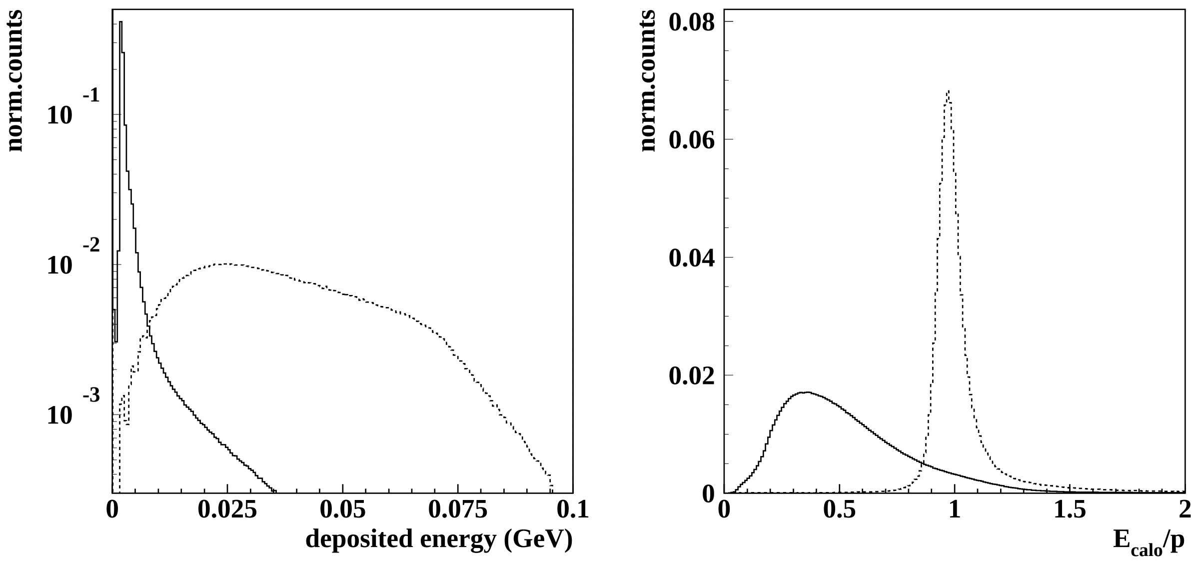

Figure 3.12: The normalized preshower (**left**) and calorimeter (**right**) responses for hadrons (solid line) and positrons (dashed line). The whole momentum range is shown (1997).

The calorimeter and the preshower use the different showering behaviour of cascades induced by an electromagnetic or strong interaction for particle identification. The 18 radiation lengths provided by the calorimeter wall make it most likely that a shower started by a photon or a positron is completely contained in the material. Hence, for photons, positrons, and electrons the ratio of deposited energy to momentum (E_{CALO}/p) is equal to one (Fig. 3.12, right). Hadrons deposit only a fraction of their energy in the calorimeter ($E_{CALO}/p < 1$).

3.3.3 Luminosity Monitor

The luminosity monitor, consists of two small electromagnetic calorimeters installed 7.21 m downstream the target on the left and right of the positron beam line (Fig. 3.13). The luminosity monitor is moved away from the beam during injection. Each calorimeter of the luminosity monitor consists of an array of 3×4 radiation resistant NaBi(WO$_4$)$_2$ crystals. The charged particles of an electromagnetic shower produce Čerenkov light in the crystals. Photo multipliers collect the light and allow a measurement of the deposited energy.

Figure 3.13: Top view of the HERMES luminosity monitor at the positron beam line.

The luminosity is measured by determining the rate of Bhabha scattering and annihilation events [134] where a beam positron collides with an electron of a target atom. (For an electron beam the Møller rate is measured.) The events selected are quasi symmetric Bhabha and annihilation events where each of the final state particles hits one of the calorimeters. Background is suppressed by requiring coincident hits of more than 4.5 GeV in each calorimeter. The rate of these events is proportional to the luminosity at the HERMES interaction point. Residual asymmetries from the small spin-dependence of the Bhabha cross section are corrected in the offline analysis [135]. Furthermore, the influences of beam position and beam slope drifts on the accepted events have to be taken into account. This can be done by a detailed Monte-Carlo simulation [136] and yields the luminosity $\mathcal{L}$ as function of the measured rate $\mathcal{R}_{lumi}$:

$$\mathcal{L} = c_{lumi} \cdot \mathcal{R}_{lumi} \qquad \text{with} \qquad c_{lumi} = (417 \pm 30)\,\mathrm{mbarn}^{-1} \quad , \tag{3.7}$$

for standard HERMES running conditions in 2000.

3.3.4 Triggers

The HERMES Experiment is equipped with a variety of first level triggers. Since second level triggering is not necessary at HERMES, all first level triggers of the spectrometer lead to a complete readout of the detector. Exceptions are the trigger logics of the luminosity monitor and the Longitudinal Polarimeter (see Chapter 4) which activate only the readout of the corresponding components.

In order to keep the overall trigger rate low enough, most non-physics triggers are prescaled, meaning that only every second, fourth, eighth... one is recorded. This prohibits an overload of the data acquisition due to a too high overall trigger rate. Further information on the HERMES trigger system can be found in [137].

Trigger 21

The most important trigger at HERMES is *Trigger 21*, the DIS trigger. The conditions defining Trigger 21 optimize the chance of recording an event with a positron from a deep-inelastic reaction. The following three conditions have to occur in one detector half in coincidence within the time window defined by a positron bunch crossing the interaction point:

- Hodoscope H1 and H2 give signals above threshold. Photons are suppressed by this condition since they do not leave signals in the scintillators. The thresholds for H1 and H2 are set so that also minimum ionizing particles are triggered.
- The signal in hodoscope H0 is required also. In addition to the suppression of photons, this condition reduces the chance of triggers from protons originating from the proton beam by using time of flight to distinguish between forward and backward going tracks.
- The sum of two adjacent calorimeter columns results in more than E_{thr} deposited energy. This condition rejects energetic hadrons from photoproduction.

Trigger 21 is not prescaled to collect the largest DIS sample possible. For running with unpolarized target gas at high densities and for polarized running in early 1996, the *calorimeter threshold* E_{thr} was set to 3.5 GeV. For the polarized running the threshold was set to 1.4 GeV to extend the kinematic coverage of the recorded DIS events to higher values of y. About 4 - 6% of the Trigger 21 events are found to be DIS events in the offline analysis.

Trigger 28

The photoproduction *Trigger 28* was originally implemented to detect $\mu^+\mu^-$ pairs originating from J/ψ decays [82,138]. The trigger is designed to detect events with two tracks: one in the upper and one in the lower detector half. Trigger 28 does not require an energy deposition in the calorimeter. The following conditions have to be fulfilled for Trigger 28:

- Hodoscopes H0, H1 and H2 fire in coincidence for the top **and** bottom detector. This ensures two forward going tracks.
- The x-plane of BC1 must have detected a particle for the top **and** bottom detector. Thus, short tracks and background in the front region of the detector are suppressed. Since 1997, the second x-plane of BC1 is added to the trigger and the allowed time window for the drift chamber signals is increased. These measures significantly increased the efficiency of the trigger.
- The size of the H0 signal must not exceed the equivalent of eight minimum-ionizing particles. Thus, an implicit cut on the multiplicity seen in the front detector is imposed. In 1996 this condition was slightly different since, apart from the condition on H0, additional constraints on the particle multiplicity were imposed on H1, H2 and the back chamber.

Trigger 28 mostly records photoproduction events with at least a hadron in the top and one in the bottom detector whereas the positron travels going down the beam pipe and therefore is not detected. Hadron pairs at large transverse momenta do exactly match the topology required in Trigger 28. Therefore, the photoproduction trigger helps recording these events and thus plays an important role in the analysis of this thesis (Sect. 6.2.2).

Furthermore, there are physics triggers for the luminosity monitor, events of the Longitudinal Polarimeter and for the various spectrometer upgrades [139] not mentioned up to now. Triggers for diagnostic purposes and efficiency determinations of detector components complete the setup.

3.3.5 Data Acquisition, Slow Control and Data Flow

The data acquisition system (DAQ) digitizes the detector readouts and stores the information for the offline analysis. The specific readout electronics for each detector component are hosted in FASTBUS crates mounted in the electronics trailer in the East Hall (Fig. 3.14). The crates have either a CHI (CERN Host Interface) front end connection to the actual bus or they are linked to such a crate by a CI (Cluster Interconnect). After a trigger has occurred, the FASTBUS event builder at the end of the bus bundles the information from all crates and sends it over an optical link to a FASTBUS/VME interface. The interface also receives (and sends) slow control information (i.e. chamber gas pressures, target status...) via an optical link from FASTBUS/CAMAC branch drivers located in the electronics trailer. The CAMAC branch driver handles the incoming and outgoing slow control information to and from the CAMAC crates which interface to the detector.

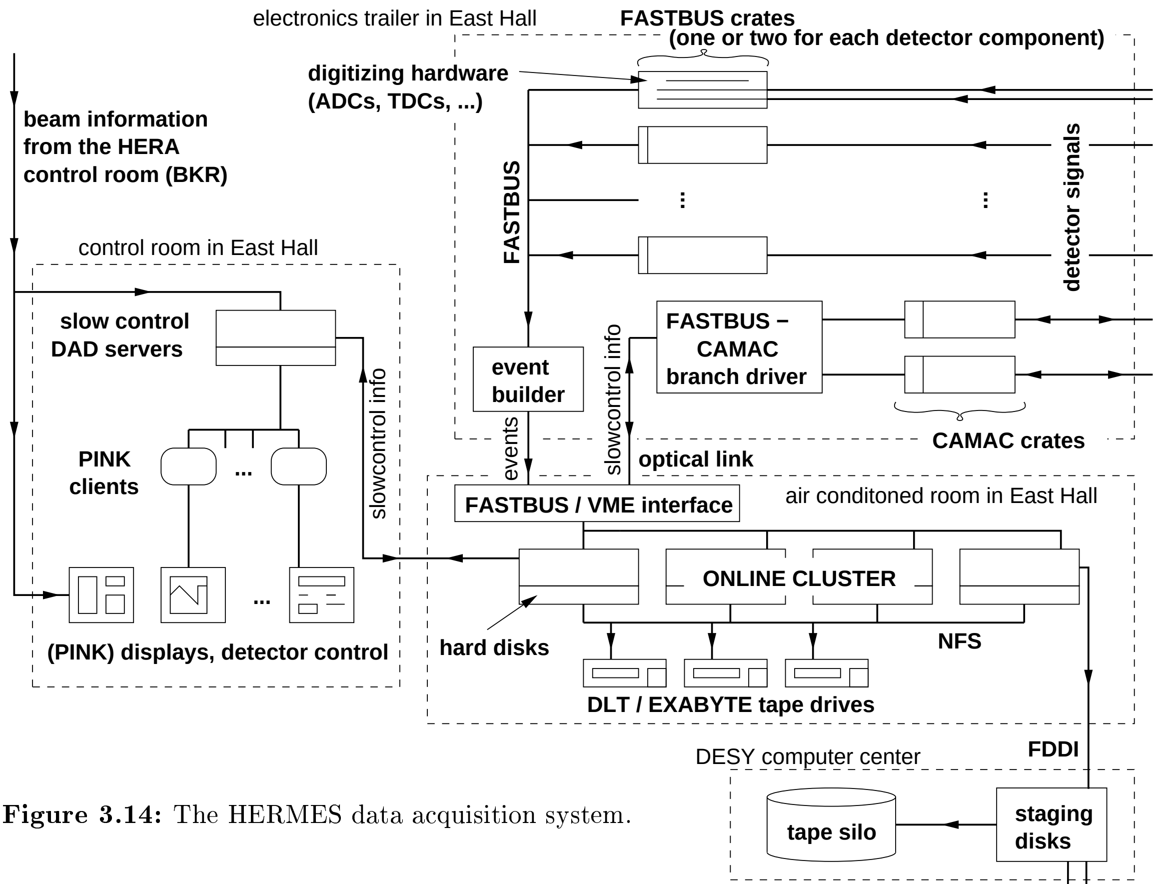

Figure 3.14: The HERMES data acquisition system.

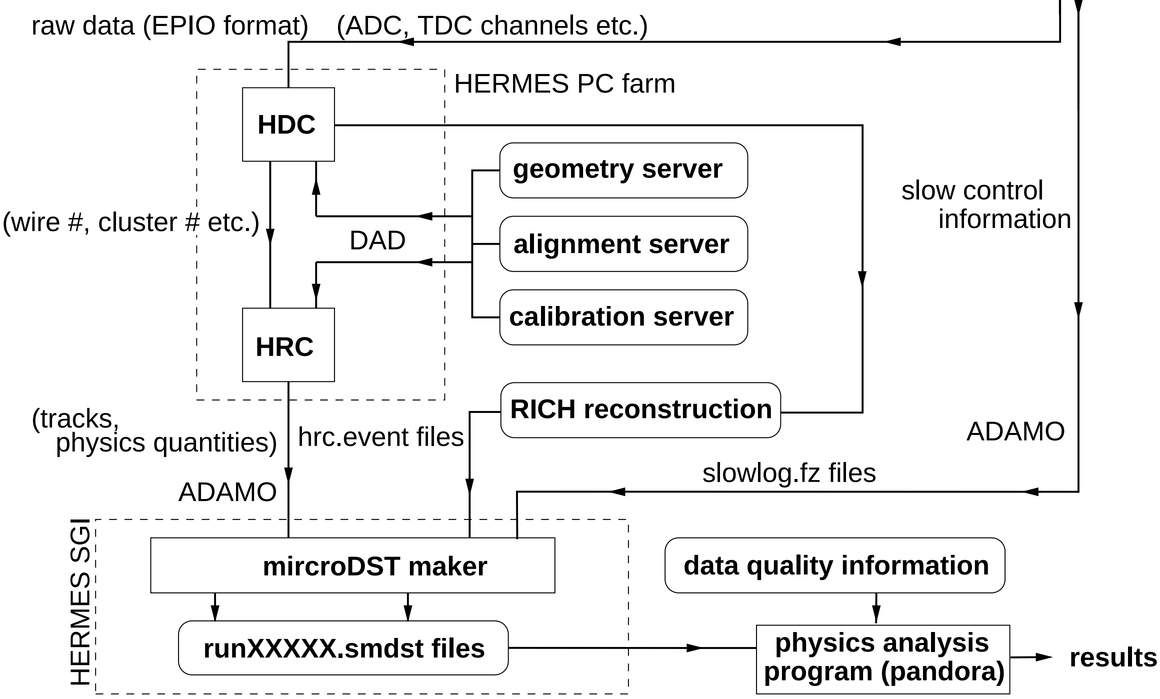

Figure 3.15: Diagram of the offline dataflow.

The FASTBUS/VME interface transfers the data to a DEC ALPHA online cluster. The online cluster buffers the information temporarily on its NFS mounted disk system. The data are sent to the DESY main site via a FDDI link and written locally to DLT tapes between fills of the storage rings. The information is staged on disk and backed up by a tape robot in the DESY computer center.

Computers in the control room handle the slow control information using a client-server architecture. The DAD [141] (Distributed ADAMO Database) servers collect the slow control data while the clients provide control tools and display the data to the user. The system utilizes a script language called PINK that enables interactive displays. The ADAMO [140] standard (a relational database) is used to store the slow control information in cross-referenced tables.

After the DAQ system has recorded the raw event data (EPIO format) they are processed by the HERMES Decoder program (HDC) on a high performance PC farm (Fig. 3.15). HDC translates the electronic detector information, such as ADC or TDC channels, to hit positions and energy depositions, for example. The information is passed on to HRC which calculates the physics quantities as measured by the detector (tracks, angles, momenta ...). HDC and HRC retrieve geometry, calibration and alignment information from a DAD database that is based on a client-server system. The database is updated corresponding to changes in calibrations and detector geometry.

The next step consists of programs that synchronize the HRC event output (hrc.event files) with the slow control information (slowlog.fz files). This is realized in a DST-production (microDST maker) program. Its output consists of run-wise data files in ADAMO format, called DSTs (Data Summary Tapes). Because the DST files contain the relevant physics quantities only, they enable reasonably fast physics analysis.

Data are grouped at HERMES using three basic time scales. The longest one is the *fill*, the time span of a positron fill in the HERA positron ring. Because the positron beam suffers losses, it has a finite duration of about 10 hours. The second time scale is about 10 min long and is called a *run*. This subdivision splits the data set into small enough pieces for storage. Additionally, the time between runs is used by the system to reinitialize certain hardware components. The smallest time interval is a so called *burst* defined as the time between two scaler readouts. Because it lasts 10 seconds, it allows to split the data with respect to the target polarization state. A burst is also the time scale on which the slow control information is synchronized to the event data and data-quality criteria are applied.

The DAQ cannot record every event occurring since it is busy for a finite time interval once it has started to record an event. A measure for the efficiency of the data acquisition system is its *livetime*. It is computed burst-wise by the ratio of accepted to generated triggers (usually above 90%). The livetime is needed for cross section measurements and is also used to rescale the luminosity rate to the data set taken.

4 Beam Polarimetry at HERA

A precise measurement of the beam polarization is essential for the determination of spin-dependent structure functions. For this purpose, two polarimeters are installed at the HERA positron ring (Fig. 3.1): The *Transverse Polarimeter* (TPOL) and the *Longitudinal Polarimeter* (LPOL), named after the polarization direction of the positrons at the corresponding locations. Both beam polarimeters exploit the spin-dependence of the Compton cross section by scattering circularly polarized laser light off the positron beam.

4.1 Polarized Compton Scattering

The process in which a photon scatters elastically on a positron is called Compton scattering. In the following, a head-on collision of positron and photon will be assumed, which is approximately realized at the HERA polarimeters. In the rest frame of the positron, the four-vector $\vec{k}_i$ ($\vec{k}_f$) of the incoming (outgoing) photon can be written as:

$$\vec{k}_i = \begin{pmatrix} 0 \\ 0 \\ 2\gamma E_\lambda \end{pmatrix} \qquad \text{and} \qquad \vec{k}_f = \frac{m_e}{1 - \cos\theta + \frac{m_e}{2\gamma E_\lambda}} \begin{pmatrix} \sin\theta\cos\phi \\ \sin\theta\sin\phi \\ \cos\theta \end{pmatrix}, \tag{4.1}$$

where m_e is the electron mass and E_λ is the initial photon energy in the lab system; the Lorentz factor of the positron is $\gamma = E_e/m_e$. In the rest frame of the positron, the direction of the outgoing photon is described by the angles θ and ϕ (Fig. 4.1, left).

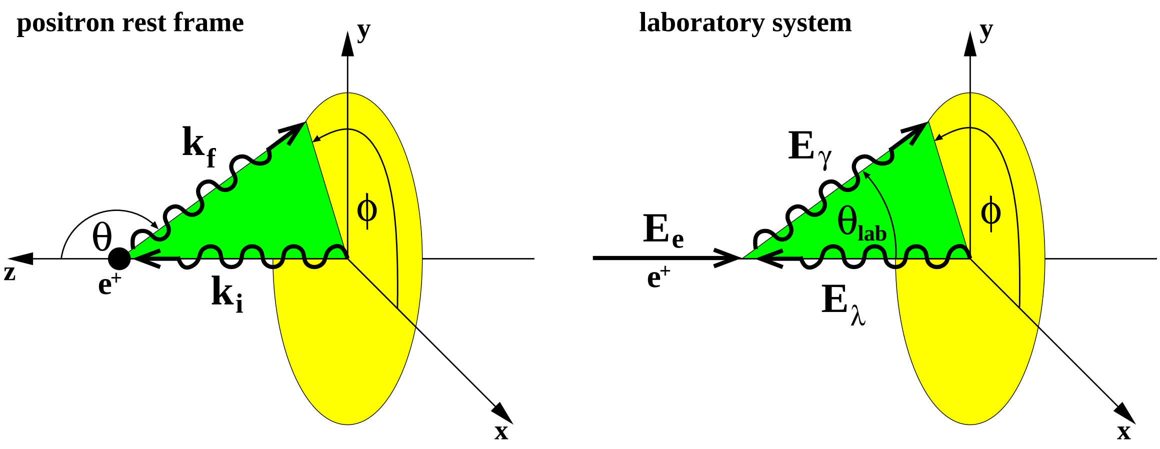

Figure 4.1: Compton scattering kinematics in the rest frame of the positron (**left**) and in the lab system (**right**). In both cases the scattered positron is not shown.

HERA operates the positron beam at an energy of $E_e = 27.56$ GeV giving a Lorentz factor of $\gamma = 5.4 \times 10^4 \gg 1$. In this case the lab energy E_γ of the outgoing photon can be expressed as:

$$E_\gamma \approx E_e \frac{1 - \cos\theta}{1 - \cos\theta + \frac{m_e}{2\gamma E_\lambda}}. \tag{4.2}$$

Because of the enormous Lorentz-boost, an incoming photon with $E_\lambda = 2.33\,eV$ (green) is backscattered to a hard gamma quantum of up to 13.6 GeV in the lab system. For the same reason the scattering angle θ_{lab} in the lab system (Fig. 4.1, right) is of the order of $100\,\mu$rad for $E_\gamma > 1$ GeV.

The differential cross section for scattering polarized photons off polarized positrons is given by [142]:

$$\frac{d\sigma}{d\Omega}(\vec{S},\vec{P}) = \frac{r_0\, k_f^2}{2\, m_e\, k_i^2}\,(\,\Sigma_0 + \Sigma_1(S_1) + \Sigma_2(S_3,\vec{P})\,)\;, \tag{4.3}$$

with the classical electron radius r_0, the unpolarized term Σ_0 and the polarized parts $\Sigma_1(S_1)$ and $\Sigma_2(S_3,\vec{P})$:

$$\begin{aligned}
\Sigma_0 &= m_e\,(\,1+\cos^2\theta\,) + (\,|\vec{k_i}| - |\vec{k_f}|\,)\,(\,1-\cos^2\theta\,) && (4.4)\\
\Sigma_1(S_1) &= S_1(\phi)\cdot m_e\,\sin^2\theta && (4.5)\\
\Sigma_2(S_3,\vec{P}) &= S_3\cdot(\,\cos\theta - 1\,)\,(\,\vec{k_i}\cos\theta + \vec{k_f}\,)\cdot\vec{P}\;. && (4.6)
\end{aligned}$$

The vector $\vec{P} = (P_x, P_y, P_z)$ contains the polarization of positron and the Stokes vector $\vec{S} = (S_0, S_1, S_2, S_3)$ describes the polarization of the initial photon. The component S_3 corresponds to the circular polarization of the photon. By convention, the photon is called left- (right-) handed for $S_3 = +1$ ($S_3 = -1$) in optics. While the TPOL makes use of the dependence on the azimuthal angle of Equation 4.6, the LPOL exploits the dependence on E_γ of the cross section to determine the beam polarization.

4.2 The Transverse Polarimeter

The TPOL [107] was installed in 1992 close to the HERA West-Hall and proved in 1993 the possibility of a high polarization build-up in HERA [143]. This development was an essential prerequisite for the approval of the HERMES Experiment. In the TPOL setup, circularly polarized light ($S_1 = S_2 = 0$) from a continuous 514 nm argon ion laser is Compton back-scattered into a position sensitive calorimeter. The helicity of the laser beam is flipped at a rate of 90 Hz. The positron beam is polarized transversely to the plane of the storage ring ($P_x = P_z = 0$). Using Equation 4.1 and Equation 4.6, the polarized parts of the Compton cross section applicable for idealized TPOL conditions follow:

$$\Sigma_1^{TPOL} = 0 \qquad \text{and} \qquad \Sigma_2^{TPOL} = S_3\, P_y\, \sin\phi\cdot(\cos\theta - 1)\,|\vec{k_f}|\,\sin\theta\;. \tag{4.7}$$

The average vertical position $\langle y\rangle^{S_3=\pm 1}$ of the back-scattered photons with an energy E_γ, within an fixed range is measured for $S_3 = -1$ and $S_3 = +1$. The beam polarization P_y then can be derived from a spatial asymmetry:

$$\Delta y(E_\gamma) = \frac{1}{2}(\langle y(E_\gamma)\rangle^+ - \langle y(E_\gamma)\rangle^-) = P_y \mathcal{A}_y(E_\gamma)\;, \tag{4.8}$$

with the analyzing power $\mathcal{A}_y(E_\gamma)$. The TPOL calorimeter is split horizontally in the middle plane into a top and a bottom part. The vertical offset y of every single photon is measured by the calorimeter by a top/bottom signal asymmetry of the energy deposited in two halves.

The TPOL measures the beam polarization to an absolute precision of $1\% - 2\%$ per minute. The analyzing power $\mathcal{A}_y(E_\gamma)$ depends on the geometry of the setup and the resolution of the calorimeter, and can be found by employing Equation 3.5 as mentioned in Section 3.1 (*rise-time calibration*). The relative systematic uncertainty of the polarization measurement amounts to 3.4% and is dominated by the scatter and number of *rise-time* measurements taken [144].

4.3 The Longitudinal Polarimeter: Concept and Setup

The Longitudinal Polarimeter is located downstream of the HERMES Experiment in the HERA-East area. The polarimeter was commissioned in fall 1996 and delivers a measurement of the longitudinal polarization between the spin rotators. Circularly polarized light from a pulsed Nd:YAG laser is scattered off the positron beam. Downstream of the photon-positron interaction point, the produced Compton photons are detected by a compact electromagnetic calorimeter. For idealized LPOL settings ($P_x = P_y = 0$) the polarized parts of the cross section become:

$$\Sigma_1^{LPOL} = 0 \qquad \text{and} \qquad \Sigma_2^{LPOL} = S_3\, P_z \,\cdot\, (\cos\theta - \cos^2\theta)\,(|\vec{k_i}| + |\vec{k_f}|)\ . \tag{4.9}$$

Hence, the cross section is independent of the polar angle ϕ and for fixed E_λ it kinematically only depends on E_γ (Fig. 4.2, left). Here, $S_3 P_z = -1$ ($S_3 P_z = +1$) corresponds to the photon-positron spin configuration $\frac{3}{2}$ ($\frac{1}{2}$) because the convention on photon helicity in particle physics is opposite to the one in optics.

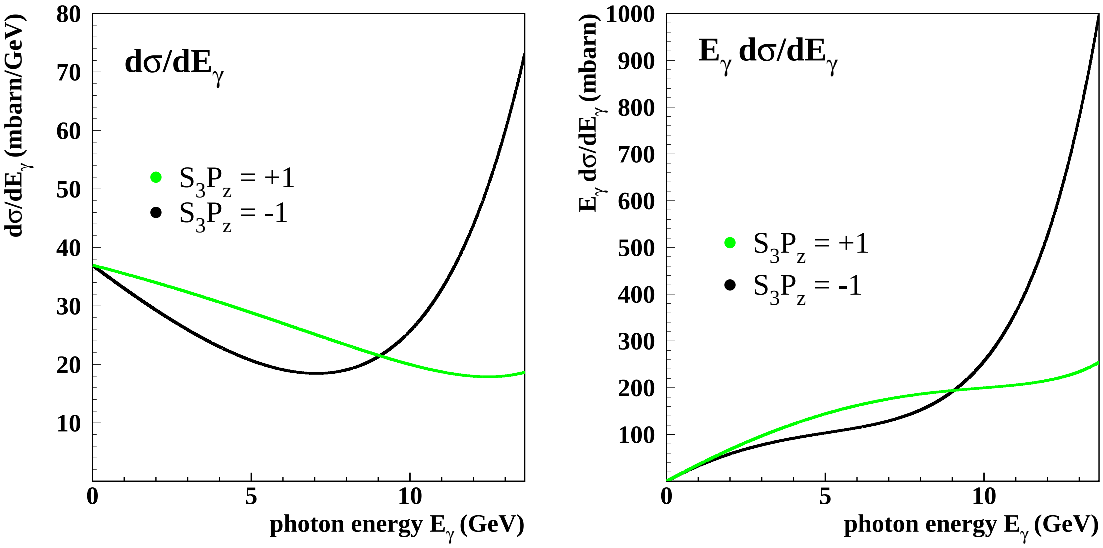

Figure 4.2: Left: The polarized Compton cross section for LPOL settings as a function of the energy E_γ of the scattered photon for $S_3P_z = -1$ (black line) and $S_3P_z = +1$ (grey line). **Right**: The energy-weighted polarized Compton cross section for the same settings.

4.3.1 The Multi-Photon Concept

In principle the LPOL could map the differential cross section as function of E_γ by measuring every single scattered photon. However, because of rather high background from bremsstrahlung[4] this is not a feasible mode of operation at the LPOL location. Instead of scattering one photon, many photons are scattered at once and the energy sum of them is detected. This approach is called *multi-photon method* and leads to a measurement of the integral of the energy-weighted cross section (integral of the functions in Fig. 4.2, right).

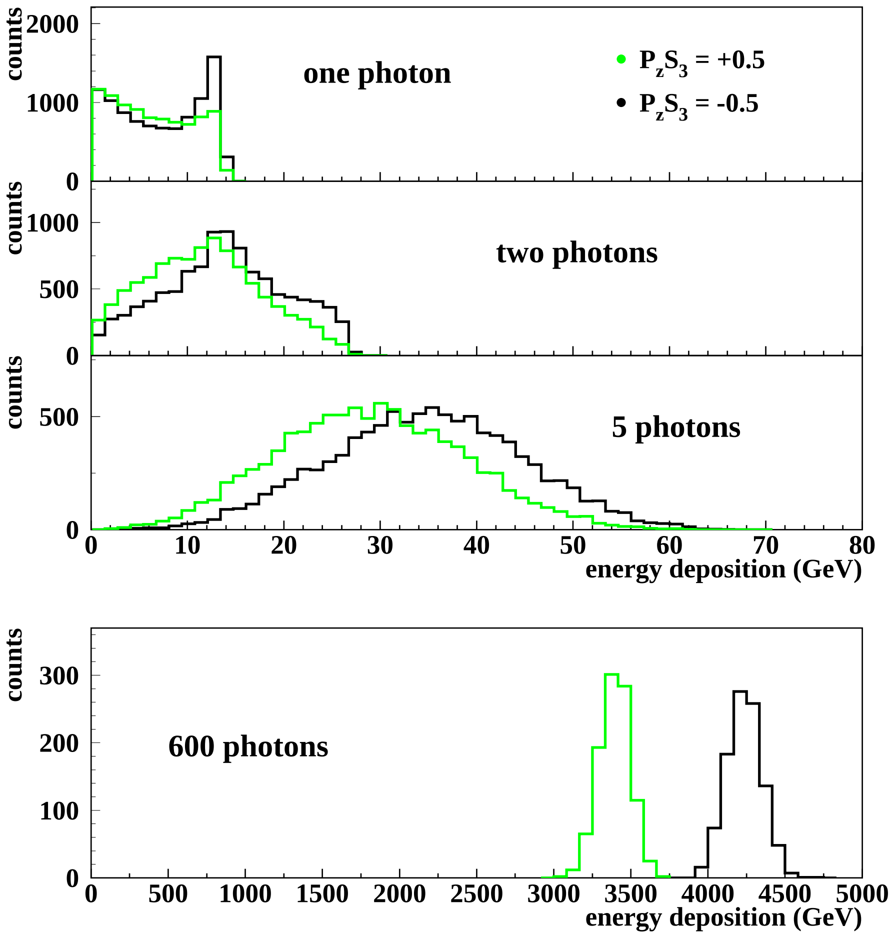

Figure 4.3: The transition from single- to multi-photon regime is shown by the results of a model calculation: energy spectra of the scattered photons in the case of one, two, five or 600 coincident Compton scatterings detected by a perfect calorimeter. The spectra are shown for realistic conditions: $S_3P_z = -0.5$ (black line) and $S_3P_z = +0.5$ (grey line).

The concept of the multi-photon method can be understood if the transition from single-photon scattering to multi-photon scattering is viewed in terms of the measured energy-spectra (Fig. 4.3). The more photons interact at once with the positron beam, the more Gaussian the energy spectra become because of the central limit theorem of statistics.

[4]The disadvantageous background conditions at the location of the Longitudinal Polarimeter become apparent in the measurements shown in Figure 4.9 in Section 4.3.3.

In case of $|S_3 P_z| = 1$, the centroids $\mathcal{I}^{\pm}$ of the energy spectra are the integrals over the energy weighted cross sections for the two spin configurations:

$$\mathcal{I}^{\pm} = \int_{E_{min}}^{E_{max}} dE_\gamma \, r(E_\gamma) \left(\frac{d\sigma}{dE_\gamma} \right)_{S_3 P_z = \pm 1} . \tag{4.10}$$

Here, $[E_{min}, E_{max}]$ is the energy interval detected and $r(E_\gamma)$ is the normalized energy response function of the calorimeter. If E_λ is 2.33 eV and the entire energy range up to the *Compton edge* (13.62 GeV) is covered with a perfectly linear device ($r(E_\gamma) = E_\gamma$), the analyzing power is obtained as asymmetry of the integrals $\mathcal{I}^{\pm}$:

$$\mathcal{A} = \frac{\mathcal{I}^+ - \mathcal{I}^-}{\mathcal{I}^+ + \mathcal{I}^-} = -0.1838 . \tag{4.11}$$

The centroids of the measured energy depositions of the LPOL setup $I^{\pm}$ can be used to determine the longitudinal beam polarization P_z:

$$P_z = \frac{1}{\mathcal{A}\, \bar{S_3}} \cdot \frac{I^+ - I^-}{I^+ + I^-} , \tag{4.12}$$

if the average circular light polarization $\bar{S_3} = \frac{1}{2}(|S_3^+| + |S_3^-|)$ is known. If the calorimeter is linear, its energy calibration cancels in Equations 4.11 and 4.12. Moreover, the multi-photon method is insensitive to single background photons and offers a good statistical accuracy for the measurement of the beam polarization.

4.3.2 Scattering off the HERA Positron Beam

A schematic overview of the LPOL area is shown in Fig. 4.4 (top). The photon-positron interaction point is located 51.7 m downstream of the HERMES target between the two bending magnets BH39 and BH90. The dipole magnet BH90 separates the Compton photons and the positron beam. At the location of the calorimeter (OR 106 m) the centroid of the scattered photon beam is only 4.2 cm apart from the positrons constraining the size of the employed photon detector (see Sect. 4.3.3).

The HERA positron machine offers 220 possible positions in 96 ns intervals for positron bunches. The beam consists of 189 bunches divided into three *trains* of 63. After the first two trains follow seven empty positions each, after the last train seventeen. Every eleventh positron bunch does not collide with a HERA proton bunch. A positron bunch is 11 mm long and is approximately distributed Gaussian with the widths $\sigma_{x,y}$ transversely to the beam direction. The widths and divergences of the beam depend on the position in the ring because of the strong focusing principle realized in the HERA synchrotron. The divergence of the positron beam broadens the distribution of the back-scattered Compton photons (Fig. 4.4) since the photons largely follow the positron kinematics. At the LPOL calorimeter, photons at the Compton edge are smeared in x-direction by $\sigma_x^c = 3.7$ mm and in y-direction by $\sigma_y^c = 1.1$ mm. This effect has to be folded with the kinematics of the Compton scattering which relates the photon energy E_γ to the scattering angle and

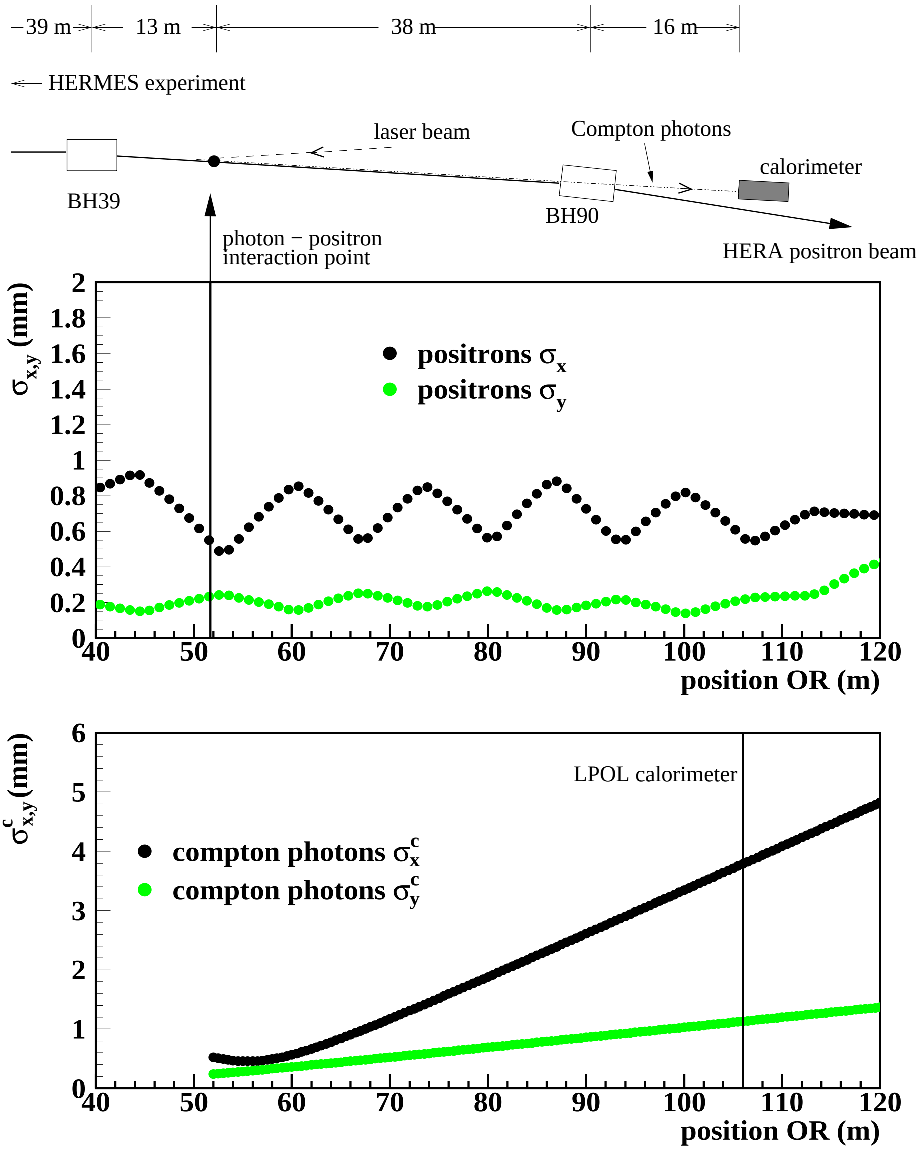

Figure 4.4: Top: arrangement in the LPOL area; the quadrupole magnets which (de)focus the positron beam are not drawn. **Middle/Bottom:** the widths of the positron beam $\sigma_{x,y}$ and the Compton photons $\sigma^c_{x,y}$ versus the position in HERA East-Right (OR).

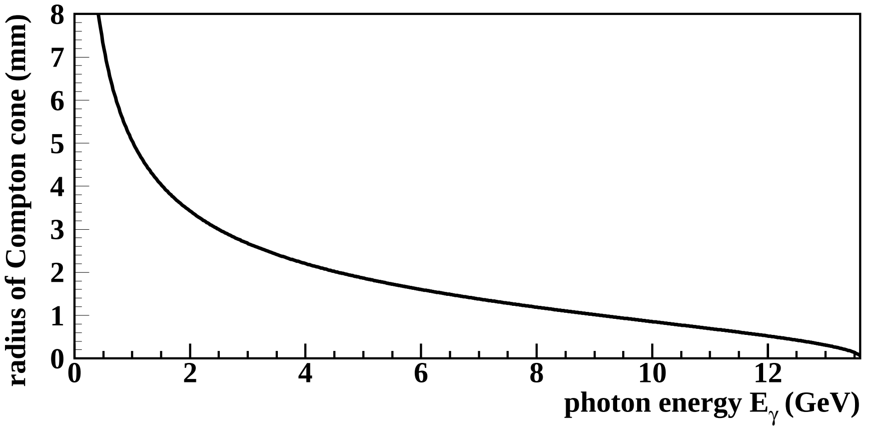

Figure 4.5: Radius of the Compton cone at the location of the LPOL Calorimeter as a function of the photon energy E_γ for vanishing divergences of the positron beam.

therefore to the position on the calorimeter front-face (Fig. 4.5). For instance, a photon at the Compton edge would hit centrally on the calorimeter, while a 3 GeV photon hits 2.7 mm off center. A dedicated survey ensured that the Compton photons do not encounter obstructions on their way to the calorimeter [145].

4.3.3 Laser System, Calorimeter Setup, and Online Control

The Laser System

The setup of the optical system in the laser room is shown in Figure 4.6. A frequency doubled Nd:YAG laser (COHERENT, Infinity 40-100) generates 3 ns long light pulses with a wavelength of 532 nm ($E_\lambda = 2.33\,\mathrm{eV}$). The laser is fired at a rate of 97.8 Hz in synchronization with the positron bunches. The laser beam is guided by a pair of mirrors through an attenuator consisting of a rotatable half-wave plate and a Glan-Thompson prism. The prism filters the vertical linear polarization and directs the horizontal component into a beam dump. Behind the two mirrors, two photo diodes (PINs) are installed. The first diode (*PIN laser timing*) is used to measure the time of the light pulse emerging the laser head. This measurement is necessary because the time difference between triggering and firing of the laser *jitters* by a few ns. The diode behind the second mirror (*PIN laser intensity*) monitors the intensity of each laser pulse. The linearly polarized light emerging the Glan-Thompson prism is converted into circularly polarized light by traversing a Pockels cell. The Pockels cell works as variable retardation element. The phase differences between the light components with respect to the crystalline axes are proportional to the high-voltage applied. Here, for a certain high voltage setting the Pockels cell acts

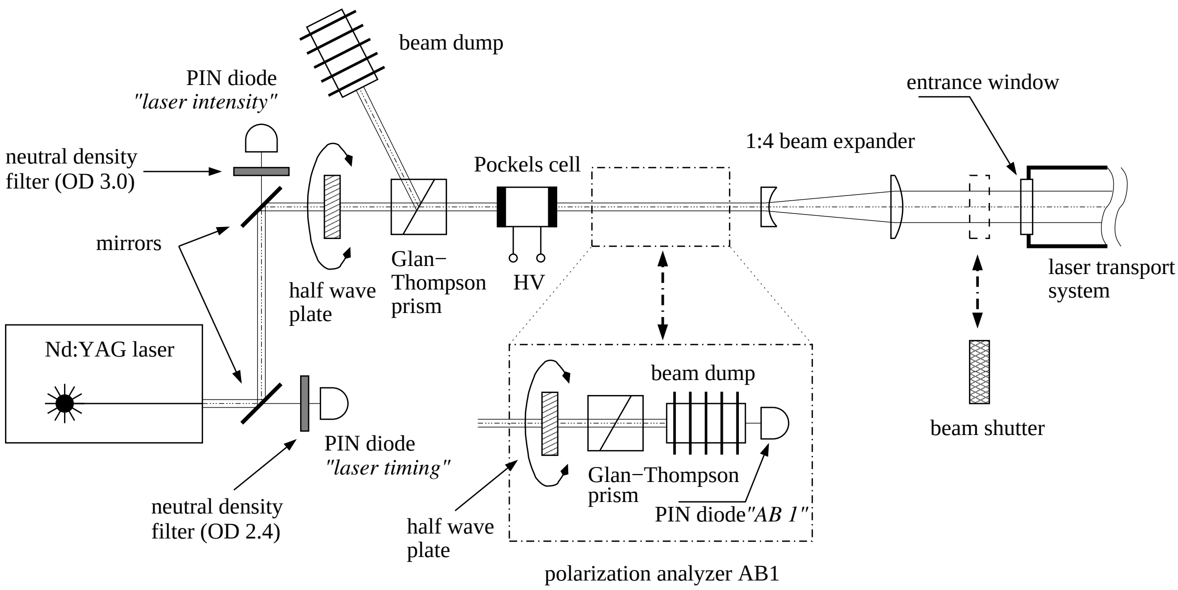

Figure 4.6: Schematic drawing of the LPOL optical system in the laser room for the generation and analysis of circularly polarized light pulses.

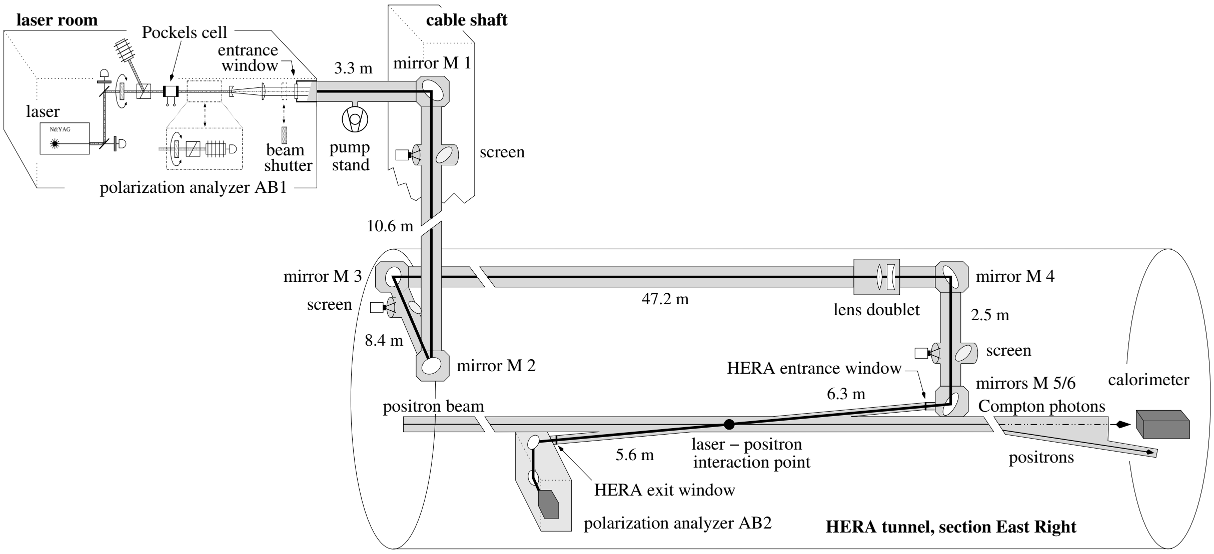

Figure 4.7: Layout of the Longitudinal Polarimeter with its laser transport system in the HERA East section.

as $\lambda/4$-wave plate. Depending on the sign of the high voltage applied to the cell, left or right handed photons are obtained. The Pockels cell allows to flip the helicity of the light for every pulse. A polarization analyzer (AB1) can be moved into the beam to analyze the degree of polarization achieved. The analyzer is built of a rotatable half-wave plate, a Glan-Thompson prism, and a beam dump hosting a photo diode [146]. If the half-wave plate is rotated, the variation of the light intensity measured by the photodiode can be used to determine the remnant linear light component. This is done by employing an analysis based on a Fourier transform of the measurement [147]. In the limit of perfect circular polarization, no intensity variation during the measurement is observed. The initial degree of circular light polarization achieved in the LPOL setup is larger than 99.9% for both helicity states.

The circularly polarized laser beam passes a 1:4 beam expander which reduces the divergence of the beam so it can travel the 72 m of the following laser transport system (Fig. 4.7). The beam expander also helps to reduce the resulting beam waist at the interaction point. The laser beam is guided by three pairs of phase compensating mirrors though the evacuated steel pipe of the transport system. Behind each of the remote-controlled mirrors, a video camera monitors the position of the laser beam. A lens doublet focuses the broadened beam on the interaction point to a diameter of about 0.5 mm where it collides with the positron beam under a crossing angle of 8.7 mrad. The vacuum of the transport system (10^{-2} mbar) is isolated from the HERA vacuum (10^{-9} mbar) by fused silica windows mounted at entrance and exit to the positron beamline. A stress-free mounting by Helicoflex gaskets ensures negligible optical retardation. After passing through the interaction point, the laser beam enters a second light polarization analyzer box (AB2) used for monitoring.

The Calorimeter

The produced Compton photons exit the HERA beam pipe 54 m downstream of the photon-positron interaction point through a 2 mm thick water-cooled copper window. Behind the window, the LPOL calorimeter is mounted on a remote-controlled table that can be steered horizontally and vertically. The calorimeter is moved behind a lead shield during injection.

Table 4.1: Properties of $NaBi(WO_4)_2$.

refractive index	2.15
Molière radius	2.38 cm
radiation length	1.1 cm
radiation hardness	$7 \cdot 10^7$ rad

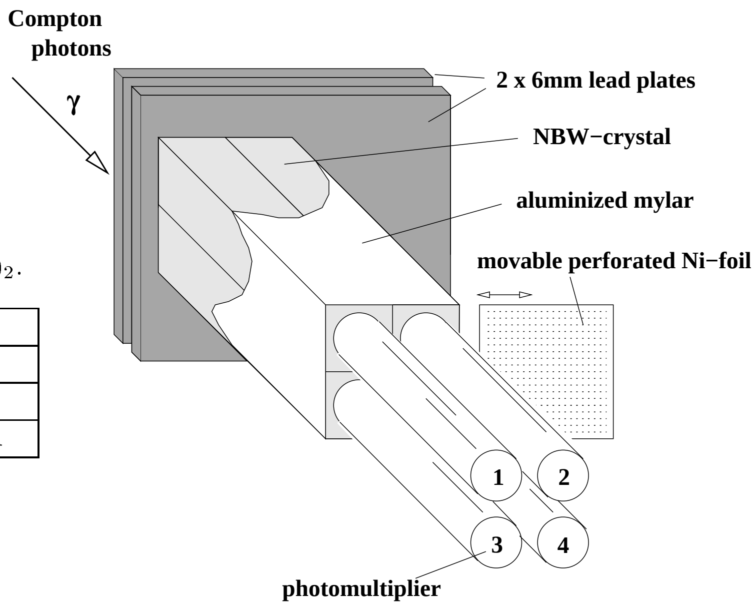

Figure 4.8: Drawing of the interior of the NBW calorimeter.

The LPOL calorimeter (Fig. 4.8) consists of a 2×2 array of $22 \times 22 \times 200$ mm^3 $NaBi(WO_4)_2$ crystals (NBW). The NBW crystals have a high refractive index (see Tab. 4.1) giving a high yield of Čerenkov light produced by the charged particles in an electromagnetic shower. In addition, the material is radiation hard and compact. The length of the crystals covers 19 radiation lengths. Each crystal is wrapped in aluminized mylar which optimizes the light output to the photo-multiplier mounted at the rear. The segmentation of the calorimeter enables a position measurement of the Compton cone. The two 6 mm thick lead plates in front of the NBW array protect the setup from synchrotron radiation (from BH90) and act as preshower for the Compton photons. Except for the side plate at the the positron beam, which is made of tungsten, the calorimeter is hosted in a light-tight aluminum box. The design of the LPOL calorimeter is very compact to meet the spatial constraints mentioned above (Sect. 4.3.2) and needs to be centered on the Compton cone during data taking to avoid systematic effects from transverse shower leakage.

In order to attenuate the light coming from the crystals, until 1999 an air-pressure driven perforated nickel-foil was inserted into the small air gap between crystals and photomultipliers. This was foreseen to cut the high light intensity during multi-photon operation by a factor of 80, enabling the photo-multipliers to run at regular gain. This solution turned out to be problematic because two effects induce signals on the photo-cathodes: The Čerenkov light coupled out from the crystals, and charged particles from the tail of the electromagnetic shower leaking into the photo-multipliers. If the nickel-foil is inserted, the latter dominates the signal. The signal from the charged particle leakage is non-linear since the shower depth grows logarithmically with the energy. This results in an analyzing power of -0.23 deviating 25% from the theoretical expectation of -0.1838. If the light coming from the crystals is not attenuated, the direct light dominates resulting in an analyzing power of $\mathcal{A}^{LPOL} = -0.1929$.

The analyzing powers were obtained from DESY and CERN test beam measurements with the NBW calorimeter. Further test series with neutral density filters instead of the Ni-foil completed the picture. The test measurements and the derivation of the relevant analyzing powers are described in detail in Appendix A.1. These investigations delivered the key to the successful calibration of the Longitudinal Polarimeter. After summer 1999, the LPOL calorimeter was operated without the Ni-foil.

An important confirmation for the functioning of the LPOL setup is a measurement in single-photon configuration. For this dedicated measurement, the laser light was attenuated by $2 \cdot 10^3$ while the gains of the photo-multipliers were increased by a factor of 20 by turning up the high-voltage. The obtained energy spectra (Fig. 4.9) for each helicity state nicely confirm the course of the differential cross section (Fig. 4.2, left). Excellent agreement is found with a model calculation [148] which includes background from bremsstrahlung and blackbody-Compton photons as well as the energy response and the resolution of the calorimeter.

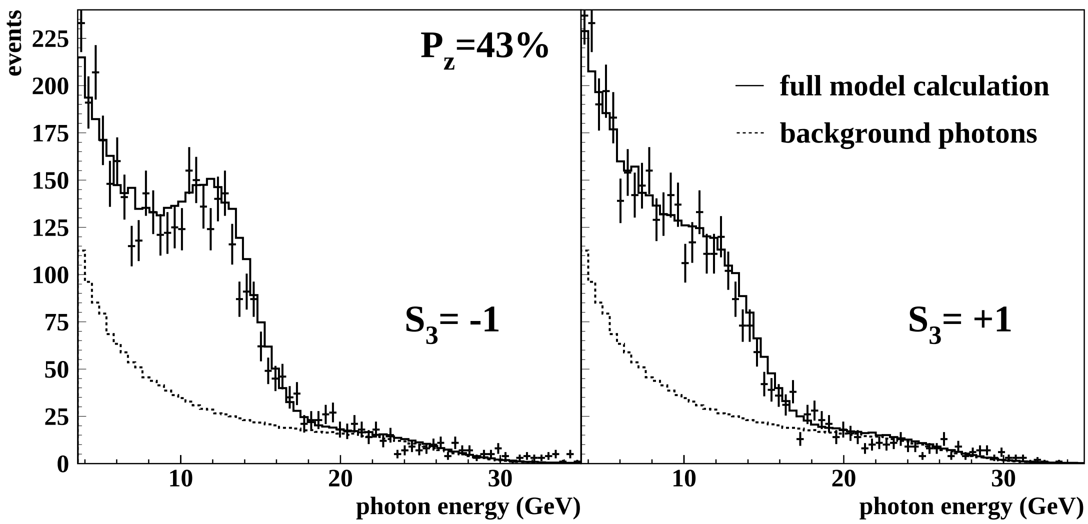

Figure 4.9: Energy spectra measured by the NBW calorimeter during single-photon operation. The model calculation contains a Compton photon probability of 2.5% per bunch crossing ($E_\gamma > 2$ GeV). The background consists of bremsstrahlung (1.8% per bunch crossing) and blackbody Compton photons (6.0% per bunch crossing).

The Online Control System

The following components constitute the online control system: the LPOL data acquisition which is integrated into the HERMES DAQ, the front-end control for the user (Compton Polarimeter Control, COP [149]) including all displays, and the underlying online-analysis program (LPONL).

The digitization of all relevant signals is triggered about 200 times per second. Four consecutive triggers each are synchronized to a random positron bunch with the help of a *bunch trigger module* and a digital signal processor (DSP). These four events contain for each of the two light helicity states one pedestal event and one event where the laser was fired. Additional triggers record events of the gain monitoring system (see Sect. 4.4.3) and bunch-free pedestal events (taken in the gap after the last bunch train). The DSP decides on the bunch sequence triggered and bundles 450 consecutive LPOL events to a *user event*. About every two seconds, a user event is transmitted to the HERMES DAQ where it is handed to the DEC ALPHA online cluster and finally taped.

The COP program delivers a graphical user interface for handling the Longitudinal Polarimeter. Via VME, RS232, and CAN-Bus interfaces, the control of all hardware components like mirrors, laser, Pockels cell and polarization analyzers is achieved. Furthermore, the program contains an *auto-pilot* which automates the LPOL operation. The auto-pilot starts up the laser at the beginning of a fill and shuts down the polarimeter at the end. With the data from the online program LPONL, the calorimeter table position is adjusted automatically as well as the trigger timing of the laser. The latter is needed to keep the overlap of laser pulse and positron bunch maximal. If the luminosity at the photon-positron interaction point drops below a preset value, it is brought back up by an automatic scan of mirror M4. The interaction of the programs COP and LPONL represent the vital feedback loop of the polarimeter.

The heart of the online control system is the online-analysis program LPONL. It receives the LPOL user events and calculates in real-time the relevant quantities needed for control. The program checks for the status of the machine and reads the positron bunch currents from the HERA server. Together with the LPOL data, the program derives the beam polarization every 60 seconds. Also, all other quantities needed for the (automatic) control of the polarimeter are delivered: laser status and timing, Compton cone positions on the calorimeter, specific luminosity, and the mean signals of the photo-multipliers. Other control data like single bunch polarizations and gains of the photo-multipliers are transmitted every five or twenty minutes, respectively. Moreover, the online program recognizes erroneous conditions and reports them to the server. The course of the analysis implemented in LPONL is described in Section 4.4. The results can be viewed online in the HERMES and HERA control rooms.

4.4 The Longitudinal Polarimeter: Data Analysis

Before the photo-multiplier (PMT) signals can be used to compute the beam polarization or Compton cone positions, they have to be corrected for noise effects, the jitter of the laser pulse, and for eventually different gains. For matching the gains of the PMTs, a special technique was developed which resolves the ambiguity between off-center Compton cone positions and mismatched gains.

4.4.1 Signal Corrections

Since the LPOL setup contains quite long signal lines, noise pickup from the laser power supply, the electronics trailer, and the HERA tunnel is inevitable. To correct for these effects, which ultimately limit the resolution of the polarimeter, each signal is amplified and split into two signal lines. The second line is installed to an additional ADC channel. Each of these extra channels is delayed by 96 ns so only the actual noise level instead of the signal plus noise is gated by the ADC. The linear correlation coefficient b and offset a of the noise channel $\mathcal{P}_{noise}$ to the signal channel $\mathcal{P}$ can be computed (Fig. 4.10, left). The corrected response $\mathcal{P}^c$ has a factor of two better resolution (Fig. 4.10, right) and follows from:

$$\mathcal{P}_i^c = \mathcal{P}_i - (\mathcal{P}_i^{noise} - a_i)/b_i - c_i^{laser} \quad , \quad i = 1\ldots4 \text{ (PMT numbering see Fig. 4.8).} \tag{4.13}$$

Here, c^{laser} is an additional correction needed when the laser fires. Since the laser power supply is stabilized a few μs before and after each shot, the noise on the lines is reduced to half and the pedestal slips by a few channels. The correction c^{laser} is deduced by the signal derived by laser-on and laser-off events for empty bunch positions.

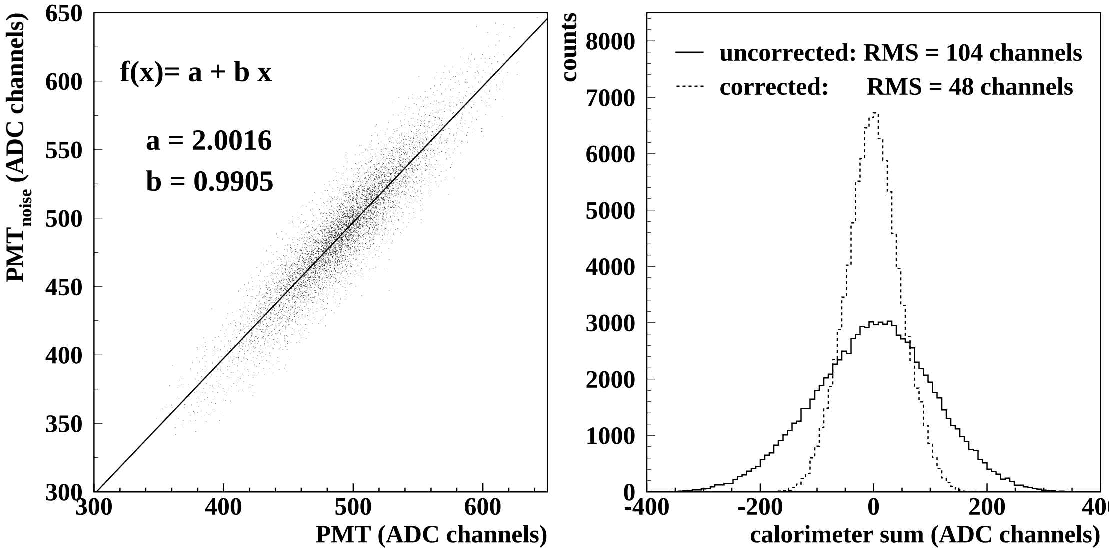

Figure 4.10: Noise correction at the LPOL. **Left**: correlation for a single PMT between the signal channel and the noise channel for pedestal events. **Right**: Distribution of the PMT signal sum before (solid line) and after (dashed line) correcting each of the four PMTs using Equation 4.13.

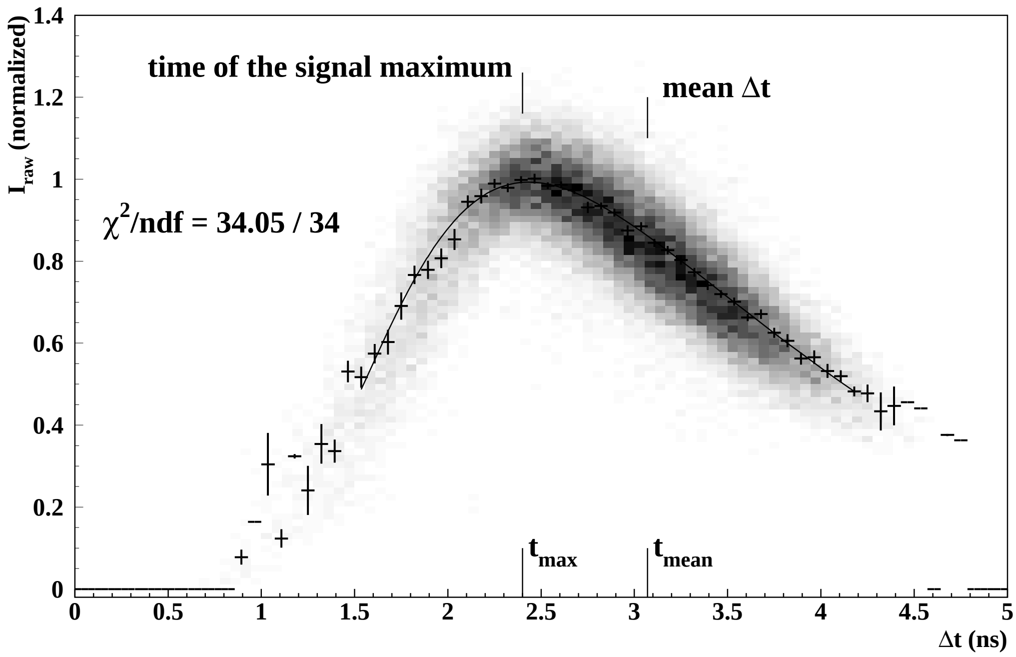

Figure 4.11: The temporal profile of the laser pulse shape: The noise and gain corrected calorimeter signal I_{raw} versus Δt (the time between the trigger and *PIN laser timing*) for a single bunch and $S_3 = -1$. The fit used for the timing correction is superimposed: Equation 4.15 with $N = 1$, t_{max}=2.4 ns, $\sigma = 0.59$ ns, and $\xi = 1.15$.

Before the PMT signals are added to give the raw *calorimeter sum* I_{raw}, they are weighted with the appropriate gain factors g_i (see Sect. 4.4.3) of the individual PMTs:

$$I_{raw} = \sum_{i=1}^{4} \mathcal{P}_i^{gm} \qquad \text{with} \qquad \mathcal{P}_i^{gm} = g_i \cdot \mathcal{P}_i^c \,. \tag{4.14}$$

The internal electronics of the laser responds with a jitter of ± 1.5 ns to the trigger. Thus, different parts of the about 1 m long laser pulse are sampled by the 11 mm positron bunches. A TDC measures the time difference Δt between the trigger and *PIN laser timing* (Fig. 4.6). If the calorimeter signal I_{raw} is viewed versus the time difference Δt, the temporal profile of the laser pulse becomes visible (Fig. 4.11). During data taking, a model for the laser pulse:

$$l(\Delta t) = N \cdot \exp\left(-\frac{\tau^2}{\sigma^2(1+\arctan(\tau \cdot 2\xi/\pi))^2}\right) \quad \text{with} \quad \tau = \Delta t / t_{max} - 1 \tag{4.15}$$

is fit every minute to the data and used to correct every single pulse:

$$I^{\pm} = \frac{1}{n}\sum_{i}^{n} \frac{I^{\pm}_{raw,i}}{l(\Delta t_i)} \qquad \text{with} \qquad S_3 = \pm 1. \tag{4.16}$$

The fit of the laser pulse is done for one spin state only and is used to correct data of both spin states equally to avoid systematic bias on the determination of the energy asymmetry.

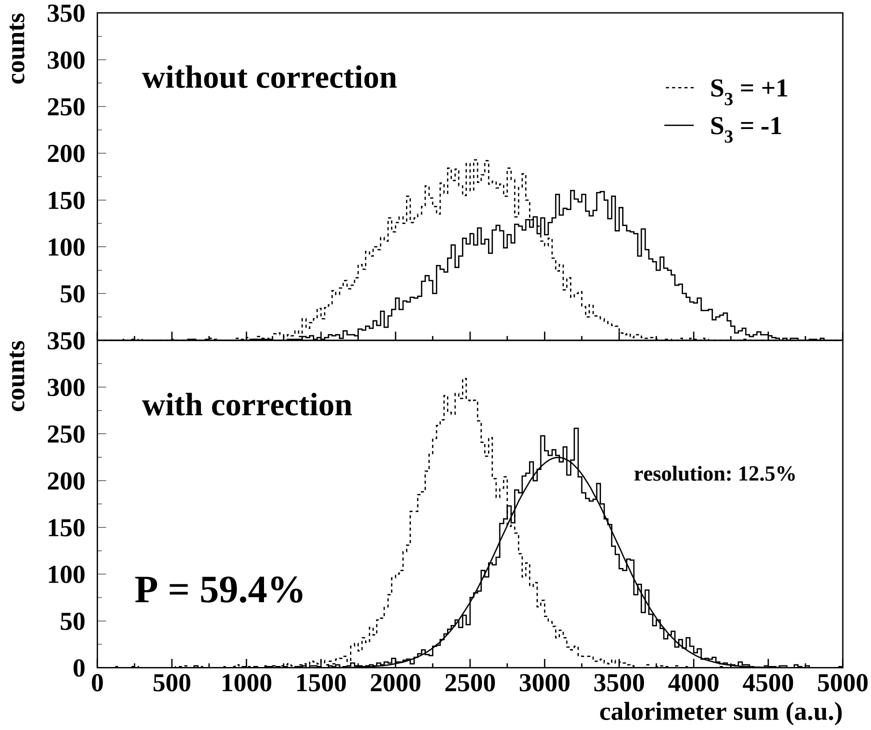

Figure 4.12: Effect of the timing correction: uncorrected (**top**) and corrected (**bottom**) spectra of the calorimeter sum for both laser beam helicities $S_3 = +1$ (dashed line) and $S_3 = -1$ (solid line). The data for a single bunch is shown.

The fit finds the normalization N, the time of maximum signal height t_{max}, width σ, and asymmetry ξ of the pulse. Together with the reduced χ^2, σ and ξ are measures for the data-quality of the running conditions. The effect of the timing correction is demonstrated in Figure 4.12. On the one hand, the jitter of the laser introduces complications to the analysis, on the other hand the difference of t_{max} and the mean trigger time t_{mean} is used to derive the *laser trigger delay* $(0.5ns + t_{max} - t_{mean})$ needed for an automated optimization of the photon-positron collision. The laser trigger delay is sent to the COP program which sets the trigger timing to a new value if necessary.

4.4.2 Determination of the Beam Polarization

Once the signals are timing-corrected they are used to derive the specific luminosity L and the responses l_i of the single PMTs:

$$L = \frac{1}{2}\sum_{b=1}^{189} i_b \cdot (I_b^+ + I_b^-) \qquad \text{and} \qquad l_i = \frac{1}{2}\sum_{b=1}^{189} i_b \cdot (\mathcal{P}_{i\,b}^{gm+} + \mathcal{P}_{i\,b}^{gm-}) , \tag{4.17}$$

where i_b is the fraction of the current of a bunch b of the total positron current. The x- and y-positions $\mathcal{C}_x$ and $\mathcal{C}_y$ of the Compton cone on the calorimeter front face are calculated by left-right and up-down asymmetries η_x and η_y of the calorimeter segments:

$$\mathcal{C}_{x,y} = \zeta_{x,y}(\eta_{x,y}) \qquad \text{with} \qquad \eta_x = \frac{l_1 + l_3 - l_2 - l_4}{l_1 + l_3 + l_2 + l_4} \quad \text{and} \quad \eta_y = \frac{l_1 + l_2 - l_3 - l_4}{l_1 + l_3 + l_2 + l_4} , \tag{4.18}$$

using the *eta-to-x (eta-to-y)* transformation $\zeta_{x\,(y)}$ derived from test beam data (App. A.1.2). Specific luminosity, Compton cone position, and single PMT responses are sent to the server which deliver the information to the COP program and the displays.

The beam polarization P can be computed by the polarizations of P_b of every single bunch using Equation 4.12:

$$P = \sum_{b=1}^{189} i_b \cdot P_b \qquad \text{with} \qquad P_b = \frac{1}{\mathcal{A}^{LPOL}\,\bar{S}_3} \cdot \frac{I_b^+ - I_b^-}{I_b^+ + I_b^-}\,. \tag{4.19}$$

The LPOL achieves an absolute statistical precision of 1% in a one-minute measurement. An example of polarization measurements is shown in Figure 4.13 together with the specific luminosity and the reduced χ^2 of the timing correction. The χ^2 distribution for this data set and the corresponding probabilities are shown in Figure 4.14. The probability distribution exhibits an excess at low probabilities coming from data points where the auto-pilot introduced small changes to the LPOL system (by resetting the laser-timing for example).

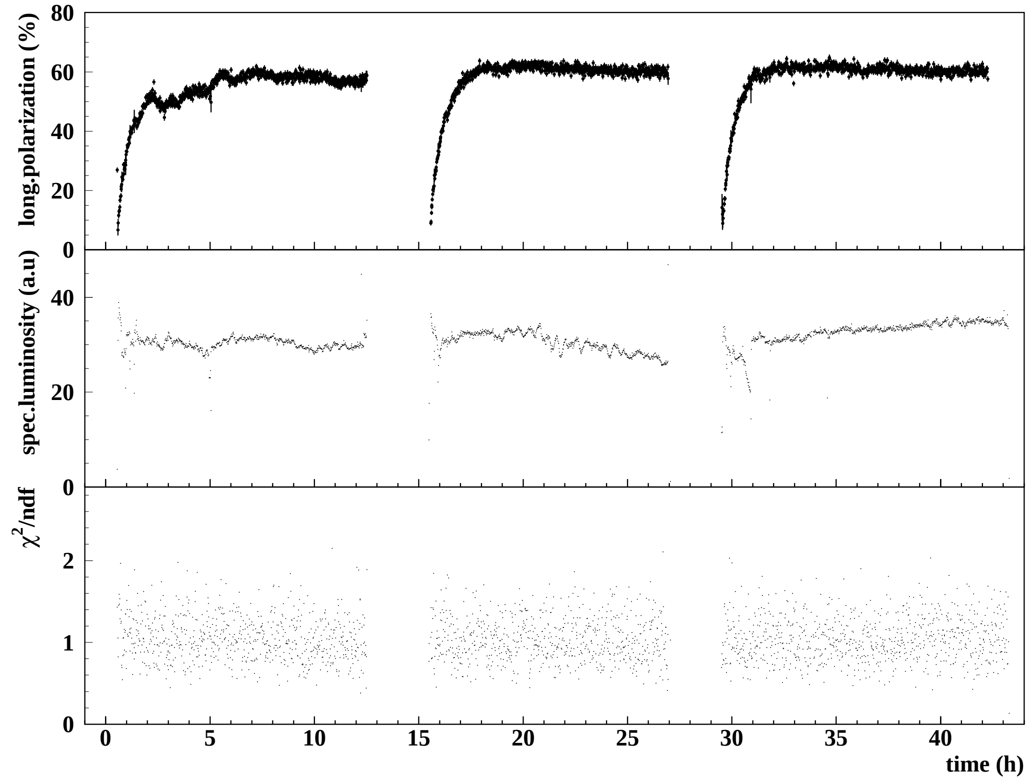

Figure 4.13: LPOL measurement of the longitudinal beam polarization for three consecutive fills on 20/21.11.1999. Three panels are shown: beam polarization (**top**), specific luminosity at the photon-positron interaction point (**middle**), and the reduced χ^2_{ndf} (**bottom**) of the timing correction.

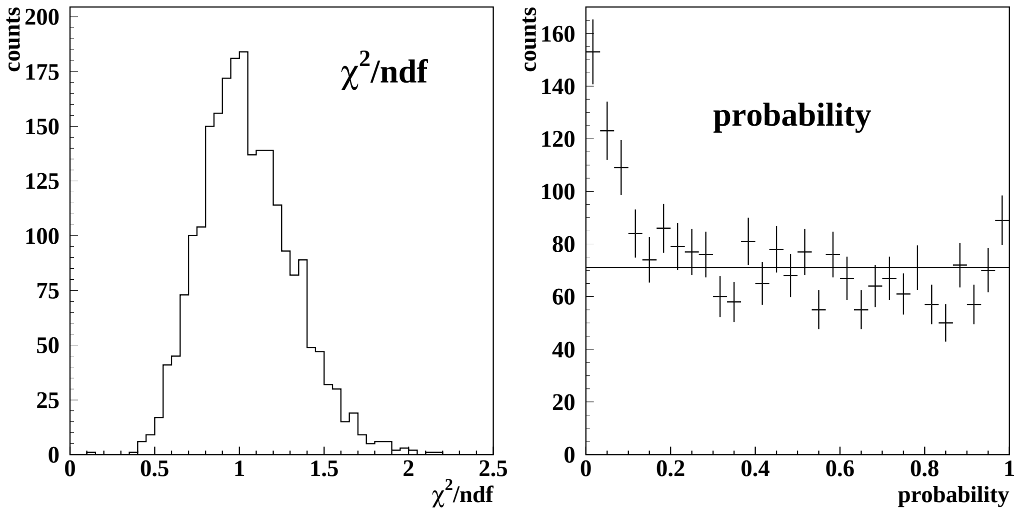

Figure 4.14: Distribution of the reduced χ^2_{ndf} (**left**) of the timing correction and the corresponding probabilities (**right**) for the data shown in Fig. 4.13.

The single bunch polarizations P_b are averaged over five minutes (Fig. 4.15, right) and can disclose a difference in polarization for different bunch classes. Bunches that collide with the HERA protons can have a tune-shift compared to the non-colliding bunches due to beam-beam interactions. Hence, the polarization of colliding and non-colliding bunches usually is different. The polarization of the two bunch classes can change in the course of a HERA fill (Fig. 4.15, left) and can be used to tune the polarization. Information on the polarization of single bunches is crucial for the measurement of spin observables at H1 and ZEUS after the HERA luminosity upgrade [150].

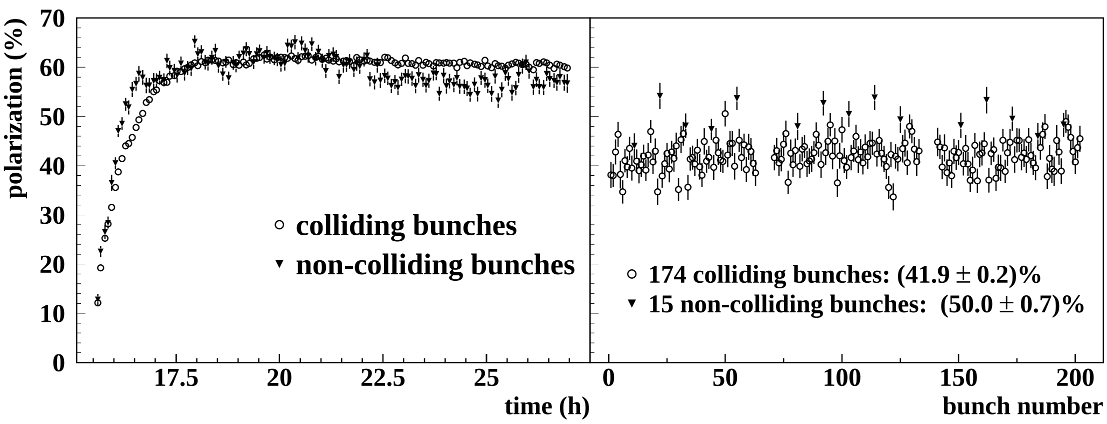

Figure 4.15: Left: Development of the polarization for colliding and non-colliding bunches over the course of the fill shown in the middle of Fig. 4.13. **Right**: example of a polarization measurement of the individual bunches averaged over 20 minutes (from 16.2 h, left picture).

4.4.3 Gain Matching

Proper matching of the four PMT gains is needed to obtain optimum resolution of the polarization measurement as well as to determine unbiased Compton cone positions for the table control. Obviously, in multi-photon operation a gain mismatch cannot be distinguished from an off-center Compton cone. The following calibration method is used to solve this problem.

First, at constant specific luminosity and constant beam position and polarization, the calorimeter table is used to scan the inner 2×2 cm^2 of the calorimeter with the Compton cone. The resulting event distribution over the front-face does not need to be uniform. The spatial asymmetries η_x and η_y are calculated using the last known set of gain factors g_i. Four windows in η_x-η_y-space are defined, one for each PMT (Fig. 4.16, left). The mean signal height $\langle P_i^{gm} \rangle$ of events which fall into the window of PMT number i is used to define a new gain factor:

$$g_i = \frac{\langle P_i^{gm} \rangle}{\sum_{j=1}^{4} \langle P_j^{gm} \rangle} \qquad \text{with} \qquad i = 1 \ldots 4 \ . \tag{4.20}$$

The gains g_i are now used to recompute the P_i^{gm} according to Equation 4.14. The whole procedure is iterated until the gains g_i converge (Fig. 4.16, right). The procedure usually converges in less than five steps. The non-uniform density of events shown in Fig. 4.16 is a result of the datataking and does not influence the iteration. The rectangular area scanned is reconstructed correctly compared to the unsatisfactory situation before (Fig. 4.16, left). The systematic uncertainty of the gain factors turns out to be less than 3%.

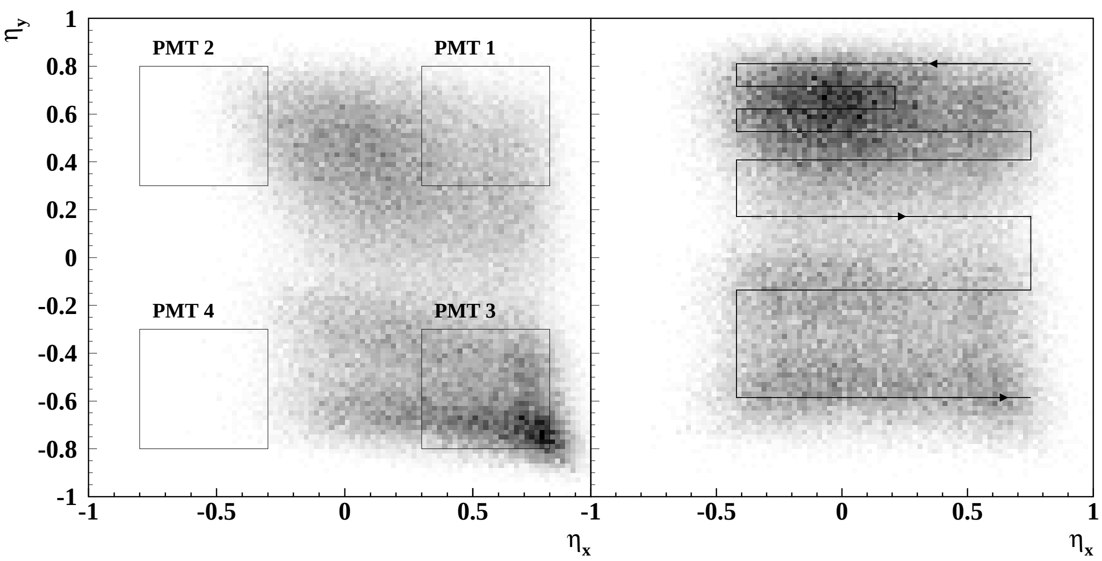

Figure 4.16: Example of the benefit of the iterative gain matching procedure (measurement from 4.12.1999): a **rectangular area** on the calorimeter front-face was scanned with the Compton cone by moving the table. **Left:** Distribution of events in η_x-η_y-space before the gain matching procedure with the four areas assigned to the PMTs superimposed. The rectangular area is not properly reconstructed and appears distorted. **Right:** The event distribution after the gain matching procedure. The **rectangular shape** of the scan (solid line) becomes visible. Apart from small gain changes for PMTs 1-3, the gain of PMT4 is now increased by a factor of two. All values of η_x are larger than -0.7 because the calorimeter movement was limited by the positron beam pipe.

Besides the determination of the absolute gains, the relative gains can be monitored using the HERMES *Gain Monitoring System* (GMS). Green light pulses from a dye-laser laser with a filter wheel in front are guided by glass fibers via an attenuation unit to the cathode of each photo-multiplier and a reference diode. The filter wheel can host eight filters and turns synchronous to the laser to the next filter position at a rate of three times a second. Five positions in the wheel are equipped with neutral density filters while three positions let the laser light pass unattenuated. The resulting six different light intensities can be used to deduce a slope between diode response and the PMT signal. The slope corresponds to the relative gain of the PMT and is computed every twenty minutes for the LPOL setup.

4.5 The Longitudinal Polarimeter: Systematic Uncertainties

The variety of effects which can influence the LPOL measurements are described in this Section. Detailed Listings and Figures of the corresponding studies can be found in Appendix A.2. Besides the calibration of the NBW calorimeter, systematic uncertainties arise from imperfect light polarization, an eventual Pockels cell misalignment, the location of the Compton cone on the calorimeter front face, or from improper gain matching of the photo-multipliers. The considered systematic effects are listed in Table 4.1.

The systematic uncertainty on the analyzing power $\mathcal{A}^{LPOL}$ amounts to 0.9% and is described in detail in Appendix A.1. A change of the analyzing power during a transition from single- to multi-photon operation could be excluded to a precision of 0.8% (Fig. A.5). The long-term stability of the analyzing power of the NBW calorimeter was cross-checked periodically by employing a TPOL-type sampling calorimeter instead. These measurements show no trend with time and prove an analyzing power stability of 0.5% (Fig. A.6), resulting in a total 1.3% contribution to the total systematics.

The light polarization in the laser room was regularly checked, and the Pockels cell adjusted to give more than 99.9% circular light polarization. However, in principle the mirrors of the laser transport system, or the fused silica windows could destroy the circular component. Test measurements at several locations of the laser transport system were performed with light analyzer box AB1. The studies yielded slightly lower polarizations giving, together with the systematic precision (0.1%) of the method, a 0.2% contribution to the overall systematics. No correction on the beam polarization value is made since the reason for the slight decrease of the circular component could be the silica exit window which follows behind the interaction point.

In principle, a misaligned Pockels cell could introduce a false asymmetry into the polarization measurement by shifting, attenuating, or focusing the two helicity states differently so the Compton rate will be biased. An upper limit of 0.4% on the influence of these effects was inferred using two different methods: In one case several measurements at stable beam polarization were done with and without an additional half-wave plate in the light path which interchanges left and right handed circular light polarizations. It was found that within 0.3% the magnitude of the measured beam polarization stayed the same (Tab. A.2, Fig. A.7), only its sign changed as expected. In the other case, a helicity dependent luminosity was excluded (< 0.3%) by changing the overlap of laser and positron beam. By steering mirror M4 to extreme settings, an overlap of only the lateral part of the Gaussian laser beam profile with the positron beam was achieved (Tab. A.3).

If the Compton cone is not centered on the calorimeter, lateral shower leakage occurs which could bias the measurement. Within ±3 mm off the center, the calorimeter was scanned at stable beam conditions (Tab. A.4). No significant effects were observed; a limit of 0.6% could be set on the influence on the polarization measurement. Another worry could be the slow horizontal positron beam slope drifts during a fill. A possible influence on the measurement, by setting the beam slope at the interaction point to extreme settings while leaving the Compton cone centered, could not be proven (Tab. A.5). An upper limit of 0.5% could be inferred giving a total contribution of 0.8% by possible Compton cone instabilities.

Slow gain drifts of the PMTs can occur over months because of aging of the PMT dynodes or regeneration effects after a longer shutdown when the NBW calorimeter was switched off. These issues were resolved by the gain matching method described in the previous Section and by the analysis of GMS events. Latter showed also 20-30% gain drifts during the course of a fill, mostly due to temperature changes in the tunnel. But since the gains of the PMTs drift together and the LPOL does not rely on an absolute energy calibration, influences are expected to be small. Undisclosed long-term drifts in several cases caused a mismatch between two PMTs of about a factor of two. To estimate the systematic effect, regular datasets where re-calculated with intentionally mismatched PMT configurations of the same magnitude. It was found that the influence of such a severely mismatched calorimeter is at most 0.3%.

Table 4.1: Contributions to the fractional systematic uncertainty of the polarization measurement.

systematic effect	$\Delta P/P$	
analyzing power		1.3%
calibration in test beam	0.9%	
transition single- to multi-photon amplification	0.8%	
stability of $\mathcal{A}^{LPOL}$	0.5%	
light polarization		0.2%
helicity dependent luminosity		0.4%
Pockels cell	0.3%	
light path	0.3%	
Compton cone stability		0.8%
Compton cone x-position	0.4%	
Compton cone y-position	0.5%	
drifts of the horizontal positron beam slope	0.5%	
gain matching		0.3%
total systematic uncertainty		1.6%

Conclusion

The total relative systematic scale uncertainty of 1.6% of the Longitudinal Polarimeter is derived as the quadratic sum of the contributions treated above. Together with an absolute statistical precision of the measurement of 1% per minute, and a good running performance, the LPOL measurements play a major role for the precision of the HERMES polarized datasets taken in 1999 and 2000. The work of this thesis contributed to a large part to the calibration efforts, the data analysis and data taking by creating the LPOL online-program, and the determination of the systematic uncertainty of the Longitudinal Polarimeter. The final results went into the publication of the LPOL apparatus [151].

In future, several upgrades of the LPOL setup are planned. A fast, dedicated data acquisition and a Fabry-Perot cavity substituting the pulsed laser are proposed [152]. The main idea is to improve the statistical precision and to enable a continuous calibration by running in a *few-photon* configuration (cf. Fig. 4.3, middle).

5 Modeling of the Fragmentation Process

In this Chapter, HERMES data on hadron production in semi-inclusive DIS will be used to derive a data-descriptive model of the hadronic final state using LUND string fragmentation. The results and insights are carried over as a best possible model to understand photoproduction events at HERMES (Chapters 6 and 7).

5.1 Fragmentation Models

High-energy collisions between two particles typically lead to many particles in the final state depending on the center-of-mass energy of the reaction. While the initial electroweak or strong physics processes at small time scales can be explained by QED or QCD, theoretical calculations of the transformation of the resulting coloured partons into colourless hadrons (hadronization) is not established up to day. Quantum chromodynamics is the theory of choice in this case but reaches its practical limits when trying to carry out the non-perturbative calculations needed in the case of hadronization. Additional difficulties are introduced by the large number of final state particles which will lead to a very complex structure of the matrix elements.

The gap of the present understanding of hadronization is filled by phenomenological models. Historically, the need for explanations of the observed hadronic final states in e^+e^- annihilation events triggered the development of various models, generally realized by Monte Carlo simulations. The most important approaches are the *independent fragmentation model*, the *cluster fragmentation*, and the *string model*. Each model bases on different ad hoc assumptions.

5.1.1 Independent and Cluster Fragmentation

The independent fragmentation model assumes the hadronization to be the incoherent sum of the fragmentation of the individual partons. In the model, a quark q originating from a hard interaction produces a jet of hadrons by the following scheme (Fig. 5.1, left): based on a probability distribution $f(z)$ a hadron $q\bar{q}_1$ with energy fraction z is created, leaving a quark q_1 with the energy fraction $(1-z)$ behind. The procedure is repeated with the corresponding left-over quark until z_i falls below a threshold. The last quark in the chain q_i is neglected. The incorporation of strangeness production, particle decay and some transverse momentum properties lead to the Field-Feynman model [153] with its longitudinal fragmentation function:

$$f(z) = 1 - a + 3a(1-z)^2 \qquad \text{with} \qquad a = 0.77 \text{ (default)} . \tag{5.1}$$

The concept of independent fragmentation leads to small violations of the conservation of flavour, energy and momentum. Also the model ansatz is not Lorentz covariant and does not naturally contain gluon jets, needed for the explanation of 3-jet events. Several extended descriptions tried to fix these problems (for instance the Hoyer-Model [154] or QCDJET [155]).

The cluster fragmentation concept derives the hadronic final state by two steps. In the first step, a *parton shower* is evolved by $q \to qg$, $g \to q\bar{q}$ and $g \to gg$ branchings according to a leading logarithmic QCD approximation similar to the Altarelli-Parisi splitting functions. The shower is ended below a certain energy threshold and all remaining gluons are split non-perturbatively into $q\bar{q}$ pairs. In the second step, nearby partons in phase space are collected to *clusters* which isotropically decay into two hadrons (Fig. 5.1, right). Low-mass clusters are eventually transformed to a single hadron. The most prominent representatives of the cluster fragmentation are the Webber model [156] (HERWIG program [157]) which includes interference effects of the parton shower, and the CALTECH-II model [158] which does not enforce the final $g \to q\bar{q}$ branching and allows for cluster decay into multiple hadrons. The cluster fragmentation concept is Lorentz-covariant and has few free parameters such as energy cut-offs. On the other hand, the clustering itself is not motivated by QCD and the parton shower evolution is not applicable at lower energies like at HERMES.

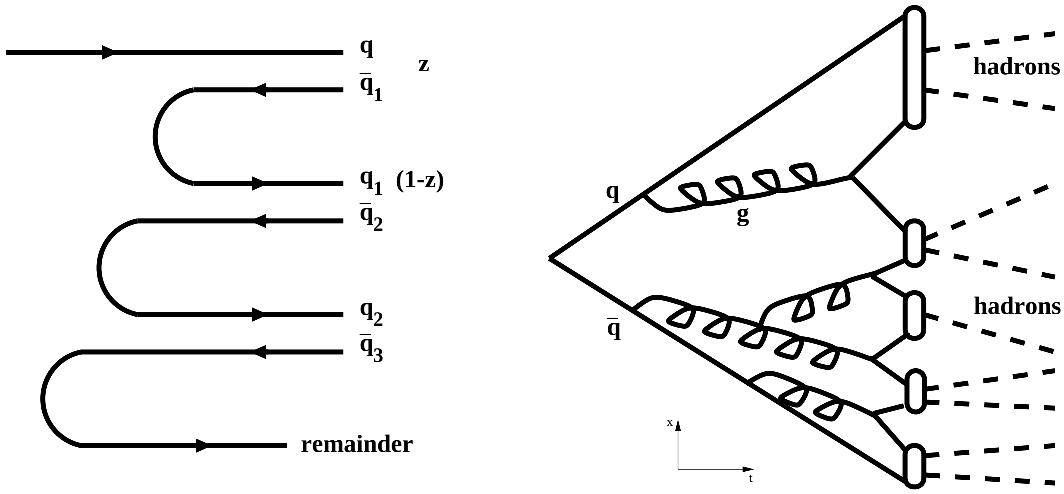

Figure 5.1: Left: Independent fragmentation scheme. **Right**: Fragmentation of a $q\bar{q}$ pair in the cluster fragmentation. The rounded boxes symbolize the *clusters* of quarks and anti-quarks which are decayed to hadrons.

5.1.2 Concept of the LUND String Model

The LUND string model is realized by the JETSET program [159] which allows to adjust the parameters of the model. The string description [160] intuitively depicts the linear quark confinement expected at large distances in QCD. For example, a $q\bar{q}$ pair moving apart stretches the gluon field in between. The field can be imagined as a cylindrical flux-tube with about 1 fm in diameter or simply as a *string* between the quark and the anti-quark. The string (the gluon field) gains energy by $\kappa \approx 1$ GeV/fm when stretched apart. The string constant (or field energy density) κ is known from hadron spectroscopy in connection with the Regge model [161] and sets the scale of a linear potential $V(r) = \kappa r$ between the two partons at distance r. If the string has reached a length of more than 1 fm, it may break by production of a new $q\bar{q}$ pair (Fig. 5.2, left). The resulting two strings can split again according to the same scheme, until an energy threshold is reached. In a quantum mechanical sense, the quark and the anti-quark are produced in one point and tunnel out with some finite longitudinal and transverse momentum gained from the energy of the field. Thus, the probability for a $q\bar{q}$ pair with quark mass m and transverse momentum p_T is proportional to:

$$P \sim \exp\left(-\frac{\pi m_T^2}{\kappa}\right) = \exp\left(-\frac{\pi m^2}{\kappa}\right) \exp\left(-\frac{\pi p_T^2}{\kappa}\right) , \tag{5.2}$$

where $m_T^2 = m^2 + p_T^2$ is called the transverse mass. The total transverse momentum is balanced between the quarks. The LUND model assumes p_T to be distributed Gaussian with a width $\sigma \approx 0.35$ GeV (adjustable parameter PARJ(21) in JETSET). Additionally, a small admixture f_t (parameter PARJ(23)) of a second Gaussian with larger width $t \cdot \sigma$ ($t \approx 2$, PARJ(24)) is introduced. The relative occurrence of flavours is governed by the quark masses and Equation 5.2 giving $u : d : s : c \approx 1 : 1 : 0.3 : 10^{-11}$. This mechanism can be adjusted in the LUND model by changing the probability for the production of strange quarks compared to non-strange quarks $s_{supp} \approx 0.3$ (parameter PARJ(2)).

For the longitudinal sharing of energy and momentum the LUND model gives the probability distribution for a string breakup per invariant time τ:

$$P(\tau)\, d\tau^2 \sim (\tau\kappa)^{2a} e^{-b\tau^2\kappa^2} d\tau^2 , \tag{5.3}$$

with the free parameters a (PARJ(41)) and b (PARJ(42)). If used iteratively, the result of this ansatz is *symmetric* on whether the string breaking is started from the left or the right end of the initial string. From Equation 5.3 follows the LUND *symmetric* fragmentation function for a hadron (or string) with longitudinal energy fraction z:

$$f(z) \sim z^{-1}\, (1-z)^a\, e^{-bm_T^2/z} . \tag{5.4}$$

In principle, a and b can depend on the quark flavour of the produced quark-antiquark pair although this assumption is not necessary to describe most of the higher energy data like at PETRA, where $a = 1$ and $b = 0.7$ was found.

Baryons are produced by the so-called popcorn mechanism [162] where successive production of a $q'\bar{q}'$ and a $q''\bar{q}''$ pair occurs. Together with the original quark q and the anti-quark $\bar{q}$, a baryon B ($qq'q''$) and an anti-baryon $\bar{B}$ ($\bar{q}\bar{q}'\bar{q}''$) is produced, for example. In principle even more pairs can be created leading to additional mesons M generated in between the hadrons resulting in a $BM\bar{B}$ configuration. The probabilities for $B\bar{B}$ and $BM\bar{B}$ occurrences relative to an ordinary string break are controlled by the ad hoc probabilities $b_{B\bar{B}} \approx 0.1$ (parameter PARJ(1)) and $b_{BM\bar{B}}$ (parameters PARJ(5-7)). The parameter a of the symmetric fragmentation function is increased in these cases to be PARJ(41) + PARJ(45) leading to a shift towards lower z values for baryons and related mesons.

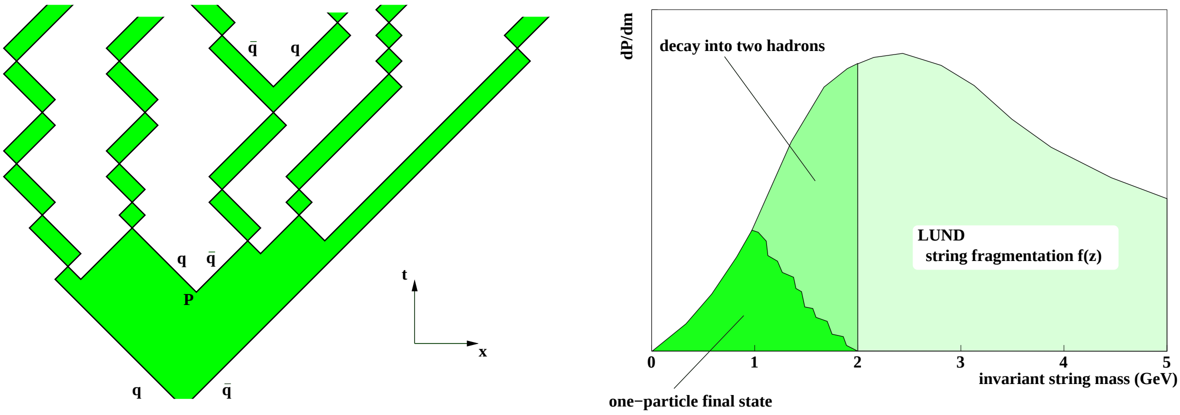

Figure 5.2: Left: String-breaking in the LUND approach. The initial $q\bar{q}$ pair moves apart with a gluon field in between (grey area). The first string break occurs at the point P. **Right**: Illustration of the differential probability (dP/dm) for the (final) steps of the LUND fragmentation versus invariant string mass.

Once the invariant mass of a string falls below a threshold (defined with the help of PARJ(33)) the string with its (di)quarks is converted into a meson or baryon with the corresponding quark content. Hadrons with higher spin are properly suppressed depending on the number of their spin states. Nevertheless, this suppression of particles with non-zero spin can be altered by changing the model parameters PARJ(11-17) but is left untouched in this work because the spin-state counting concept would be destroyed otherwise.

Because of the limited invariant mass of the hadronic final state ($W < 7.2$ GeV) at HERMES, the low-energy behaviour of the LUND model is of some importance. In such a case only a few string breaks occur, so the treatment of the transformation of the final strings into hadrons gains influence on the overall hadron kinematics. The fragmentation of a string according to Equation 5.3 is stopped if its invariant mass falls below a certain threshold (for example 2 GeV in Fig. 5.2, right). Now, either a one-hadron or a two-hadron final state is produced. In the latter case the *standard JETSET* program (Version 7.4.10 [159], implemented in LEPTO/PEPSI [163, 164]) splits the string for a last time and decays it isotropically into two hadrons. This treatment leads to a 50% chance that a hadron will have a similar rapidity as the quark which it inherited from the corresponding end of the string. Consequently, the actual kinematics of this final fragmentation step does not depend on any of the model parameters. The most recent, *enhanced JETSET* (part of PYTHIA6 package 6.158 [165]) treats the above situation differently [167]: the two hadrons are emitted non-isotropically with just a small chance p of wrong rapidity ordering:

$$p \sim \frac{1}{1 + e^{b\,\Delta}} \quad , \tag{5.5}$$

with the LUND fragmentation parameter b and a function Δ which depends on kinematics. If b goes to zero the rapidity ordering is randomized as in the standard JETSET scheme. Additionally, in the enhanced JETSET the emittance of the two hadrons is dampened exponentially in the transverse direction relative to the string direction by $\exp(-p^2_{T,hadrons}/2\sigma^2)$. This restores a behaviour equivalent a regular string break which now depends on the parameters b and σ.

Furthermore, the LUND model naturally contains gluon jets, which can be imagined arising from *kinks* in a string. Also, parton showers can be employed before the LUND string fragmentation. This option is not applicable for HERMES energies so the standard string fragmentation is used only here (MSTJ(41)=0). The LUND model was chosen in the subsequent analysis because it comprises several advantages: the model is motivated by QCD, possesses a well-defined space time picture (i.e. is Lorentz-invariant), contains gluon jets, conserves the colour charge and flavours, and allows for baryon production. Moreover, the LUND model has advanced to a standard tool in high-energy physics to derive the hadronic final state so findings on the various free parameters of the model can be compared among experiments.

5.2 Adaption to HERMES Kinematics

This Section treats the analysis and simulation of HERMES DIS data. Especially, the modifications and settings of the different parts of the DIS simulation needed for best possible agreement with the data are elucidated. The HERMES DIS Monte Carlo program used (gmc_dis) also incorporates POLRAD [168] which is used for radiative corrections here. Furthermore, the influence of detector material and tracking on the measurement, deduced from a GEANT [169] simulation of the HERMES detector (HMC), is discussed. The resulting DIS Monte Carlo analysis is compared to DIS data on an unpolarized hydrogen target. Subsequently, a strategy to adapt the LUND model to the measured hadronic final state is defined and conducted.

5.2.1 Deep Inelastic Scattering: Data Analysis

The HERMES experiment took data with an unpolarized hydrogen target at multiple occasions from 1996 to 2000 in between regular polarized data taking. Here, the unpolarized runs on hydrogen from 2000 are used for comparison with the simulations for two reasons: it is the largest data set taken in one running period (about $6 \cdot 10^6$ DIS events) and, in contrast to earlier years, the RICH detector is available to identify the hadron types. The burst-wise data quality criteria applied for the analysis are similar to the ones explained in the next Chapter (see Tab. 6.2 in Sect. 6.2.1).

Acceptance and Kinematics

For real data as well as for simulated events, acceptance cuts need to be imposed to account for the edges of the HERMES detector. The cuts listed in Table 5.1 ensure that the tracks come from the target cell, traverse the entire spectrometer, and are contained in the calorimeter wall. The angular variables θ_x and θ_y used in HERMES analyses are the horizontal and vertical projections of the polar scattering angle θ:

$$\theta_x = \arctan(\cos(\phi)\tan(\theta)) \qquad \text{and} \qquad \theta_y = \arctan(\sin(\phi)\tan(\theta)) \ , \tag{5.6}$$

with the azimuthal angle ϕ. The angles were also corrected for small changes in the external alignment of the top detector relative to the bottom detector (see [170]). Hadrons with momenta below 4 GeV were discarded to ensure good (RICH) particle identification and good agreement with the momentum acceptance modeling in the Monte Carlo Simulation. Further cuts on the positron kinematics ensure deep inelastic scattering processes (Tab. 5.2). At least one positron track in the event has to fulfill the conditions $Q^2 > 1$ GeV^2 and $W^2 > 10$ GeV^2 to be labeled a DIS event. The upper cut on y of 0.83 is imposed to exclude a region where radiative corrections and their systematic uncertainties become too large to be incorporated. This cut supersedes the requirement of an energy deposition by the positron of at least 1.4 GeV in the calorimeter, needed to assure proper triggering of Trigger 21. The requirements on Q^2 and W^2 result in a lower y cut of 0.195. Semi-inclusive hadrons from the current region are selected by requiring $z > 0.2$ and $x_F > 0.1$. Together with the W^2 cut, these cuts correspond to the Berger criterion [39].

The DIS events identified so far have to be corrected for charge symmetric background. Background events are processes where the positron identified is not the one that scattered off the nucleon. A produced γ, for example, could create a e^+e^- pair in the detector material where the $e+$ could be mistagged as DIS positron. The correction algorithm counts all events with DIS-like electrons and subtracts them from the DIS-like positron events. The same is done to the statistics of the hadrons which come in coincidence with the DIS-like particles. This algorithm exploits the charge symmetry of the background and gives the real number of (semi-inclusive) DIS events.

Table 5.1: Acceptance cuts applied to each track.

cut	boundary
$\|\theta_x\| < 0.192$ mrad	opening of the magnet
$\|\theta_y\| < 0.148$ mrad	frame of MC 3
$\|\theta_y\| > 0.040$ mrad	steel plate
$\|z_{vertex}\| < 18$ cm	length of the target cell
$r_{vertex} < 0.75$ cm	diameter of the target cell
$\|x_{calorimeter}\| < 175$ cm	shower contained in left/right calorimeter edge
$\|y_{calorimeter}\| < 108$ cm	shower contained in upper calorimeter edge
$\|y_{calorimeter}\| > 30$ cm	shower contained in lower calorimeter edge
$p_{hadron} > 4$ GeV	PID and simulation
$\sum_i p_i < 28$ GeV	proper reconstruction, background

Table 5.2: Kinematic cuts imposed on the positron track to select deep inelastic scattering.

cut	motivation
$Q^2 > 1$ (2) GeV^2	scattering off a single quark
$W^2 > 10$ GeV^2	discard resonance region, current region
$y < 0.83$	limit influence of radiative corrections
$x_F > 0.1$	current region (Berger criterion)
$z > 0.2$	current region (Berger criterion)

Particle Identification

In order to achieve the highest possible efficiency at lowest possible contaminations in separating positrons from hadrons, the responses of the four particle identification detectors (Figures 3.8,3.10(left),3.12) are combined. For each of the detectors a probability analysis of the signals leads to a likelihood $\mathcal{L}^i$ of a certain particle type i to have given a certain measured response (*conditional probability*) [171]. The *real probability* $\mathcal{P}^i$ of a response to be caused by a certain particle type is found by Bayes' Theorem (see for instance [172]):

$$\mathcal{P}^i = \frac{p_i \cdot \mathcal{L}^i}{\sum_k p_k \cdot \mathcal{L}^k} , \tag{5.7}$$

where p_i is the relative abundance (or flux) of a particle of type i. In the simplified case of positrons (electrons) and hadrons as the only two particle types the logarithmic likelihood of the two corresponding probabilities is formed:

$$PID' = \log_{10} \frac{\mathcal{P}^e}{\mathcal{P}^h} = \log_{10} \frac{\mathcal{L}^e}{\mathcal{L}^h} - \log_{10} \phi . \tag{5.8}$$

The quantity PID' is larger than zero if a particle is more likely to be a positron than a hadron. The *flux factor* $\phi = p_h/p_e$ is the ratio of the number of hadrons to positrons incident on the detector. The quantity ϕ depends on charge, scattering angle, and momentum and can be found by a Bayesian iteration [132]. The logarithmic likelihoods of all detectors can be joined:

$$PID_{35} \equiv \log_{10} \frac{\mathcal{L}^e_{Cer}\mathcal{L}^e_{TRD}\mathcal{L}^e_{Pre}\mathcal{L}^e_{Cal}}{\mathcal{L}^h_{Cer}\mathcal{L}^h_{TRD}\mathcal{L}^h_{Pre}\mathcal{L}^h_{Cal}} \qquad \text{resp.} \qquad PID'_{35} = PID_{35} - \log_{10} \phi(\theta, p) . \tag{5.9}$$

For the data taken from 1998 to 2000, the RICH was not used to discriminate hadrons over positrons so that the following quantities were used:

$$PID_{25} \equiv \log_{10} \frac{\mathcal{L}^e_{TRD}\mathcal{L}^e_{Pre}\mathcal{L}^e_{Cal}}{\mathcal{L}^h_{TRD}\mathcal{L}^h_{Pre}\mathcal{L}^h_{Cal}} \qquad \text{resp.} \qquad PID'_{25} = PID_{25} - \log_{10} \phi(\theta, p) . \tag{5.10}$$

In the data analysis, positrons and electrons were identified by requiring $PID'_{25} > 2$, while hadrons had to fulfill $PID'_{25} < -1$. The flux factors were derived from the data set itself by a Bayesian iteration. The positron efficiency with these cuts is larger than 99% and contaminations are always below 0.5%. For comparison with the Monte Carlo simulations below, the finite efficiency of the particle identification is corrected for. The determination of efficiencies and contaminations was achieved by the methods outlined in [173].

The identification of the hadron type (π, K, p) by the RICH is done by using the likelihood response of the DRT or IRT method (cf. Sect. 3.3.2). The particle type i with the largest likelihood is assigned to the measured track if the *RICH Quality Parameter*:

$$Q = \log_{10} \frac{\mathcal{L}^i_{RICH}}{\mathcal{L}^j_{RICH}} \qquad (j: \text{ second most likely particle type}) \ , \tag{5.11}$$

is larger than zero. The efficiency of the RICH PID is better than 99% for pions but still under study for the other particle types. Thus, the comparison of data and simulation concerning the hadron types will be restricted to cross-checks.

5.2.2 Deep Inelastic Scattering: Simulation

The HERMES DIS Monte Carlo program (gmc_dis) consists of a chain of four distinct programs (Fig. 5.3). The first program (DIS) generates the four-vector of the scattered positron using the structure function F_2 or the unpolarized quark densities according to Eq. 2.35. Then, radiative corrections are applied on the virtual photon by POLRAD [168], leaving the original positron kinematics unchanged. In a third step, the virtual photon is handed to LEPTO [163] which decides on the quark struck in the nucleon using the unpolarized quark densities as input. The fourth program is JETSET which takes the struck quark and the target remnant and derives a hadronic final state using the LUND model. The output of gmc_dis in form of four-vectors for each particle is written to ADAMO tables (gmc.devent files). This output can either be used directly for analysis or can be piped into a full GEANT Monte Carlo simulation of the HERMES detector (HMC).

The simulation result of LEPTO as stand-alone program with old HERMES fragmentation settings (Tab. 5.3, Sect. 5.3.1) can be viewed as starting point of the following efforts. Since the output of the simulation consists only of four-vectors, the positions at the calorimeter location are found by the momentum lookup-table of the tracking program HRC. This table is used to look up the deflection of the particles by the magnetic field depending on momentum and scattering angles. After the acceptance and DIS cuts listed in the previous Section are applied, the resulting spectra on the inclusive quantities Q^2 and W^2 show the necessity of improvements if compared to unpolarized hydrogen data (Fig. 5.4). Also, the observed semi-inclusive hadron multiplicity is overestimated in such a simulation setup.

One reason for the discrepancy lies in the construction of the structure function F_2: LEPTO generates its inclusive positron kinematics using F_2^p from Equation 2.35 which leads to discrepancies at low Q^2 since all parton density functions available are fit to high-energy data with $Q^2 > 4$ GeV^2 (Fig. 5.5). The DIS-program goes one step further and generates according to the ALLM parameterization of F_2^p which is an excellent fit to the world data for $Q^2 > 1$ GeV^2 [174].

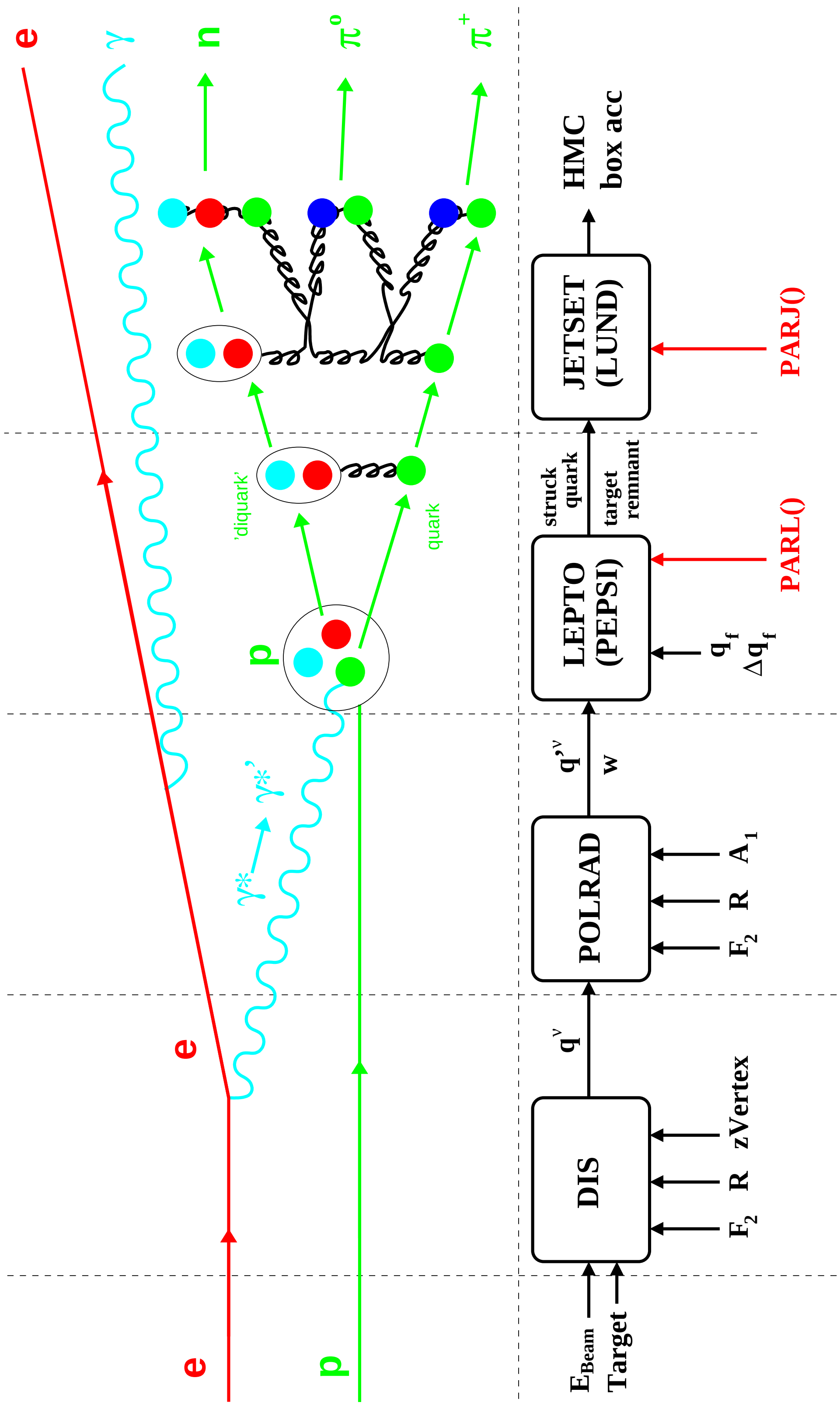

Figure 5.3: Program structure of gmc_dis. The upper part of the figure depicts the steps in the simulation of the physics process, the lower part visualizes the sub-programs with the inputs used.

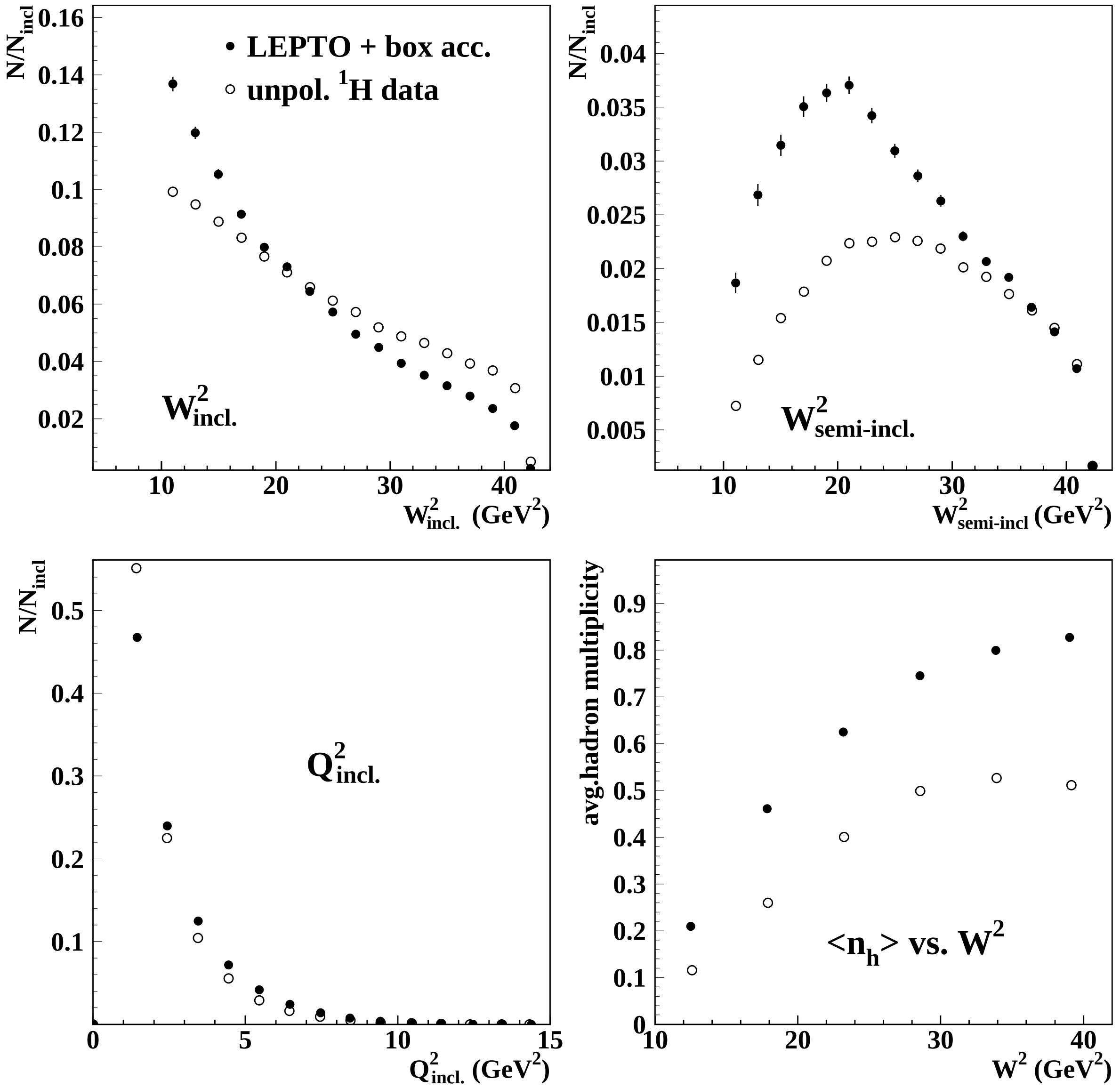

Figure 5.4: Result of a simulation with LEPTO using CTEQ5 parton distributions together with angular acceptance cuts and the HRC momentum lookup-table (box-acceptance). **Top**: Comparison of the inclusive and semi-inclusive W^2 distribution between data (empty circles) and simulation (solid circles); normalized to the number of inclusive events N_{incl}. **Bottom**: Comparison of the inclusive Q^2 distribution and the average observed hadron multiplicity $\langle n_h \rangle$.

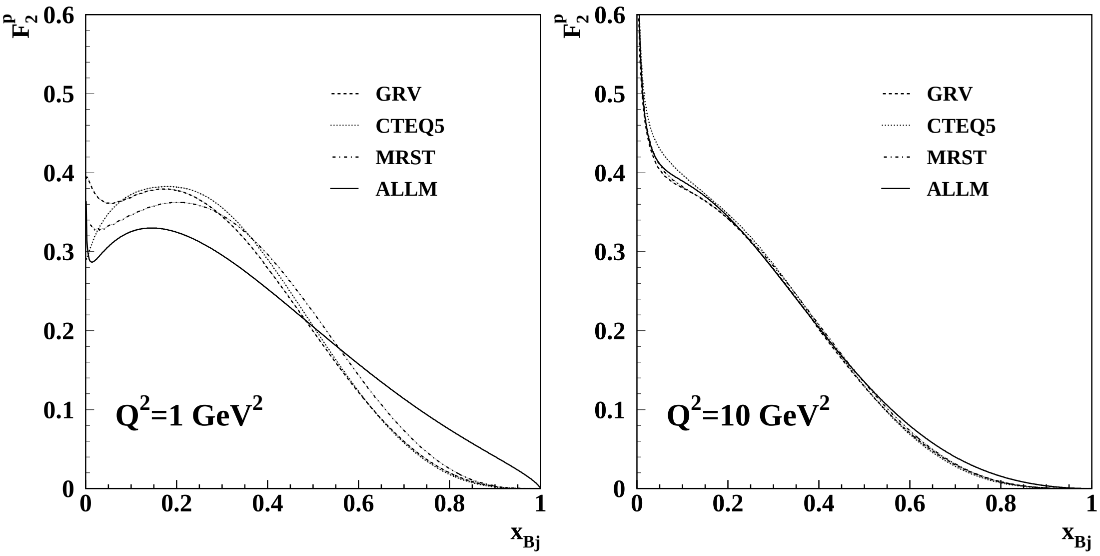

Figure 5.5: The structure function F_2^p as function of Bjørken x. The ALLM parameterization [174] is compared to the F_2^p obtained from GRV (98LO) [52], CTEQ5 (CTEQ5F3) [175], and MRST (COR01) [176] using the simple quark-parton model formula (Eq. 2.35).

To avoid further complications, the DIS-program re-normalizes all input parton density functions $q_f(x, Q^2)_{input}$ to add up to the correct F_2:

$$q_f(x, Q^2)_{corr} = q_f(x, Q^2)_{input} \cdot \frac{F_2^{ALLM}}{\sum_i e_i^2 \, x \, q_i(x, Q^2)_{input}} \, . \tag{5.12}$$

Thus, the densities of the quark flavours f relative to each other stay untouched. Moreover, this re-normalization has the advantage that F_2^{ALLM} can be consistently used by the radiative correction procedure which then becomes independent of the unpolarized parton densities chosen.

5.2.3 Deep Inelastic Scattering: Radiative Corrections

Up to now, deep inelastic scattering has been discussed in the Born approximation of one-photon exchange (cf. Fig. 2.1, Sect. 2.1). But the measured events in the defined DIS region (Tab. 5.2) can also come from higher-order processes (Fig. 5.6). For instance, in DIS events in which a higher-order process occurred the measured positron will display different x, y, Q^2, and W^2 values (measured kinematics) than actually were truly involved in the virtual photon-nucleon interaction (true kinematics). Generally, this will shift events to lower measured y and higher measured W^2 values. The latter results in a lower observed hadron multiplicity. Also events from the tail of elastic scattering can appear to be DIS if the positron radiated a sufficiently hard photon. This effect will actually increase the number of measured inclusive events in the selected DIS region, especially at lower Q^2.

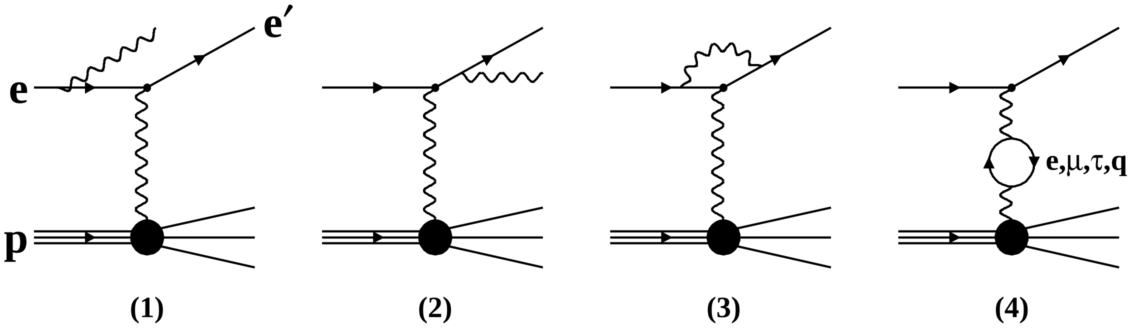

Figure 5.6: Feynman graphs of the higher order QED processes in deep inelastic scattering: initial state bremsstrahlung (1), final state bremsstrahlung (2), vertex correction (3), and vacuum polarization (4).

The application of the radiative corrections is realized by the POLRAD [168] program which integrates the applicable cross sections and contains the expression of the higher order processes. In principle POLRAD works for polarized DIS where radiative corrections on the measured inclusive asymmetry A_1 can be inferred iteratively. However, here the program is used only to correct for the unpolarized kinematics. For each kinematic point on a $x - y$ grid the probability of a Born-like event to be a radiative event with the *same* positron kinematics is tabulated. For every event received from the DIS-program POLRAD decides using its tables whether this event was radiative or not. If it was, the event is re-weighted according to the relevant cross section of the radiative process determined, the kinematics of the virtual photon is altered correspondingly, and a real radiative photon is added when needed. The effects of the radiative corrections are displayed as comparison between measured and true kinematics in Figure 5.7. The inclusive spectrum is changed in shape and population, thus the normalization for the hadron multiplicities also changes.

The resulting virtual photon is handed to LEPTO which decides on the struck quark. In this analysis, also the simulation of photon-gluon fusion and QCD-Compton process is turned on (LST(8)=1) during the tuning of the p_T spectra with LEPTO to be consistent with PYTHIA6. The matrix elements for virtual photon-quark scattering implemented in LEPTO are applicable for *true* virtual photon kinematics with $Q^2 > 1$ GeV^2 and $W^2 > 4$ GeV^2 only. If RADCOR decided on a radiative correction which pushed the true kinematics below one of these limits, no hadronic final state can be delivered by LEPTO (so-called *low-E* events). In order to fix these events, a proton with the remaining four-momentum is produced by gmc_dis. This results in a number of unphysical events (Fig. 5.8) that naturally would have come from the resonance region (which is not modeled by these programs). These low-E events appear at low measured Q^2 and increase with measured W^2. To avoid implications of this low-E treatment, an analysis cut of $Q^2 > 2$ GeV^2 is imposed in the following to allow for an unbiased hadron analysis in the region where the Monte Carlo simulation is actually applicable.

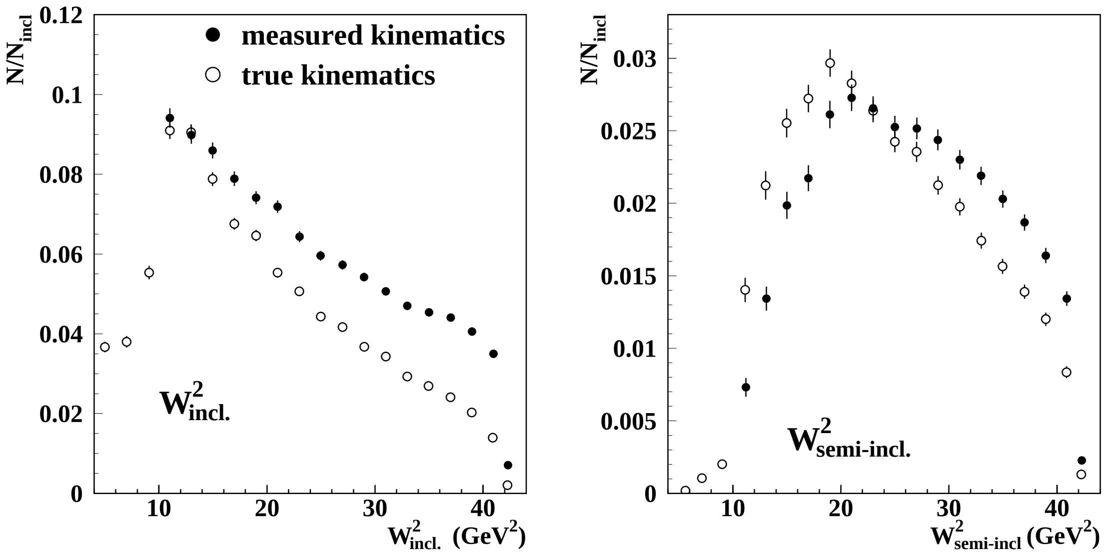

Figure 5.7: Influence of the radiative corrections done by POLRAD. The comparison of detected and true kinematics for a LEPTO Monte Carlo simulation is shown for the W^2 distributions of all events ($W^2_{incl.}$) and semi-inclusive events ($W^2_{semi-incl.}$) which have at least one hadron in coincidence with the positron.

5.2.4 Influence of Detector and Reconstruction

Since interactions with the detector material change the four-momenta of the particles, these influences must be regarded in a DIS analysis. This so-called *smearing* changes the values of the reconstructed kinematic quantities, especially the ones, where the positron is involved. The required investigations were done using the HERMES Monte Carlo (HMC), a full GEANT simulation of the detector response (example for a semi-inclusive DIS event see Fig. 5.9). The detector effects can be disclosed by comparing the four-vectors of the particles as they emerge the vertex with the reconstructed values after modeling by HMC. For the measurement of the momentum this is displayed in Figure 5.10 (left) where the tail of positrons which radiated bremsstrahlung becomes apparent. About 16% of all positrons radiate in the detector material.

Ideally, the output of gmc_dis is piped directly into HMC/HRC to account for detector effects. However, since the processing of one GEANT event takes about[5] four seconds, this is not practical for iteratively fitting a fragmentation model where on the order of 10^5 to 10^6 events are needed. A solution lies in parameterizing all smearing and resolution effects so that a small and fast program could replace a full GEANT Monte Carlo simulation. This was realized by the development of a dedicated program (HERMES-Smearing-Generator, HSG) described in the following.

[5] All statements on computing speed apply to a 350 MHz PENTIUM-II PC.

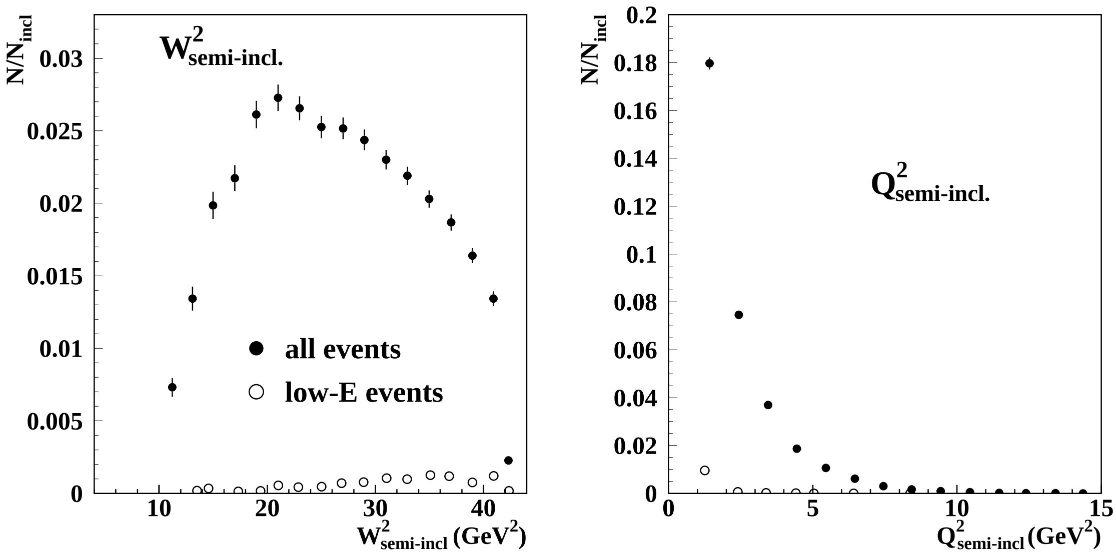

Figure 5.8: The measured W^2 and Q^2 distributions of all semi-inclusive Monte Carlo events (solid circles) superimposed with the fraction of events for which LEPTO is not able to derive a hadronic final state after radiative corrections (*low-E* events, empty circles).

The detector effects were studied on 10^8 generated DIS events on ^{1}H processed by HMC and reconstructed by HRC. The best suited quantities which describe the resolution are:

$$\Delta\Theta_y = \Theta_y^{rec} - \Theta_y^{GMC} \tag{5.13}$$
$$\Delta\Theta_x = \Theta_x^{rec} - \Theta_x^{GMC} \tag{5.14}$$
$$\Delta p/p = (p^{rec} - p^{GMC})/p^{GMC} \ , \tag{5.15}$$

where the superscripts GMC and rec refer to the kinematic values determined by gmc_dis and found by the track reconstruction by HRC after HMC, respectively. These quantities are uncorrelated to a large extent but all depend on the particle momentum. The only clear correlation was found between the momentum resolution and the angular resolution in x-direction, $\Delta\Theta_x$ (Fig. 5.10, right). This correlation is a logical consequence of the momentum determination by the measured horizontal deflection in the magnetic field. For a first approach, this effect will be neglected, but should be taken into account if close agreement is wanted for kinematic variables which comprise angle and momentum, like invariant masses for example.

In a first step, the central resolutions in momentum $\Delta p/p$ and angles $\Delta\theta_x, \Delta\theta_y$ were fit with Gaussians. The results are shown in Fig. 5.11 (left) $f^i(p)$ for positrons and in Fig. 5.11 (right) $f^i(p)$ for hadrons ($i = \Delta p/p, \Delta\theta_x, \Delta\theta_y$). Since the resolutions have non-Gaussian tails, a histogram database had to be established. The actual resolutions were divided by the central resolutions, to obtain histograms which only weakly depend on the momentum; for example:

$$\Delta\theta_x' = \Delta\theta_x / f^{\Delta\theta_x}(p) \ . \tag{5.16}$$

The scaled resolutions were histogrammed in 1 GeV wide bins giving a smearing database for the HSG program.

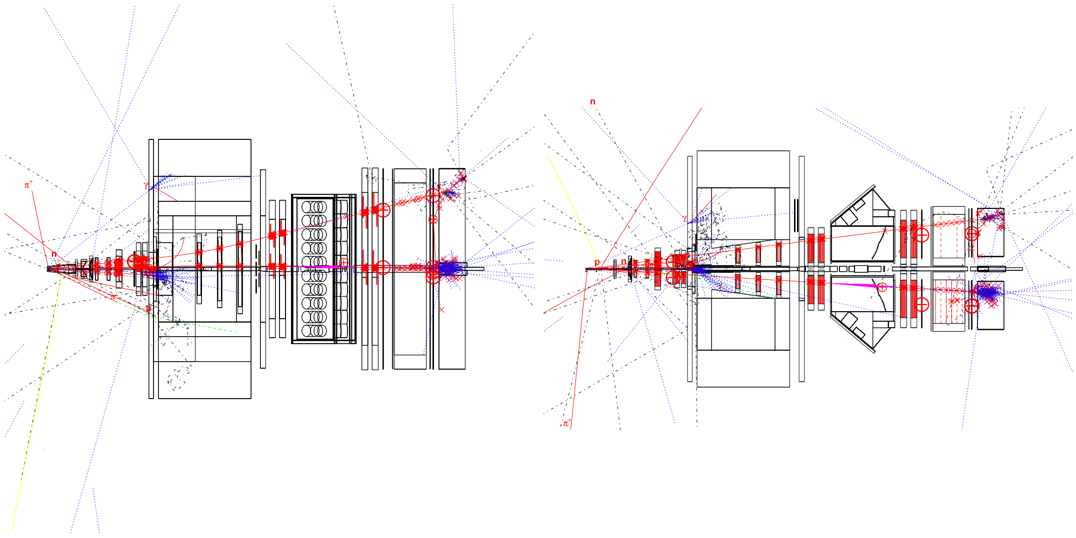

Figure 5.9: Left: The top view of a semi-inclusive event simulated in HMC by GEANT. **Right**: Side view of the same event. The positron enters the bottom detector while the pion travels into the top left of the apparatus.

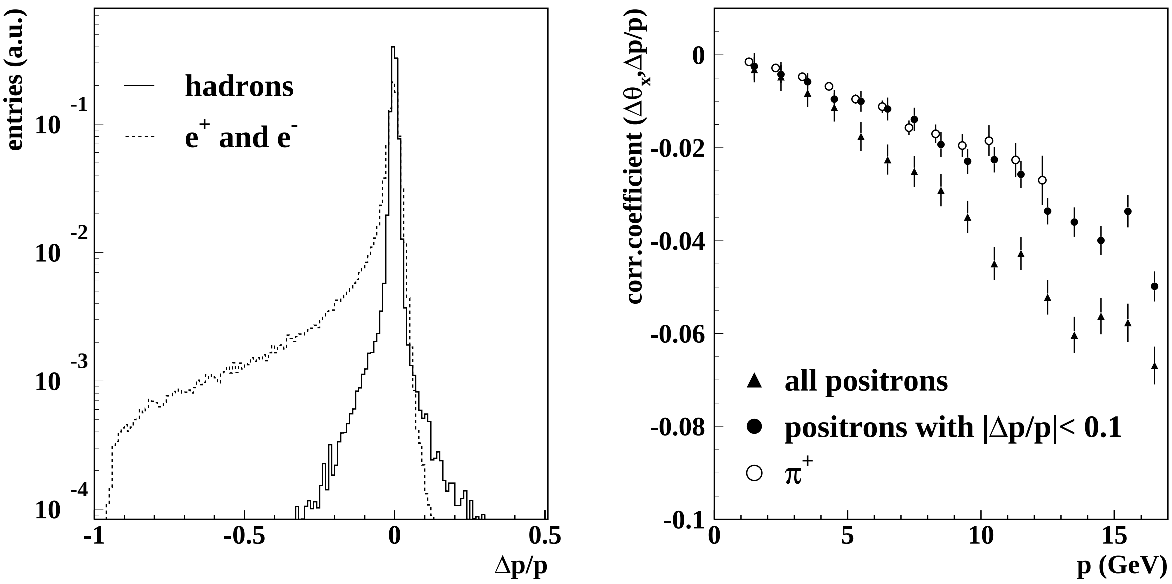

Figure 5.10: Left: Momentum resolution of positrons/electrons and hadrons integrated over all momenta. **Right**: Correlation between $\Delta\theta_x$ and $\Delta p/p$ versus momentum for different particle samples. Positrons/electrons which did not radiate in the detector material show the same correlation behaviour like pions, confirming this effect to be a tracking artefact.

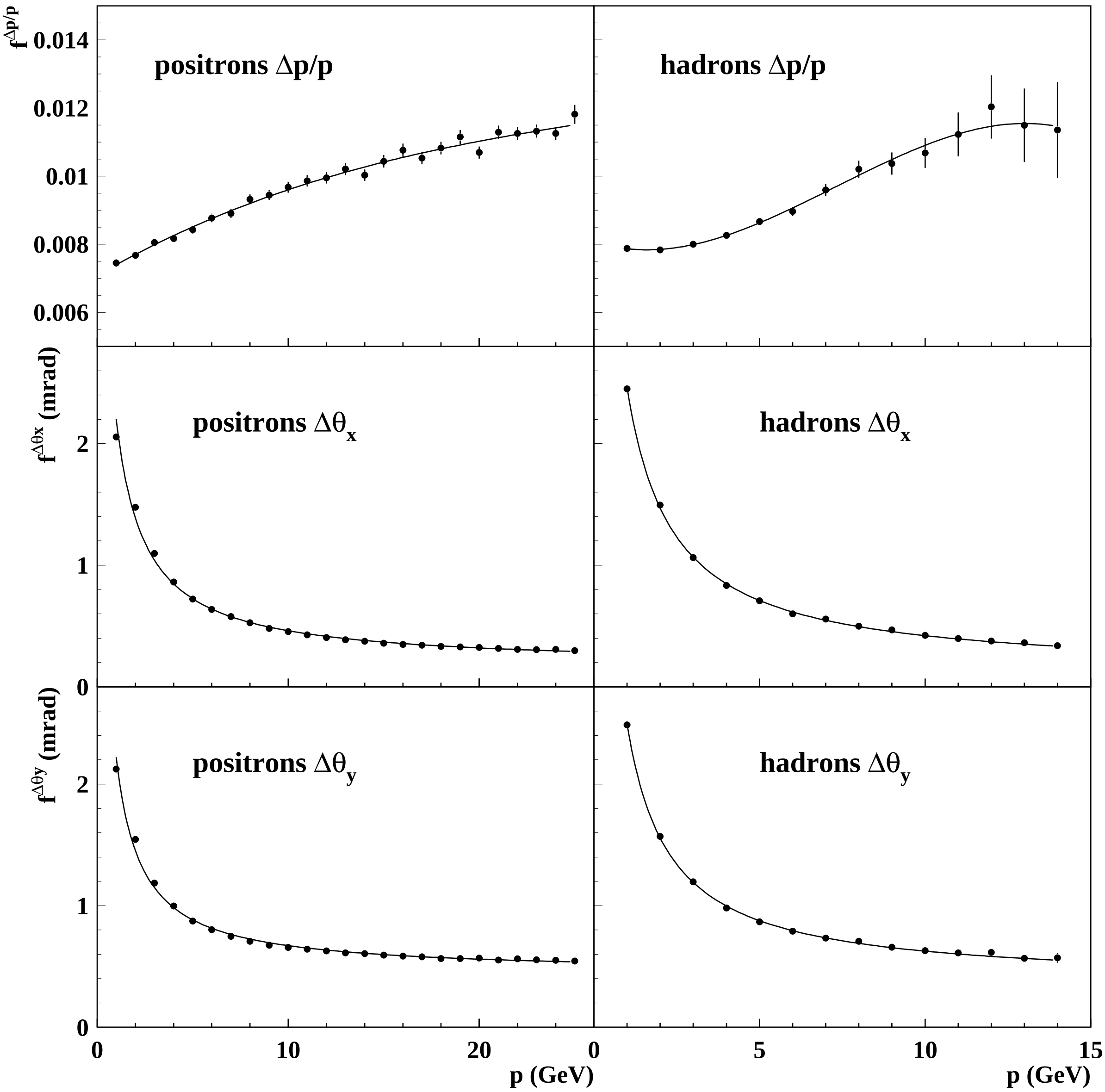

Figure 5.11: Momentum and angular resolutions of the HERMES detector for positrons (**left**) and hadrons (**right**). The superimposed fits f^i (solid lines) go into the modeling of the resolutions by the smearing generator (HSG). For this study HMC was used with the detector geometry of 1997.

A simulation result on the level of particle four-vectors including detector effects is performed by running HSG: for each track, a scaled resolution in $\Delta p/p', \Delta\theta'_x$, and $\Delta\theta'_y$ is dialed randomly by a generator using the histogrammed database. Then, these values are re-scaled by the central resolutions to give the real smearing and the smeared kinematic variables:

$$p^{smear} = p^{GMC} \cdot (\Delta p/p' \cdot f^{\Delta p/p}(p^{GMC}) + 1) \tag{5.17}$$
$$\Theta_x^{smear} = \Theta_x{}^{GMC} + \Delta\Theta'_x \cdot f^{\Delta\theta_x}(p^{GMC}) \tag{5.18}$$
$$\Theta_y^{smear} = \Theta_y{}^{GMC} + \Delta\Theta'_y \cdot f^{\Delta\theta_y}(p^{GMC}) \quad . \tag{5.19}$$

Because of large-angle multiple scattering, particle decay ($\pi \to \mu\nu$), and the finite accuracy of HRC and the tracking system, small inefficiencies occur in particle detection and reconstruction. While for positrons the reconstruction efficiency of 95% is almost independent of momentum, the total hadron efficiency rises slightly from 91% (1 GeV) to 95% (10 GeV). After smearing, HSG also regards these finite efficiencies on a statistical basis.

The migration of events due to radiative corrections and smearing has to be regarded when choosing generation limits and analysis cuts (generator settings see App.B.1). The consistent approach used here is shown in Figure 5.12. The generation of Born level DIS events (gmc_disNG) fills the phase space needed for LEPTO and a subsequent DIS analysis embedded. The influence of the inclusion of the detector effects and radiative corrections

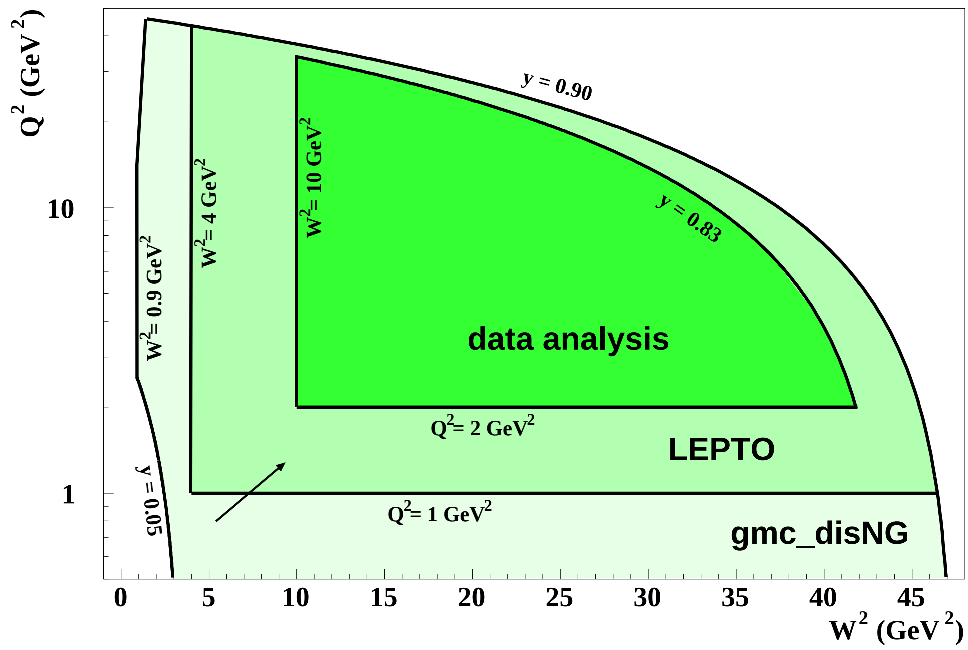

Figure 5.12: Schematic picture of the consistent cut strategy realized in the generation of Monte Carlo events. The arrow indicates the main direction of event migration.

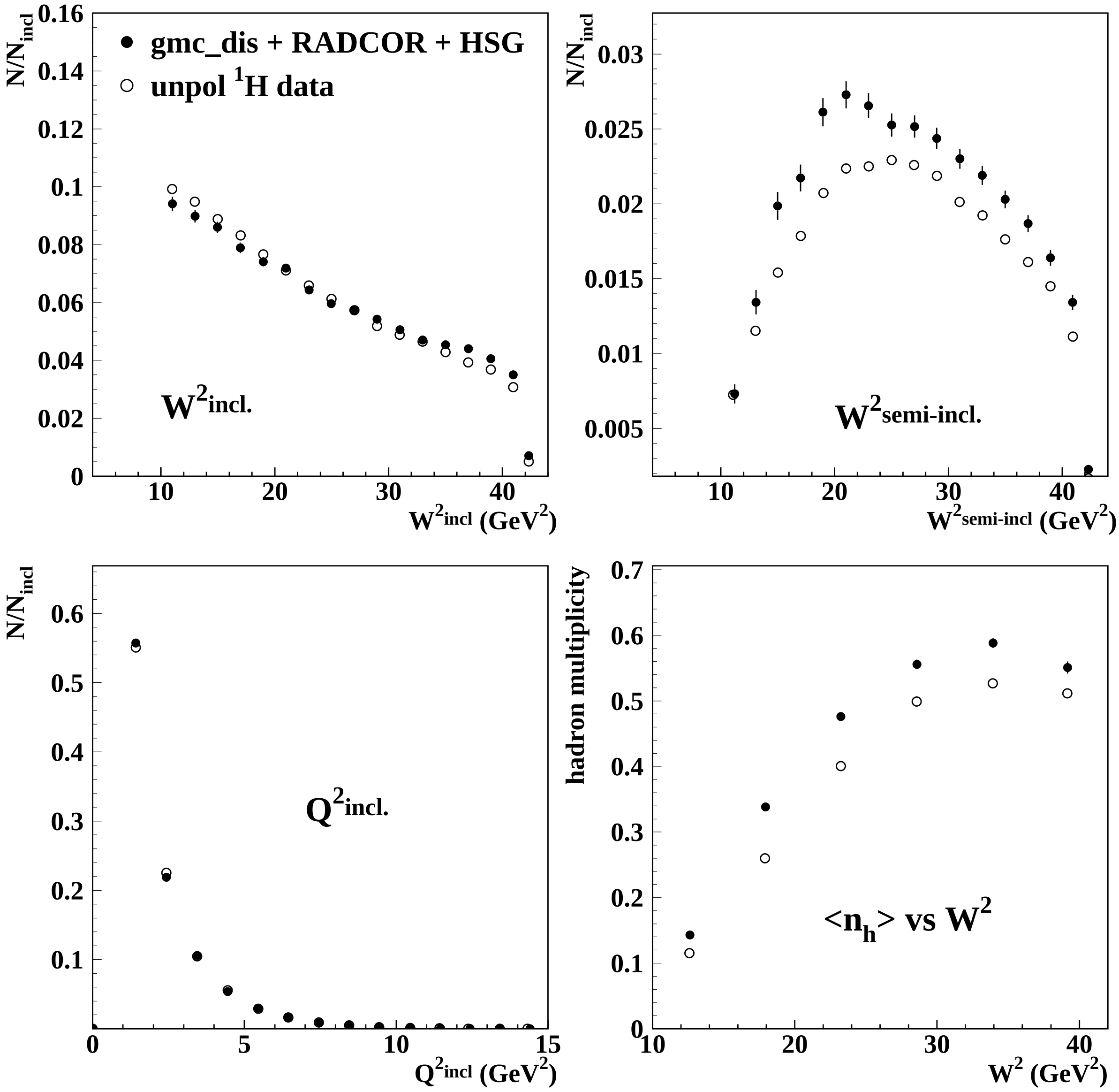

Figure 5.13: Result of a simulation with gmc_dis with radiative corrections and the inclusion of detector effects (HMC/HSG). **Top**: Comparison of the inclusive and semi-inclusive W^2 distribution between HERMES data (empty circles) and simulation (solid circles); normalized to the number of inclusive events N_{incl}. **Bottom**: Comparison of the inclusive Q^2 distribution and the average observed hadron multiplicity $< n_h >$.

on the DIS spectra using this consistent approach is displayed in Fig. 5.13 (to be compared to Fig. 5.4). The inclusive spectra now show good agreement between Monte Carlo simulation and data while the improvement of the semi-inclusive spectra will be discussed in the following Sections. The generation (gmc_dis), smearing (HSG) and analysis of an event takes 4 ms, an improvement of a factor of 1000 compared to a setup involving HMC.

5.2.5 The Fitting Procedure

With a consistent and fast Monte Carlo simulation at hand, the actual adaption of the free LUND model parameters could be encountered. To be able to take advantage of the LUND low energy modifications and to be consistent with the PYTHIA6 simulation [165], the *enhanced JETSET* (see Sect. 5.1.2) was implemented [177] into LEPTO which then became part of a new generator for HERMES (gmc_disNG). The actual determination of the model parameters was realized by iteratively fitting the simulation to the extracted hydrogen data (Fig. 5.14). The radiatively corrected DIS events produced by gmc_disNG are handed to HSG which then pipes the smeared data to an analysis program. The analysis program collects the appropriate histograms which are then compared to histograms of the measured data by means of a χ^2-test. The supervising program utilizes the MINUIT package [178] to decide using the SIMPLEX algorithm [179] on a new set of fragmentation parameters. The parameters are handed via an FF-Card file to gmc_disNG and the entire procedure is repeated until convergence is achieved.

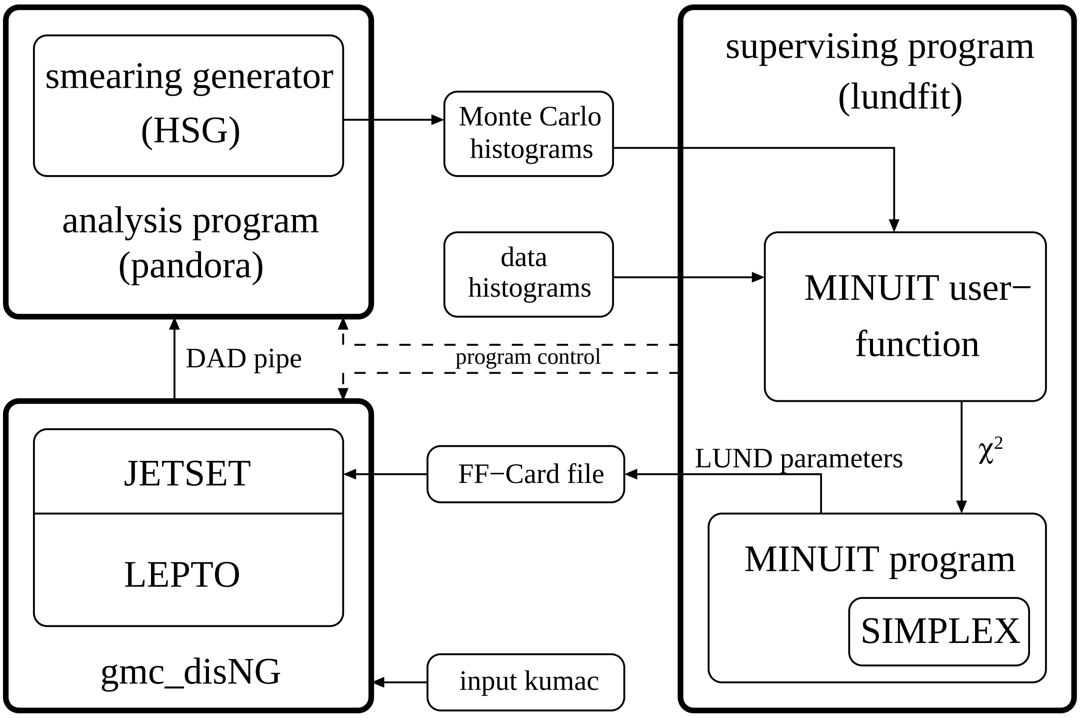

Figure 5.14: The structure of the interacting programs created for the adaption of the LUND fragmentation model to HERMES data.

The z-spectra of positive and negative hadrons as well as the their common p_T-distribution relative to the virtual photon have been selected for fitting. All three spectra were normalized to the total number of inclusive DIS events. For an unbiased fit, the z-range has been limited to $z < 0.8$ since the LUND model does not include exclusive processes. The hadrons where identified by using PID'_{25}. The spectra of the individual hadron types (π, K, p) were not used for fitting to avoid systematic influences of the still not well determined efficiencies of the RICH detector. However, the information was used to adjust the di-quark production (PARJ(1)) and the strangeness production (PARJ(2)) by hand to the right order of magnitude.

Since the simulation statistics is limited by the computing time available, the χ^2 values can only be determined to a certain precision. The *downhill SIMPLEX method* [179] was chosen because it does not rely on derivatives and is proven to be very robust against noisy χ^2 surfaces such as here. SIMPLEX uses a multi-dimensional *simplex*, the n-dimensional generalization of a tetrahedron, in parameter space where the χ^2 of the problem is derived for its corners. By stretching and contracting its corners, the simplex walks into the minimum, even in complex topologies. The quantity which had to be minimized by the SIMPLEX algorithm was chosen to be the maximum of the reduced χ^2 values of the three spectra:

$$\chi^2_{max} = \max(\,\chi^2_{ndf,\ z(h^+)}\,,\,\chi^2_{ndf,\ z(h^+)}\,,\,\chi^2_{ndf,\ p_T}\,)\ . \tag{5.20}$$

This choice was made to avoid the perfect modeling of a single kinematic quantity at the cost of the other quantities. This inevitably happens if the total reduced χ^2 of all histograms is used. The minimization of χ^2_{max} has the advantage that the running algorithm always tries to mend the histogram which matches worst the data giving a better overall agreement.

The LUND parameters a, b, σ, f_t, and t were tuned during fitting as well as the intrinsic transverse momentum in the nucleon. The latter is assumed by LEPTO to be distributed Gaussian with width k_T (PARL(3)). The parameters a and b are largely determined by the shape and the charge-dependence of the z-spectra. The width of the p_T spectrum is sensitive to the transverse momentum coming from fragmentation (modeled by σ) whereas the centroid of the p_T spectrum is sensitive to the intrinsic k_T. The additional tail in p_T regulated by f_t and t is basically constrained by events with $p_T > 3\sigma$. These two parameters could be fixed after an initial fit since they are not significantly correlated to other parameters. The baryon production had to be constrained to the $B\bar{B}$ case to eliminate correlations to the meson production via $BM\bar{B}$ string breaks (PARJ(5-7)=0). This simplification has only minor implications on the modeling since the $BM\bar{B}$ configuration is anyhow largely suppressed at low energies like at HERMES. The additional increase of the a parameter in di-quark production was also studied but finally remained at the default (PARJ(45)=0.5) value since no improvements on the spectra could be achieved. This leaves the fitting procedure with a reasonable number of four parameters to be fit.

5.3 Results and Systematic Limits

In subsequent fits with increasing statistics from 100000, 200000, 500000, to 10^6 DIS events per iteration step, the parameters where determined in less than 50 iterative steps per run until convergence was achieved. Tuning with 10^6 DIS events took about one hour per iteration which sets the practical limit for a further increase of statistics.

5.3.1 Model Parameters for HERMES

Two fits to the HERMES data were conducted: one fit covering the entire kinematics (*all-W^2 fit*), and one fit regarding only events with $W^2 > 25$ GeV^2 (*high-W^2 fit*). The latter is motivated for the study of photoproduction which evidently occurs at HERMES at an average W^2 of about 34 GeV^2 (see also Fig. 7.3). The model parameters found for various fits are listed in Table 5.3 together with the default settings for PETRA and older fits to HERMES data [180, 181]. Also, two older studies which utilized the old program gmc_dis are listed. These older fits mended the low energy problem by relaxing PARJ(33).

In general it seems that the LUND model without parton showering is not universal with respect to the center-of-mass energy of the modeled collision. This explains the different results for the all-W^2 and the high-W^2 fit. In the latter case, the parameters a and b are closer to the PETRA default ($\sqrt{s} \approx 35$ GeV). The low b-values of the HERMES fits indicate the practical limits of the LUND model since too low b-values tend to randomize the rapidity ordering of the hadrons (Sect. 5.1.2). The σ parameter seems to be independent of the center-of-mass energy; even at LEP a compatible value of 0.35 (DELPHI [182]) was found. The larger intrinsic values of $k_T \approx 0.8$ GeV found in the all-W^2 and high-W^2 fits do not correspond to the physical interpretation of transverse momentum of quarks in the nucleon anymore. Since the parton shower concept had to be rejected for this analysis, the missing resummation of soft gluons now has to be made up by an increase of intrinsic k_T in the model. In this case $k_T \approx 0.8$ GeV consists of the intrinsic transverse momentum of quarks in the nucleon in combination with p_T acquired in the fragmentation at low energies which is not accounted for in the model. In the adaption of the LUND model to results of EMC (μp,$\sqrt{s} \approx 23$ GeV) the intrinsic k_T had to be set from 0.44 GeV to 0.88 GeV when parton showers were switched off [183]. These findings nicely support the fit results of the HERMES analysis conducted here. In addition, the small extra tail in p_T was broadened a little bit (PARJ(24)=2.0 $\rightarrow$ 2.5) and increased from 1% to 3% to satisfy the measured spectra. The lower values for the parameters involving strangeness and baryon production as compared to the PETRA defaults can also be explained: at HERMES ($\sqrt{s} = 7.2$ GeV) the available phase space for heavy strings is very limited which should suppress baryon-antibaryon production as well as the production of strange particles.

The comparison of the kinematic spectra of data and simulation is depicted in Figures 5.15 and 5.16. A clear advance in quality compared to the PETRA setting and the old HERMES tune is visible. Especially, the variation of the mean p_T versus z shows that the fit describes the entire kinematic plane. The ability of the tuned LUND model to

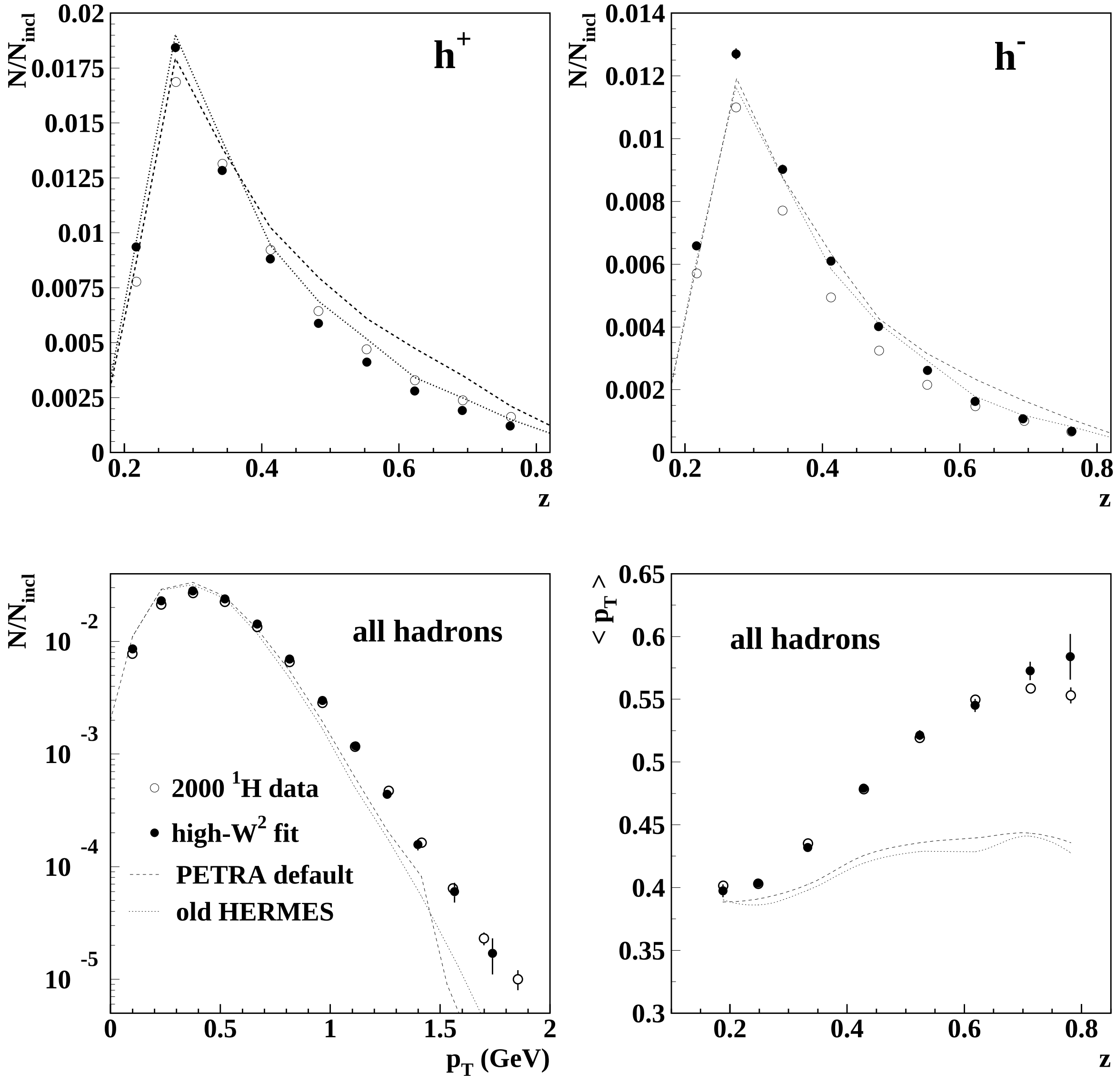

Figure 5.15: Comparison of data (open circles) and DIS simulation for the high-W^2 fit (solid circles), the PETRA default (dashed line), and the old HERMES settings (dotted line) (see also Tab. 5.3). **Top**: Normalized z-spectra for positive and negative hadrons. **Bottom, left**: Spectrum of the transverse momentum of all hadrons. The p_T spectrum of the 2000 ^{1}H data was used together with the spectra on top of the page to fit the LUND model. **Bottom, right**: The average transverse momentum versus z for all hadrons. This histogram was not used for the model adaption.

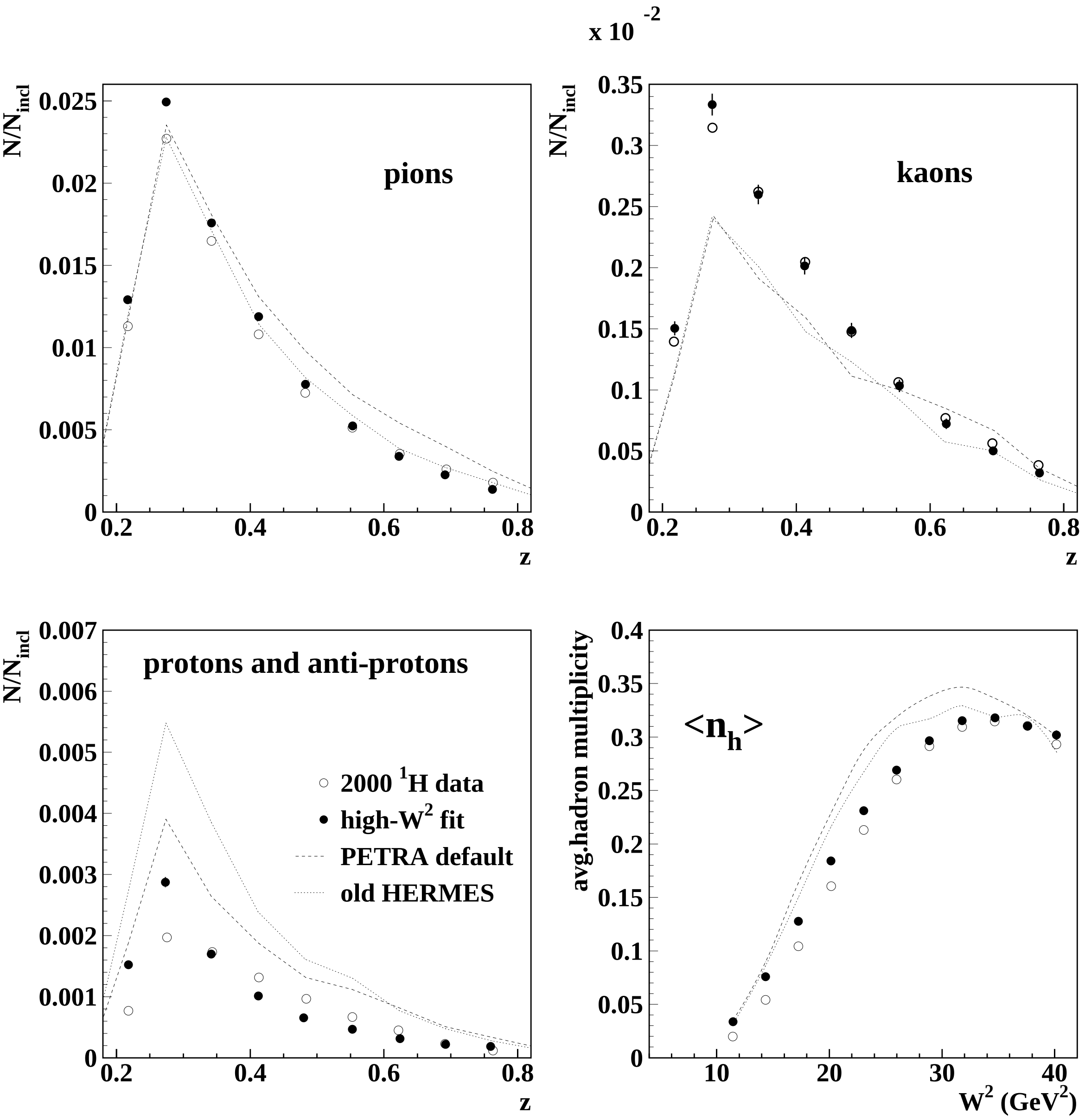

Figure 5.16: Top and **bottom, left**: Comparison of the normalized z-spectra for different hadron types between data and the different simulation settings. **Bottom, right**: The average observed hadron multiplicity versus W^2. None of the spectra displayed was used for fitting the LUND model.

Table 5.3: List of the various fragmentation tunes of the LUND model. In the lower part of the table the reduced χ^2 values for histograms comprising all W^2 and $W^2 > 25$ GeV^2 are listed. All parameters apply to JETSET settings with parton showers switched off. All values are either unit-less or in GeV or respectively in GeV^{-2}.

parameter	PETRA default	old [180, 181] HERMES	**all-W^2 fit**	**high-W^2 fit**	study no.1	study no.2
a PARJ(41)	1.00	0.82	**1.74**	**1.14**	1.00	0.79
b PARJ(42)	0.70	0.24	**0.23**	**0.35**	0.54	0.10
σ PARJ(21)	0.36	0.34	**0.37**	**0.34**	0.43	0.43
f_t PARJ(23)	0.01	0.01	**0.03**	**0.03**	0.01	0.01
t PARJ(24)	2.00	2.00	**2.50**	**2.50**	2.00	2.00
k_T PARL(3)	0.44	0.44	**0.78**	**0.85**	0.44	0.44
$b_{B\bar{B}}$ PARJ(1)	0.10	0.10	**0.02**	**0.03**	0.10	0.10
s_{supp} PARJ(2)	0.30	0.16	**0.20**	**0.20**	0.30	0.30
PARJ(33)	0.80	0.80	**0.80**	**0.80**	0.27	0.27
PARJ(5-7)	0.50	0.50	**0.00**	**0.00**	0.50	0.50
χ^2_{ndf} all W^2	290	210	**33**	41	132	107
χ^2_{ndf} high W^2	116	91	60	**21**	-	-
MC program	gmc_disNG	gmc_dis	**gmc_disNG**	**gmc_disNG**	gmc_dis	

reproduce this so-called $sea - gull$ shape gives confidence in the σ and k_T settings found. The overall multiplicity is reasonably described as well as the distributions of the different hadron types (π, K, p) as a function of z. These fit results are trustworthy to be carried over for the description of photoproduction events where they become an important piece of the analysis.

5.3.2 Concluding Remarks

Systematic evaluations, especially the correlation of parameters is hindered by the lack of sufficient computing power. Nonetheless, it was verified by scans around the final parameter settings that a minimum was found indeed (for example Fig. 5.17). From this the statistical uncertainties on the parameters found were estimated to be below 5% for PARJ(21,41,42) and PARL(3). The uncertainty on the strangeness suppression PARJ(2) amounts to approximately 50% since the K^+ and K^- spectra are not described equally well. The at present poorly known particle identification efficiencies of the RICH detector hinder further investigations on PARJ(2). The same holds for the production of protons/anti-protons and related parameters. The influence on the choice of parton distributions was tested by using alternatively GRV [52] and MRS [176] parameterizations instead of the default CTEQ5 [175] parton densities. Significant effects on the parameters could not be inferred which is not surprising since all parton distributions model the quark decomposition of the valence region equally well for $Q^2 > 2$ GeV^2.

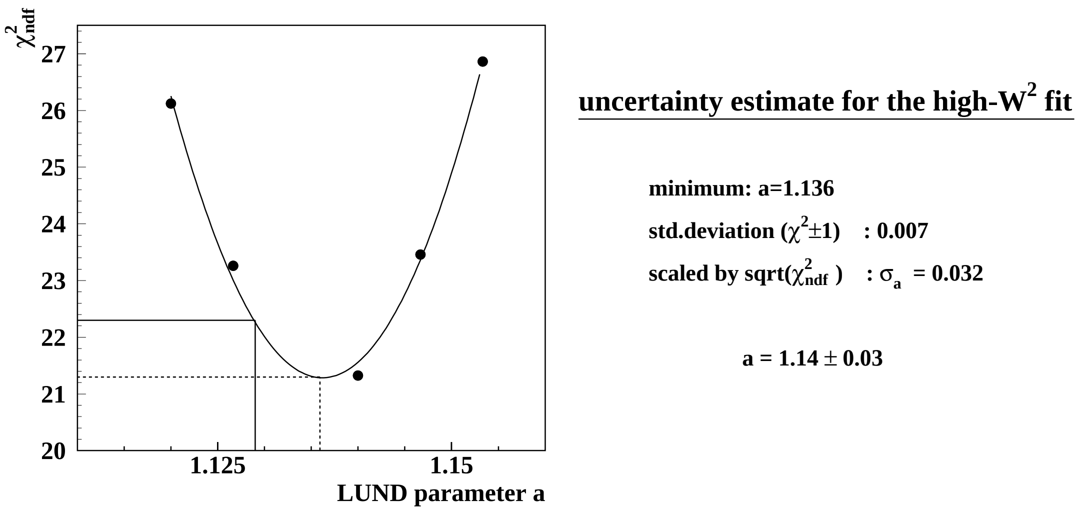

Figure 5.17: Example for an estimate of parameter uncertainties. Here, the minimum of the high-W^2 fit for LUND parameter a was scanned and fit with a parabola.

A dedicated scan of the a-b parameter space was conducted. The resulting χ^2_{max} surface discloses a strong correlation of the two parameters (Fig. 5.18). The values for a and b are positively correlated giving a diagonally stretched low-χ^2 valley from lower to higher values of a and b. This is an intrinsic property of the LUND model and is expected due to the constraint on the correct average multiplicity (see Sect. 14.5.2 of [166]). It also shows the stiffness of the model which poses the main obstacle for achieving better agreement with the measured spectra. An example for a detailed analysis on the correlation of the other LUND parameters using LEP data can be found in [182].

Two data-descriptive LUND settings for the HERMES data were found: The adaption to the entire W^2-region is intended for the use in polarized DIS analyses. Recent analyses already exploited the results of this Chapter to derive the polarized quark densities of the nucleon (see [184], for example). The high-W^2 fit is suited to model the hadronic final states of photoproduction events at HERMES. Especially, the proper modeling of the p_T distribution has been verified. This puts the influence of the fragmentation in the steps taken in Chapters 6 and 7 on solid grounds.

Future tuning efforts will profit from precise RICH detector information so that the understanding of the strangeness production could be refined. Via associated $\Lambda - K$ production, the connection of meson and baryon production in the LUND model could be understood better at HERMES energies (PARJ(45),PARJ(5-7)). Also, the suppression of vector mesons over pseudoscalar mesons in the LUND model could be varied (PARJ(11-17)) to achieve better agreement. However, for such an approach the associated meson pairs (for instance ρ, ϕ) will have to be reconstructed with full control over the detection efficiencies. The yield of neutral particles like reconstructed π^0 which together with reconstructed $K_s^{(*)}$ could be used to constrain the numerous parameters even further. In addition, diffractive vector meson production which could be misidentified as semi-inclusive DIS will have to be regarded at a certain stage.

The practical limitations in terms of computing time could be overcome by distributed calculations in a network of computers. This would finally lead to fits where the Monte Carlo statistics supersedes the data statistics. In that case, more sophisticated statistical methods like Kolmogorov-tests could lead to faster convergence and improved results. Also the division of the relevant z and p_T spectra into several bins of W^2 could lead to a better fitting of the hadronic final state.

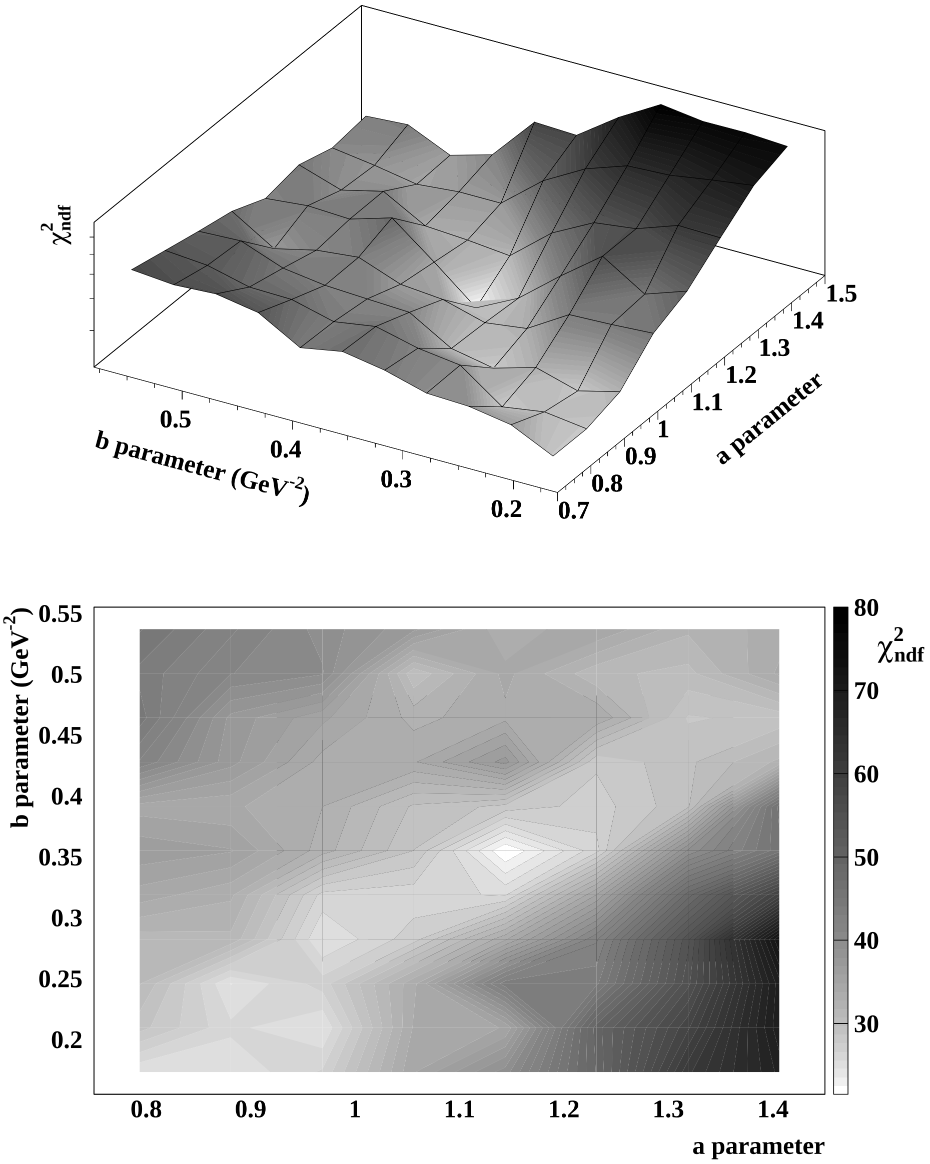

Figure 5.18: Values of the reduced χ^2 for the comparison of the high-W^2 histograms as function of LUND parameters a and b. The **top** plot displays the χ^2 surface with logarithmic z-axis. The **bottom** plot shows the same information as contour plot. The point of minimum χ^2 at $a = 1.14,\ b = 0.35\ \mathrm{GeV}^{-1}$ has the lightest colour.

6 Extraction of Spin Asymmetries at Large Transverse Hadron Momenta

The aim of the following data analysis is to derive a measurement of double spin asymmetries in two-hadron photoproduction events. The asymmetries are viewed for a phase space region where a significant photon-gluon fusion contribution is expected and disturbing effects are suppressed. HERMES data on hydrogen (1996/1997) and deuterium (1998-2000) is reviewed in that respect.

6.1 Event Selection

This Section defines the relevant kinematic quantities for the asymmetry analysis. Subsequently, the PYTHIA6 Monte Carlo simulation will be used to derive a cut strategy for the asymmetry extraction.

6.1.1 Kinematic Quantities

The event topology chosen here will correspond to the conditions for Trigger 28 (see Sect. 3.3.4) which contributes largely to the number of collected events. Therefore, in the following investigation one hadron track in the top and one in the bottom detector half is required. If more than two hadrons are detected, the most energetic ones are chosen for the analysis. Because the scattered positron is not measured, kinematic information can only be derived from the detected hadrons, giving six possible independent kinematic quantities which can be derived from the hadron momentum vectors $\vec{p}_1$ and $\vec{p}_2$. Since the kinematics is symmetric with respect to rotations around the beam axis, five independent variables remain (Fig. 6.1):

- The invariant mass $m_{\pi\pi} = \sqrt{(p_1^\nu + p_2^\nu)^2}$ of the hadron pair, assuming they are pions,
- The energy sum of the hadron pair, assuming they are pions,
- The coplanarity $\Delta\phi = \phi_1 - \phi_2$ of the two hadrons relative to the beam axis.

And two of the following three quantities where $\vec{n}_z$ denotes the unit-vector in direction of the beam:

- The minimum transverse momentum relative to the beam axis:

$$p_\perp^{min} = \min(|\vec{n}_z \times \vec{p}_1|, |\vec{n}_z \times \vec{p}_2|) \ , \tag{6.1}$$

- The maximum transverse momentum relative to the beam axis:

$$p_\perp^{max} = \max(|\vec{n}_z \times \vec{p}_1|, |\vec{n}_z \times \vec{p}_2|) \ , \tag{6.2}$$

- The transverse momentum of the two hadrons relative to each other:

$$p'_T = \left|\vec{p}_1 \times \frac{\vec{p}_1 + \vec{p}_2}{|\vec{p}_1 + \vec{p}_2|}\right| = \frac{|\vec{p}_1 \times \vec{p}_2|}{|\vec{p}_1 + \vec{p}_2|} \ . \tag{6.3}$$

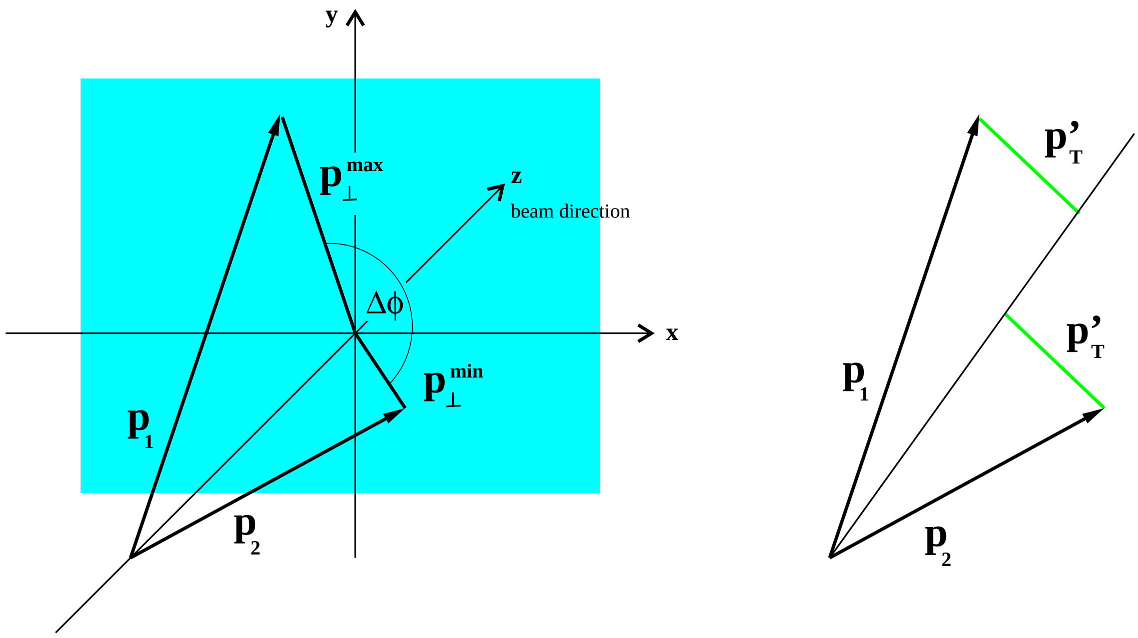

Figure 6.1: Left: Definition of the kinematic quantities $p_\perp^{min}$, $p_\perp^{max}$, and $\Delta\phi$. **Right**: Visualization of the relative transverse momentum p'_T.

The quantity p'_T has the advantage to be the same for both hadrons. The projections $p_\perp^{min}$ and $p_\perp^{max}$ are less intuitive and can be sizable even if $\Delta\phi$ is small. The quantity p_T will be used for the transverse momentum relative to the virtual photon while $\hat{p}_T$ is reserved for the transverse momentum of the actual parton subprocess. The aim is to define a cut series to enhance the photon-gluon process in the data sample and to identify a measurable quantity that is related to $\hat{p}_T$ using the PYTHIA6 Monte Carlo simulation (for settings see App.B.2).

6.1.2 Motivation of Kinematical Cuts

By requiring a h^+h^- pair with an invariant mass $m_{\pi\pi} > 1$ GeV, QCD Compton reactions and vector meson production is suppressed, leading to an increase of photon-gluon fusion to an amount of 1% in the remaining sample. The positron is required not to be in the acceptance to keep the photon virtuality as low as possible and to suppress semi-inclusive DIS. Further cuts should maximize the fraction of PGF events in the sample, ensure that a hard-scale reaction took place, and prove that the corresponding hadrons are correctly tagged.

Since photon-gluon fusion involves a sizable $\hat{p}_T$ on the parton level it should become apparent in the kinematics of the final state hadrons. Therefore, the three transverse momentum quantities defined in the previous Section are studied for a further separation of PGF events (Fig. 6.2). In this context, a cut-efficiency is defined as the fraction of the

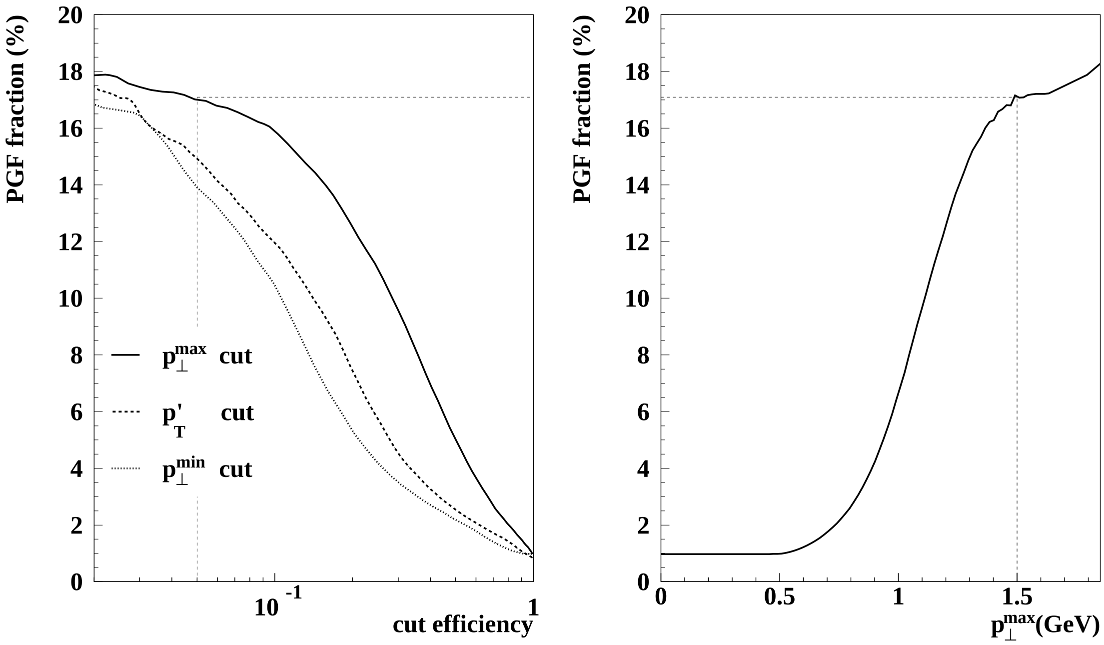

Figure 6.2: Left: PGF fraction in the leftover sample versus the efficiency of an applied cut on $p_\perp^{max}$, p'_T, or $p_\perp^{min}$. The condition $m_{\pi\pi} > 1$ GeV is required for the analysis plotted. **Right**: PGF fraction in the leftover sample versus a cut on $p_\perp^{max}$. The slim dashed line indicates the cut selected in the analysis.

leftover sample after the respective cut is placed compared to the uncut event sample. In a first step, the largest fraction of PGF events, at the highest possible cut-efficiency, is achieved by a cut on $p_\perp^{max}$. The requirement of $p_\perp^{max} > 1.5$ GeV raises the PGF fraction to 17% which cannot be achieved by sole cuts on $p_\perp^{min}$ or p'_T at the same efficiency. Thus, the Monte Carlo simulation indicates that a good PGF signature is the observation of two hadrons with one of them having a large transverse momentum component relative to the beam axis.

The QCD calculation of the parton-level cross section for PGF (Eq. 2.74) (and therefore the result of the Monte Carlo simulation) can only be trusted for $\hat{p}_T^2 > 1$ GeV^2. Below this limit no accurate description of the cross section is known. Nevertheless, in nature such soft events appear. It is therefore important for a cut series to show its ability to suppress soft events. To study this case, a PGF event sample was created with the intrinsic $\hat{p}_T^2$ cut-off in PYTHIA6 lowered from 1.0 GeV^2 to 0.5 GeV^2. It can be shown that cuts on $p_\perp^{min}$ and p'_T are able to suppress events with $\hat{p}_T^2 < 1$ GeV^2 (Fig. 6.3, top). In the modeled case a hard scale can be selected to a large amount by $p'_T > 1.2$ GeV (86%) or $p_\perp^{min} > 1.0$ GeV (77%) at approximately the same cut efficiency.

A main issue of the analysis is the question of correct hadron tagging. The cut series has to ensure that the tagged hadrons indeed contain the quark and the antiquark produced in

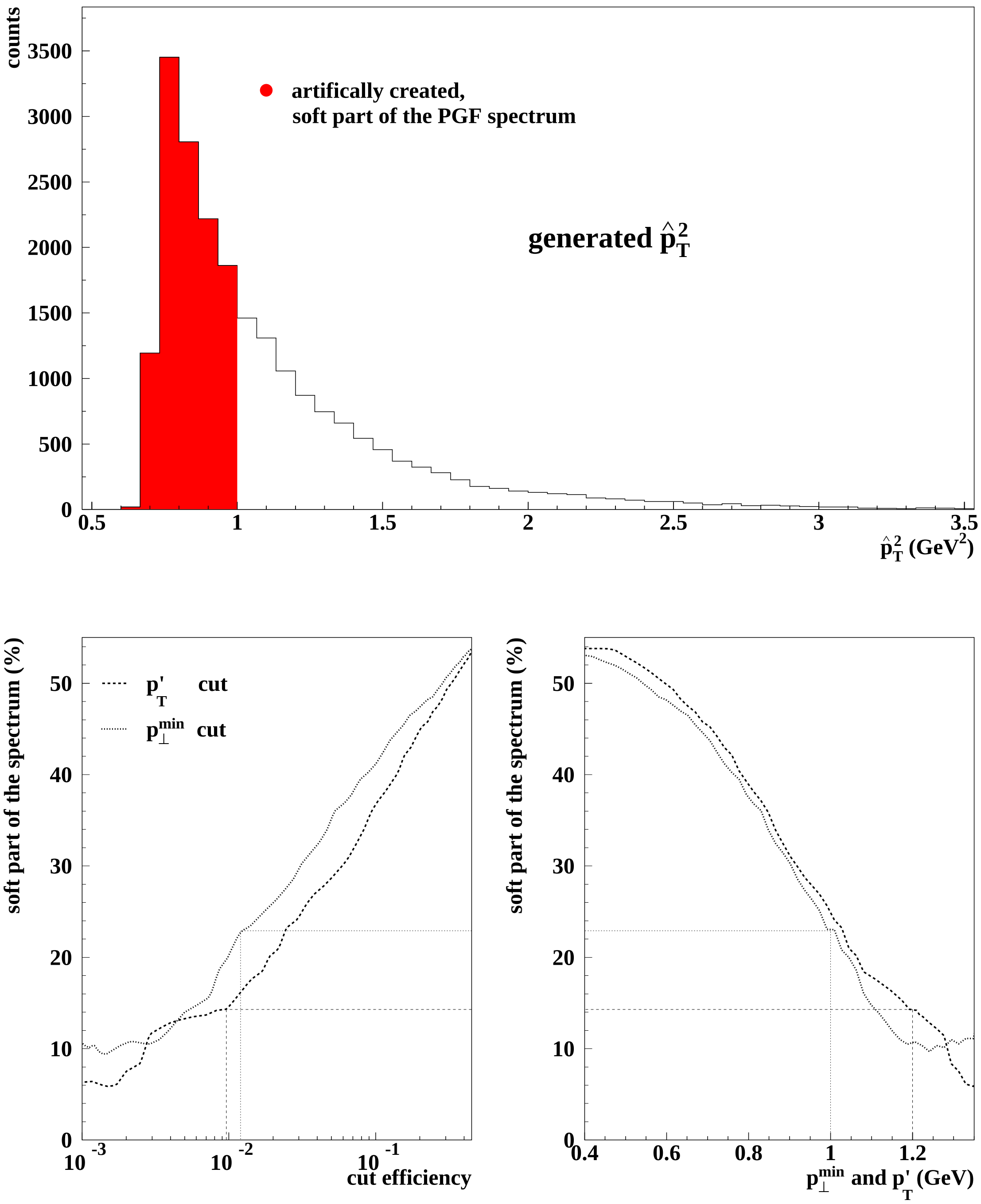

Figure 6.3: Top: Generated $\hat{p}_T^2$ spectrum for photon-gluon fusion (PYTHIA6) for the sample of events selected by $m_{\pi\pi} > 1$ GeV and $p_\perp^{max} > 1.5$ GeV. The lowest possible $\hat{p}_T^2$ was lowered to 0.5 GeV^2 to create soft events. **Bottom**: Study on the suppression of soft events. **Left**: Fraction of the leftover soft part of the spectrum versus the efficiency of a $p_\perp^{min}$ or p'_T cut. **Right**: Fraction of the soft part of the spectrum versus a $p_\perp^{min}$ or p'_T cut. The cuts selected in the analyses are indicated by a dashed and a dotted slim line.

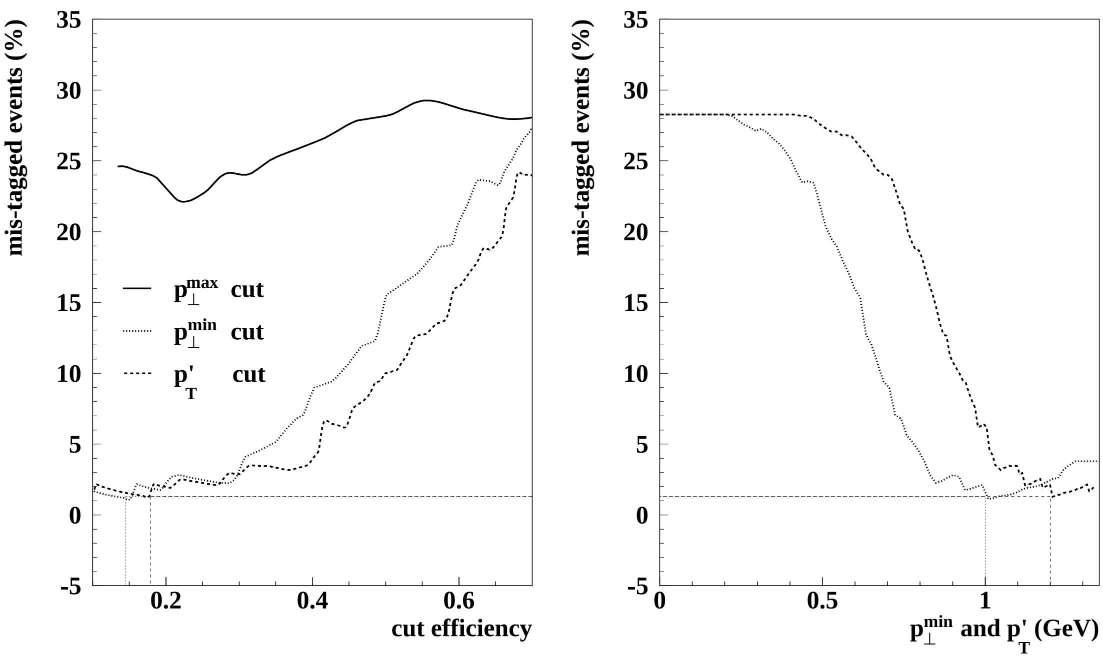

Figure 6.4: Left: The fraction of events where only one or none of the hadrons containing the PGF quarks was tagged, plotted versus the efficiency of a $p_\perp^{min}$ or a p'_T cut ($m_{\pi\pi} > 1$ GeV and $p_\perp^{max} > 1.5$ GeV is also required). The solid line represents a further increase of the $p_\perp^{max}$ cut above 1.5 GeV without cuts on $p_\perp^{min}$ or p'_T. **Right**: Mistagged event fraction versus cuts on $p_\perp^{min}$ or p'_T.

a photon-gluon fusion process. Otherwise the analysis could be biased by hadrons which do not belong to the current fragmentation region. To show that the main idea of tagging the hadrons which inherited the PGF quarks works, a pure PGF sample was studied with $\hat{p}_T^2 > 1$ GeV^2 (Fig. 6.4, $p_\perp^{max} > 1.5$ GeV). While a further increase of the cut on $p_\perp^{max}$ is rather insensitive to mistagged events, the cuts $p'_T > 1.2$ GeV or $p_\perp^{min} > 1.0$ GeV can ensure proper tagging in 99% of all cases. Again, the intuitive quantity p'_T is the most efficient one to cut on.

The correlation of the relative transverse momentum p'_T with the scale $\hat{p}_T^2$ (correlation coefficient: 0.62) is stronger than for $p_\perp^{min}$ (correlation coefficient: 0.45). This motivates to view a measured asymmetry versus p'_T to see the influence on that critical variable. For $p'_T > 1.2$ GeV, a clear relation between p'_T, $\hat{p}_T^2$ and x_g becomes visible (Fig. 6.5). This again indicates that sensitivity to PGF events can only be achieved by the hard cuts discussed. Moreover, the cuts on p'_T or $p_\perp^{min}$ increase the PGF fraction in the sample to about 20%.

Table 6.1 summarizes the cut strategy discussed (*new analysis*) together with the approach which is motivated by the HERMES publication [96, 185] (*standard analysis*) [6],

[6] The small differences between the *standard analysis* and the publication [96] are described in detail in Appendix C.1.3.

and the proposed cuts on COMPASS data [93]. The latter publication and the analysis cuts suggested in this thesis are based on Monte Carlo simulations. The cuts of the published HERMES approach were chosen ad hoc but nevertheless fulfill all necessary criteria as was shown in this Section. For consistency and comparison reasons, both the standard analysis scheme and the new analysis, which is the most efficient and consistent, will be regarded in the following analysis. In both cases, the acceptance cuts of Table 5.1 had to be fulfilled as well to ensure proper containment of the tracks in all parts of the detector.

Table 6.1: A list of the different cut schemes for asymmetry analyses at large transverse hadron momenta with the aim of enhancing photon-gluon fusion in the measured sample. The cut $m_{\pi\pi} > 1.0$ GeV turns out not to be necessary in the analysis (see Fig. 7.5, Sect. 7.1.3).

std.analysis	new analysis	COMPASS, Bravar *et al.* [93]
($m_{\pi\pi} > 1.0$ GeV)		$m_{h^+h^-} > 2.5$ GeV
$p_\perp^{max} > 1.5$ GeV		$p_T^{h+} > 1.0$ GeV $p_T^{h-} > 1.0$ GeV
$p_\perp^{min} > 1.0$ GeV	$p'_T > 1.2$ GeV	$\Delta\phi = 180^\circ \pm 30^\circ$
positron is not detected		muon is tagged
$p_h > 4$ GeV		$z > 0.1$, $x_F > 0$ $0.5 < y < 0.9$

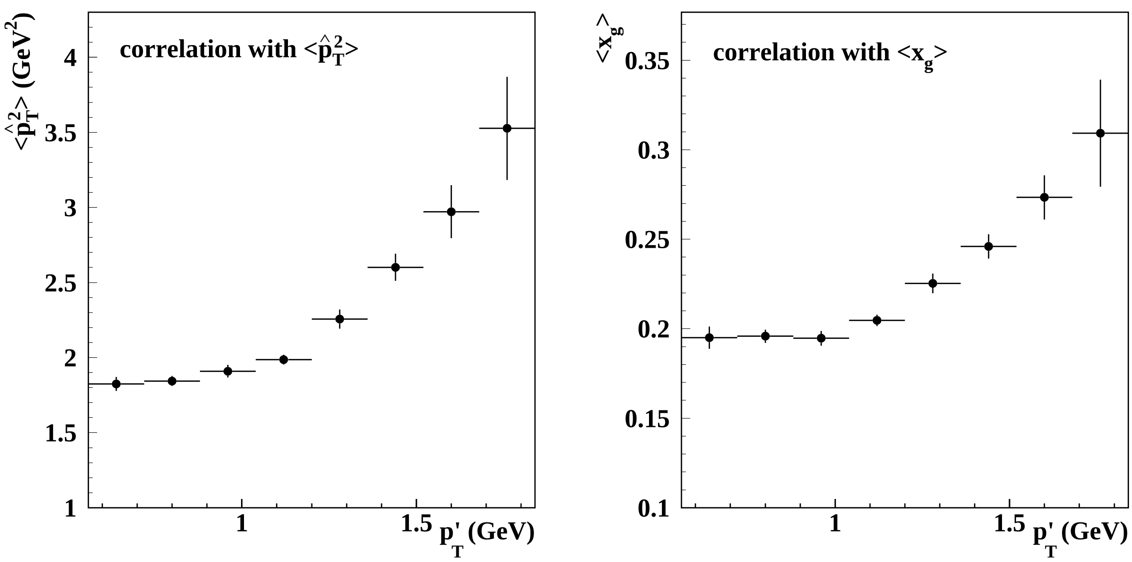

Figure 6.5: The correlation of p'_T with $\hat{p}_T^2$ (**left**) and x_g (**right**) obtained from PYTHIA6 Monte Carlo events ($m_{\pi\pi} > 1$ GeV and $p_\perp^{max} > 1.5$ GeV). The vertical error bars display the spread of the distribution while the horizontal error bars indicate the bin sizes.

6.2 Data Analysis

6.2.1 Data Quality

A clean and unbiased subset of data was chosen for the asymmetry analysis. After a basic data-quality via logbook entries was ensured run-wise, quality criteria were applied for each burst (Tab. 6.2) using the so-called *bad-bit list* [186]. The bad-bit list contains a bit-pattern for each burst. Each bit corresponds to a specific detector or accelerator condition. The quality criteria ensure a stable operating detector, good beam conditions, and target performance. Restrictions on beam current and luminosity ensure stable running of the accelerator. High beam and target polarization are required to limit the uncertainty in the weighting of the asymmetries. Also the livetime of the data acquisition and the duration of the bursts have to be within reasonable limits. Together with the rejection of the first and last burst of a run, data taken at too large DAQ load is cut out. Depending on the running year the quality criteria reject 14%-38% of the data of the preselected runs (Tab. 6.3).

Table 6.2: The data quality conditions which had to be fulfilled for the polarized data analyses from 1996 to 2000. The last column (unpol.) contains a $\surd$ if the corresponding criterion is also applicable to the unpolarized data analysis of Section 5.2.1.

data quality condition		unpol.
raw target polarization	$0.8 < P_{T_{BRP}} < 1.5$	
defined target spin state	4 or 8 (no tensor pol.)	
beam polarization	$30\% < P_{B_{fit}} < 80\%$	
last beam pol.measurement	< 300 s ago	
DAQ livetime	$0.5 < \epsilon_{DAQ} \leq 1.0$	$\surd$
burst length	$0 < l_{burst} \leq 11$ s	$\surd$
beam current	$5 < I_B < 50$ mA	$\surd$
luminosity rate	$5 < R_{lumi} < 60\ \mathrm{s}^{-1}$	
measurement on target parameters α_0 and α_r available		
reject first and last burst of a run		$\surd$
no high-voltage trips		$\surd$
PID detectors ok, no bad blocks in luminosity monitor		$\surd$

Table 6.3: Properties of the analyzed polarized datasets after data quality criteria were applied (Tab. 6.2).

year	DSTprod	target	good data	$\langle P_B P_T \rangle$	$\langle \epsilon_{DAQ} \rangle$	good DIS events
1996	96c1	^{1}H	62%	0.39	0.96	$0.6 \cdot 10^6$
1997	97c1	^{1}H	79%	0.46	0.98	$1.6 \cdot 10^6$
1998	98b4	^{2}H	76%	0.45	0.98	$1.2 \cdot 10^6$
1999	99b2	^{2}H	66%	0.48	0.96	$1.2 \cdot 10^6$
2000	00b1	^{2}H	82%	0.49	0.96	$6.1 \cdot 10^6$

6.2.2 Trigger Efficiencies

For a cross section comparison between data and Monte Carlo simulation and for yield studies (Sect. 6.3.3), the knowledge of the trigger efficiency is necessary. Events where Trigger 21 or Trigger 28 fired were used for the two-hadron analysis so that the total trigger efficiency can be written as:

$$\epsilon_{trig} = \epsilon(tr28)_{hh} + \epsilon(tr21)_{hh} - \epsilon(tr28)_{hh} \cdot \epsilon(tr21)_{hh} \ . \tag{6.4}$$

The individual trigger efficiencies can be derived by the efficiencies of the involved detector components. In the special case of one hadron track in the top and one in the bottom detector half, the efficiencies can be calculated as[7]:

$$\text{Trigger 28:} \qquad \epsilon(tr28)_{hh} = \epsilon^2(H0) \cdot \epsilon^2(H1) \cdot \epsilon^2(H2) \cdot \epsilon(BCmult)_{hh} \tag{6.5}$$

$$\text{Trigger 21:} \qquad \epsilon(tr21)_{hh} = \epsilon(tr21)_h \, (2 - \epsilon(tr21)_h) \tag{6.6}$$

$$\text{with} \qquad \epsilon(tr21)_h = \epsilon(H0) \cdot \epsilon(H1) \cdot \epsilon(H2) \cdot \epsilon(CALO)_h \ , \tag{6.7}$$

under the assumption of the top and the bottom detector having the same efficiencies. While Trigger 28 has a two track topology designed in, Trigger 21 will be set off by at least one track in either detector half. The efficiencies of the individual detector components can be found by employing the various sub-triggers (Tab. 6.4). For example, in events where Trigger 20 did but Trigger 21 did not respond, hodoscope H2 apparently was inefficient. The hodoscope efficiencies can be derived by:

$$\epsilon(H0) = \frac{\#(Tr18 \wedge Tr21)}{\#(Tr21)}, \quad \epsilon(H1) = \frac{\#(Tr19 \wedge Tr21)}{\#(Tr21)}, \quad \text{and} \quad \epsilon(H2) = \frac{\#(Tr20 \wedge Tr21)}{\#(Tr21)} \ .$$

The single hadron efficiency of the calorimeter $\epsilon(CALO)_h$ can be inferred from two hadron events using Trigger 28 and Trigger 21:

$$\epsilon(CALO)_h = 1 - \sqrt{1 - \epsilon(CALO)_{hh}} \quad \text{with} \quad \epsilon(CALO)_{hh} = \frac{\#(Tr21 \wedge Tr28)}{\#(Tr28)} \ . \tag{6.9}$$

The combined efficiency of the BC x-plane(s) and the multiplicity constraint on hodoscope H0 can be computed as:

$$\epsilon(BCmult)_{hh} = \frac{\#(Tr28 \wedge Tr21)}{\#(Tr21)} \ . \tag{6.10}$$

The average efficiency of Trigger 21 for the two hadron top-bottom topology is 79% with the calorimeter threshold at 1.4 GeV and about 31% with the calorimeter threshold at 3.5 GeV. Trigger 28 was 57% efficient on average in 1996 and 62-87% efficient in the other running years. The total trigger efficiency ϵ_{trig} for the two-hadron events investigated here is histogrammed for each running period in Figure 6.6.

[7] The trigger settings changed over the years (see caption of Table 6.4). In the discussion here, the last trigger settings intact at the end of 2000 are assumed. Deviating settings were regarded in the analysis as well as the different efficiencies for the top and the bottom detector.

Table 6.4: The HERMES trigger logics as realized in the second half of the 2000 running. Triggers 19 and 20 are swapped with respect to 1996/97. Triggers 18-20 include the magnet chambers since April 2000. Hodoscope H2 was not part of Trigger 28 in 1999 and during the first half of the 2000 running.

Trigger	logical condition
18	$(H1 \wedge H2 \wedge CALO \wedge MC)_{top} \vee (H1 \wedge H2 \wedge CALO \wedge MC)_{bot}$
19	$(H0 \wedge H2 \wedge CALO \wedge MC)_{top} \vee (H0 \wedge H2 \wedge CALO \wedge MC)_{bot}$
20	$(H0 \wedge H1 \wedge CALO \wedge MC)_{top} \vee (H0 \wedge H1 \wedge CALO \wedge MC)_{bot}$
21	$(H0 \wedge H1 \wedge H2 \wedge CALO)_{top} \vee (H0 \wedge H1 \wedge H2 \wedge CALO)_{bot}$
28	$(H0 \wedge H1 \wedge H2 \wedge BC)_{top} \wedge (H0 \wedge H1 \wedge H2 \wedge BC)_{bot} \wedge H0 \leq 8$

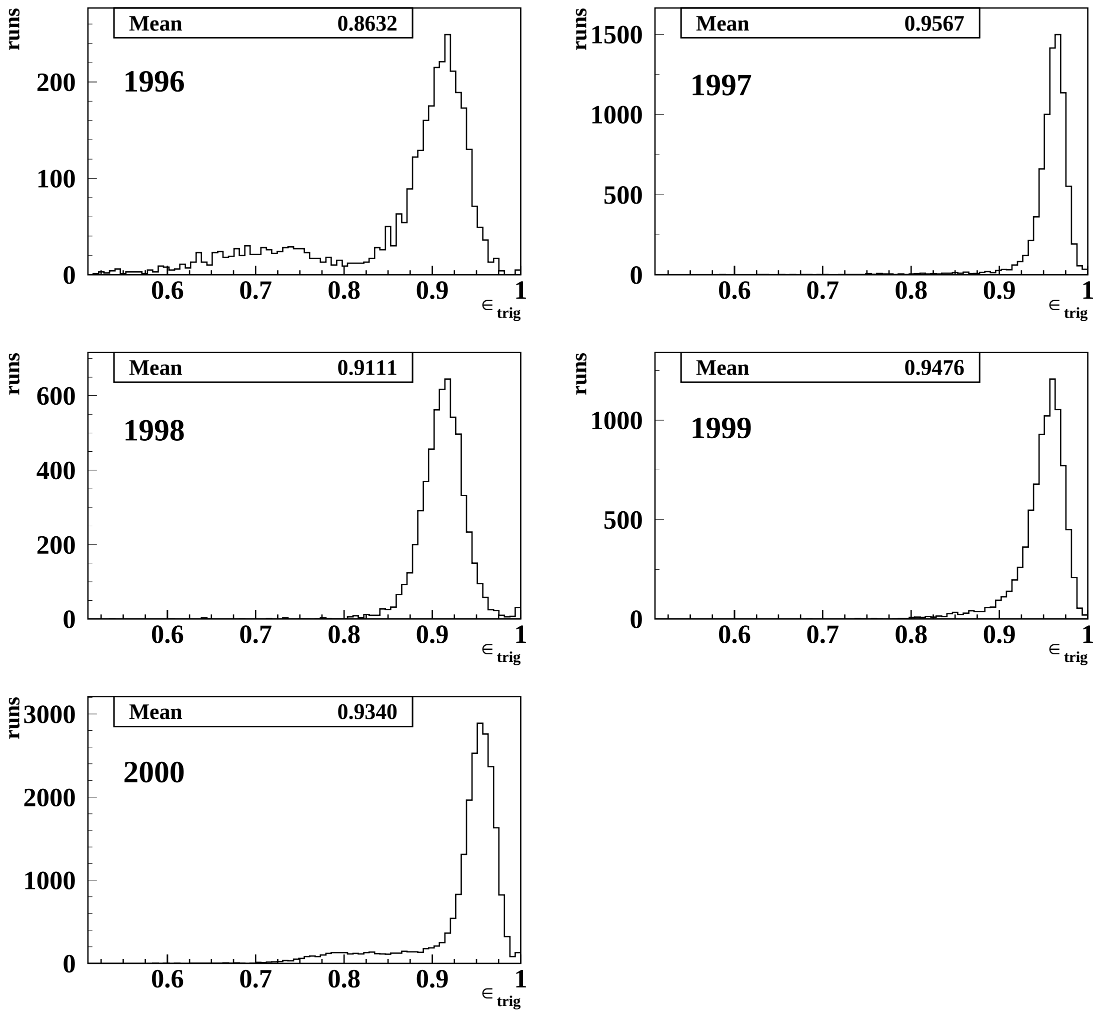

Figure 6.6: Histograms of the run-wise calculated total trigger efficiency ϵ_{trig} (Eq. 6.4) for the running years 1996 to 2000. The efficiencies around 0.7 in the 1996 dataset are from times where the calorimeter threshold was at 3.5 GeV; correspondingly the hadron efficiency of Trigger 21 was lower than in the other years. The tail to lower efficiencies in the 2000 dataset arises from a period (runs 11500-13500) when Trigger 28 had rate problems.

6.2.3 Double Spin Asymmetries

The polarized electroproduction cross section $\sigma^{\pm}_{tot}$ can be split into an unpolarized part σ_0 and a polarized part $\Delta\sigma$:

$$\sigma^{\pm}_{tot} = \sigma_0 \pm \Delta\sigma = \sigma_0(1 \pm A_{\parallel}) \qquad \text{with} \qquad A_{\parallel} = \frac{\Delta\sigma}{\sigma_0} \,. \tag{6.11}$$

Here $+(-)$ denotes anti-parallel (parallel) orientation of projectile and target spin, and $A_{\parallel}$ is the electroproduction double spin asymmetry. The observed cross section in an experiment $\sigma^{\pm}_{obs}$ is diminished by the finite acceptance and reconstruction efficiency ϵ_{exp}. Spin asymmetries are diluted by limited target and projectile polarization, P_T and P_B:

$$\sigma^{\pm}_{obs} = \epsilon_{exp}\,(\,\sigma_0 \;\pm\; P_B P_T\,\Delta\sigma\,)\,. \tag{6.12}$$

The number of events $N^{\pm}$ observed per spin state can be written as an integral over the corresponding time periods:

$$\begin{aligned} N^{\pm} &= \int dt\;\; \epsilon_{exp}(t)\,(\sigma_0 \pm P_B(t)P_T(t)\Delta\sigma)\,\mathcal{L}^{\pm}(t) & (6.13)\\ &= \sigma_0\epsilon_{acc}\epsilon_{rec}\epsilon_{trig}\int dt\;\; \mathcal{L}^{\pm}(t)\,\epsilon_{DAQ}(t)\,(1 \pm P_B(t)P_T(t)A_{\parallel})\,, & (6.14)\end{aligned}$$

assuming acceptance ϵ_{acc}, reconstruction efficiency ϵ_{rec}, and trigger efficiency ϵ_{trig} to vary much slower than the reversal of the spin orientations. The time-dependent luminosity $\mathcal{L}^{\pm}(t)$ is measured by the luminosity monitor (Eq. 3.7). The time scale of a burst is practical to evaluate the integral, thus Equation 6.14 becomes a sum over all analyzed bursts:

$$N^{\pm} = \sum_i^{bursts\pm} n_i \;=\; \sigma_0\,\epsilon_{acc}\,\epsilon_{rec}\,\epsilon_{trig} c_{lumi} \sum_i^{bursts\pm} l_i\,r_i\,\epsilon_{DAQ,i}\,(\,1 \;\pm\; p_i\,A_{\parallel}\,) \tag{6.15}$$

$$N^{\pm} \;\propto\; \underbrace{\sum_i^{bursts\pm} l_i\,r_i\,\epsilon_{DAQ,i}}_{L^{\pm}} \pm A_{\parallel} \underbrace{\sum_i^{bursts\pm} l_i\,r_i\,\epsilon_{DAQ,i}\,p_i}_{L_p^{\pm}}\;\;, \tag{6.16}$$

Here, n_i is the number of events observed in a burst with livetime $\epsilon_{DAQ,i}$ of the data acquisition. The measured event rate of the luminosity monitor is denoted as r_i, the length of the burst as l_i, and the burst-wise product of beam and target polarization as p_i. From Equation 6.16, the electroproduction double spin asymmetry can be derived.

$$A_{\parallel} = \frac{N^+L^- - N^-L^+}{N^+L_p^- + N^-L_p^+}\,. \tag{6.17}$$

If the asymmetry is not close to one and the $N^{\pm}$ are Poisson distributed, the statistical uncertainty on the asymmetry is found by:

$$\delta A_{\parallel} = \frac{L^+L_p^- + L^-L_p^+}{(N^+L_p^- + N^-L_p^+)^2}\sqrt{N^+N^-(N^+ + N^-)}\,. \tag{6.18}$$

Table 6.5: Definition of the binnings for the new analysis (**left**) and the standard analysis (**right**).

bin	p'_T range (GeV)
1	0.4 - 0.8
2	0.8 - 1.2
3	1.2 - 1.3
4	1.3 - 1.4
5	>1.4

bin	$p_{\perp}^{min}$ range (GeV)
1	0.5 - 0.8
2	0.8 - 1.0
3	1.0 - 1.2
4	1.2 - 1.5
5	>1.5

Equation 6.17 is used to calculate the electroproduction asymmetry for hydrogen $A_{\parallel}^{p}$ and deuterium $A_{\parallel}^{d}$ in bins of $p_{\perp}^{min}$ (std.analysis) and p'_T (new analysis) for the event class discussed. The binnings in $p_{\perp}^{min}$ and p'_T (Tab. 6.5) are motivated by the findings of Section 6.1.2 and are chosen to divide the the statistics as uniform as possible. According to Section 6.1.2 bins 3 to 5 should be relevant for an analysis ansatz which is sensitive to photon-gluon fusion.

In the deuteron the proton and the neutron mostly occupy a $^3S_1$ state where the nucleon spins are aligned with the total spin of the nucleus. However, at a probability of $\omega_D = 0.05 \pm 0.01$ [187,188] the nucleons occupy the $^3D_1$ state with the nucleon spins aligned oppositely to the spin of the nucleus. This results in an effective nucleon polarization of 92.5% compared to the polarization of the deuteron. Thus the measured deuterium asymmetry $A_{\parallel}^{d}$ appears diluted compared to an effective proton-neutron asymmetry $A_{\parallel}^{pn}$ [189]:

$$A_{\parallel}^{d} = A_{\parallel}^{pn}(1 - \frac{3}{2}\omega_D) \tag{6.19}$$

$$\text{with} \quad A_{\parallel}^{pn} = \frac{1}{\sigma_d}(\sigma_p A_{\parallel}^{p} + (\sigma_d - \sigma_p)A_{\parallel}^{n}) \ , \tag{6.20}$$

where σ_d and σ_p are the corresponding cross sections on deuterium and hydrogen. The asymmetry $A_{\parallel}^{pn}$ corresponds to a 100% polarized proton-neutron configuration with spins aligned and is applicable whenever parton-level calculations are done.

The extracted h^+h^- asymmetries in the large transverse momentum region are shown for the individual HERMES running years in Figure 6.7 (new analysis) and Figure 6.8 (std.analysis). During 1996 and 1997 HERMES took data with a hydrogen target while from 1998 to 2000 a deuterium target was employed. Also the combined asymmetry of all years is displayed under the approximate assumption that the same quantity is measured regardless of the target type. The asymmetry measurement tends to be negative at large transverse hadron momenta, supporting the existence of a photon-gluon fusion contribution in the sample. In the last three transverse momentum bins, the new analysis contains 95% of the events of the standard analysis which make up for only 77% of the sample of the new analysis. Because of the optimized cut strategy, the new analysis contains 23% more events than the standard analysis in the last three bins. In that respect and through the motivation of the kinematic cuts (Sect. 6.1.2) the new analysis is viewed as the best possible approach.

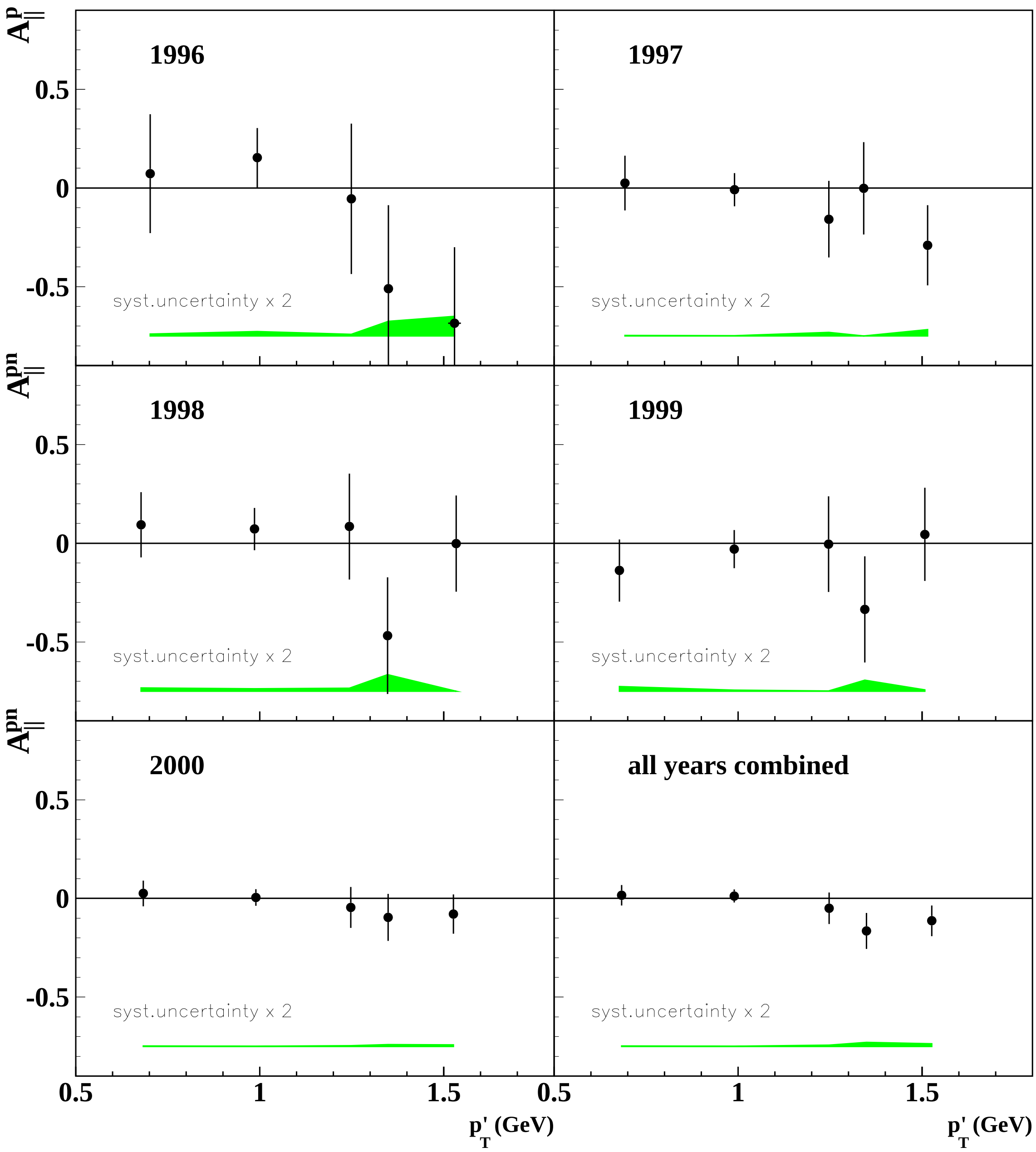

Figure 6.7: The extracted double spin asymmetry $A_{\parallel}$ for photoproduced h^+h^- pairs versus p'_T (new analysis) for the HERMES running years 1996 to 2000. The grey bands indicate the systematic uncertainties scaled up by a factor of two to allow a clear representation.

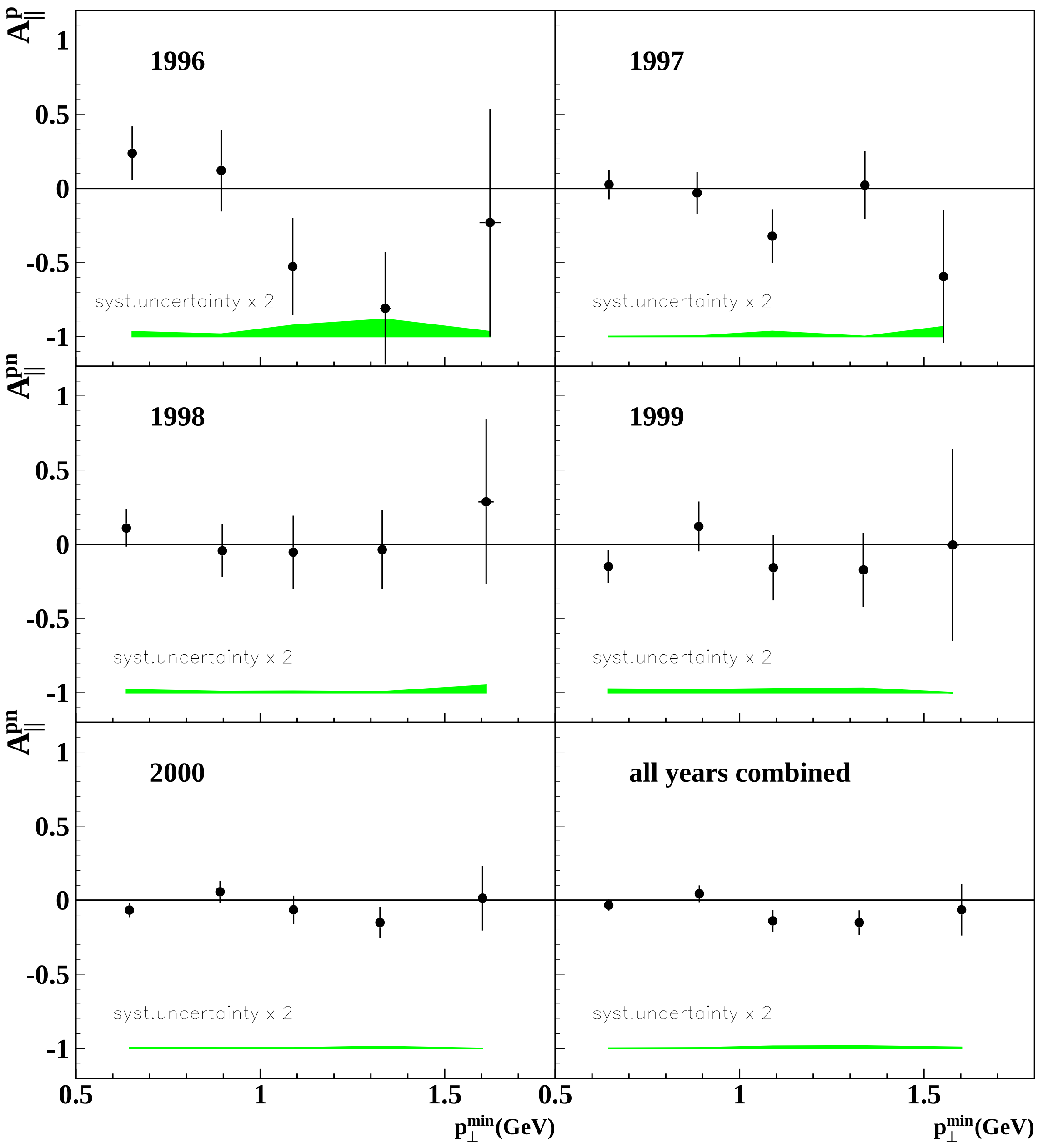

Figure 6.8: The extracted double spin asymmetry $A_{\parallel}$ for photoproduced h^+h^- pairs versus $p_{\perp}^{min}$ (std.analysis) for the HERMES running years 1996 to 2000. The grey bands indicate the systematic uncertainties scaled up by a factor of two to allow a clear representation.

6.3 Systematic Uncertainties

This Section summarizes systematic influences on the asymmetry measurement. The main source of systematic uncertainties can be attributed to the measurements of beam and target polarization. In contrast, the influence of the particle identification on the measurement is shown to be negligible. Together with the calculated trigger efficiencies of Section 6.2.2 it can be shown that events with hadron pairs are distributed evenly in the dataset. A final discussion investigates the consistency of the measured asymmetries among the datasets of the different years.

6.3.1 Beam and Target Polarization

Beam Polarization

The beam polarization measurement of the Transverse Polarimeter was used for the running years 1996-1998 since the Longitudinal Polarimeter relied on a cross-calibration to the TPOL during that period. Times at which the TPOL measurement was not available were patched by the cross-calibrated LPOL measurement. Thus, the asymmetry measurements of the datasets 1996-1998 will be assigned a relative systematic uncertainty of 3.4% (see Sect. 4.2, [144]) arising from the measurement of the beam polarization.

For the data sets of 1999 and 2000 the measurement of the Longitudinal Polarimeter was used because of the smaller systematic uncertainty (1.6%, Sect. 4.5) of the calibration compared to the Transverse Polarimeter. Whenever LPOL measurements were not available these periods were patched by TPOL measurements with 3.4% systematic uncertainty. The weighted relative systematic uncertainties on the beam polarization amount to 1.8% for 1999 and 1.9% for 2000.

Target Polarization

The target polarization was calculated according to Equation 3.6 with a fractional uncertainty of 4.5% for the running year 1997. In 1996 the average value of the molecular fraction α_r was 0.88 compared to 0.97 in 1997. This rather low value of α_r gives rise to a large systematic uncertainty since the knowledge on β is limited. To reduce the systematics, the raw target polarization $P_{BRP} \cdot \alpha_0$ was cross-calibrated to the measurement from

Table 6.6: Systematic contributions of beam and target polarization to the systematic scale uncertainty of $A_{\parallel}$ for the running years 1996 2000.

year	$\delta P_T/P_T$	from $\delta\omega_d$	$\delta P_B/P_B$	$\delta A_{\parallel}/A_{\parallel}$
1996	6.5%	-	3.4%	7.3%
1997	4.5%	-	3.4%	5.6%
1998	8.0%	1.75%	3.4%	8.9%
1999	8.0%	1.75%	1.8%	8.4%
2000	4.0%	1.75%	1.9%	4.8%

1997 by multiplication with a correction factor $c_{97/96} = 0.929 \pm 0.043$. The correction factor $c_{97/96}$ was deduced from the comparison of the inclusive DIS positron asymmetry between 1996 and 1997. The fractional uncertainty on the target polarization for 1996 is obtained from the uncertainty on the target polarization of 1997 and $\delta c_{97/96}/c_{97/96}$ added in quadrature (6.5%).

For the deuterium target, the analysis of the 1998 and 1999 data is not completed yet. A preliminary fractional uncertainty of 8% is assigned to these datasets. A detailed analysis of the 2000 running period yields a relative systematic uncertainty of 4.0% on the target polarization [190]. For the extraction of $A_{\parallel}^{pn}$ from data on a deuterium target, the influence of the uncertainty on the fraction of the D-wave state in deuterium $\delta\omega_d = 0.01$ has to be also regarded (1.75%). The systematic uncertainties discussed in this Section are summarized in Table 6.6.

6.3.2 Particle Identification

For the particle identification, the following cuts on PID_{35} and PID_{25} were used (see definition in Sect. 5.2.1):

	hadrons	e^+/e^-
1996-1997:	$PID_{35} < -1$	$PID_{35} > 2$
1998-2000:	$PID_{25} < -1$	$PID_{25} > 2$

Since the kinematics for this analysis is very constrained, the particle flux ϕ is almost constant and the particle identification with the flux-corrected quantities PID'_{35} and PID'_{25} only corresponds to a shift of the PID cut. A systematic bias on the asymmetry measurement could be caused by misidentifying a e^+X^- or X^+e^- event as h^+h^- configuration. The quantity PID_{25} of positively charged particles is shown in Figure 6.9 (running year 2000) for the case $p_{\perp}^{max} > 1.5$ GeV and $m_{\pi\pi} > 1$ GeV. From exponential fits to the valley of this distribution, a e^+X^- contamination of 0.8% of the sample h^+X^- can be inferred for $PID_{25} < -1$ (Fig. 6.9, top). The cut efficiency is better than 98%. Once the positive particle is identified as hadron, the probability for the negative particle is 99.9% also to be a hadron (Fig. 6.9, bottom). Thus less than 0.9% of the h^+h^- sample contains misidentified event configurations therefore the influence on the measured asymmetries is negligible. The PID scheme discussed identifies h^+h^- events with an efficiency better than 97%.

Furthermore, if a measured negative asymmetry was significantly contaminated with semi-inclusive DIS e^+h^- events, which have a positive double spin asymmetry, the measured asymmetry should become even more negative if the cut on $PID_{25(35)}$ is lowered. A cut series showing the combined asymmetry of the last three bins of the standard analysis as a function of $PID_{25(35)}$-cut is displayed in Fig. 6.10. Within the statistical precision, neither a variation of the result is observed nor the measured asymmetry becomes more negative. The observed shapes of the PID-spectra and the stable behaviour of the asymmetry against different PID cuts lead to no assignment of a systematic uncertainty to the measurement of the asymmetries arising from particle identification.

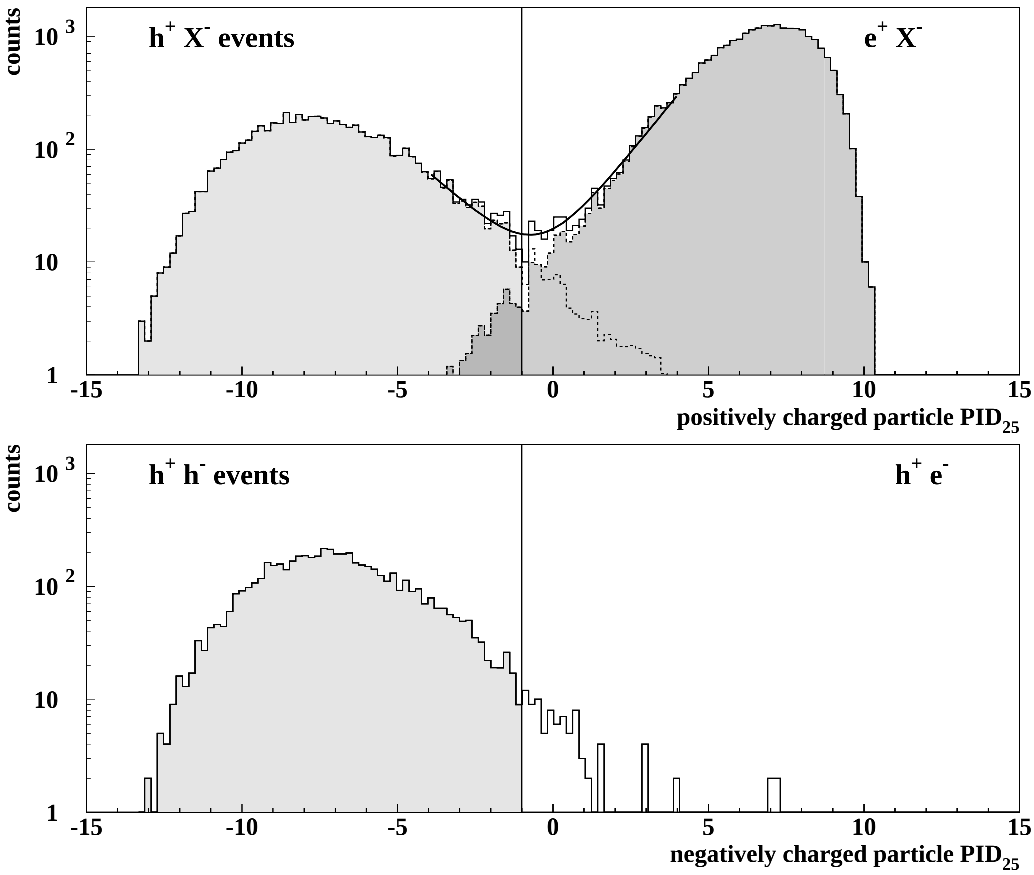

Figure 6.9: Top: Logarithmic likelihood PID_{25} of the **positively charged** particle of the event topology discussed in the text. A sum of two exponentials is fit to the valley around zero. The fit result is used to estimate the e^+X^- contamination (darkest grey) of the h^+X^- sample. The vertical line indicates the cut applied in the analysis. The data shown is from running year 2000. **Bottom**: PID_{25} of the **negatively charged** particle after the positive hadron is identified.

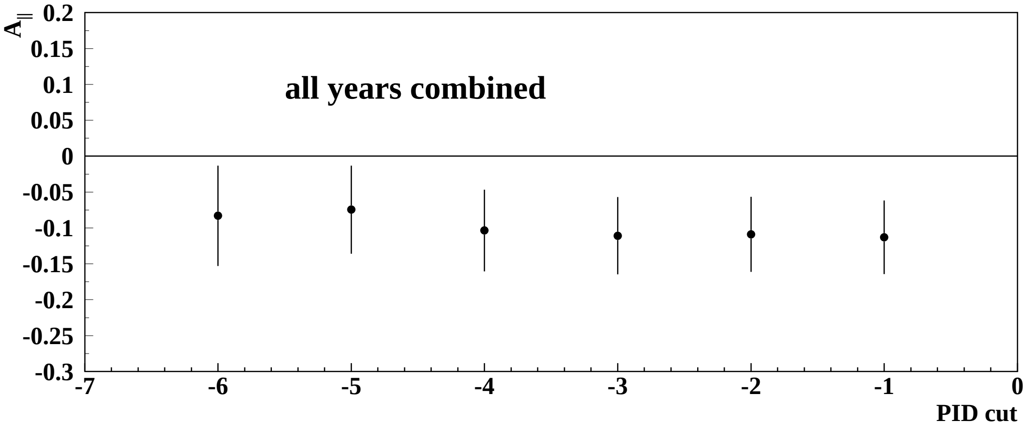

Figure 6.10: Combined asymmetry (1996-2000) of the last three $p_\perp^{min}$ bins as a function of the PID cut applied (std.analysis).

6.3.3 Normalized Yields

A way to disclose systematic influences is to check for a statistically distributed occurrence of the investigated events over a running period. For this purpose, a normalized yield can be defined for a time interval:

$$Y = \frac{\sum_i n_i}{\sum_i r_i l_i \epsilon_{DAQ} \epsilon_{trig}} \ . \tag{6.21}$$

The observed number of events $\sum_i n_i$ is corrected by the luminosity $r_i l_i$, the livetime of the data acquisition ϵ_{DAQ}, and the trigger efficiency ϵ_{trig}. The normalized yield was calculated fill-wise for events with $p_\perp^{min} > 0.5$ GeV and $p_\perp^{max} > 1.5$ GeV (example: Fig. 6.11). No significant variation with time was observed. Fits with constants gave reduced χ^2 values around one for all running years (Table in Fig. 6.11). Consequently, no systematic uncertainty from possible yield fluctuations was assigned to the asymmetry measurement.

6.3.4 Data Comparison of Different Years

The Monte Carlo analysis in Chapter 7 indicates that the fraction of photon-gluon fusion events in the sample is approximately the same for scattering off hydrogen and deuterium. If background processes are assumed to have zero asymmetry, then the measured asymmetries $A_\parallel^p$ and $A_\parallel^{pn}$ should be compatible within their statistical uncertainties. The dependence of the asymmetries on p_T' or $p_\perp^{\rm min}$ is statistically consistent between the individual years (Fig. 6.7 and Fig. 6.8). For further comparisons, the measured double spin asymmetries of the last three bins are combined ($p_\perp^{min} > 1$ GeV or $p_T' > 1.2$ GeV) to reduce statistical fluctuations (Tab. 6.7). The double spin asymmetries from 1996 to 2000 are consistent as χ^2 tests show (Fig. 6.12, Tab. 6.8). The standard analysis gives an overall value for χ^2_{ndf} of 1.6 while the new analysis results in a better consistency with $\chi^2_{ndf} = 0.7$. If the proton data is compared to the deuterium data, $\chi^2_{ndf} = 3.6$ is obtained if the standard analysis is employed. On the other hand, the new analysis yields $\chi^2_{ndf} = 1.7$ in this case (Tab. 6.8).

On the one hand, the overall comparison of the asymmetries shows the expected consistency for the new analysis. On the other hand, there might be a systematic difference between the proton and deuterium asymmetries. The latter could be due to a systematic problem of the 1996 dataset, which has the worst χ^2_{ndf} in the yield study (Table in Fig. 6.11). However, none of the systematic studies shown here as well as additional studies on PID, top and bottom detector, charge dependences of $p_\perp^{max}$, and the ensurance of matching of momentum and horizontal bend in the magnet, disclosed a source of bias in the 1996 or other data [191]. If the 1996 data set is left out in a comparison, both old and new analysis give consistent results (Tab. 6.8). Furthermore, the differences on the hydrogen and deuterium data become less if the new analysis is employed. The cuts of the new analysis were chosen in an unbiased way, motivated by a Monte Carlo simulation. In contrast, the standard analysis was first applied to the 1996/1997 hydrogen data and yielded rather large asymmetries by an ad hoc cut scheme. If the $p_\perp^{max}$ or the $p_\perp^{min}$ cut in the standard analysis is relaxed only by 0.1 GeV the 1996/1997 hydrogen asymmetries already become smaller, supporting a statistical fluctuation in this case.

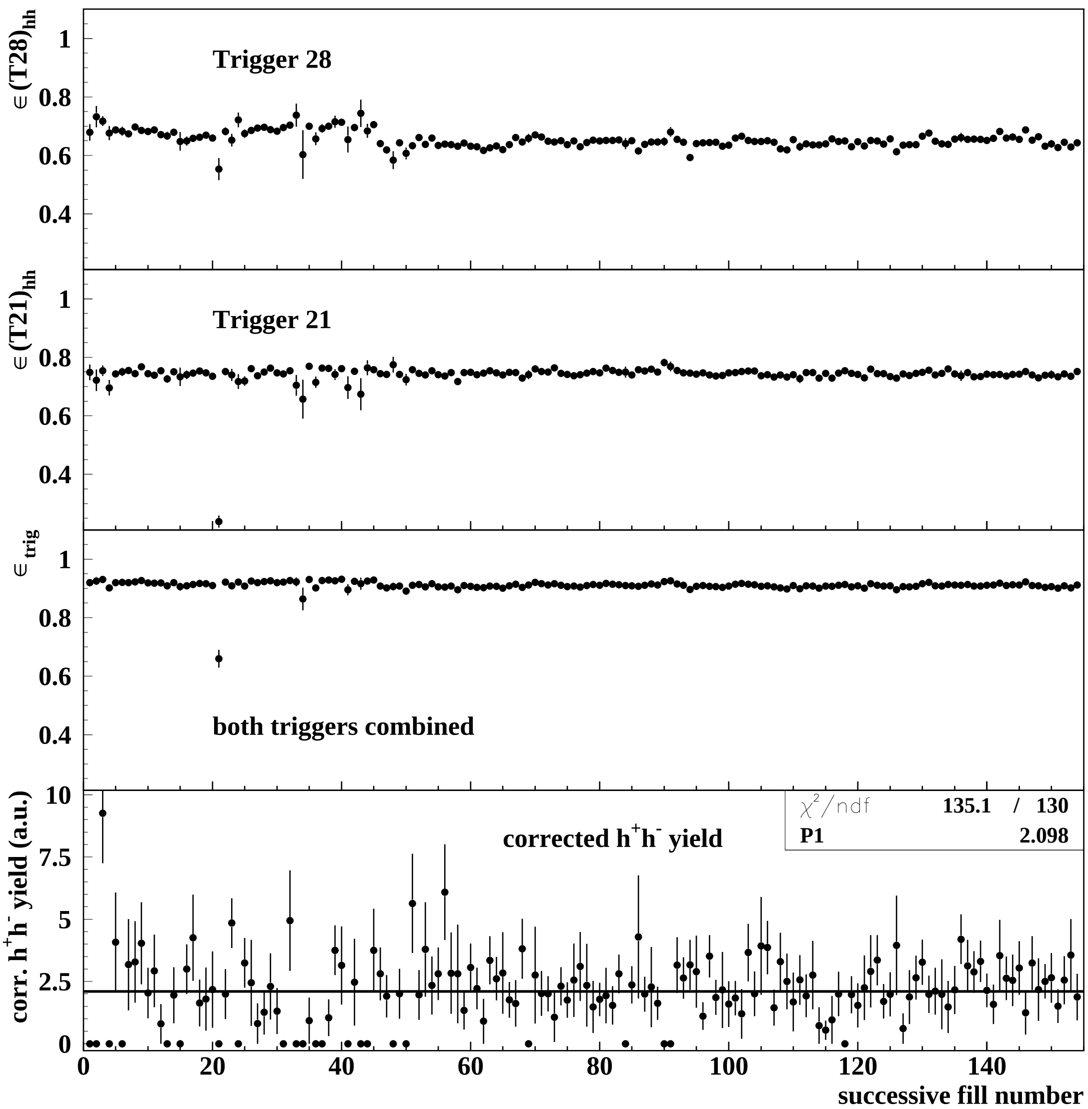

Figure 6.11: The corrected hadron yield (diagram, **bottom**) for $p_{\perp}^{min} > 0.5$ GeV and $p_{\perp}^{max} > 1.5$ GeV is shown for the running year 1998 with a constant fit superimposed. The efficiencies ϵ_{hh} for Triggers 28, 21 and both triggers combined are shown in the **top** panels of the diagram. The χ^2 tests of the corrected yields for all running years are listed in the table (**right**) with the corresponding degrees of freedom. Fills which did not yield events were excluded from the χ^2 tests.

year	χ^2	ndf	χ^2_{ndf}
1996	79.7	59	1.35
1997	151.0	167	0.90
1998	135.1	130	1.04
1999	120.7	107	1.13
2000	246.2	253	0.97

The new analysis presented in this thesis gives reasonable χ^2_{ndf} values for the data comparisons which supports the consistency of the hydrogen and deuterium data. Therefore, the data extraction is assumed to be consistent within the acquired statistics and no additional systematic uncertainty is assigned to any of the data sets.

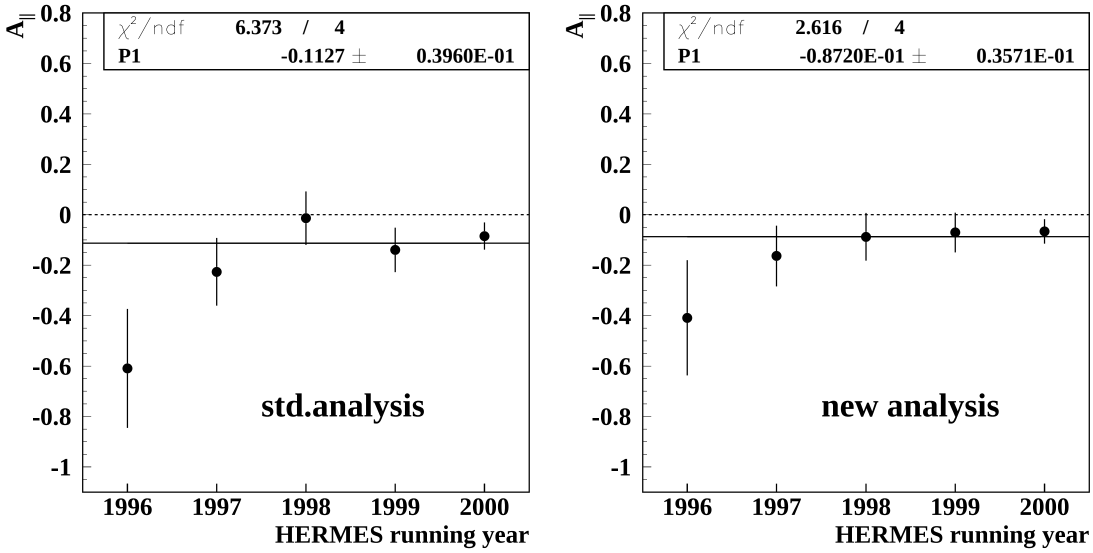

Figure 6.12: Comparison of the combined asymmetries $A_{\parallel}^{p,pn}$ of the last three $p_{\perp}^{min}$- and p_T'-bins for 1996-2000.

Table 6.7: Combined asymmetries $A_{\parallel}^{p,pn}$ of the last three $p_{\perp}^{min}$- and p_T' -bins for different time periods used for comparison in Table 6.8.

year(s)		$A_{\parallel}$ std.analysis	$A_{\parallel}$ new analysis
1996-2000	all data	-0.113 ± 0.040	-0.087 ± 0.036
1996-1997	^{1}H data	-0.320 ± 0.117	-0.217 ± 0.106
1998-2000	^{2}H data	-0.086 ± 0.042	-0.071 ± 0.038
1997	only	-0.226 ± 0.134	-0.164 ± 0.120

Table 6.8: Comparisons by χ^2 tests of the double spin asymmetries at large transverse momenta (Tab. 6.7) for various subsets of the analyzed data.

comparison	χ^2_{ndf} std.analysis	χ^2_{ndf} new analysis
all data	1.6	0.7
all ^{1}H	2.0	0.9
all ^{2}H	0.4	0.1
^{1}H to ^{2}H	3.6	1.7
1997 to ^{2}H	1.0	0.5

7 Interpretation

In this Chapter results of a PYTHIA6 Monte Carlo simulation for hadron pair events at large transverse momenta will be used to extract $\Delta g/g$ from the measured double spin asymmetries treated in the previous Chapter. After an introduction into the theoretical foundations of the modeling implemented in PYTHIA6, a comparison to HERMES data is presented. The Chapter concludes with the extraction of $\Delta g/g$ and the treatment of systematic uncertainties.

7.1 The PYTHIA Monte Carlo Simulation

The interpretation of the analysis of the HERMES publication [96] was based on a Monte Carlo simulation using the PYTHIA5 generator [192]. Due to the lack of a virtual photon generator, PYTHIA5 was used to simulate real γp events. Each event was then re-weighted for its kinematic variables ν and Q^2 according to the Weizsäcker-Williams approximation of the virtual photon flux [18, 19]. Thus, a quasi-conversion of the photoproduction cross section to a leptoproduction cross section was achieved. PYTHIA5 incorporated the processes of photon-gluon fusion, QCD Compton, diffractive and non-diffractive vector meson production based on photoproduction cross sections, as well as anomalous photon processes[8].

The PYTHIA6 Monte Carlo simulation [165] used in the analysis here is more evolved compared to PYTHIA5. The treatment of virtual photons was implemented so that leptoproduction is simulated directly and no re-weighting by the user according to the virtual photon flux is needed. Also deep inelastic scattering is implemented in this version. The most profound change (and most helpful for this work) is the implementation of a unified description of the transition from real to virtual photons based on a phenomenological model [193, 194]. The consistent treatment of vector meson production, anomalous photon, and direct processes is one of the advantages of this simulation. Therefore, the Monte Carlo analysis presented in the following is thought to supersede the one corresponding to the HERMES publication [96]. In particular, the original claim of a fraction of $\sim 60\%$ photon-gluon fusion processes at large transverse momenta is rectified to be around 20%.

7.1.1 From Real to Virtual Photons

PYTHIA6 models the total virtual photon - proton cross section by the incoherent sum of leading-order deep inelastic scattering (LO DIS), photon-gluon fusion (PGF), QCD Compton processes (QCDC), vector meson production (VMD), and anomalous photon processes (GVMD) (see Figs. 2.8 and 2.11 in Chapter 2):

$$\sigma^{\gamma^* p} = \sigma^{\gamma^* p}_{LO\ DIS} + \underbrace{\sigma^{\gamma^* p}_{PGF} + \sigma^{\gamma^* p}_{QCDC}}_{\sigma^{\gamma^* p}_{dir}} + \xi(Q^2, W^2) \cdot (\sigma^{\gamma^* p}_{VMD} + \sigma^{\gamma^* p}_{GVMD}) \ . \tag{7.1}$$

The suppression of VMD and GVMD processes for low W^2 and non-zero Q^2 is modeled

[8]The publication analysis disregarded deep inelastic scattering and anomalous photon processes which certainly should not be done in the unified approach of PYTHIA6 (see Sect. 7.1.2).

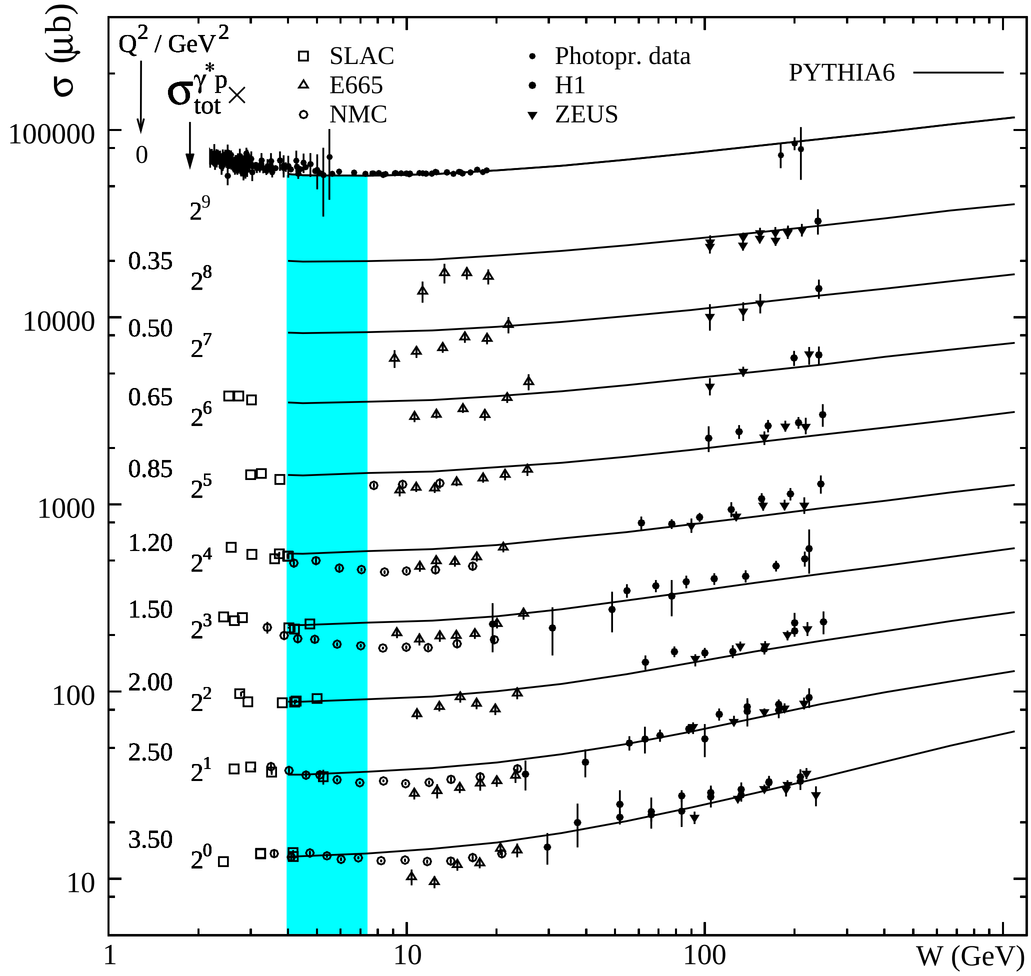

Figure 7.1: The total photon-proton cross section as a function of the invariant mass W of the $\gamma^* p$ system for different values of Q^2. The measurements from SLAC, HERA, and CERN are superimposed with the model (Eq. 7.1) used in PYTHIA6 (Figure according to [193]). The grey area indicates the kinematic coverage of the analyzed HERMES data.

by a phenomenological factor $\xi(Q^2, W^2) = (1 + Q^2/W^2)^{-3}$. This avoids double counting in the transition region between VMD and DIS (see also Sect. 7.1.2). Equivalently, the vanishing of the deep inelastic scattering cross section in the photoproduction limit is achieved through a phenomenological suppression by a Sudakov form factor. Thus, the ansatz:

$$\sigma^{\gamma^* p}_{LO\ DIS} = \sigma^{\gamma^* p}_{DIS} \cdot \exp\left(-\sigma^{\gamma^* p}_{dir} / \sigma^{\gamma^* p}_{DIS}\right) \quad \text{with} \quad \sigma^{\gamma^* p}_{DIS} \sim F_2(x, Q^2) \cdot (1 + m_\rho^2/Q^2)^{-2} \,, \quad (7.2)$$

is made for leading-order DIS, where m_ρ denotes the mass of the ρ meson. Photon-gluon fusion and the QCD Compton process which add up to the contribution $\sigma^{\gamma^* p}_{dir}$ are modeled by the respective partonic cross sections (see Eqs. 2.74 and 2.80).

The contribution from vector mesons is accounted for by the vector meson dominance model where the vector meson amplitude is assumed to dominate the hadronic part of the photon wave function. If the photon fluctuated into a vector meson which interacts with a proton, the cross section σ^{Vp} can be described by the common Reggeon-Pomeron ansatz for hadronic cross sections [195] as a function of the center-of-mass energy s:

$$\sigma^{Vp}(s) \sim c_r^{Vp} \cdot s^{\epsilon} + c_p^{Vp} \cdot s^{-\eta} \qquad \text{with } \epsilon = 0.0808 \text{ and } \eta = 0.4525 \ , \tag{7.3}$$

where c_r^{Vp} and c_p^{Vp} are process dependent parameters. The first term in Equation 7.3 describes an interaction via Pomeron exchange while the second term expresses the classical Regge trajectory (see for instance [161]). PYTHIA6 also simulates diffractive vector meson production according to the diffraction model in combination with Regge theory. This results in a typical dependence of the cross section as a function of the four-momentum t transferred to the target [196]:

$$\frac{d\sigma^{Vp}}{dt} \sim e^{-b(s)|t|} \quad \text{with} \quad b(s) \approx 2b_V + 2b_p + 2\alpha' \ln(s/\text{GeV}) \ , \tag{7.4}$$

and the energy dependent slope parameter b. In the simple black-disk diffraction model, the square roots of the parameters b_V and b_p are proportional to the interaction radii of vector meson and proton. The parameter α' is the slope of the Reggeon or Pomeron trajectory which intercepts for $s = 0$ at $(1 - \eta)$ or $(1 + \epsilon)$, respectively. The transition from real to virtual photons is accommodated by [197]:

$$\sigma_{VMD}^{\gamma^* p} = \sum_{V=\rho^0,\omega,\phi,J/\psi} \frac{4\pi\alpha}{f_V^2} \left(\frac{m_V^2}{m_V^2 + Q^2} \right)^2 \sigma^{Vp} \ , \tag{7.5}$$

with the appropriate vector meson-photon couplings f_V^2. Here, transverse photons are assumed to dominate the cross section (setting MSTP(17)=0 in PYTHIA6, cf. Listing B.2.2). The cross section of the anomalous photon processes[9] is calculated by the integration and summation over the appropriate $q\bar{q}$ states of the photon:

$$\sigma_{anom}^{\gamma p} = \frac{\alpha}{\pi} \sum_q e_q^2 \int_{k_0} \frac{d k_T^2}{k_T^2} \sigma^{(q\bar{q})\,p} \tag{7.6}$$

depending on the intrinsic k_T of the partons in the photon with a lower cut-off k_0 (see also Fig. 7.2). The treatment for virtual photons leading to $\sigma_{anom}^{\gamma p} \to \sigma_{GVMD}^{\gamma^* p}$ is achieved by weighting the states with a factor $(1+Q^2/4k_T^2)^{-2}$ in the integrand in Equation 7.6 [193].

With all the above contributions summed up, the total photon-proton cross section is completely modeled. A comparison of the modeled $\sigma^{\gamma^* p}$ with data is shown in Figure 7.1 over a wide range of W and Q^2.

[9] The terms *anomalous photon* and *GVMD* differ in meaning throughout literature. In this work the nomenclature of reference [194] is adopted.

7.1.2 Modeled Processes

Two different scales govern the process classification scheme in PYTHIA6 (Fig. 7.2): the intrinsic k_T of the partons in the photon and the intrinsic p_T of the involved parton of the proton or neutron (e.g. the gluon in Fig. 7.2, left). If at small values of p_T the intrinsic k_T^2 is much smaller than Q^2, deep inelastic scattering dominates in this part of the phase space. As k_T increases, the direct processes PGF and QCD Compton become important (note the similarity to the Feynman graph in Fig. 2.8, left). If k_T stays below a threshold k_0 (cf. Eq. 7.6) PYTHIA6 will generate vector mesons according to the VMD model. Above the threshold and at values of $p_T > k_T$ the GVMD (or anomalous) states will dominate (Fig. 7.2, right). In nature, smooth transitions between these different processes are believed to exist instead of clear-cut boundaries. However, for generating events with a Monte Carlo simulation the phase space has to be divided. The PYTHIA6 classification scheme avoids double counting of the processes to a large extent when modeling the total cross section.

All processes in PYTHIA6 are identified by process numbers which correspond to physics processes on the partonic level. This information is delivered for every event generated by the Monte Carlo simulation and allows the subdivision of the sample with respect to the underlying physics process. An overview of the nomenclature used in the following Monte Carlo analysis is given in Table 7.1.

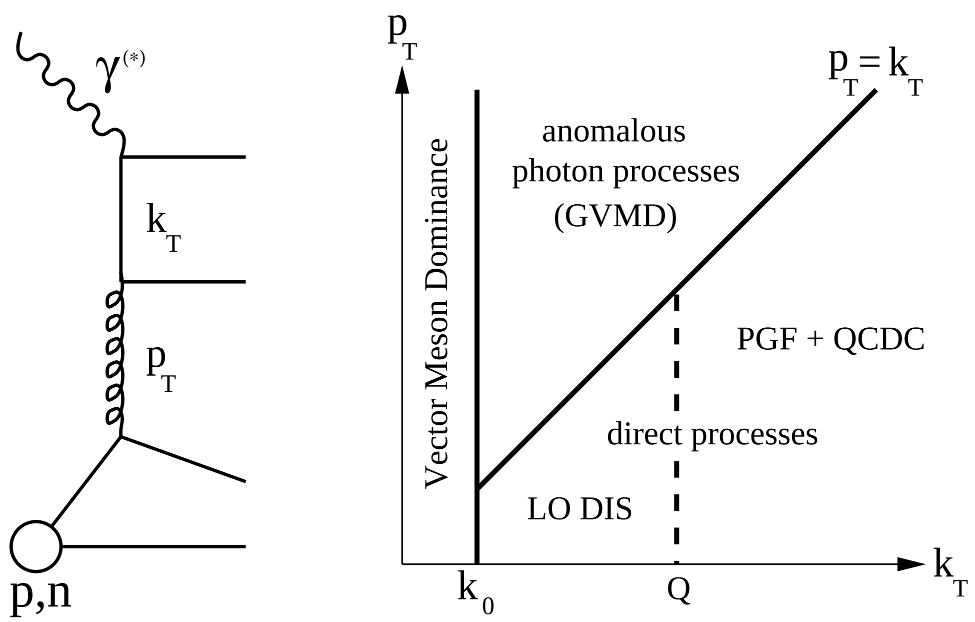

Figure 7.2: Illustration of the process classification scheme for $\gamma^{(*)}N$ reactions realized in PYTHIA6. Leading-order DIS (LO DIS) disappears from the diagram on the right as Q^2 goes to zero (Figure according to [193]).

Table 7.1: The PYTHIA6 process classification and the nomenclature used in the analysis. Transverse photons are denoted as γ_T^*, longitudinal photons as γ_L^*.

process	no.	name
GVMD states ($\gamma^* \to q\bar{q}$)	10-20	anomalous photon
elastic $\gamma^* + p \to V + p \quad (t \to 0)$	91	VMD
single diffractive $\gamma^* + p \to V + p$	92	
single diffractive $\gamma^* + p \to V + X$	93	
double diffractive $\gamma^* + p \to V' + X$	94	
low-p_T phase space	95	
$\gamma^* + q \to q$	99	DIS
$\gamma_T^* + q \to q + g$	131	QCDC
$\gamma_L^* + q \to q + g$	132	
$\gamma_T^* + g \to q + \bar{q}$	135	PGF
$\gamma_L^* + g \to q + \bar{q}$	136	

7.1.3 Comparison with HERMES Data

The spectra of the kinematic variables Q^2 and ν as determined by PYTHIA6 for two hadrons observed in opposite detector halves is shown in Figure 7.3. As expected, the average virtuality of the photons is very low at $\langle Q^2 \rangle = 0.01$ GeV^2 and the relative energy transfer y is always above 0.3 with an average value of $\langle y \rangle = 0.65$. Due to the acceptance limit of small scattering angles, the positron is detected in only 2.6% of all cases in coincidence with a hadron pair. In 1.7% of the events an additional slow hadron is detected. Most importantly, the average $\langle W^2 \rangle \approx 34$ GeV^2 is higher than for the deep inelastic scattering dataset at HERMES ($\langle W^2 \rangle \approx 25$ GeV^2). The higher W^2 values in photoproduction motivate the high-W^2 fit in Section 5.3.1 which is applied for all PYTHIA6 results discussed here unless noted otherwise. The average value of W^2 rises if a minimum cut on $p_\perp^{max}$ is placed. For $p_\perp^{max} > 1.0$ GeV the average W^2 is about 40 GeV^2 raising to 45 GeV^2 for $p_\perp^{max} > 1.5$ GeV (Fig. 7.3, right).

Furthermore, after discussions with the program author [198] several default settings of the PYTHIA6 package were changed to account for the center-of-mass energy of the HERMES experiment. The PYTHIA6 setting for PARP(111), which controls the minimum invariant mass of a hadronic remnant system, has been set to zero in the same way as for the DIS simulation with LEPTO (cf. PARP(111) in Listings B.2.2 and B.1.2). This modification is needed to open up the phase space at the lower HERMES energies which normally is discarded for simulations at higher energies. The simulated physics processes are just extended to lower energies, no additional physics enters the simulation by these changes. Equally, the minimum allowed $\hat{s}$ for partonic processes was lowered from 2 GeV^2 to 0 GeV^2 in the simulation. The complete parameter settings of the PYTHIA6 Monte Carlo program as applied in this work are listed in Appendix B.2.

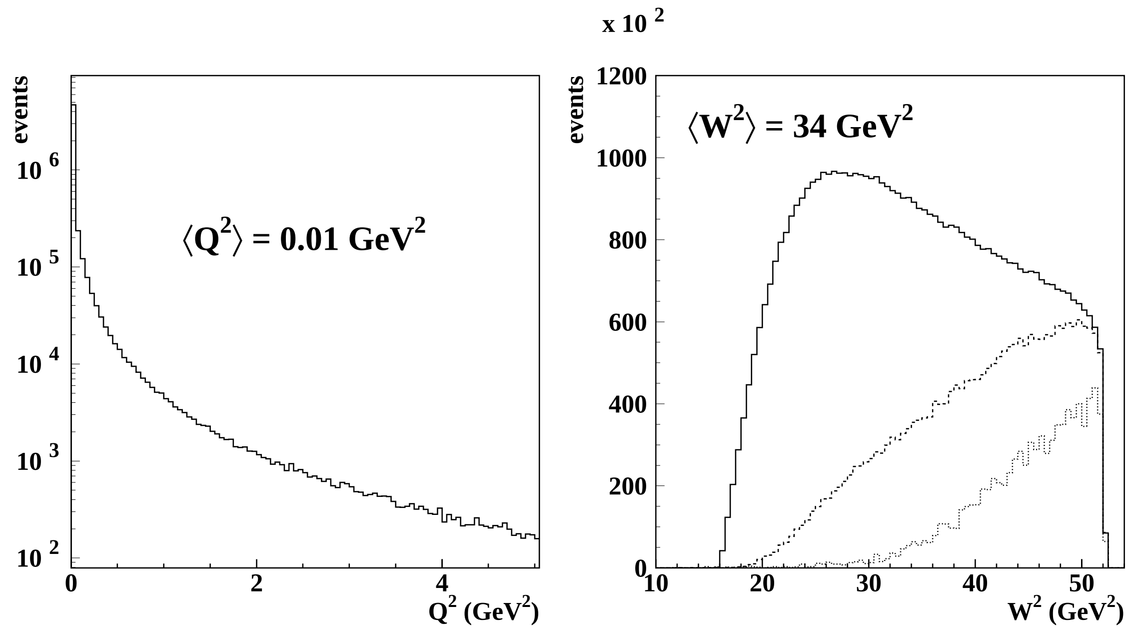

Figure 7.3: The Q^2 (**left**) and W^2 (**right**) spectra for two hadrons detected in opposite halves of the HERMES detector ($m_{\pi\pi} > 1$ GeV) as determined by a PYTHIA6 simulation. **Right:** The W^2 spectrum for all events (solid line), for $p_\perp^{max} > 1$ GeV (dashed line, $\times 7$), and for $p_\perp^{max} > 1.5$ GeV (dotted line, $\times 60$).

Data and simulation can be compared by means of observed cross sections if the luminosity monitor is used for normalization:

$$\sigma_{obs} = \epsilon_{acc}\, \sigma_{tot} = \frac{n}{\mathcal{L} \cdot \epsilon_{DAQ} \cdot \epsilon_{trig} \cdot \epsilon_{rec}} \ , \tag{7.7}$$

where the observed number of events n is corrected by the normalized luminosity $\mathcal{L} = \sum c_{lumi} \cdot r \cdot l$. The normalized luminosity can be calculated by the summation over the product of the observed coincidence rate r of the luminosity monitor, the duration of a burst l, and the constant c_{lumi} (see also Eq. 3.7). Also the livetime of the data acquisition ϵ_{DAQ}, the trigger efficiency ϵ_{trig}, and the reconstruction efficiency ϵ_{rec} have to be regarded. The observed cross section σ_{obs} is the detector acceptance ϵ_{acc} times the total cross section σ_{tot}. The observed cross section σ_{obs} is a helpful quantity for comparisons. Since the acceptance of the detector is modeled in the Monte Carlo simulation, ϵ_{acc} does not have to be derived for a comparison with the data. This avoids systematic uncertainties on the total cross section σ_{tot} from the unknown shape of the spectra outside of the kinematic acceptance of the detector.

Figure 7.4 shows the observed cross section compared between HERMES data on a hydrogen target and a PYTHIA6 simulation in the large transverse momentum region of h^+h^- events. Two different simulation results are shown: one with the PETRA default settings of PYTHIA6 and one with the high-W^2 settings for HERMES kinematics derived in Chapter 5. The benefit of the dedicated adaption to HERMES kinematics is clearly visible as this option describes the observed cross section fairly well. The standard setting (PETRA default) largely underestimates the cross section since apparently the hadron multiplicity and the accumulated p_T in the fragmentation are not matched (cf. Fig. 5.15, bottom/left) to the HERMES kinematic environment. However, even with the best available modeling of the fragmentation differences remain. This is not unexpected because radiative corrections are not included in the leading-order model used here. Secondly, the total virtual photon - proton cross section is modeled with an accuracy of 20%-30% by PYTHIA6 (see Fig. 7.1) so deviations in comparison with the data could be explained.

The quality of the modeled kinematics in the large transverse momentum region is shown in Figure 7.5 by a comparison between hydrogen data and a Monte Carlo simulation ($p_\perp^{max} > 1.5$ GeV). Good agreement is found for the energy sum of the two hadrons and their invariant mass spectrum. The latter shows that the cut on $m_{\pi\pi}$ in the asymmetry analysis is apparently superfluous if the two hadron tracks are found in opposite detector halves. Also the coplanarity ϕ seems to be modeled well. Furthermore, the cut of the new analysis for the signal region $p_T' > 1.2$ GeV is almost equivalent to the condition $\Delta\phi = 180^\circ \pm 30^\circ$ demanded by Bravar *et al.* [93]. Thus, the condition $p_T' > 1.2$ GeV nicely ensures an observation of hadrons appearing back-to-back in the detector as intuitively expected for photon-gluon fusion events.

The comparisons between data and Monte Carlo simulation shown in this Section were found to be satisfying. Therefore, the simulation by PYTHIA6 is thought to be trustworthy to conduct an extraction of the gluon polarization.

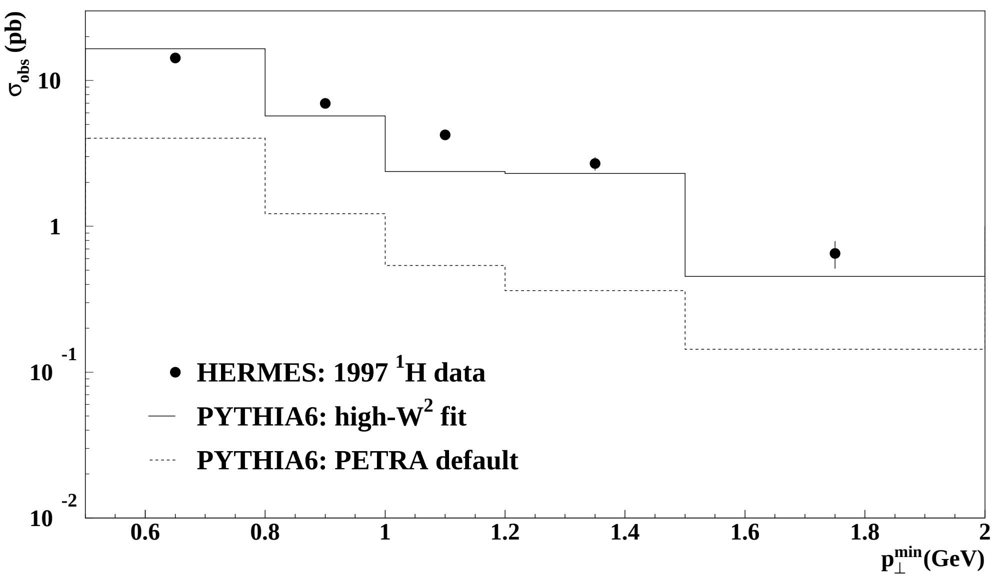

Figure 7.4: A comparison of the observed cross section between 1997 hydrogen data and a PYTHIA6 Monte Carlo simulation. The latter is shown for two fragmentation model settings: the high-W^2 fit (solid line) and the PETRA default (dashed line, cf. reference [191]). For the respective fragmentation settings see Table 5.3 in Section 5.3.1.

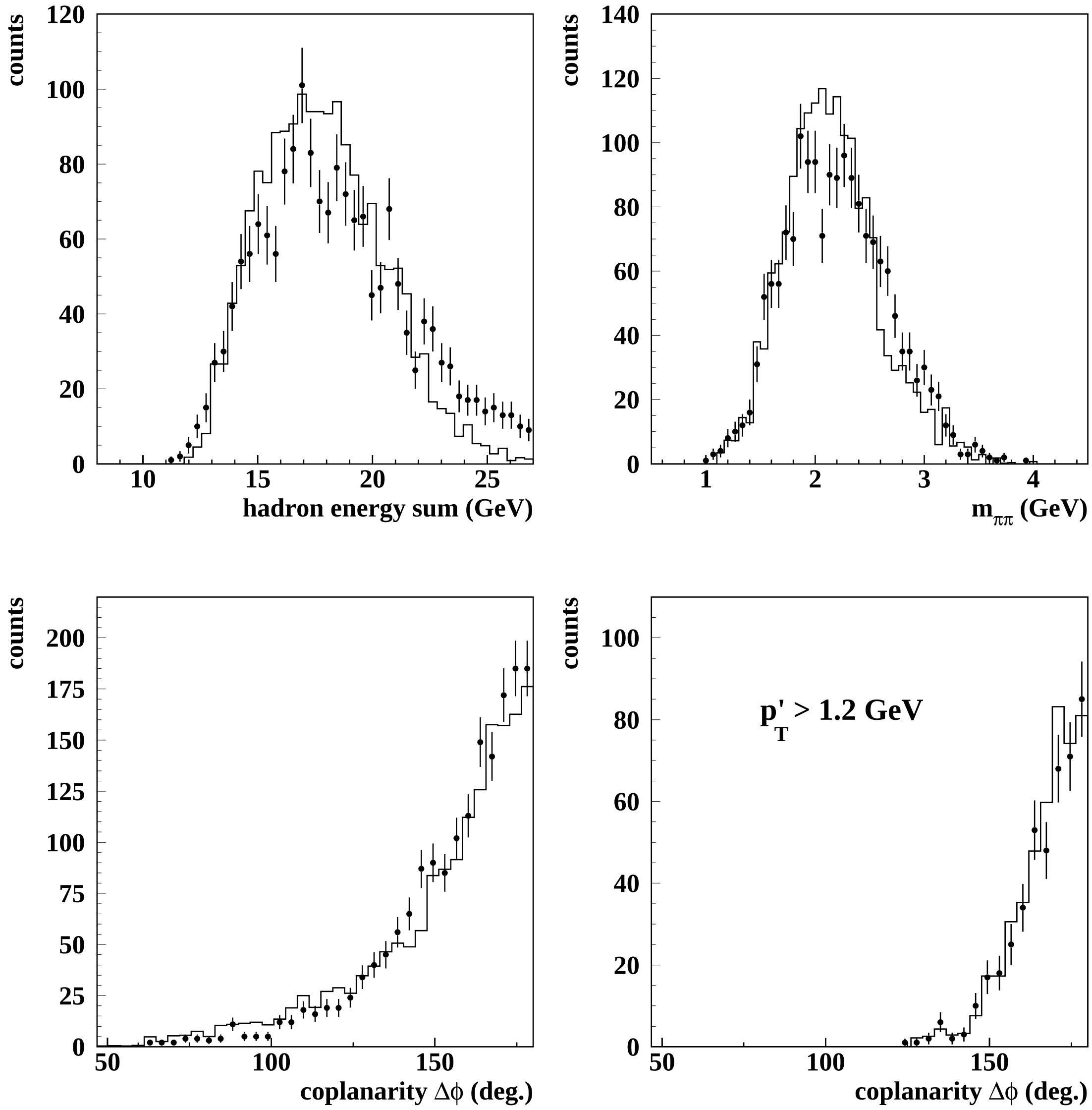

Figure 7.5: Comparison of a PYTHIA6 simulation result (solid line) and the 1997 HERMES hydrogen data (solid circles) for h^+h^- events with $p_\perp^{max} > 1.5$ GeV. The spectra are normalized to equal areas. **Top, left**: The energy sum of the two hadrons assuming they are pions. **Top, right**: Invariant mass of the two hadrons hadrons assuming they are pions. **Bottom**: Coplanarity $\Delta\phi$ relative to the beam axis (left) and with the additional cut $p_T' > 1.2$ GeV (right).

7.2 Extraction of the Gluon Polarization

7.2.1 Processes at Large Transverse Momenta

A measured double spin asymmetry in the production of two hadrons can be written as the superposition of spin asymmetries arising from different processes:

$$A_{\parallel}(p'_T) = \sum_{j=PGF,QCDC,DIS,VMD,anom} f_j(p'_T)\, A_j(p'_T) \qquad \text{with} \qquad \sum_j f_j(p'_T) = 1 \ . \tag{7.8}$$

The spin asymmetries of the various subprocesses A_j contribute according to the corresponding fractions f_j. The double spin asymmetries involved can be expressed by:

$$A_{PGF}(p'_T) = \frac{1}{n}\sum_i^n \frac{\hat{a}_{PGF}}{D(Q_i^2, y_i)} \frac{\Delta g(x_{g\,i}, \hat{p}_{T\,i})}{g(x_{g\,i}, \hat{p}_{T\,i})} \ , \tag{7.9}$$

$$A_{QCDC}(p'_T) = \frac{1}{n}\sum_i^n \frac{\hat{a}_{QCDC}(\hat{s}, \hat{u})}{D(Q_i^2, y_i)} \frac{\Delta q_i(x_i, \hat{p}_{T\,i})}{q_i(x_i, \hat{p}_{T\,i})} \ , \tag{7.10}$$

$$A_{DIS}(p'_T) = \frac{1}{n}\sum_i^n \frac{1}{D(Q_i^2, y_i)} \frac{\Delta q_i(x_i, Q^2)}{q_i(x_i, Q^2)} \ , \tag{7.11}$$

where the sum indicates the summation over the applicable phase space (or Monte Carlo events). The asymmetries defined in Equations 7.10 and 7.11 can be evaluated as a function of p'_T by employing Monte Carlo generated events. Equation 7.8 can be inverted to obtain the average gluon polarization for each p'_T-bin:

$$\frac{\Delta g}{g} = \frac{1}{f_{PGF} D} \cdot (A_{\parallel} - f_{QCDC} A_{QCDC} - f_{DIS} A_{DIS}) \ , \tag{7.12}$$

with the assumption of vanishing asymmetries $A_{VMD} = A_{anom} = 0$ for vector meson production and anomalous photon events. This approach regards the different asymmetry contributions point-wise for all simulated kinematic quantities. Consequently, the asymmetries A_{QCDC} and A_{DIS} as well as the corresponding process fractions have to be calculated for a hydrogen ($A_{\parallel}^p$) and a deuterium ($A_{\parallel}^{pn}$) target separately. The latter is achieved by appropriately joining PYTHIA6 data samples on a proton and a neutron target since the simulation does not comprise deuterium as a possible target.

The modeled process fractions f_j and the background asymmetries from DIS and QCD Compton process according to Equations 7.10 and 7.11 are displayed in Figure 7.6 for a ^{1}H and a ^{2}H target. The PGF fraction in the sample amounts to 17%-25% for both targets, slightly rising versus p'_T. The QCD Compton process on average contributes 7% while its fraction decreases with rising p'_T. Deep inelastic scattering contributes up to 10% to the overall sample at lowest p'_T, above $p'_T > 1.2$ GeV its contribution becomes insignificant. With about 67%, the largest part of the sample is occupied by VMD and anomalous photon processes.

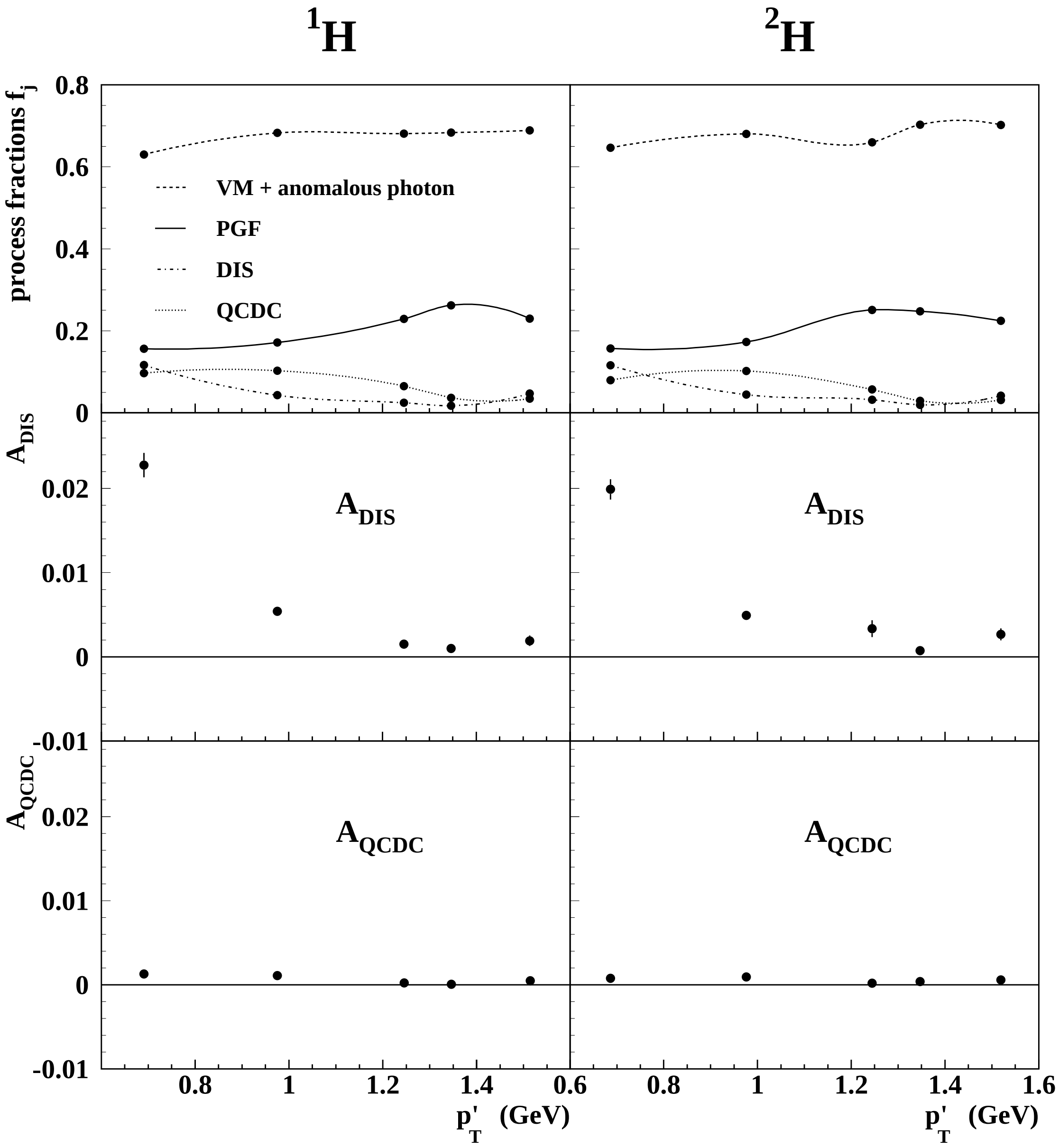

Figure 7.6: The process fractions f_j (**top**) from a PYTHIA6 simulation and the asymmetries A_{DIS} (**middle**) and A_{QCDC} (**bottom**) evaluated from parameterizations of the polarized parton distributions (GRSV std.scenario [57]) using the Monte Carlo event kinematics. The shown quantities are derived for each p'_T-bin (cf. Tab. 6.5). The data points are plotted at the bin centers and for the case of the process fractions f_j joined by smooth lines for display purposes. The statistical uncertainties on the f_j are not displayed. The results are shown for a hydrogen (**left row**) and a deuterium target (**right row**).

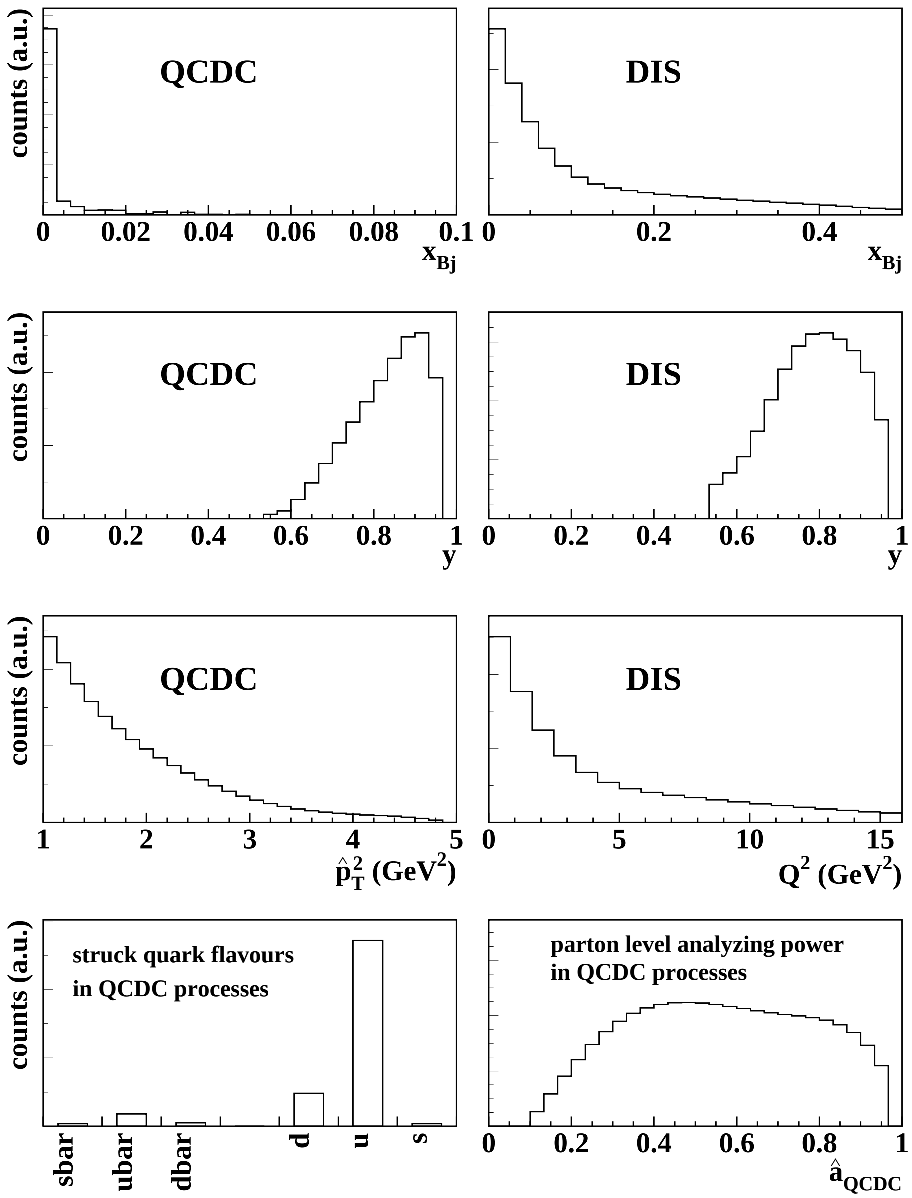

Figure 7.7: Top three panels: The distributions of Monte Carlo generated kinematic variables for the QCD Compton process (**left row**) and deep inelastic scattering (**right row**) for $p_\perp^{max} > 1$ GeV on a proton target. **Bottom, left**: The flavour of the struck quark in QCD Compton processes as determined by the Monte Carlo Simulation. **Bottom, right**: The distribution of the parton level analyzing power $\hat{a}_{QCDC}$ for the QCD Compton process. For a clear representation the kinematic spectra were smoothed by a small amount to reduce statistical fluctuations caused by the finite Monte Carlo statistics.

The background asymmetries A_{DIS} and A_{QCDC} were calculated according to Equations 7.10 and 7.11 using the polarized quark distribution functions from reference [57] for the respective struck quarks q_i. Since the DIS approximation of the depolarization factor $D(Q^2, y)$ according to Equation 2.29 leads to unphysical results (i.e. $D > 1$) at low Q^2 values, a more precise expression (according to [58]) was used here:

$$D(Q^2, y) = \frac{y(2-y)(1+\frac{1}{2}\gamma^2 y)}{y^2(1+y^2)(1-2m_e^2/Q^2) + 2(1-y-\frac{1}{4}\gamma^2 y^2)(1+R_{DIS})} \,. \tag{7.13}$$

For the calculation of the depolarization factor, a parameterization of the ratio $R_{DIS}(x, Q^2) = \sigma_L/\sigma_T$ was taken from reference [21]. The asymmetries at large transverse hadron momenta in deep inelastic scattering are of the order 0.01 since mostly x-values below 0.1 are probed while the average Q^2 falls from 6 GeV^2 to 0.8 GeV^2 as p_T' increases. The asymmetries arising from the QCD Compton process are comparably small ($|A_{QCDC}| < 0.002$) since the probed x-values are mostly below 0.01 where A_1 is almost zero. Nonetheless, the parton level analyzing power $\hat{a}_{QCDC}(\hat{s}, \hat{u})$ is evaluated for each Monte Carlo event according to Equation 2.81 and turns out to range from 0.1 to 1 (Fig. 7.7, bottom). The average values of the kinematic variables for every p_T'-bin is listed in Tables C.13 and C.15 in the Appendix.

The underlying kinematic variables of photon-gluon fusion events are histogrammed in Figure 7.8. Most of the PGF reactions were initiated at $Q^2 < 0.01$ so that the approximation of $\hat{a}_{PGF} \cong -1$ is accurate to better than 0.4%. The gluon distribution is probed

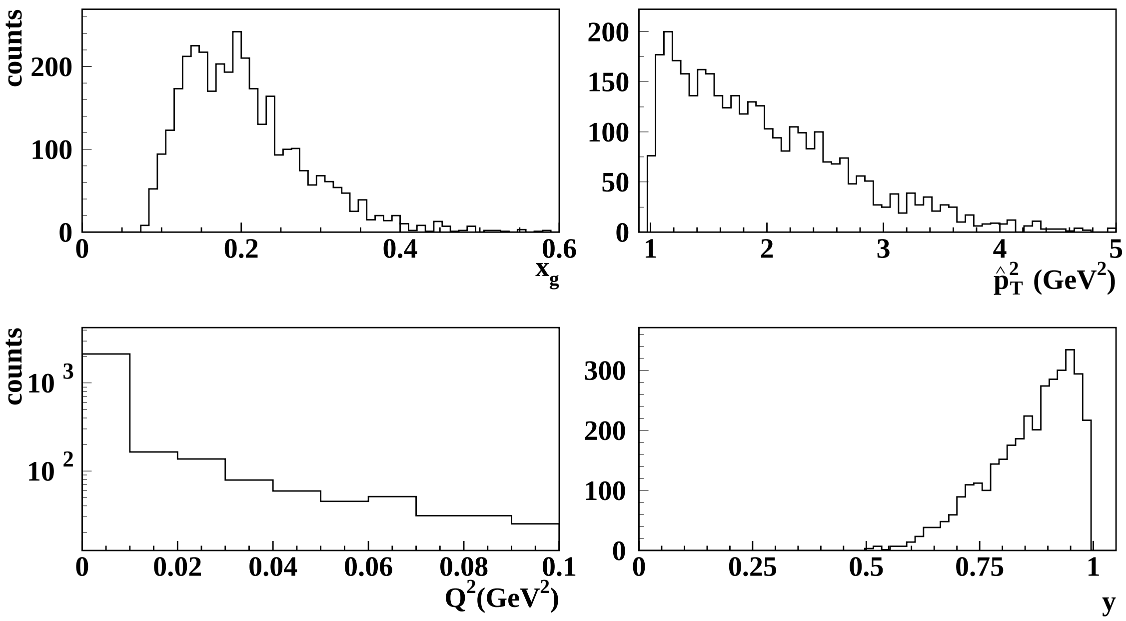

Figure 7.8: The generated distributions for various kinematic variables from PYTHIA6 for photon-gluon fusion events with the cut $p_\perp^{max} > 1.5$ GeV.

at an average $\langle x_g \rangle = 0.20$ and at an average scale of $\langle \hat{p}_T^2 \rangle = 2.0$ GeV^2. In correspondence to Figure 6.5 (Sect. 6.1.2) the average values of x_g and $\hat{p}_T^2$ rise with increasing p'_T: for the upper three p'_T-bins $\langle x_g \rangle = 0.23$ and $\langle \hat{p}_T^2 \rangle = 2.4$ GeV^2 is found. The average relative energy transfer of the virtual photon is $\langle y \rangle = 0.86$ resulting in little depolarization of the virtual photon ($\langle D \rangle = 0.94$) since Q^2 is mainly below 0.01 GeV^2 for PGF events. The average kinematic values are given in the Tables C.12 and C.14 in the Appendix.

7.2.2 Results and Comparison with QCD Fits

Since the process fractions and background asymmetries differ slightly for a hydrogen and a deuterium target, the extraction of the gluon polarization is done for each target separately. Equation 7.12 is applied for each p'_T-bin using the ^{1}H and ^{2}H datasets for $A_\parallel$ (Fig. 7.9, top). The resulting values for $\Delta g/g$ for each target are then combined to the final result (Fig. 7.9, middle/bottom). The extracted values of $\Delta g/g$ are zero for small transverse momenta and rise as p'_T increases. Following the argumentation of Section 6.1.2 the last three p'_T-bins can be interpreted in terms of the gluon polarization. If these three bins and data on both targets are combined, the final result of the extraction is:

$$\mathbf{\Delta g/g = 0.47 \pm 0.21}_{\mathbf{(stat)}} \, ,$$

at $\langle x_g \rangle = 0.23$ and an average scale $\langle \mu^2 \rangle \equiv \langle \hat{p}_T^2 \rangle$ of 2.4 GeV^2. If only the data on the hydrogen (deuterium) target is regarded a value of 0.95 ± 0.47 (0.35 ± 0.23) is yielded for the gluon polarization.

The final result on $\Delta g/g$ from PGF events is compared to several QCD analyses of the polarized structure functions $g_1^{p,n}(x, Q^2)$ or the experimental asymmetries $A_1^{p,n}(x, Q^2)$ (Fig. 7.10, top). The two most recent fits are from the Asymmetry Analysis Collaboration (AAC) [56] and from Blümlein and Böttcher (BB) [27] and regard the latest measurements on the polarized structure functions from the experiments HERMES, E143, and E155. The analysis of Blümlein and Böttcher features a full error propagation of all experimental and theoretical uncertainties (grey band in Fig. 7.10). Since all QCD fits give $\Delta g(x, \mu^2)$ as result, this quantity is best compared to the data (Figure 7.10). This comparison of Δg instead of $\Delta g/g$ has the additional advantage of a smaller systematic uncertainty for the point extracted from data. The process fraction for photon-gluon fusion, f_{PGF}, is proportional to the unpolarized input gluon density chosen in the Monte Carlo simulation (CTEQ4LQ [54]). In this case the unpolarized gluon density in Equation 7.12 cancels to first order thus reducing the influence on the systematic uncertainty.

7.3 Systematic Uncertainties

Systematic uncertainties on the value of the gluon polarization arise from the scale uncertainty of the measured asymmetries, the assumptions on the various background asymmetries, and from the model implemented in PYTHIA6. The relative experimental scale uncertainty from the measurement of beam and target polarization amounts to 6.2% combined for the analyzed running years 1996 to 2000 (cf. Tab. 6.6).

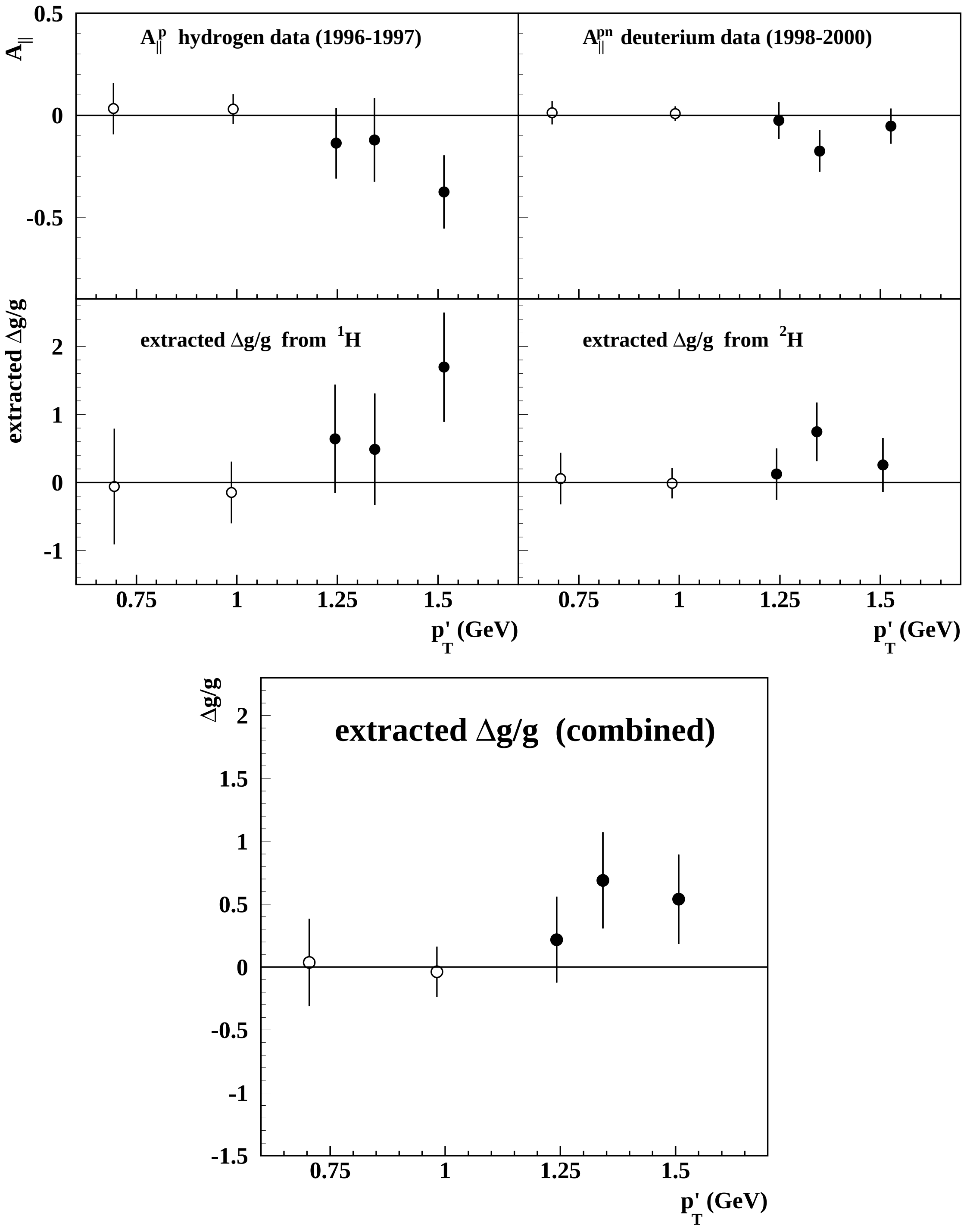

Figure 7.9: The unfolding of the measured asymmetries. **Top**: Double spin asymmetries for hydrogen (**left**) and deuterium (**right**). The average combined asymmetry of the uppermost three p'_T-bins on both targets amounts to 0.104 ± 0.047. **Middle**: The unfolded $\Delta g/g$ values using Equation 7.12 and the process fractions displayed in Figure 7.6. **Botton**: The final result on $\Delta g/g$ versus p'_T from combining the extraction on hydrogen and deuterium. Only for the solid data points an interpretation of the measured double spin asymmetries in terms of the gluon polarization is justified (see text).

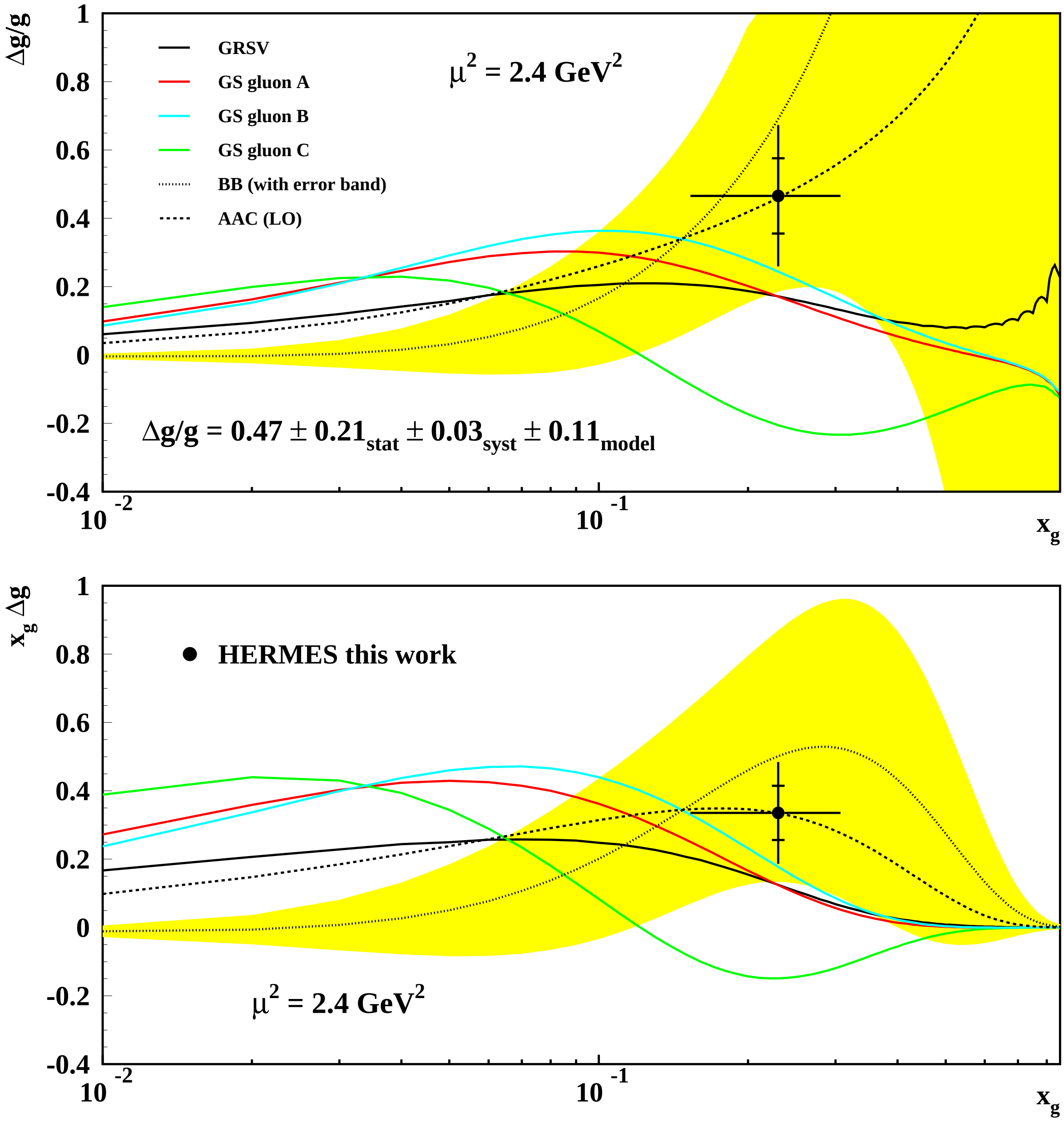

Figure 7.10: Comparison of the extracted gluon polarization from hadron pairs at large transverse momenta from HERMES data at $\langle x_g \rangle = 0.23$ with various QCD fits to $A_1(x, Q^2)$ or $g_1(x, Q^2)$ (GS [55], AAC [56], BB [27], GRSV [57]). The inner vertical error bar indicates the model uncertainty while the horizontal error bar depicts the rms of the probed x_g distribution. **Top:** Comparison of $\Delta g/g(x_g, 2.4\,\mathrm{GeV}^2)$. The unpolarized gluon density GRV98 [52] which was used to compute $\Delta g/g$ in this figure causes unphysical values of $\Delta g/g > 1$ from the AAC and BB fits. **Bottom:** Comparison of $x_g \cdot \Delta g(x_g, 2.4\,\mathrm{GeV}^2)$. The grey error band indicates the 1σ uncertainty of the BB QCD fit.

7.3.1 Background Asymmetries

The sensitivity of the resulting values of $\Delta g/g$ on the polarized quark distributions was tested by employing different parameterizations. By alternatively using the various polarized quark distributions from Gehrmann and Stirling (GS, model A to C) [55] and GRSV (valence scenario), the relative deviations on the extracted gluon polarization turn out to be less than 0.2%.

Potential background asymmetries could arise from vector meson production processes, which are dominated by the production of ρ mesons. In diffractive vector meson production a zero double spin asymmetry follows from the theoretical argument of s-channel helicity conservation. In this case the vector meson retains the helicity of the virtual photon. A way to constrain the background asymmetries experimentally is to calculate a double spin asymmetry according to Equation 6.17 for an invariant mass $m_{\pi\pi}$ of the hadron pair around the mass of the ρ meson ($m_\rho = 0.77$ GeV). Such an extraction was conducted based on HERMES data from all running years (Fig. 7.11). The measured asymmetries $A_{\parallel}^{\rho}$ are consistent with zero even if the two hadrons are required to be identified pions ($\rho^0 \to \pi^+\pi^-$). These findings confirm a recent detailed analysis on double spin asymmetries in ρ production at HERMES [199]. Accounting for the precision of the data on the proton target a conservative estimate of $|A_{\parallel}^{\rho}| < 0.01$ can be made. If this assumption is inserted as $A_{VMD} = A_{anom} = \pm 0.01$ into the extraction of the gluon polarization the influence of such background asymmetries on the final result is at most 6.4%.

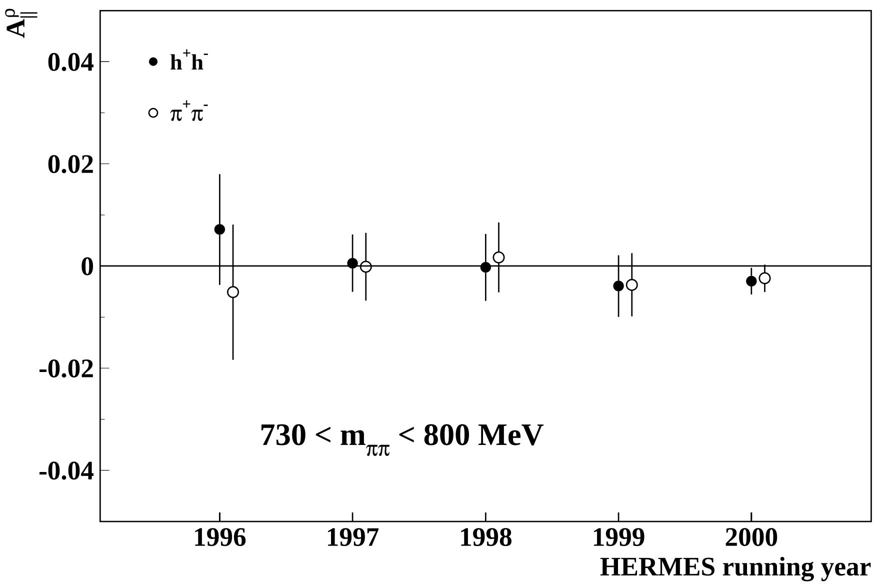

Figure 7.11: Double spin asymmetry in the production of h^+h^- ($\pi^+\pi^-$) pairs in the ρ mass region derived from HERMES data of the running years 1996 to 2000.

7.3.2 Model Uncertainties

The main uncertainties on the cross section modeling in PYTHIA6 are due to the unpolarized gluon density and the accuracy of the description of the vector meson production. The influence of these two items on the obtained gluon polarization was tested by reweighting the events in the Monte Carlo sample.

The modeling of the vector meson production was tested by normalizing the observed invariant mass spectrum of h^+h^- pairs according to Equation 7.7 to the integrated luminosity. A comparison of the luminosity normalized spectra between HERMES hydrogen data and PYTHIA6 is shown in Figure 7.12 (left). The invariant mass spectrum is nicely described in shape whereas PYTHIA6 overestimates the observed cross section by a factor of two. This observation is in qualitative agreement with the excess of modeled total γ^*p cross section with respect to world data (Fig. 7.1). Further investigations show that in the ρ mass region (Fig. 7.12, right) the production of elastic and diffractive ρ mesons largely dominates over the anomalous photon contribution. Thus the observed cross section comparison only constrains the process fraction f_{VMD}. If the extraction of the gluon polarization is conducted with the VMD contribution altered by factors of two, the final result varies by 16%, since at large transverse momenta the anomalous photon processes become dominating (Fig. 7.13)

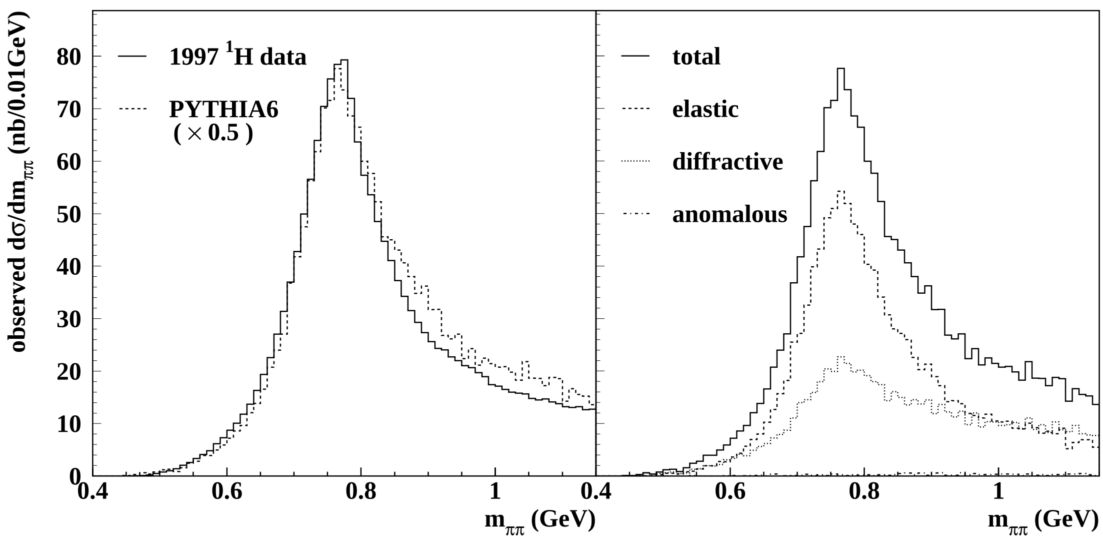

Figure 7.12: Left: Comparison between PYTHIA6 (dashed line, ×0.5) and HERMES data (solid line) of the observed cross section of h^+h^- pairs in the HERMES acceptance versus the invariant mass $m_{\pi\pi}$. **Right**: The contribution of the different subprocesses to the spectrum. The dashed histogram gives the contribution of elastic VM production (process 91, see Tab. 7.1), the dotted histogram the diffractive VM production (92-95). Here, the smallest contribution arises from anomalous photon processes (10-20, dash-dotted line).

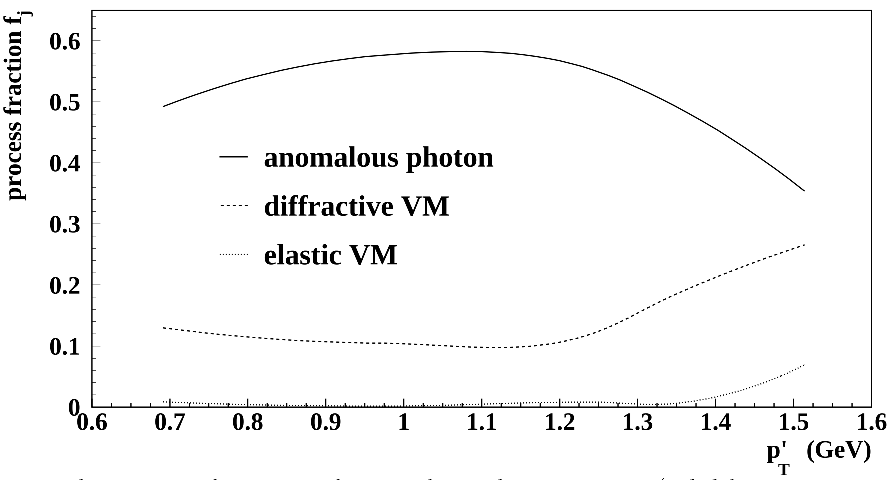

Figure 7.13: The process fractions of anomalous photon events (solid line, processes 10-20, see Tab. 7.1), diffractive (dashed line, procs.92-95) and elastic vector meson production (dotted line, proc.91) in the large transverse momentum region.

The anomalous photon contribution could not be constrained by comparisons to the data so that an accuracy of 20% is assumed leading to a systematic influence of about 9.4% to the gluon polarization. The modeled DIS cross sections from PYTHIA6 and LEPTO were compared and found to agree within 21%. If f_{DIS} is changed by this amount the final answer on the gluon polarization varies by about 1%.

In order to estimate the influence of the unpolarized gluon density on the result, the extraction was alternatively conducted with unpolarized quark and gluon densities from reference [53] (cf.fig2.7, top). This changed the extracted value of $\Delta g/g$ by about +15%. Recent QCD analyses of jet data and F_2 include a full error evaluation on the unpolarized parton densities [200, 201]. From these analyses an uncertainty of about 12% on the extracted gluon polarization can be inferred at scales between 1 GeV^2 and 10 GeV^2.

The resulting variations of the extracted value of $\Delta g/g$ from all systematic studies discussed above are listed in Table 7.2 and displayed in Figure 7.14. For an estimate of the total model uncertainty, the individual terms are added in quadrature, neglecting eventual correlations between them. Including also the systematic uncertainty on $\hat{a}_{PGF}$ and the statistical accuracy of the conducted Monte Carlo simulation, this leads to a total systematic uncertainty of 24% arising from the model dependent extraction using PYTHIA6. Thus, the final result reads:

$$\mathbf{\Delta g/g = 0.47 \pm 0.21\,(stat) \pm 0.03\,(syst) \pm 0.11\,(model)}\ .$$

Table 7.2: The various contributions considered for the systematic model uncertainty.

source of bias		$\delta(\Delta g/g)/(\Delta g/g)$
$\hat{a}_{PGF} = -1$		0.4%
finite Monte Carlo statistics		4.6%
polarized parton distributions		0.2%
GS gluon A	-0.04%	
GS gluon B	-0.09%	
GS gluon C	-0.21%	
GRSV valence scenario	-0.01%	
DIS cross section		1.1%
$A_{VMD,anom} \neq 0$		6.4%
VMD cross section		16.1%
anomalous photon cross section		9.4%
unpolarized gluon density		13.0%
MRST central-gluon	$+15.8\%$	
MRST high-gluon	$+13.9\%$	
MRST low-gluon	$+15.5\%$	
QCD fits to F_2	$\sim 12\%$	
total estimated model uncertainty		24.1%

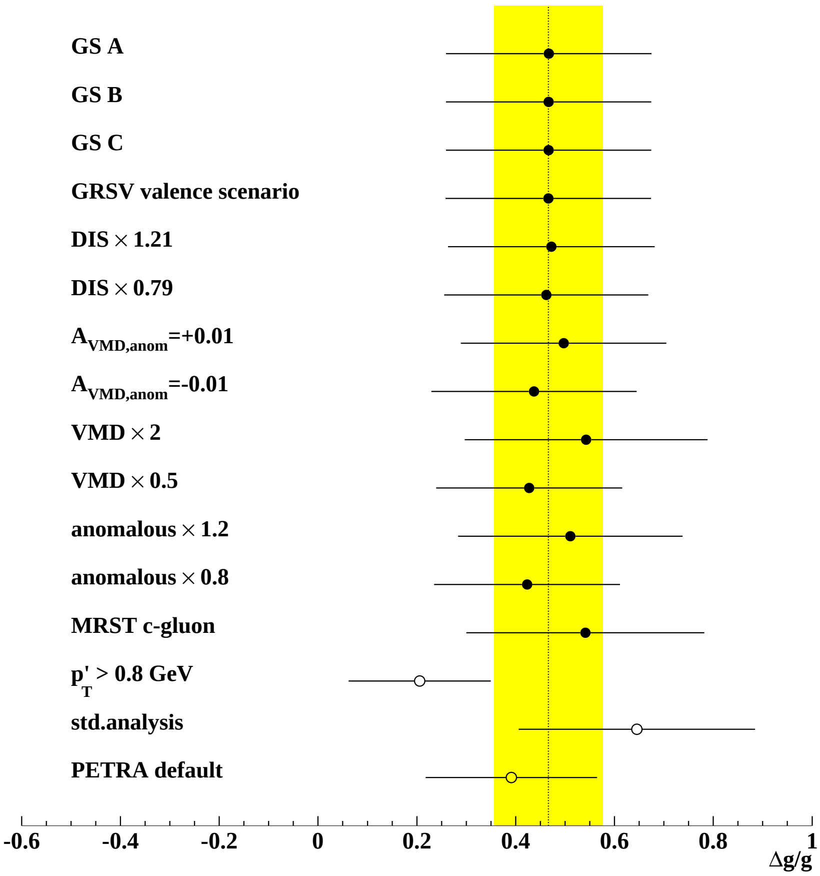

Figure 7.14: The results of the various systematic studies compared to the final result on $\Delta g/g$ (dotted line). The vertical error bars indicate the statistical uncertainties while the grey band displays the total model uncertainty. The open points show additional studies which have not been used for estimating the model uncertainty.

8 Conclusion and Outlook

The aim of the HERMES experiment at HERA is the investigation of the spin structure of the nucleon. This work adds to the efforts of the HERMES experiment by the treatment of three different topics. At first, a contribution to the experimental program is presented by the calibration and analysis of a Compton back-scattering beam polarimeter. Secondly, an analysis leading to a substantially improved description of the hadronization at HERMES energies is exposed. The third topic contributes directly to the investigation of the spin structure of the nucleon: a consistent Monte Carlo based extraction of the gluon polarization using measured double spin asymmetries in the photoproduction of hadron pairs at large transverse momenta is conducted.

The Longitudinal Polarimeter at HERA achieves a determination of the longitudinal positron beam polarization at an absolute precision of 1% per minute by Compton back-scattering laser photons off the positron beam. Chapter 4 summarizes the hardware contribution of this thesis: Via systematic testing of the single components, in particular of the electromagnetic calorimeter, a calibration with a small relative systematic uncertainty of 1.6% is presented. Furthermore, the optimum analysis strategy of the beam polarization data is elucidated which was implemented into the online control system of the polarimeter. All these efforts largely contributed to the publication of the polarimeter apparatus [151].

The understanding of the hadronization process at comparably low center-of-mass energies like at HERMES ($\sqrt{s}$ = 7.2 GeV) is crucial for the description of the hadronic final states in semi-inclusive deep inelastic scattering and photoproduction. The largely improved description using the LUND string model is explained in the analysis of Chapter 5. In comparison to results from an analysis of deep inelastic scattering (DIS) data the LUND model is carefully adjusted to HERMES kinematics. The treatment of radiative corrections and of systematic influences of the detector are found to be necessary for a good description and were included. Finally, two fragmentation descriptions are presented, one suitable for the analysis of polarized semi-inclusive DIS data at intermediate W^2 values and one for photoproduction at higher invariant masses of the hadronic final states.

Within the framework of the quark parton model the nucleon consists of quarks which are interconnected by gluons, the field quanta of the strong interaction. The gluons, which also carry momentum and spin of the nucleon, are of particular interest. A positive gluon polarization could pose the missing part in the decomposition of the nucleon spin. The polarized gluon density in the nucleon can be determined via the photon-gluon fusion reactions in quasi-real photoproduction. In Chapter 6 a strategy for tagging photon-gluon fusion at HERMES is developed by using a Monte Carlo simulation. The investigations show that more than 20% of a sample of h^+h^- pairs with large transverse momenta is expected to arise from photon-gluon fusion reactions. Moreover, the presented cut strategy addresses the suppression of soft events and is able to ensure the proper tagging of the emerging hadrons over other debris from the hadronization. The cut scheme is applied to the HERMES polarized datasets taken in the years 1996 to 2000. The measurements yield negative double spin asymmetries which already give an indication for a positive gluon polarization.

In Chapter 7, a value for the gluon polarization is extracted from the measured double spin asymmetries in the applicable phase space by extending and rectifying an earlier HERMES publication [96] on this topic. Necessary for the extraction is a Monte Carlo simulation (PYTHIA6) which is employed to retrieve the contribution of the different processes to the hadronic final states at large transverse momenta. The agreement of the Monte Carlo simulation with data is reviewed whereas large benefits result in the improved modeling of the hadronic final state conducted in Chapter 5. By using this model and regarding possible background processes a value for the gluon polarization of:

$$\mathbf{\Delta g/g\,(x_g, \mu^2) = 0.47 \pm 0.21\,(stat) \pm 0.03\,(syst) \pm 0.11\,(model)}\ .$$

at $\langle x_g \rangle = 0.23$ and $\langle \mu^2 \rangle = 2.4\ \mathrm{GeV}^2$ could be extracted. In terms of the employed model, this direct measurement poses a first glimpse at the poorly known gluon polarization in the nucleon. A positive value of the gluon polarization matches nicely with contemporary concepts of the spin structure of the nucleon spin.

Future experiments will continue to unveil the nucleon spin structure. Extended efforts are foreseen to map the polarized gluon distribution. An overview of the anticipated precision on measurements of the gluon polarization by the COMPASS experiment at CERN, the STAR experiment at BNL, the E161 experiment at SLAC, and a study on a polarized TESLA-N fixed target proposal is shown in Figure 8.1. These experiments promise to probe the polarized gluon distribution with very different systematics using photon-gluon fusion of light and charm quarks in lepto- and photoproduction as well as prompt photon and jet production in proton-antiproton collisions. Research on the nucleon spin structure will result in further deep insights of the structure of matter thus remaining one of the most exciting fields of high-energy physics in the next decades.

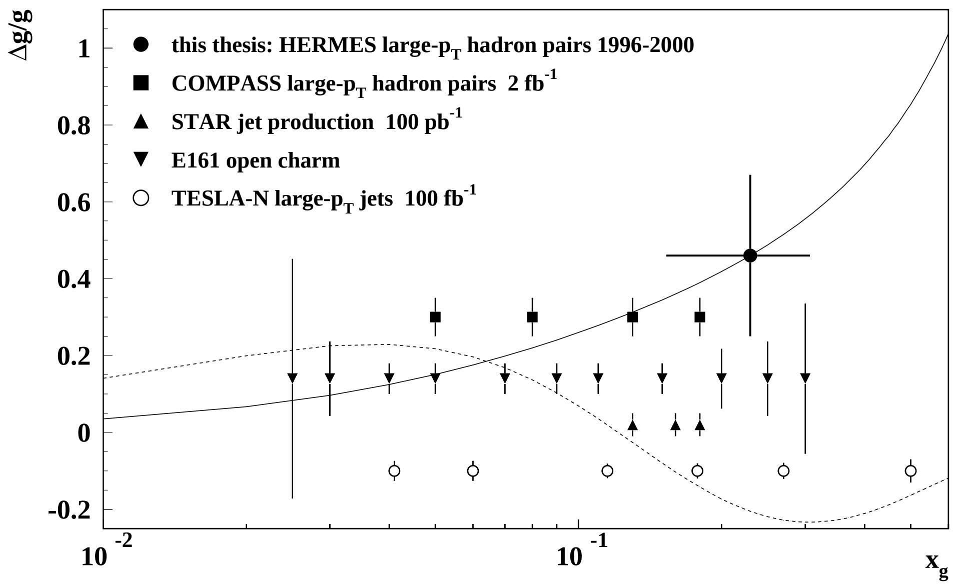

Figure 8.1: The expected statistical precision on $\Delta g/g$ from the future experiments COMPASS [93], STAR [99], E161 [79], and TESLA-N [202] in comparison with the result of this work. For a clear representation, all projected data for future experiments were set to arbitrary values of $\Delta g/g$. The lines display the QCD fits of AAC [56] (solid line) and GS-C [55] (dashed line).

A Appendix: LPOL Calibration and Systematics

A.1 Test Beam Results

The energy dependent response of the NBW calorimeter, with the Ni-foil removed, was measured using electron beams of variable energy at DESY T22 (1-5 GeV) and CERN beamline X5 (5-35 GeV) and turned out to be crucial for the derivation of the analyzing power $\mathcal{A}^{LPOL}$. The *eta-to-y (eta-to-x)* transformation $\zeta_{x,y}$ needed for the position determination of the electromagnetic showers was mapped as well during special test runs. To minimize systematic influences, the same power supply was used with the same settings at both test beams.

A.1.1 Derivation of the Analyzing Power

Since the test setups at CERN and DESY were very similar, only the CERN X5 test setup is described in the following. The CERN X5 beamline supplies electrons from 5 to 68 GeV which are passed through a user-controlled magnet system. Behind the end of the beam pipe a pair of overlapping trigger scintillators was mounted followed by the 16-layer silicon tracker of the COMPASS test experiment. The NBW calorimeter was positioned downstream of the tracker (Fig. A.1). Coincident signals in the trigger scintillators were used to initiate the recording of an event with a HERMES-like data acquisition (see Sect. 3.3.5). In the offline analysis, positions and angles of the incident electrons where reconstructed by a dedicated reconstruction code (CoRe, [203]) which was modified to incorporate the digitized PMT responses of the calorimeter as well. After the alignment of the silicon layers was done by the reconstruction code, events with one particle only were filtered containing tracks with angles no larger than 5μrad with respect to the beam axis. A spatial resolution of 50μm for the track positions at the calorimeter front face was achieved.

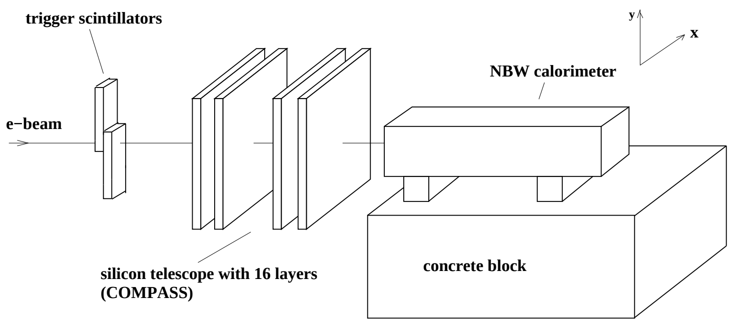

Figure A.1: Perspective view of the test beam setup used at CERN beamline X5.

Corresponding to the average Compton cone size (see Sect. 4.3.2), electrons which hit the innermost part of the calorimeter (less than 3 mm off center) were selected to determine the energy response. The response $r(E_\gamma)$ found (Fig. A.2, left) is slightly non-linear: the calorimeter shows an excess of signal for higher beam energies. The normalization of

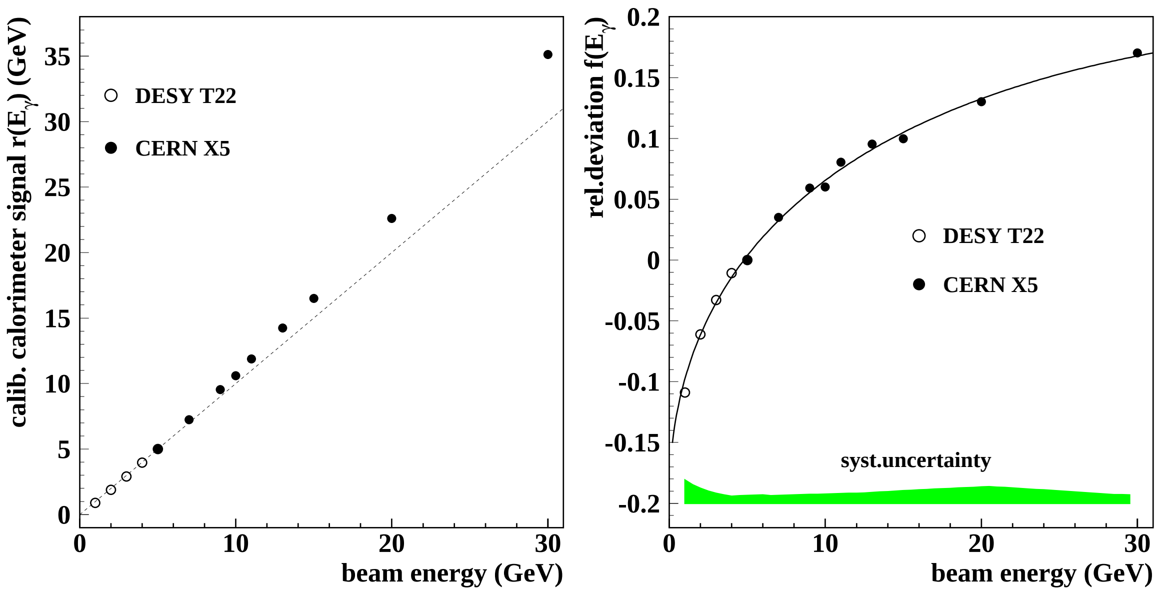

Figure A.2: Left: Energy response of the NBW calorimeter as determined by test measurements at CERN and DESY. The 5 GeV data point is common to both tests and is used as a normalization point for the calorimeter response. The dashed line shows the response of a perfectly linear device. **Right:** fractional deviation from linearity with respect to 5 GeV with a parameterization superimposed. For all data points the statistical uncertainty is smaller than the size of the symbols used for plotting.

the response is chosen such that $r(5\,\mathrm{GeV}) \equiv 5\,\mathrm{GeV}$ since the DESY and CERN test beams overlap at this energy. This choice is arbitrary but anyhow cancels in calculation of the analyzing power. The deviation from linearity $f(E_\gamma) = r(E_\gamma)/E_\gamma - 1$ together with a parameterization is shown in Figure (A.2, right). The functional form used for the parameterization is:

$$f(E_\gamma) = p_1 + p_2 \cdot E_\gamma/\mathrm{GeV} + p_3 \cdot \sqrt{E_\gamma/\mathrm{GeV}}\,. \tag{A.1}$$

A fit yields $p_1 = -0.1955$, $p_2 = -0.0070$ and $p_3 = 0.1047$. The non-linearity $f(E_\gamma)$, together with the found low energy cutoff $E_{min} = 140$ MeV of the calorimeter, inserted into Equation 4.10, leads via Equation 4.11 to the applicable analyzing power of $\mathcal{A}^{LPOL} = -0.1929$. The signal excess at higher electron energies lead to a 5% increase of the analyzing power compared to a perfect setup. If the DESY T22 data is disregarded and only the CERN X5 data are fit, the analyzing power amounts to -0.1926.

Since the test measurements have sufficient statistics, the systematic uncertainty on the analyzing power is driven by systematic effects of the tests. The relative systematic influences on $f(E_\gamma)$ were: the precision of the achieved gain-matching (5%), energy resolution (1.4%) of the test beams, the cross-normalization between the two test beams (0.3%), and a slow time-dependent increase of the overall gain during the CERN test measurements

(Fig. A.3, left). The gain drift was most likely caused by a slow temperature increase of the calorimeter during the 16 hours of continuous test measurements. The gain drift dominates the total the systematic uncertainty which is derived by the quadratic sum of all the effects mentioned above (error band in Fig. A.2, right).

The systematics effect on the analyzing power in the LPOL case $\mathcal{A}^{LPOL}$ is estimated by two extreme parameterizations for $f(E_\gamma)$. These two extreme assumptions f_{min} and f_{max} are found by considering the course of the polarized Compton cross section. The cross sections for the two helicity states cross over at 9.1 GeV (Fig. 4.2) and will be weighted with $f(E_\gamma)$ in the integral of Equation 4.10. Thus, the largest possible analyzing power in this case is caused by a function f_{max} (with functional form of Eq. A.1) running from the lower border of the systematic error band at low energies, through the middle of the band at 9.1 GeV, ending at the higher border at the Compton edge (Fig. A.3, right). The result is $\mathcal{A}^{LPOL}_{max} = -0.1946$. Correspondingly, f_{min} is found giving an analyzing power of $\mathcal{A}^{LPOL}_{min} = -0.1912$. These deviations are taken as conservative estimates for the systematic error yielding $\mathcal{A}^{LPOL} = -0.1929 \pm 0.017$, which corresponds to a relative systematic uncertainty of 0.9%.

After these measurements, which took place in fall 1998, the calorimeter was installed back into the HERA tunnel without a physical change and was operated from 1999 on without the Ni-foil attenuator, exactly as under test conditions. For running in multi-photon operation, the gains of the PMTs were lowered and the laser intensity was reduced to avoid a saturation of the calorimeter response.

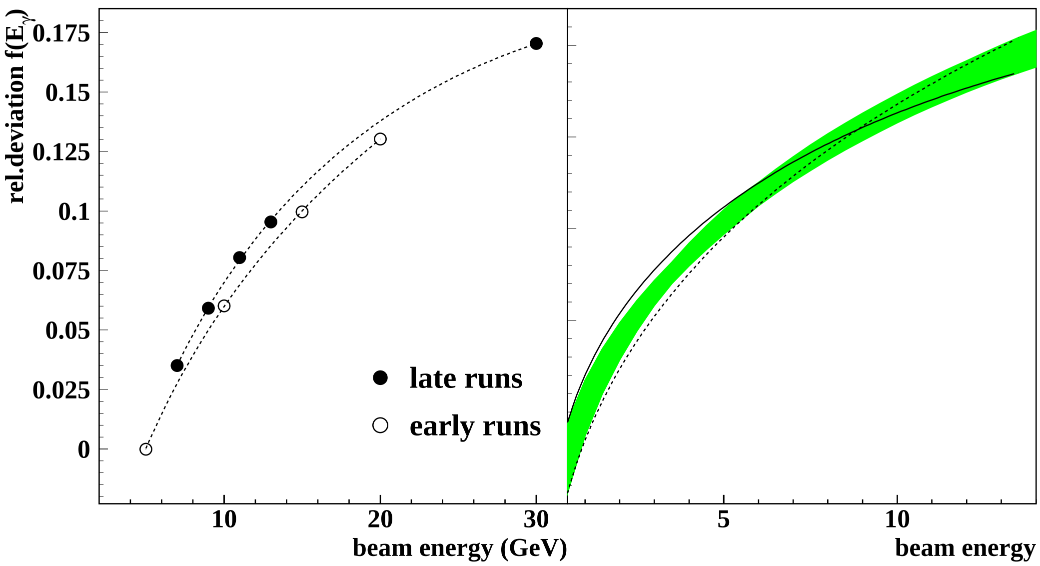

Figure A.3: Left: The CERN X5 dataset split into the first four and the last five runs. **Right**: The systematic uncertainty (grey band) in the relevant energy region. The assumptions for the largest possible analyzing power f_{max} (dashed line) and the smallest possible analyzing power f_{min} (solid line) are shown.

A.1.2 Energy and Spatial Resolution of the NBW Calorimeter

The single particle energy resolution of the NBW calorimeter was measured at the DESY T22 and the CERN X5 test beam and is shown together with the parameterization:

$$\frac{\sigma(E_\gamma)}{E_\gamma} = \frac{(25.9 \pm 0.4)\%}{\sqrt{E_\gamma/\mathrm{GeV}}} \oplus (11.7 \pm 0.1)\% \ , \tag{A.2}$$

in Figure A.4 (left). Also, the eta-to-y and eta-to-x transformations ζ_x and ζ_y were measured in the CERN X5 test beam at a beam energy of 10 GeV using the position information from the silicon tracker (Fig. A.4, right). As expected, $\zeta_x \approx \zeta_y$ was found.

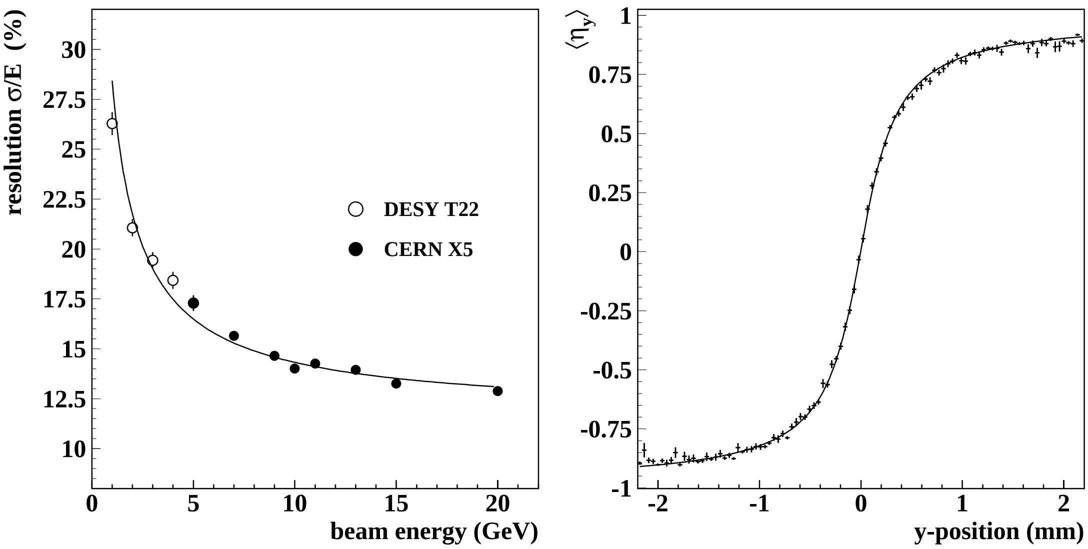

Figure A.4: Left: Measured energy resolution of the NBW calorimeter with a parameterization (Eq. A.2) superimposed. **Right**: The mean spatial asymmetry $\langle\eta_y\rangle$ versus y-position. The data are fit with $\langle\eta_y\rangle = 0.63389 \cdot \mathrm{atan}(3.4902(y/\mathrm{mm}))$. The eta-to-y transformation $\zeta_y = \tan(\langle\eta_y\rangle/0.63389)/3.4902$ is the inverse function to $\langle\eta_y\rangle$.

A.2 Determination of the Systematic Uncertainties

This Section completes the explanations of Section 4.5. It contains the individual measurements used for the determination of the systematic uncertainties on the polarization measurement of the Longitudinal Polarimeter. The effects listed here are the (long-term) stability of the analyzing power, possible helicity dependencies of the laser light transmission or phase space, and the stability of the Compton cone position.

Stability of the Analyzing Power

The analyzing power derived from single particle test beam data can only be applied to multi-photon operation if the needed reduction in amplification of the photo-multipliers does not change the linearity of the device. Hence, the polarization was measured changing the laser intensity and the PMT gain by over two orders of magnitude (Fig. A.5) and was compared to a simultaneous measurement of the Transverse Polarimeter. The resulting ratio is unity within errors. Effects on the analyzing power can be excluded to a level of 0.8%.

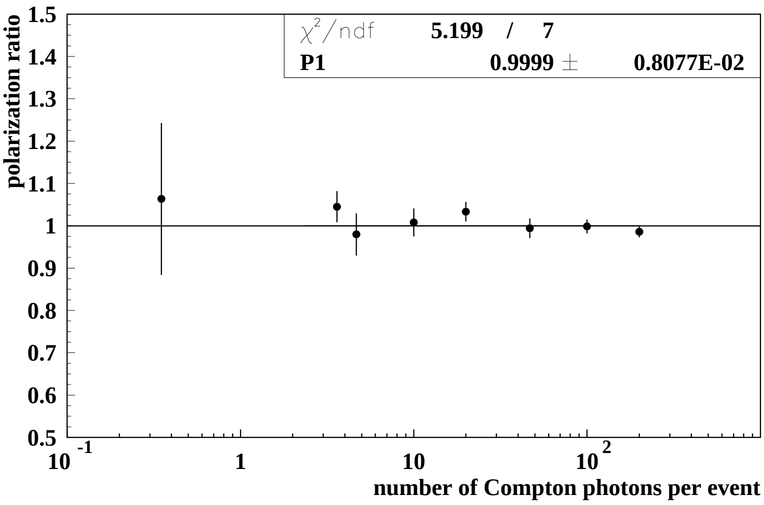

Figure A.5: LPOL polarization measurement relative to the TPOL covering the entire amplification range from single-photon to multi-photon operation. The calibration of the intensity scale in number of Compton photons was achieved by the rates found in the measurement of Figure 4.9 in Section 4.3.3.

The analyzing power could change on large time scales (1 year) due to radiation damage of the NBW crystals or other aging effects. Such an influence could be excluded to 0.5% by comparing the measurement of the NBW calorimeter with the polarization measurement of a TPOL-type sandwich calorimeter at four occasions within a time span of ten months (Fig. A.6, Tab. A.1). During regular operation, the additional sandwich calorimeter was not exposed to the radiation in the beam plane since it was mounted on top of the NBW calorimeter and was moved into the Compton-beam by lowering the mounting table when needed.

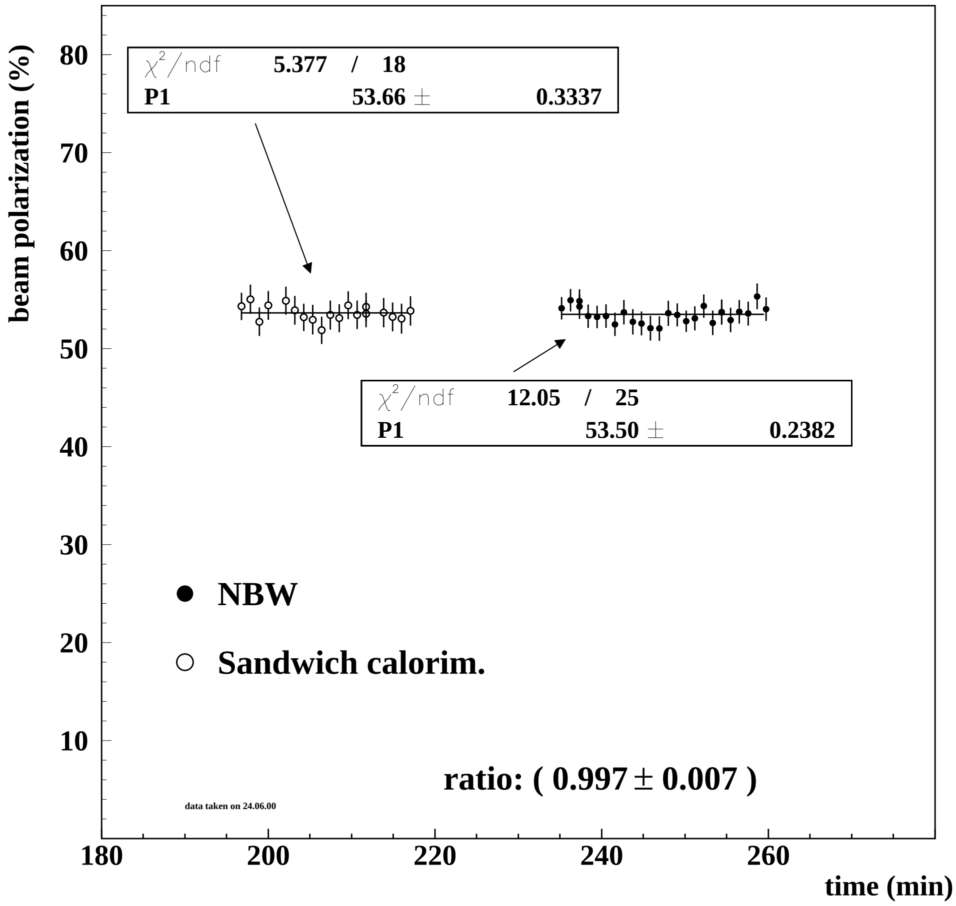

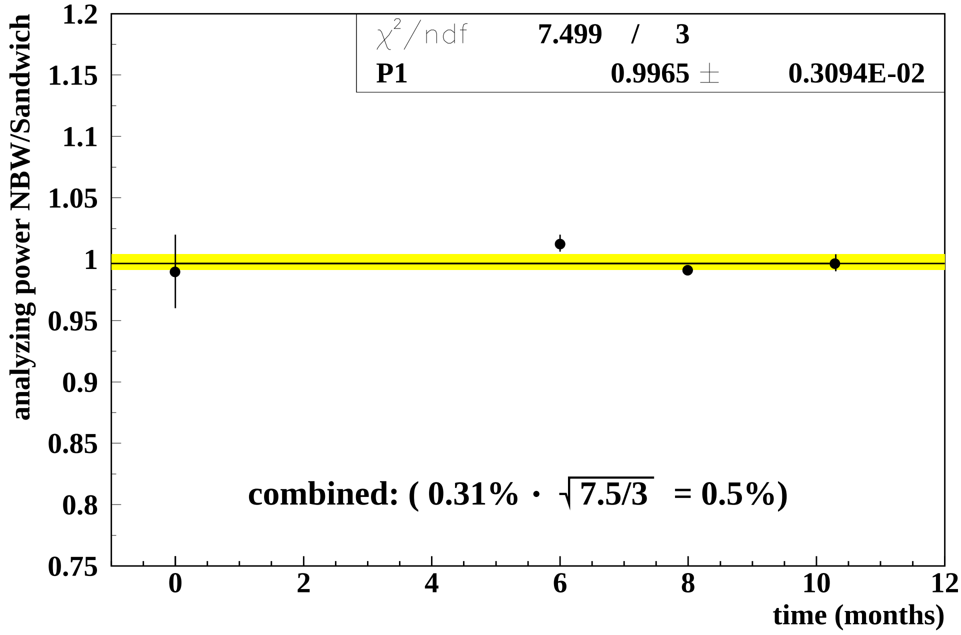

Figure A.6: Top: Example of polarization measurements by the NBW and sandwich calorimeter at stable beam polarization. The gap in the measurement corresponds to the time needed for mechanically switching between the two devices. **Bottom**: Ratios of the polarization measurements using the NBW and sandwich calorimeter versus time.

Table A.1: Ratios of the polarization measurements using the NBW and sandwich calorimeters.

measurement (date)	$P_{NBW}/P_{Sandwich}$
1. (16.8.99)	0.990 ± 0.030
2. (10.2.00)	1.013 ± 0.007
3. (12.4.00)	0.991 ± 0.004
4. (24.6.00)	0.997 ± 0.007
combined ($\chi^2_{ndf} = 2.5$)	0.9965 ± 0.0031

The following studies were done at stable beam polarization to avoid the usage of an extra calorimeter or the division by the TPOL measurement. Possible influences on the polarization measurement were determined by measuring the (stable) beam polarization once at standard conditions and subsequently with the desired test setting. The TPOL measurement was used only to monitor the stability of the beam polarization.

Light Path

Systematic influences coming from the Pockels-cell were excluded to a level of 0.3% by inserting several times a half-wave plate into the light path (Tab. A.2, Fig. A.7) to invert the light helicity. As expected, the measured positron beam polarization changed sign but the magnitude stayed the same. The pointing stability of the optical setup which could lead to a helicity-dependent luminosity was tested by steering the laser beam to the left and right limit of overlap with the positron beam. This was done by changing the x-position of mirror 4 by ±60 steps. No effect was observed within 0.6% (Tab. A.3). Since the normal positron beam drifts require settings within ±30 steps, a maximum influence on the analyzing power of 0.29% could be deduced taking the course of the luminosity as a function of overlap into account.

Table A.2: Study of the polarization ratio with and without a half-wave plate inserted into the light path.

measurement (date)	ratio
1. (29.5.00)	0.9944 ± 0.0053
2. (30.5.00)	1.0061 ± 0.0050
3. (30.5.00)	0.9997 ± 0.0058
total	1.0001 ± 0.0031

Table A.3: Polarization ratios for different horizontal settings of mirror M4.

measurement (date) $\quad M4_x$:	$+60$ steps	-60 steps
1. (26.5.00)	1.008 ± 0.009	0.992 ± 0.009
2. (30.6.00)	0.989 ± 0.008	1.009 ± 0.008
combined	0.999 ± 0.006	1.001 ± 0.006

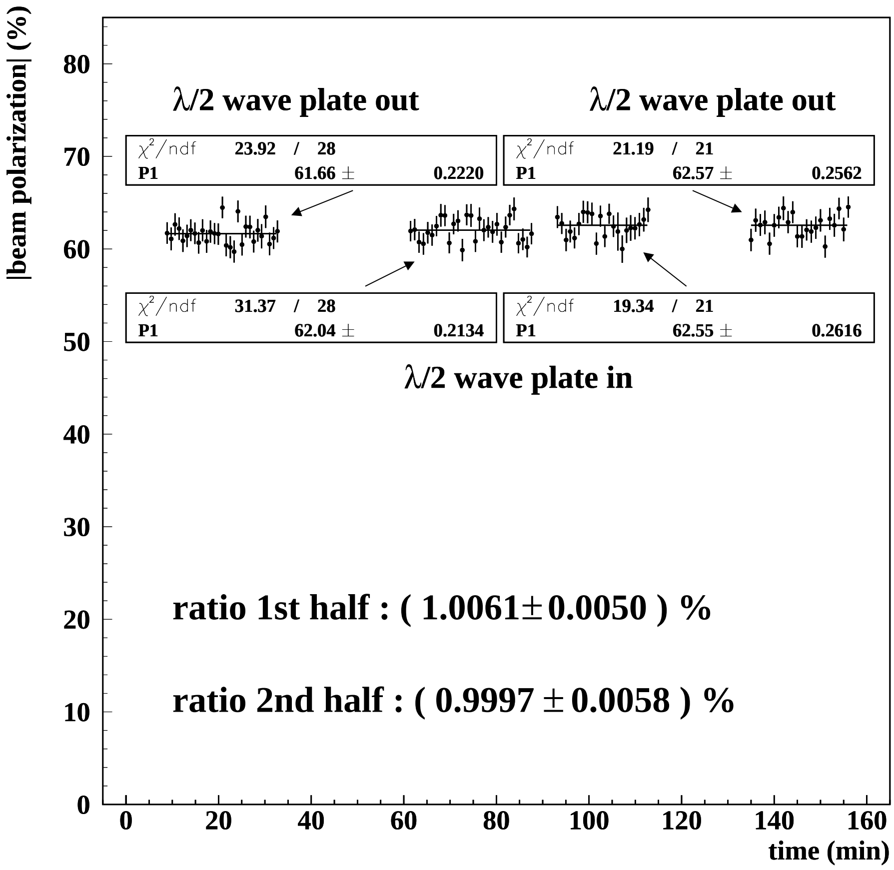

Figure A.7: Example of beam polarization measurements with and without a half-wave plate inserted into the light path. The half-wave plate was inserted between 60 and 111 min.

Compton Cone Stability

The influence of an off-center Compton cone on the calorimeter was studied by moving the calorimeter table at stable beam conditions. Altering the x-position (Tab. A.4, left) within the relevant limits resulted in a maximum of 0.4% systematic bias. In y-direction, the auto-pilot always is able to center the calorimeter better than a millimeter. Studies within these limits yielded an influence of less than 0.46% within the statistical uncertainties (Tab. A.4, right).

Over the course of a fill the horizontal slope of the positron beam at the laser-positron interaction point usually drifts by −0.15 mrad. The influence on the LPOL measurement was estimated by changing the slope two times by about −0.2 mrad. No significant change was noted within 0.5% (Tab. A.5).

Table A.4: Left: Polarization ratios of the x-position study. **Right**: Study for different y-positions. The data were taken on 30.06.00/01.07.00.

x-position	ratio
$+3$mm	1.004 ± 0.007
-3mm	0.990 ± 0.008
$+5$mm	0.997 ± 0.007
combined	0.997 ± 0.004

y-position	ratio
$+1$mm	0.9977 ± 0.0065
-1mm	0.9973 ± 0.0064
combined	0.9975 ± 0.0046

Table A.5: Polarization ratios of the LPOL with changed/unchanged horizontal positron beam slope.

measurement (date)	horizontal beam slope	polarization ratio (rel.to 0 mrad)
1. (27.5.00)	-0.19 mrad	1.009 ± 0.007
2. (01.7.00)	-0.20 mrad	0.993 ± 0.007
combined		1.001 ± 0.005

B Appendix: Settings of the Monte Carlo Simulations

B.1 LEPTO Settings

B.1.1 gmc_disNG

```
macro gmcrun name=gmc seed1=21764356 seed2=78123445 events=1
kuip/set_show/filecase keep

name EVEN [name].pipe WPIP      : Output: primary events to pipe
name NORM [name].norm.kumac !   : Output: normalization info
name HBOO [name].hbook !        : Output: HBOOK file
name TARG hmc.targ !            : Input: target density histogram
name SELE hmc.select !          : Input: selector file (NOT USED)
name CARD tunecard.ffr !        : Input: LEPTO & JETSET data card
Set RunNo           1                 : run number always set to one
Set Generator       DIS               : select generator
Set bStop           NO                : stop on error
Set TarA            1                 : target atomic number
Set TarZ            1                 : target charge
Set EneBeam         27.57             : beam energy (GeV)
Set PBValue         0.                : beam polarization
Set PTValue         0.                : targ polarization
Set VerPosX         0.                : x-position of vtx (cm)
Set VerPosY         0.                : y-position of vtx (cm)
Set VerPosZ         0.                : z-position of vtx (cm)
Set VerSizX         0.                : width in x of vtx distrib (cm)
Set VerSizY         0.                : width in y of vtx distrib (cm)
Set VerSizZ         40.               : length in z of vtx distrib (cm)
Set VerPrecision    0.01              : min separation for new vtx (cm)
Set BeamParType     POSI              : beam particle type = positron
Set PBeam           L                 : longitudinal beam polarization
Set PTarget         L                 : longitudinal target polarization
Set VerLon          DIST              : type of longit.vtx distrib
Set VerTra          GAUS              : type of transv.vtx distrib
Set iPrint          10000             : info line every iPrint events
Set ListInit        NO                : list initialization steps
Set ListEvent       NO                : list event processing steps
Set PriInit         NO                : print detailed initialization info
Set PriEvent        NO                : print detailed event info
Set Q2Min           0.025             : min Q2
Set Q2Max           48.64             : max Q2
Set NuMin           1.37              : min nu (energy transfer)
Set NuMax           24.82             : max nu (energy transfer)
Set W2Min           0.9               : min W2
```

```
Set W2Max           49.52              : max W2
Set XMin            0.01               : min x Bjorken
Set XMax            0.99               : max x Bjorken
Set YMin            0.05               : min y (nu/Ebeam)
Set YMax            0.90               : max y (nu/Ebeam)
Set Pmin            0.00               : min momentum
Set Pmax            27.57              : max momentum
Set TheMin          0.039              : min theta
Set TheMax          0.3                : max theta
Set TheXMin         0.0                : min theta_x
Set TheXMax         0.193              : max theta_x
Set TheYMin         0.039              : min theta_y
Set TheYMax         0.15               : max theta_y
Set CutVertex       YES                : apply cuts on vertex kinematics
Set CutScat         YES                : apply track cuts to scat lepton
Set UseSelector     NO                 : no selector
Set UseCards        YES                : read in FFREAD cards
Set wOutput         YES                : write events into output file
Set wHBOOK          NO                 : write user-defined HBOOK objects to file
Set bValid          YES                : mcSet table on GAF is valid
Set GenKine         1                  : select kinematics flat in Nu,log(Q2)
Set PartonSet       150                : PDF set CTEQ5=150
Set MaxSeaFl        3                  : heaviest sea flavour (LST(12))
Set MaxFusFl        3                  : heaviest PGF flavour (LST(13))
Set Shower          1                  : parton showers (LST(8))
Set LepQ2Min        1.0                : Q2 minimum for PEPSI/LEPTO (CUT(5))
Set LepW2Min        4.0                : W2 low cut for PEPSI/LEPTO (CUT(7))
Set GenRad          POL                : radiative effects (NO,YES,POL)
Set PA1asym         A1EX               : parametrization of asymmetry A1(x,Q2)
Set FStruct         ALLM               : structure function parametrization
Set R               1990               : param. of R=sL/sT (1990, 1998 or 0 for R=0)
Set GenHadrons      YES                : generate hadrons with Lund program
Set GenLUT          NO                 : generate LUT for pol. rad. corr.
Set UseLUT          YES                : use LUT for pol. rad. corr.
Set DecayPiK        NO                 : Have Lund decay charged pi,K and K0_L?
Set DecayLamKs      YES                : Have Lund decay Lambda,Sigma,Xi,Omega,K0_S?
Set PriQCDW         NO                 : print prob for q, qg, qqg events after
init
MC/RESET [seed1] [seed2]
ev [events]
exit
```

B.1.2 FF-Card File

```
LIST
C   choice of generation variables, generation, and cut scheme
LST    1=1
LST    2=2
C   output and error handling
LST    3=1
C   choice of frame and lepton scattering plane
LST    5=3
LST    6=0
C   ME for DIS,PGF, and QCDC
LST    8=1
C   numerical integration of xsec in LINIT
LST   10=1
C   inclusion of F_L, target mass, and higher twist
LST   11=0
C   max number of sea quark and PGF flavours (no charm!)
LST   12=3
LST   13=3
C   treatment of target remnant
LST   14=4
C   running of EM coupling alpha
LST   18=2
C   use suitable grid to store probabilities for qg and qqbar
LST   19=1
C   use JADE scheme for cutoffs against divergences
LST   20=1
C   switch for soft colour interaction
LST   34=2
C   turn on new sea quark treatment
LST   35=1
C   Gaussian width of primordial k_t
PARL   3= see Table 5.3 in Chapter 5
C   sin(theta_W)
PARL   5=0.2294
C   cutoffs against divergencies in first order QCD ME
PARL   8=0.005
PARL   9=2.0
C   width of Gaussian distribution for the virtuality of sea quarks
PARL  10=0.44
C   no intrinsic charm in the proton
PARL  12=0.
C   width of Gaussian distribution in transverse momentum
```

```
C   when a non-trivial target remnant is split into two particles
PARL  14=0.35
C   diquark suppression P(qq)/P(q)
PARJ   1= see Table 5.3 in Chapter 5
C   strange quark suppression P(s)/P(u)
PARJ   2= see Table 5.3 in Chapter 5
C   suppression of BMBbar to BBbar in popcorn model
PARJ   5= see Table 5.3 in Chapter 5
C   suppression of BMBbar to BBbar Bstrange
PARJ   6= see Table 5.3 in Chapter 5
C   suppression of BMBbar to BBbar Mstrange
PARJ   7= see Table 5.3 in Chapter 5
C   amount of extra tail in pt
PARJ   23= see Table 5.3 in Chapter 5
C   corresponding width of extra tail
PARJ   24= see Table 5.3 in Chapter 5
C   minimum allowable energy for colour-singlet jet system
PARJ   32=1.0
C   minimum energy used to stop fragmenting a jet
PARJ   33= see Table 5.3 in Chapter 5
C   width of transverse momentum distribution
PARJ   21= see Table 5.3 in Chapter 5
C   a parameter for symmetric Lund fragmentation function
PARJ   41= see Table 5.3 in Chapter 5
C   b parameter for symmetric Lund fragmentation function
PARJ   42= see Table 5.3 in Chapter 5
C   a=PARJ(41)+PARJ(45) for baryons
PARJ   45=0.5
C   choose LUND string fragmentation
MSTJ   1=1
C   baryon production model: popcorn
MSTJ   12=2
C   no Bose-Einstein effects
MSTJ   51=0
C   number of flavours assumed in alpha_s expression
MSTU   112=3
MSTU   113=3
MSTU   114=3
MSTU   115=0
C   sin(theta_W)
PARU 102=0.2294
C   selection of minimum invariant mass of hadronic system
PARP 111=0.0
STOP
```

B.2 PYTHIA Settings

B.2.1 gmc_pythia6

```
kuip/set_show/filecase keep
base = pyT6
name EVEN [base]_[run].devents.gz WFIL   : Output: Primary events GAF
name NORM [base]_[run].norm.kumac !      : Output: normalization info
name HBOO [base]_[run].hbook !           : Output: HBOOK file
name TARG hmc.targ !                     : Input: target density histogram
name SELE 2had.minv !                    : Input: selector file
name CARD pyt.W2MOD.ffr !                : Input: PYTHIA/JETSET data card
Set RunNo             1         : run number
Set Generator         PYTH      : select generator
Set bStop             NO        : do not stop on error
Set TarA              1         : target atomic number
Set TarZ              1         : target charge  (=0 for neutron!)
Set EneBeam           27.57     : beam energy (GeV)
Set PBValue           0.        : beam polarization
Set PTValue           0.        : targ polarization
Set VerPosX           0.        : x-position of vtx (cm)
Set VerPosY           0.        : y-position of vtx (cm)
Set VerPosZ           0.        : z-position of vtx (cm)
Set VerSizX           0.        : width in x of vtx distrib (cm)
Set VerSizY           0.        : width in y of vtx distrib (cm)
Set VerSizZ           40.       : length in z of vtx distrib (cm)
Set VerPrecision      0.01      : min separation for new vtx (cm)
Set BeamParType       POSI      : beam particle type = positron
Set PBeam             L         : longitudinal beam polarization
Set PTarget           L         : longitudinal target polarization
Set VerLon            DIST      : type of longit.vtx distrib
Set VerTra            GAUS      : type of transv.vtx distrib
Set iPrint            1000      : info line every iPrint events
Set ListInit          NO        : list initialization steps
Set ListEvent         NO        : list event processing steps
Set PriInit           NO        : print detailed initialization info
Set PriEvent          NO        : print detailed event info
Set Q2Min             0.0       : min Q2
Set Q2Max             60.0      : max Q2
Set NuMin             0.        : min nu (energy transfer)
Set NuMax             27.57     : max nu (energy transfer)
Set W2Min             10.0      : min W2
Set W2Max             500.      : max W2
Set XMin              0.        : min x Bjorken
Set XMax              1.        : max x Bjorken
```

```
Set YMin              0.        : min y (nu/Ebeam)
Set YMax              1.        : max y (nu/Ebeam)
Set Pmin              0.        : min momentum
Set Pmax              27.57     : max momentum
Set TheMin            0.037     : min theta
Set TheMax            0.3       : max theta
Set TheXMin           0.0       : min theta_x
Set TheXMax           0.192     : max theta_x
Set TheYMin           0.040     : min theta_y
Set TheYMax           0.148     : max theta_y
Set CutVertex         YES       : apply cuts on vertex kinematics
Set CutScat           NO        : apply track cuts to scat lepton
Set UseSelector       YES       : apply selector file
Set UseCards          YES       : read in FF-card file
Set wOutput           YES       : write events into output file
Set wHBOOK            NO        : no not write user-defined HBOOK file
Set bValid            YES       : mcSet table on GAF is valid
Set PyModel           ALL       : include DIS and Photoproduction
Set PhotoStruc        30        : photon structure parameter (MSTP(14))
Set PhotoType         0         : photoproduction generation type
Set Pyphocontr        2         : user control switch (MSEL, 9.2.)
Set PyMaxFl           3         : max flavour
Set PartonSet         4041      : PDF set for PYTHIA
Set PyMhatMin         0.0       : min sqrt(s_hat) in PYTHIA (CKIN(1))
Set PyPtMin           1.00      : pt min for singular proc (CKIN(5,6))
Set DecayPiK          NO        : Have Lund decay charged pi,K and K0_L?
Set DecayLamKs        YES       : Have Lund decay Lambda,Sigma,Xi,Omega,K0_S?
init
MC/RESET 12345678 23456780
ev 100000
exit
```

The settings above were used together with the following track selector (2had.minv):

```
!
! selector file for two hadron tracks with m_inv>1 GeV
!
! HERMES acceptance with momentum cut
-1  0.0 0.192 0.040 0.148 4.0 1000.0
!
! two hadrons in the acceptance
1 ***** 2 -1 lund
!
! hh pair with m_inv>1 GeV
0 MSYS 1 1. 1000. 1 0.13957 1 0.13957
```

B.2.2 FF-Card File

PYTHIA6 was used with the fragmentation settings of the high-W^2 fit (Tab. 5.3, Sect. 5.3.1).

```
LIST
C   trap all errors
MSTU   21=2
C   select incolved processes  (2: lN interaction)
MSEL 1=2
C   alpha_s calculation according to first order QCD
MSTP   2=1
C   take lambda_QCD corresponding to chosen parton set
MSTP   3=2
C   running alpha_em, theta_w fixed
MSTP   8=0
C   initial state bremsstahlung OFF
MSTP   11=0
C   selection of 2 range over which electrons are assumed to radiate photons
MSTP   13=2
C   photon structure: all proc. DIS/direct/VMD/anormalous
MSTP   14=30
C   regulation of pt_min treatment for anomalous/VMD
MSTP   15=5
C   use y as photon fractional energy
MSTP   16=1
C   no extra factor for resolved processes from long.photons
MSTP   17=0
C   x,Q2 NOT forced to be real x and real Q2
MSTP   23=0
C   use best literature for total elastic and diffractive cross sections
MSTP   31=1
C   selection  of hard scattering scale
MSTP   32=8
C   no K factors is hard processes in parton/parton interactions
MSTP   33=0
C   interference terms in QCD processes ON
MSTP   34=1
C   threshold setting of heavy flavour production
MSTP   35=0
C   resonance decays ON
MSTP   41=1
C   masses generated according to Breit-Wiegner
MSTP   42=1
C   neglect Z^0
MSTP   43=1
```

```
MSTP   44=1
C   CTEQ4lowQ2 proton parton distribution: genSet_PartonSet
MSTP   51=4041
C   use pdflib see MSTP(51)
MSTP   52=2
C   set pion parton distribution to GRV LO
MSTP   53=3
C   use internal pythia see MSTP(53)
MSTP   54=1
C   PDF set of the Photon to be SaS 1D in DIS scheme
MSTP   55=5
C   use internal pythia see MSTP(55)
MSTP   56=1
C   use Q2 dependence as parameterized in PDFs
MSTP   57=1
C   extension of real photon PDF to virt.photons
MSTP   60=7
C   master switch QCD and QED ISR is set to OFF
MSTP   61=0
C   master switch QCD and QED FSR is set to OFF
MSTP   71=0
C   multiple interactions OFF
MSTP   81=1
MSTP   82=1
C   switch primordial p_t in the hadrons to be Gaussian
MSTP   91=1
C   switch primordial p_t in the photon to be Gaussian
MSTP   93=1
C   hadron remnant treatment
MSTP   94=3
C   select structure of diffractive systems
MSTP   101=3
C   select decay kinematics of the rho
MSTP   102=1
C   LUND fragmentation ON
MSTP   111=1
C   cuts on partonic events (string cuts)
MSTP   112=1
C   intermediate mass/energy calculations ON
MSTP   113=1
C   NO colour reconnection
MSTP   115=0
C   raise maximum is too large xsec value found
MSTP   123=2
```

```
C   frame as selected by PYINIT
MSTP   124=1
C   list short summary of hard process
MSTP   125=1
C   no NOT call PYKCUT
MSTP   141=0
C   do NOT call event weighting procedure
MSTP   142=0
C   do NOT smear vertex
MSTP   151=0
C   NO variable energies from event to event
MSTP   171=0
MSTP   172=2
C   NO user weight
MSTP   173=0
C   min CMS energy allowed for event as a whole (GeV)
PARP   2=0.0
C   max Q2 scale allowed for photoproduction
PARP   13=1.0
C   numerical precision
PARP   14=0.01
C   intrinsic kT of initial state partons in the nucleon
PARP   91= see Table 5.3 in Chapter 5 corresponding to PARL(3)
C   intrinsic kT cutoff of five sigma
PARP   93=5.
C   intrinsic kT of initial state partons in the photon
PARP   99= see Table 5.3 in Chapter 5 corresponding to PARL(3)
C   intrinsic kT cutoff of five sigma
PARP   100=5.
C   diquark suppression P(qq)/P(q)
PARJ   1= see Table 5.3 in Chapter 5
C   strange quark suppression P(s)/P(u)
PARJ   2= see Table 5.3 in Chapter 5
C   suppression of BMBbar to BBbar in popcorn model
PARJ   5= see Table 5.3 in Chapter 5
C   suppression of BMBbar to BBbar Bstrange
PARJ   6= see Table 5.3 in Chapter 5
C   suppression of BMBbar to BBbar Mstrange
PARJ   7= see Table 5.3 in Chapter 5
C   amount of extra tail in pt
PARJ   23= see Table 5.3 in Chapter 5
C   corresponding width of extra tail
PARJ   24= see Table 5.3 in Chapter 5
C   minimum allowable energy for colour-singlet jet system
```

```
PARJ   32=1.0
C   minimum energy used to stop fragmenting a jet
PARJ   33= see Table 5.3 in Chapter 5
C   width of transverse momentum distribution
PARJ   21= see Table 5.3 in Chapter 5
C   a parameter for symmetric Lund fragmentation function
PARJ   41= see Table 5.3 in Chapter 5
C   b parameter for symmetric Lund fragmentation function
PARJ   42= see Table 5.3 in Chapter 5
C   a=PARJ(41)+PARJ(45) for baryons
PARJ   45=0.5
C   choose LUND string fragmentation
MSTJ   1=1
C   use std.LUND fragmentation function
MSTJ   11=1
C   conserve flavour and momentum
MSTJ   3=0
C   baryon production model: popcorn
MSTJ   12=2
C   switch parton showers OFF
MSTJ   41=0
C   selection of minimum invariant mass of hadronic system
PARP 111=0.0
C    range of m^ = sqrt(s^)     0-infinity
CKIN    1=0.0
CKIN    2=-1.
C    range of p^_t (DIS = Q^2)  0-infinity
CKIN    3=0.0
CKIN    4=-1.
C p^_t,min for singular processes in limit p^_t -> 0 (in GeV)
CKIN    5=1.00
STOP
```

C Appendix: Tables of Results

C.1 Double Spin Asymmetries

C.1.1 Standard Analysis

Table C.6: Results on $A_{\parallel}$ from the standard analysis together with the observed counts per spin state $N^{\pm}$ and the average $p_{\perp}^{min}$ for each bin. **Left:** 1996 dataset. **Right:** 1997 dataset.

bin	$\langle p_{\perp}^{min} \rangle$	N^+	N^-	$A_{\parallel}$
1	0.65	107	89	0.237 ± 0.182
2	0.89	45	41	0.121 ± 0.276
3	1.09	23	35	-0.528 ± 0.329
4	1.34	14	27	-0.809 ± 0.379
5	1.62	5	6	-0.231 ± 0.768

$\langle p_{\perp}^{min} \rangle$	N^+	N^-	$A_{\parallel}$
0.65	244	238	0.025 ± 0.099
0.89	116	119	-0.030 ± 0.142
1.09	61	82	-0.321 ± 0.180
1.34	46	45	0.022 ± 0.228
1.55	8	14	-0.595 ± 0.446

Table C.7: Results on $A_{\parallel}$ from the standard analysis together with the observed counts per spin state $N^{\pm}$ and the average $p_{\perp}^{min}$ for each bin. **Left:** 1998 dataset. **Right:** 1999 dataset.

bin	$\langle p_{\perp}^{min} \rangle$	N^+	N^-	$A_{\parallel}$
1	0.64	185	172	0.102 ± 0.116
2	0.90	86	91	-0.040 ± 0.165
3	1.09	45	48	-0.049 ± 0.228
4	1.33	39	41	-0.033 ± 0.246
5	1.61	10	8	0.266 ± 0.512

$\langle p_{\perp}^{min} \rangle$	N^+	N^-	$A_{\parallel}$
0.64	196	223	-0.138 ± 0.101
0.89	94	84	0.112 ± 0.155
1.09	48	55	-0.146 ± 0.204
1.34	37	43	-0.160 ± 0.231
1.58	6	6	-0.005 ± 0.599

Table C.8: Results on $A_{\parallel}$ from the standard analysis of the 2000 dataset together with the observed counts per spin state $N^{\pm}$ and the average $p_{\perp}^{min}$ for each bin.

bin	$\langle p_{\perp}^{min} \rangle$	N^+	N^-	$A_{\parallel}$
1	0.64	981	1034	-0.061 ± 0.046
2	0.89	462	436	0.053 ± 0.069
3	1.09	266	280	-0.059 ± 0.088
4	1.33	202	230	-0.140 ± 0.099
5	1.60	52	51	0.013 ± 0.202

C.1.2 New Analysis

Table C.9: Results on $A_{\shortparallel}$ from the new analysis together with the observed counts per spin state $N^{\pm}$ and the average p'_T for each bin. **Left:** 1996 dataset. **Right:** 1997 dataset.

bin	$\langle p'_T \rangle$	N^+	N^-	$A_{\shortparallel}$
1	0.70	37	35	0.073 ± 0.301
2	0.99	152	135	0.153 ± 0.151
3	1.25	22	23	-0.055 ± 0.381
4	1.35	14	21	-0.510 ± 0.424
5	1.53	15	26	-0.685 ± 0.385

$\langle p'_T \rangle$	N^+	N^-	$A_{\shortparallel}$
0.69	125	122	0.025 ± 0.138
0.99	333	335	-0.008 ± 0.084
1.25	58	67	-0.158 ± 0.194
1.34	43	43	-0.002 ± 0.235
1.52	49	64	-0.290 ± 0.203

Table C.10: Results on $A_{\shortparallel}$ from the new analysis together with the observed counts per spin state $N^{\pm}$ and the average p'_T for each bin. **Left:** 1998 dataset. **Right:** 1999 dataset.

bin no.	$\langle p'_T \rangle$	N^+	N^-	$A_{\shortparallel}$
1	0.68	106	100	0.086 ± 0.153
2	0.99	252	242	0.066 ± 0.099
3	1.24	40	38	0.078 ± 0.248
4	1.35	25	38	-0.433 ± 0.273
5	1.53	47	48	-0.001 ± 0.225

$\langle p'_T \rangle$	N^+	N^-	$A_{\shortparallel}$
0.68	95	107	-0.128 ± 0.146
0.99	268	274	-0.028 ± 0.089
1.25	43	43	-0.005 ± 0.224
1.34	29	39	-0.310 ± 0.249
1.51	46	44	0.042 ± 0.219

Table C.11: Results on $A_{\shortparallel}$ from the new analysis of the 2000 dataset together with the observed counts per spin state $N^{\pm}$ and the average p'_T for each bin.

bin	$\langle p'_T \rangle$	N^+	N^-	$A_{\shortparallel}$
1	0.68	586	569	0.024 ± 0.060
2	0.99	1377	1362	0.005 ± 0.039
3	1.25	226	234	-0.042 ± 0.096
4	1.35	167	181	-0.089 ± 0.110
5	1.53	240	256	-0.073 ± 0.092

C.1.3 Comparison with Published HERMES Data

A comparison between the asymmetries found by the *standard analysis* defined in this thesis and the published HERMES data from 1999-1997 is shown in Figure C.8. The small visible differences can be accounted for by the following changes in the standard analysis compared to the published analysis:

- The standard analysis uses a more recent burst-level data quality for 1996 which supersedes the one used for the publication. The re-analysis of the target performance contributes strongly to the differences in data quality selection [204].
- The analysis of the publication does not require the two hadrons to be in different detector halves. This influences the statistics below $p_{\perp}^{min} = 1.0$ GeV.
- Different particle identification cuts were used. The published analysis identifies a hadron via $PID_{35} < -2$ and positrons via $PID_{35} > 0$ (to be compared to Sect. 6.3.2).
- A momentum cut for all hadrons of $p > 4.5$ GeV is imposed for the publication as opposed to $p > 4.0$ GeV in the standard analysis defined here.
- The analysis of the publication does not require $\sum_i p_i < 28$ GeV for an event.

These conditions alter the number of collected events for $p_{\perp}^{min} > 1.0$ GeV by three events total. When the listed conditions were adapted, the published results were reproduced.

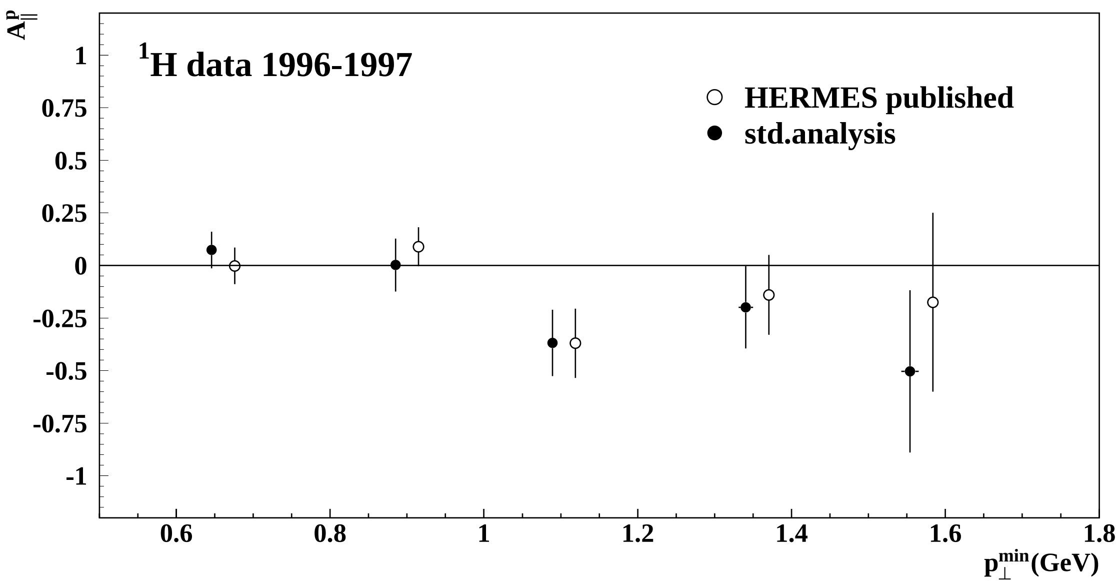

Figure C.8: The double spin asymmetries at large transverse hadron momenta for 1996-1997 (^{1}H-target). The *standard analysis* defined in this thesis is compared to the published HERMES data [96]. The $p_{\perp}^{min}$ values of the published data are shifted to allow a clear representation.

C.2 Interpretation with PYTHIA6

C.2.1 Process Fractions and Background Asymmetries

Table C.12: Left: The PGF process fractions and the corresponding average kinematic variables for a hydrogen target. **Right**: The process fractions for elastic and diffractive vector meson production as well as the fractions for anomalous photon processes. These results were obtained by a PYTHIA6 simulation for a hydrogen target.

bin	$\langle p'_T \rangle$	$\langle D \rangle$	$\langle x_g \rangle$	$\langle \hat{p}_T^2 \rangle$	f_{PGF}
1	0.69	0.95	0.20	1.8	0.156
2	0.97	0.94	0.20	1.9	0.171
3	1.25	0.94	0.22	2.1	0.229
4	1.35	0.95	0.23	2.3	0.263
5	1.51	0.97	0.26	2.8	0.230

$f_{VM,elas}$	$f_{VM,diff}$	f_{anom}
0.008	0.130	0.492
0.001	0.105	0.577
0.008	0.122	0.551
0.006	0.183	0.494
0.069	0.266	0.354

Table C.13: The process fractions and asymmetries together with the corresponding average kinematic variables for DIS (**left**) and QCD Compton processes (**right**) for a hydrogen target.

bin	$\langle p'_T \rangle$	$\langle D \rangle$	$\langle x \rangle$	$\langle Q^2 \rangle$	A_{DIS}	f_{DIS}
1	0.69	0.84	0.17	6.9	0.023	0.117
2	0.98	0.85	0.10	4.3	0.005	0.043
3	1.25	0.83	0.04	1.7	0.002	0.024
4	1.35	0.87	0.04	1.6	0.001	0.017
5	1.51	0.93	0.02	1.0	0.002	0.047

$\langle D \rangle$	$\langle x \rangle$	$\langle \hat{p}_T^2 \rangle$	A_{QCDC}	f_{QCDC}
0.85	0.003	2.0	0.0013	0.097
0.86	0.003	1.8	0.0011	0.103
0.84	0.003	2.1	0.0002	0.065
0.84	0.003	1.9	0.0001	0.036
0.89	0.004	2.5	0.0001	0.035

Table C.14: Left: The PGF process fractions and the corresponding average kinematic variables for a deuterium target. **Right**: The process fractions for elastic and diffractive vector meson production as well as the fractions for anomalous photon processes. These results were obtained by PYTHIA6 simulations for a proton and a neutron target combined.

bin	$\langle p'_T \rangle$	$\langle D \rangle$	$\langle x_g \rangle$	$\langle \hat{p}_T^2 \rangle$	f_{PGF}
1	0.69	0.95	0.20	1.8	0.157
2	0.98	0.94	0.20	1.9	0.173
3	1.24	0.94	0.22	2.2	0.251
4	1.35	0.95	0.23	2.3	0.248
5	1.52	0.97	0.25	2.7	0.224

$f_{VM,elas}$	$f_{VM,diff}$	f_{anom}
0.010	0.148	0.489
0.002	0.109	0.569
0.007	0.128	0.525
0.022	0.186	0.496
0.065	0.253	0.385

Table C.15: The process fractions and asymmetries together with the corresponding average kinematic variables for DIS (**left**) and QCD Compton processes (**right**) for a deuterium target.

bin	$\langle p'_T \rangle$	$\langle D \rangle$	$\langle x \rangle$	$\langle Q^2 \rangle$	A_{DIS}	f_{DIS}
1	0.69	0.83	0.15	6.0	0.020	0.116
2	0.98	0.81	0.09	3.7	0.005	0.044
3	1.24	0.86	0.08	3.3	0.003	0.032
4	1.35	0.91	0.02	1.9	0.001	0.020
5	1.52	0.93	0.03	1.0	0.002	0.042

$\langle D \rangle$	$\langle x \rangle$	$\langle \hat{p}_T^2 \rangle$	A_{QCDC}	f_{QCDC}
0.86	0.003	2.0	0.0008	0.080
0.85	0.003	1.8	0.0001	0.102
0.88	0.003	1.9	0.0002	0.057
0.87	0.004	2.2	0.0004	0.029
0.91	0.003	2.0	0.0005	0.031

C.2.2 Extracted Gluon Polarization

Table C.16: Extracted gluon polarization (new analysis) for each p'_T-bin using the measured double spin asymmetries tabulated in Section C.1.2 and the process fractions listed in the previous Section. The extracted gluon polarizations are given for the datasets on hydrogen (**left**) and deuterium (**right**) targets.

bin	$\langle p'_T \rangle$	$\Delta g/g$
1	0.70	-0.061 ± 0.851
2	0.99	-0.146 ± 0.455
3	1.24	0.641 ± 0.799
4	1.34	0.488 ± 0.821
5	1.51	1.696 ± 0.804

bin	$\langle p'_T \rangle$	$\Delta g/g$
1	0.70	0.057 ± 0.380
2	0.98	-0.012 ± 0.223
3	1.24	0.123 ± 0.379
4	1.34	0.746 ± 0.432
5	1.51	0.258 ± 0.396

Table C.17: Extracted gluon polarization (new analysis) for each p'_T-bin combined from the values on hydrogen and deuterium targets from the previous two tables.

bin	$\langle p'_T \rangle$	$\Delta g/g$
1	0.70	0.037 ± 0.347
2	0.98	-0.038 ± 0.200
3	1.24	0.218 ± 0.342
4	1.34	0.690 ± 0.382
5	1.51	0.540 ± 0.355

Bibliography

[1] D.M.Dennison, *A Note on the Specific Heat of the Hydrogen Molecule*, Proc.Roy.Soc. **A115** (1927) 483.

[2] W.Kapuscinski, J.G.Eymers, *Intensity Measurements in the Secondary Spectrum of Hydrogen*, Proc.Roy.Soc. **A122** (1929) 58.

[3] J.Ashman *et al.*, *A Measurement of the Spin Asymmetry and Determination of the Structure Function g_1 in Deep Inelastic Muon-Proton Scattering*, Phys.Lett. **B206** (1988) 364.

[4] T.Sloan *et al.*, *The Quark Structure of the Nucleon from the CERN Muon Experiments*, Phys.Rep. **162** (1988) 45.

[5] F.E.Close, *The Nucleon Spin Crisis Bible*, Rutherford Appleton Laboratory (1993), RAL-93-034.

[6] R.Brandelik *et al.*, *Evidence of a Spin One Gluon in Three Jet Events*, Phys.Lett. **B97** (1980) 453.

[7] C.N.Yang, R.L.Mills, *Conservation of Isotopic Spin and Isotopic Gauge Invariance*, Phys.Rev **96** (1954) 191.

[8] M.Gell-Mann, *A Schematic Model of Baryons and Mesons*, Phys.Lett **8** (1964) 214.

[9] F.E.Close, *An Introduction to Quarks and Partons*, Academic Press, 1979.

[10] F.Halzen and A.D.Martin, *Quarks & Leptons*, J.Wiley & Sons, 1984.

[11] A.V.Manohar, *An Introduction to Spin Dependent Deep Inelastic Scattering*, Proc.of the 7. Lake Louise Winter Institute 1992, B.A.Cambell *et al.* (eds.), World Scientific Singapore (1992).

[12] M.Anselmino, A.Efremov, E.Leader, *The Theory and Phenomenology of Polarized Deep Inelastic Scattering*, Phys.Rept. **261** (1995) 1, erratum ibid. **281** (1997) 399.

[13] D.E.Groom *et al.*, Particle Data Group, *Review of Particle Physics*, Eur.Phys.J. **C15** (2000) 1.

[14] L.W.Whitlow *et al.*, *Precise Measurements of the Proton and the Deuteron Structure Functions from a Global Analysis of the SLAC Deep Inelastic Electron Scattering Cross Sections*, Phys.Lett. **B282** (1992) 475.

[15] A.C.Benvenuti *et al.*, *A High Statistics Measurement of the Proton Structure Functions $F_2(x,Q^2)$ and R from Deep Inelastic Muon Scattering at High Q^2*, Phys.Lett. **B223** (1989) 485.

[16] M.R.Adams *et al.*, *Proton and Deuteron Structure Functions in Muon Scattering at 470 GeV*, Phys.Rev. **D54** (1996) 3006.

[17] M.Arneodo *et al.*, *Measurement of the Proton and the Deuteron Structure Functions, F_2^p and F_2^d*, Phys.Lett. **B364** (1995) 107.

[18] C.F.v.Weizsäcker, *Radiation Emitted in Collisions of Very Fast Electrons*, Z.Phys **88** (1934) 612.

[19] E.J.Williams, *Nature of the High-Energy Particles of Penetrating Radiation and Status Ionization and Radiation Formulae*, Phys.Rev **45** (1934) 729.

[20] L.N.Hand, *Experimental Investigation of Pion Electroproduction*, Phys.Rev. **129** (1963) 1834.

[21] L.W.Whitlow *et al.*, *A Precise Extraction of $R = \sigma_L/\sigma_T$ from a Global Analysis of the SLAC Deep Inelastic ep and ed Scattering Cross-Section*, Phys.Lett. **B250** (1990) 193. Note: this reference has a typographic mistake. Correct is $b_1 = 0.0635$.

[22] K.Abe *et al.*, *Measurements of $R = \sigma_L/\sigma_T$ for $0.03 < x < 0.1$ and Fit to World Data*, Phys.Lett. **B452** (1999) 194.

[23] C.G.Callan, D.J.Gross, *High-Energy Electroproduction and the Constitution of the Electric Current*, Phys.Rev.Lett. **22** (1969) 156.

[24] T.Pussieux, R.Windmolders, *A Collection of Formulas for Spin Dependent Deep Inelastic Scattering*, DAPNIA/SPhN 95-10 (1995).

[25] D.Hasch, *Messung der polarisierten Strukturfunktion $g_1(x, Q^2)$ des Protons mit dem HERMES Experiment*, Dissertation (1999), Humboldt-Univ.Berlin, HERMES Internal Note 99-065.

[26] U.Stösslein, *Measurement of the Spin Structure Function g_1 of the Proton and the Deuteron* Proc.of 14.Int.Spin Physics Symposium (SPIN 2000), Osaka, (2000).

[27] J.Blümlein, H.Böttcher, *QCD Analysis of Polarized Deep Inelastic Scattering Data*, hep-ph/0107317, DESY-01-107.

[28] K.Abe *et al.*, *Measurement of the Proton and Deuteron Spin Structure Function g_1 and g_2*, Phys.Rev. **D58** (1998) 112003.

[29] B.Adeva *et al.*, *Spin Asymmetries A_1 and Structure Functions g_1 of the Proton and the Deuteron from Polarized High Energy Muon Scattering*, Phys.Rev. **D58** (1998) 112001.

[30] P.L.Anthony *et al.*, *Measurement of the Proton and Deuteron Spin Structure Function g_2 and Asymmetry A_2*, Phys.Lett. **B458** (1999) 529.

[31] K.Abe *et al.*, *Measurement of the Neutron Spin Structure Function g_2 and Asymmetry A_2*, Phys.Lett. **B404** (1997) 377.

[32] P.Schmüser, *Feynman-Graphen und Eichtheorien für Experimentalphysiker*, Springer-Verlag, 1995.

[33] R.P.Feynman, *Very High-Energy Collisions of Hadrons*, Phys.Rev.Lett. **23** (1969) 1415.

[34] J.D.Bjørken, E.A.Paschos, *Inelastic Electron-Proton and γ-Proton Scattering and the Structure of the Nucleon*, Phys.Rev. **185** (1969) 1975.

[35] B.Adeva *et al.*, *Polarized Quark Distributions in the Nucleon from Semi-Inclusive Spin Asymmetries*, Phys.Lett. **B420** (1998) 180.

[36] K.Ackerstaff *et al.*, *Flavour Decomposition of the Polarized Quark Distributions of the Nucleon from Inclusive and Semi-Inclusive Deep Inelastic Scattering*, Phys.Lett. **B464** (1999) 123, DESY 99-048.

[37] J.D.Bjørken, *Applications of the Chiral $U(6) \otimes U(6)$ Algebra of Current Densities*, Phys.Rev **148** (1966) 1467.

[38] J.Ellis, R.Jaffe, *Sum Rule for Deep Inelastic Electroproduction from Polarized Protons*, Phys.Rev. **D9** (1974) 1444, erratum ibid. **D10** (1974) 1669.

[39] E.L.Berger, *Semi-Inclusive Inelastic Electron Scattering from Nuclei*, Proc.of the Workshop on Electronuclear Physics with Internal Targets, Stanford (1987), ANL-HEP-PR-87-45.

[40] J.J.Aubert *et al.*, *Measurement of the Q^2, x, and W^2 Dependence of Single Hadron Production in Deep Inelastic Muon Scattering*, Phys.Lett **B114** (1982) 373.

[41] P.Geiger, *Measurement of Fragmentation Functions at HERMES*, Dissertation (1998), Univ.Heidelberg, HERMES Internal Note 98-005.

[42] C.Adloff *et al.*, *Measurement of Event Shape Variables in Deep Inelastic ep Scattering*, Phys.Lett **B406** (1997) 256.

[43] J.Breitweg *et al.*, *Measurement of Multiplicity and Momentum Spectra in the Current and the Target Regions of the Breit Frame in Deep Inelastic Scattering at HERA*, Eur.Phys.J. **C11** (1999) 251.

[44] Y.L.Dokshitzer, *Calculation of Structure Functions of Deep-Inelastic Scattering and e^+e^- Annihilation by Perturbation Theory in Quantum Chromodynamics*, Sov.Phys.JETP **46** (1997) 641.

[45] V.N.Gribov, L.N.Lipatov, *Deep Inelastic ep Scattering in Perturbation Theory*, Sov.J.Nucl.Phys. **15** (1972) 438.

L.N.Lipatov, *The Parton Model and Perturbation Theory*, Sov.J.Nucl.Phys. **20** (1975) 94.

[46] G.Altarelli, G.Parisi, *Asymptotic Freedom in Parton Language*, Nucl.Phys. **B126** (1977) 298.

[47] G.Altarelli, *Partons in Quantum Chromodynamics*, Phys.Rep. **81** (1982) 1.

[48] R.G.Roberts, *The Structure of the Proton*, Cambridge University Press (1990).

[49] E.B.Zijlstra, W.L.van Neerven, *Order-α_s Corrections to the Polarized Structure Function $g_1(x, Q^2)$*, Nucl.Phys. **B417** (1994) 61.

[50] R.Mertig, W.L.van Neerven, *The Calculation of the Two-Loop Spin Splitting Functions $P_{ij}^{(i)}$*, Z.Phys. **C70** (1996) 637.

[51] W.Vogelsang, *Rederivation of the Spin-Dependent Next-To-Leading Order Splitting Functions*, Phys.Rev. **D54** (1996) 2023.

[52] M.Glück, E.Reya, A.Vogt, *Dynamical Parton Distributions Revisited*, Eur.Phys.J. **C5** (1998) 461.

[53] A.D.Martin *et al.*, *Parton Distributions: A New Global Analysis*, Eur.Phys.J. **C4** (1998) 463.

[54] H.L.Lai *et al.*, *Improved Parton Distributions from Global Analysis of Recent Deep Inelastic Scattering and Inclusive Jet Data*, Phys.Rev. **D55** (1997) 1280.

[55] T.Gehrmann, W.J.Stirling, *Spin-Dependent Parton Distributions from Polarized Structure Function Data*, Z.Phys. **C65** (1995) 461.

[56] Y.Goto *et al.*, *Polarized Parton Distributions of the Nucleon*, Phys.Rev. **D62** (2000) 034017.

[57] M.Glück *et al.*, *Next-To-Leading Order Radiative Parton Model Analysis of Polarized Deep Inelastic Lepton-Nucleon Scattering*, Phys.Rev. **D53** (1996) 4775.

[58] B.Adeva *et al.*, *Spin Asymmetries A_1 of the Proton and the Deuteron in the Low x and the Low Q^2 Region from Polarized High Energy Muon Scattering*, Phys.Rev. **D60** (1999) 072004.

[59] M.Roos *et al.*, Particle Data Group, *Review of Particle Properties*, Phys.Lett **B111** (1982) 1.

[60] S.L.Adler, *Axial-Vector Vertex in Spinor Electrodynamics*, Phys.Rev **177** (1969) 2426.

[61] J.S.Bell, R.Jackiw, *A PCAC Puzzle: $\pi^0 \to \gamma\gamma$ in the σ-Model*, Nuovo Cimento **A60** (1969) 47.

[62] G.Altarelli, G.G.Ross, *The Anomalous Gluon Contribution to Polarized Leptoproduction*, Phys.Lett. **B212** (1988) 391.

[63] R.D.Carlitz *et al.*, *The Role of the Axial Anomaly in Measuring Spin-Dependent Parton-Distributions*, Phys.Lett. **B214** (1988) 229.

[64] A.V.Efremov, O.V.Teryaev, *Spin Structure of the Nucleon and Triangle Anomaly*, JINR Report No. E2-88-287 (1998), unpublished.

[65] S.L.Adler, W.A.Bardeen, *Absence of Higher-Order Corrections in the Anomalous Axial-Vector Divergence Equation*, Phys.Rev. **182** (1969) 1517.

[66] W.A.Bardeen *et al.*, *Deep-Inelastic Scattering Beyond the Leading Order in Asymptotically Free Gauge Theories*, Phys.Rev. **D18** (1978) 3998.

[67] A.A.Anselm, A.Johansen, *Radiative Corrections to the Axial Anomaly* JETP Lett. **49** (1989) 214, Sov.Phys.JETP **69** (1989) 670.

[68] P.Ratcliffe, *Orbital Angular Momentum and The Parton Model*, Phys.Lett **B192** (1987) 180.

[69] J.Babcock, D.Sivers, S.Wolfram, *Quantum-Chromodynamic estimates for heavy particle production*, Phys.Rev. **D18** (1978) 162.

[70] A.D.Watson, *Spin-Spin Asymmetries in Inclusive Muon Proton Charm Production*, Z.Phys. **C12** (1982) 123.

[71] M.Glück, E.Reya, *Spin-Dependent Parton Distributions in Deep Inelastic Lepton Nucleon Scattering*, Z.Phys. **C39** (1988) 569.

[72] P.Nason, *et al.*, *The Total Cross Section for the Photoproduction of Heavy Quarks in Hadronic Collisions*, Nucl.Phys. **B303** (1988) 607.

S.Frixione *et al.*, *Differential Distribution for Heavy Flavour Production at HERA*, Nucl.Phys. **B454** (1995) 3.

[73] B.W.Harris, J.Smith, *Charm Quark and $D^{*\pm}$ Cross-Sections in Deeply Inelastic Scattering at HERA*, Phys.Rev **D57** (1998) 2806.

[74] R.K.Ellis, P.Nason, *QCD Radiative Corrections to the Photoproduction of Heavy Quarks*, Nucl.Phys. **B312** (1989) 551.

[75] C.Adloff *et al.*, *Measurement of the D^{*} Meson Cross Section at HERA and Determination of the Gluon Density in the Proton Using NLO QCD*, Nucl.Phys. **B545** (1999) 21.

[76] E.Volk, *Measurement of the $D^{*\pm}$ Cross-Section at HERMES*, Dissertation (2001), Univ.Heidelberg, DESY-THESIS 2001-002.

[77] M.Ehrenfried, *Eine Studie zur Nachweisbarkeit von open charm Ereignissen bei HERMES*, Diplomarbeit (2001), Univ.Münster, DESY-THESIS 2001-024.

[78] COMPASS Collaboration, *A Proposal for a COmmon Muon and Proton Apparatus for Structure and Spectroscopy*, CERN/SPSLC 96-14, SPSLC/P297 (1996).

[79] R.G.Arnold *et al.*, *Proposal to Measure Polarized Open Charm Photoproduction*, SLAC-PROPOSAL-E156 (1997).

[80] E.L.Berger, D.Jones, *Inelastic Photoproduction of J/ψ and υ by Gluons*, Phys.Rev. **D23** (1981) 1521.

[81] G.T.Bodwin, *et al.*, *Rigorous QCD Analysis of Inclusive Annihilation and Production of Heavy Quarkonium* Phys.Rev. **D51** (1995) 1125, erratum ibid. **D55** (1997) 5853.

[82] F.Meißner, *Measurement of the J/ψ Cross Section and Double Spin Asymmetries in Vector Meson Production in Polarized Lepton-Nucleon Scattering at HERMES*, Dissertation (2000), Humboldt-Univ.Berlin, DESY-THESIS 2000-014.

[83] D.Allasia *et al.*, *Inelastic J/ψ Production in Deep Inelastic Scattering From Hydrogen and Deuterium and the Gluon Distribution of Free Nucleons*, Phys.Lett. **B258** (1991) 493.

[84] J.Ashman *et al.*, *Muoproduction of J/ψ and the Gluon Distribution of the Nucleon*, Z.Phys. **C56** (1992) 21.

[85] G.Sterman *et al.*, *Handbook of Perturbative QCD*, Rev.Mod.Phys. **67** (1995) 157.

[86] M.Fontannaz, B.Pire, D.Schiff, *Asymmetries in Large p_T Photoproduction and the Polarized Gluon Structure Function*, Z.Phys. **C8** (1981) 349.

[87] A.Bravar, K.Kurek, R.Windmolders, *POLDIS: A Monte Carlo for POLarized Deep Inelastic Scattering*, Comp.Phys.Com. **105** (1997) 42.

[88] G.Rädel, A.De Roeck, *The Polarized Gluon Density ΔG from Di-Jet Events in NLO*, hep-ph/9909403.

[89] M.R.Adams *et al.*, *Determination of the Gluon Distribution Function of the Nucleon Using Energy-Energy Angular Pattern in Deep Inelastic Muon-Deuteron Scattering*, Z.Phys. **C71** (1996) 391.

[90] S.Aid *et al.*, *A Direct Determination of the Gluon Density in the Proton at Low x*, Nucl.Phys. **B449** (1995) 3, DESY 95-086.

[91] I.Abt *et al.*, *The Gluon Density of the Proton at Low x from a QCD Analysis of F_2*, Phys.Lett. **B354** (1995) 494, DESY 95-081.

[92] M.Derrick *et al.*, *Extraction of the Gluon Density of the Proton at Small x*, Phys.Lett. **B345** (1995) 576, DESY 94-192

[93] A.Bravar, D.v.Harrach, A.Kotzinian, *Gluon Polarization from Correlated High-p_T Hadron Pairs in Polarized Electro-Production*, Phys.Lett. **B421** (1998) 349.

[94] G.Grispos, A.P.Contogouris, G.Veropoulos, *Polarized Photoproduction of Large-p_T Hadron Pairs as a Probe of the Polarized Gluon Contribution*, Phys.Rev **D62** (2000) 014023.

[95] Y.Dong, T.Morii, T.Yamanishi, *Extraction of Polarized Gluon Distributions from Large-p_T Hadron Pair Production*, hep-ph/0108027.

[96] A.Airapetian *et al.*, *Measurement of the Spin Asymmetry in the Photoproduction of Pairs of High-p_T Hadrons at HERMES*, Phys.Rev.Lett. **84** (2000) 2584, DESY 99-071.

[97] E.Berger, J.W.Qiu, *Calculations of Prompt Photon Production in QCD*, Phys.Rev. **D44** (1991) 2002.

[98] PHENIX experiment, BNL-PROPOSAL-R5 (1992).

[99] STAR experiment, S.E.Vigdor, *The RHIC Spin Program: Snapshots of Progress*, hep-ex/9905034.

[100] S.D.Ellis, S.Soper, *Successive Combination Jet Algorithm for Hadron Collisions*, Phys.Rev. **D48** (1993) 3160.

[101] C.Bourrely *et al.*, *Spin Effects with Polarized Protons at RHIC*, Nucl.Phys **B361** (1991) 72.

P.Chiappetta *et al.*, *Hadronic Colliders as Probes of the Proton Spin Structure*, Z.Phys **C59** (1993) 629.

J.Soffer *et al.*, *Testing Various Polarized Parton Distributions at RHIC* Nucl.Phys **B509** (1998) 297.

[102] G.P.Skoro, M.V.Tokarev, Asymmetry of jet production in polarized pp Collisions at RHIC and the Sign of ΔG, Nuovo Cimento **A111** (1998) 353.

[103] J.Buon, K.Steffen, *HERA Variable Energy 'Mini' Spin Rotator and Headon ep Collision Scheme with Choice of Electron Helicity*, Nucl.Instr.Meth. **A245** (1986) 248.

D.P.Barber *et al.*, *The First Achievement of Longitudinal Spin Polarization in a High-Energy Electron Storage Ring*, Phys.Lett. **B343** (1995) 436.

[104] A.A.Sokolov, I.M.Ternov, *On Polarization and Spin Effects in the Theory of Synchrotron Radiation*, Sov.Phys.Doklady **8** (1964) 1203.

[105] Y.S.Derbenev, A.M.Kondratenko, *Polarization Kinetics of Particles in Storage Rings*, Sov.Phys.JETP **37** (1973) 968.

[106] L.Thomas, Philos.Mag. **3** (1927) 1.

V.Bargmann, L.Michel, and V.L.Telegdi, *Precession of the Polarization of Particles Moving in a Homogeneous Electromagnetic Field*, Phys.Rev.Lett. **2** (1959) 435.

[107] D.P.Barber *et al.*, *The HERA Polarimeter and the First Observation of Electron Spin Polarization at HERA*, Nucl.Instr.Meth. **A329** (1993) 79.

[108] D.P.Barber, *Acceleration and Storage of Polarized Electron Beams*, Proc.of the 13.International Symposium on High Energy Spin Physics (SPIN98) 1998, DESY 98-182.

[109] D.P.Barber, H.Mais, G.Ripken, R.Rossmanith, *A General Harmonic Spin Matching Formalism for the Suppression of Depolarization Caused by Closed Orbit Distortion in Electron Storage Rings*, DESY 85-044.

D.P.Barber, G.Ripken, *Radiative Polarization, Computer Algorithms and Spin Matching in Electron Storage Rings*, Handbook of Accelerator Physics and Engineering A.W.Chao and M.Tigner (eds.), World Scientific (1999), DESY 99-095, physics/9907034.

[110] F.Stock *et al.*, *The FILTEX/HERMES Polarized Hydrogen Atomic Beam Source*, Nucl.Instr.Meth. **A343** (1994) 334.

[111] A.Golendoukhin for the HERMES Collaboration, *The HERMES Polarized Proton Target at HERA*, Proc.of 12.Int.Symposium on High Energy Physics (SPIN96), Amsterdam 1996, C.W.de Jaeger *et al.* (eds.), World Scientific (1997) 311.

[112] J.Stewart, *The HERMES Polarized Internal Gas Target*, Proc.of 7.Int.Workshop on Polarized Gas Targets and Polarized Beams, Urbana-Champaign, R.J.Holt/M.A.Miller (eds.), AIP (1997) 96.

[113] N.Koch, *A Study on the Production of Intense Cold Atomic Beams for Polarized Hydrogen and Deuterium Targets*, Dissertation (2000), Univ.Erlangen-Nürnberg.

[114] C.Baumgarten *et al.*, *An Atomic Beam Polarimeter to Measure the Nuclear Polarization in the HERMES Gaseous Polarized Hydrogen and Deuterium Target*, submitted to Nucl.Instr.Meth., DESY 01-078.

[115] C.Baumgarten, *Studies of Spin Relaxation and Recombination at the HERMES Hydrogen/Deuterium Gas Target*, Dissertation (2000), Univ.München, HERMES Internal Note 00-038.

[116] H.Kolster, *The HERMES Gaseous Internal Polarized Proton Target and its Use in the HERA Positron Storage Ring*, Dissertation (1998), Univ.München, HERMES Internal Note 98-009.

[117] D.De Schepper *et al.*, *The HERMES Polarized* ^3He *Internal Gas Target*, Nucl.Instr.Meth. A419 (1997) 432.

[118] K.Ackerstaff *et al.*, *Flavour Asymmetry of the Light Quark Sea from Semi-Inclusive Deep-Inelastic Scattering*, DESY 98-078, Phys.Rev.Lett. **81** (1998) 5519.

[119] K.Ackerstaff *et al.*, *Observation of a Coherence Length Effect in Exclusive* ρ^0 *Electroproduction*, DESY 98-178, Phys.Rev.Lett. 2 **82** (1999) 3025.

[120] A.Airapetian *et al.*, *Hadron Formation in Deep-Inelastic Positron Scattering from* ^{14}N *and* ^2H, Eur.Phys.J. **C20** (2001) 479, DESY 00-191.

[121] A.Airapetian *et al.*, *Measurement of Longitudinal Spin Transfer to Lambda Hyperons in Deep Inelastic Lepton Scattering*, accepted by Phys.Rev.D, DESY 99-151.

[122] K.Ackerstaff *et al.*, *The HERMES Spectrometer*, DESY 98-057, Nucl.Instr.Meth. **417** (1998) 230.

[123] W.Wander, *Rekonstruktion hochenergetischer Streuereignisse im HERMES Experiment*, Dissertation (1996), Univ.Erlangen-Nürnberg, HERMES Internal Note 96-023, English Version: 97-031.

[124] The HERMES RICH-Group, *The HERMES Dual-Radiator Ring Imaging Cerenkov Detector*, to be published in Nucl.Instr.Meth. .

[125] D.De Schepper, R.Kaiser, E.Cisbani, *Particle Identification with the HERMES RICH Detector: Description of the Different Approaches*, HERMES Internal Note 98-008.

[126] R.B.Kaiser, private communication.

[127] A.T.Maas, *Particle Identification with RICH Detectors: Algorithms and their Optimization*, Diplomarbeit (2000), Univ.Darmstadt, DESY-THESIS 2000-051.

[128] J.D.Jackson, *Classical Electrodynamics*, J. Wiley & Sons (1975).

[129] C.Grupen, *Teilchendetektoren*, BI-Wiss.-Verlag (1993), Wien.

[130] X.Artru, G.B.Yodh, and G.Mennessier, *Practical Theory of the Multilayered Transition Radiation Detector*, Phys.Rev. **D12** (1975) 1289 .

[131] R.B.Kaiser, *Measurement of the Spin Structure of the Neutron using Polarised Deep Inelastic Scattering*, Ph.D.Thesis (1997), Simon-Fraser-Univ.Vancouver, HERMES Internal Note 97-017.

[132] F.M.Menden, *Measurement of the Valence Quark Spin Distributions of the Nucleon Using Deep Inelastic Scattering at HERMES*, Diplomarbeit (1997), Univ.Hamburg, HERMES Internal Note 98-001.

[133] H.Avakian *et al.*, *Performance of the Electromagnetic Calorimeter of the HERMES Experiment*, Nucl.Instr.Meth. **A417** (1998) 69.

[134] T.Benisch, *Polarisierte Bhabha-Streuung und Luminositätsmessung am HERMES-Experiment*, Dissertation (1998), Univ.Erlangen-Nürnberg, HERMES Internal Note 98-045.

[135] C.Weiskopf, *Untersuchung der Bhabha-Asymmetrien mit dem HERMES-Luminositätsmonitor*, Diplomarbeit (1998), Univ.Erlangen-Nürnberg, HERMES Internal Note 98-042.

[136] U.Elschenbroich, *Bhabha Streuung und Luminositätsmessung im HERMES Experiment*, Diplomarbeit (2001), Univ.Düsseldorf, HERMES Internal Note 01-044.

[137] G.Schnell, *Longitudinal Polarization of the Lambda in Deep Inelastic Scattering of Polarized Positrons from Nucleons*, Ph.D.Thesis (1999), New Mexico State Univ., HERMES Internal Note 99-037.

[138] F.Meißner *et al.*, *Photoproduction Trigger at HERMES*, HERMES Internal Note 96-026.

[139] M.Amarian *et al.*, *The HERMES Charm Upgrade Program: Measurement of the Double Spin Asymmetry in Charm Leptoproduction*, DESY-PRC (1997), HERMES Internal Note 97-004.

[140] Programming Techniques Group, *ADAMO - Entity-Relationship Programming System*, V.3.3, ECP Division, CERN (1993).

[141] W.Wander, *DAD - Distributed ADAMO Database System at HERMES*, Proc.of CHEP95, Rio de Janeiro, (1995).

[142] F.W.Lipps, H.A.Tolhoek, *Polarization Phenomena of Electrons and Photons I/II*, Physica **20** (1954) 85 and 395.

[143] D.P.Barber *et al.*, *High Spin Polarization at the HERA Electron Storage Ring*, DESY 93-038, Nucl.Instr.Meth. **A338** (1994) 166.

[144] B.Tipton, *Measurement of the Polarized Parton Distributions With Spin-Dependent Deep Inelastic Scattering*, Ph.D.Thesis (1999), Massachusetts Institute of Technology. HERMES Internal Note 99-034.

[145] F.M.Menden, *Mapping of the Cross Section of the Beampipe at the HERMES Longitudinal Polarimeter*, Internal Polarimeter Report 98-01.

[146] F.Burkart, *Messung der Stokes Parameter am Laserstrahl des HERA-Polarimeters*, Wissenschaftliche Arbeit (1996), Univ.Freiburg.

[147] M.Beckmann, *Extraction of Polarized Quark Distributions of the Nucleon from Deep Inelastic Scattering at the HERMES Experiment*, Dissertation (2000), Univ.Freiburg, DESY-THESIS 2000-029.

[148] C.Pascaud, F.Zomer, *Likelihood Treatment of Polarization Measurements*, private communication (1999).

[149] S.Brauksiepe, *COP: A Graphical Interface to Control and Monitor the Longitudinal Polarimeter at HERA*, Proc.of the 12.International Symposium on High Energy Spin Physics, Amsterdam, C.W.Jaeger *et al.* (eds.), World Scientific (1996), 771.

[150] R.J.Cashmore *et al.*, *Meas. of Weak Neutral Current Couplings of Quarks at HERA*, R.Beyer *et al.*, *Electroweak Precision Tests with Deep Inelastic Scattering at HERA*, both in Proc. of the Workshop on *Future Physics at HERA 1995-96*, G.Ingelman, A.De Roeck, R.Klanner (eds.), DESY, Hamburg.

[151] M.Beckmann *et al.*, *The Longitudinal Polarimeter at HERA*, accepted by Nucl.Instr.Meth. **A** (2001), DESY 00-106, physics/0009047.

[152] HERA POL2000 Group, *Proposal to Upgrade the Longitudinal Polarimeter*, HERMES Internal Note 00-040 (2000).

[153] R.D.Field, R.P.Feynman, *A Parametrization of the Properties of Quark Jets*, Nucl.Phys. **B136** (1978) 1.

[154] P.Hoyer *et al.*, *Quantum Chromodynamics and Jets in* e^+e^-, Nucl.Phys. **B161** (1979) 349.

[155] A.Ali *et al.*, *Heavy Quarks in* e^+e^- *Annihilation*, Nucl.Phys. **B168** (1980) 409.

A.Ali *et al.*, *A QCD Analysis of the High-Energy* e^+e^- *Data from PETRA*, Phys.Lett. **B93** (1980) 155.

[156] G.Marchesini, B.R.Webber, *Simulation of QCD Jets Including Soft Gluon Interference*, Nucl.Phys. **B238** (1984) 1.

B.R.Webber, *A QCD Model for Jet Fragmentation Including Soft Gluon Interference*, Nucl.Phys. **B238** (1984) 492.

[157] G.Marchesini *et al.*, *HERWIG: A Monte Carlo Event Generator for Simulation Hadron Emission Reactions With Interfering Gluons. V.5.1*, Comp.Phys.Comm. **67** (1992) 465.

G.Corcella *et al.*, *HERWIG 6.1 Release Note*, JHEP **01** (2001) 101.

G.Corcella *et al.*, *HERWIG 6.3 Release Note*, CERN-TH/2001-173 (2001), hep-ph/0107071.

[158] T.D.Gottschalk, D.A.Morris, *A New Model for Hadronization and* e^+e^- *Annihilation*, Nucl.Phys. **B288** (1987) 729.

[159] T.Sjöstrand, *The Lund Monte Carlo for Jet Fragmentation and* e^+e^- *Physics JESTET Version 6.2*, Comp.Phys.Comm. **39** (1986) 347.

[160] B.Andersson *et al.*, *Parton Fragmentation and String Dynamics*, Phys.Rept. **97** (1983) 31.

B.Andersson *et al.*, *A General Model for Jet Fragmentation*, Z.Phys. **C20** (1983) 317.

T.Sjöstrand, *The Merging of Jets*, Phys.Lett. **B142** (1984) 420, DESY 84-019.

T.Sjöstrand, *Jet Fragmentation of Nearby Partons*, Nucl.Phys. **B248** (1984) 469, DESY-T-84-01.

[161] D.H.Perkins, *Introduction to High Energy Physics*, 1st edition, Addison-Wesley (1972).

[162] B.Andersson *et al.*, *Baryon Production in Jet Fragmentation and Ypsilon Decay*, Phys.Scripta **32** (1985) 574.

[163] G.Ingelman, A. Edin, J. Rathsman, *LEPTO 6.5 - A Monte Carlo Generator for Deep Inelastic Lepton-Nucleon Scattering*, Comp.Phys.Comm. **101** (1997) 108, DESY 96-057, `http://www3.tsl.uu.se/thep/lepto/`.

[164] O.Martin, M.Maul, A.Schäfer, *Recent developments of PEPSI and SPHINX*, hep-ph/9710381 (1997).

L.Mankiewicz, A.Schäfer, M.Veltri, *PEPSI: A Monte Carlo Generator for Polarized Leptoproduction*, Comp.Phys.Comm. **71** (1992) 305.

[165] PYTHIA 6.154: T.Sjöstrand *et al.*, Comp.Phys.Com. **135** (2001) 238.

[166] PYTHIA 6.2 (latest version): T.Sjöstrand *et al.*, hep-ph/0108264.

[167] E.Norrobin, T.Sjöstrand, *Production and Hadronization of Heavy Quarks*, Eur.Phys.J. **C17** (2000) 137.

[168] I.Akushevich *et al.*, *POLRAD 2.0 FORTRAN Code for the Radiative Corrections Calculation to Deep Inelastic Scattering of Polarized Particles*, Comp.Phys.Comm. **104** (1997) 201.

I.Akushevich, N.Shumeiko, *Radiative Effects in Deep Inelastic Scattering of Polarized Leptons by Polarized Light Nuclei*, J.Phys. **G20** (1994) 513.

[169] CERN Computing and Network Division, *GEANT Detector Description and Simulation Tool*, CERN Program Library Long Writeup W5013 (1993).

[170] H.Böttcher *et al.*, *Results on the Top/Bottom Detector Alignment for the 1997 Data*, HERMES Internal Note 99-053 (1999).

[171] J.Wendland, *Improved Particle Identification at HERMES and Polarized Quark Distributions in the Proton*, MSc.Thesis (1999), Simon-Fraser-Univ.Vancouver, HERMES Internal Note 99-016.

[172] G.D'Agostini, *A Multidimensional Unfolding Method Based on Bayes' Theorem*, DESY 94-099 (1994).

[173] Y.Gärber, *Messung der Proton-Strukturfunktion g_1 bis zu kleinstmöglichen Bjorken-x mit dem HERMES-Experiment*, Dissertation (2001), Humboldt-Univ.Berlin.

[174] H.Abramowicz, A.Levy, *The ALLM Parameterization of $\sigma_{tot}(\gamma^* p)$: an Update*, DESY 97-251 (1997), hep-ph/9712415.

H.Abramowicz, E.Levin, A.Levy, U.Maor, Phys.Lett. **B269** (1991) 465.

[175] H.L.Lai *et al.*, *Global QCD Analysis of Parton Structure of the Nucleon: CTEQ5 Parton Distributions*, Eur.Phys.J. **C12** (2000) 375.

[176] A.D.Martin *et al.*, *Parton Distributions and the LHC: W and Z Production*, Eur.Phys.J. **C14** (2000) 133.

[177] M.Maul, private communication (2001), PEPSI with new JETSET (Version 7.4.11): `http://www.thep.lu.se/~maul/pepsi.html`.

[178] F.James, M.Roos, *'MINUIT' A System For Function Minimization And Analysis Of The Parameter Errors And Correlations*, Comp.Phys.Comm. **10** (1975) 343, CERN Program Library Long Writeup D506 (1994).

[179] J.A.Nelder, R.Mead, Comp.Jou. **7** (1965) 308.

[180] H.Ihssen, private communication (1998).

[181] H.A.Tallini, *A Measurement of the Quark Spin Distribution of the Nucleon at HERMES* , Ph.D.Thesis (1998), Univ. of Liverpool, HERMES Internal Note 98-024.

[182] P.Abreu *et al.*, *Tuning and Test of Fragmentation Models Based on Identified Particles and Precision Event Shape Data*, Z.Phys. **C73** (1996) 11.

K.Hamacher, M.Weierstall, *The Next Round of Hadronic Generator Tuning Heavily Based on Identified Particle Data*, hep-ex/9511011 (1995).

[183] M.Arneodo *et al.*, *Transverse Momentum of Hadrons Produced in Current and Target Jets in Deep Inelastic Muon-Proton Scattering*, Phys.Lett. **B149** (1984) 415.

[184] T.Lindemann, *Extraktion der polarisierten Quarkverteilungen des Nukleons mit besonderer Berücksichtigung der Seequarks im HERMES-Experiment*, Dissertation (2001), Univ.Hamburg.

[185] J.W.Martin, *Measurement of the Spin Asymmetry $A_{||}$ in the Photoproduction of High-p_T Hadron Pairs*, Ph.D.Thesis (2000), Massachusetts Institute of Technology, HERMES Internal Note 99-057.

[186] HERMES Data Quality Group, private communication (2001).

[187] M.Lacombe *et al.*, *Parameterization of the Paris NN Potential*, Phys.Rev. **C21** (1980) 861.

[188] B.Desplanques *et al.*, *Deuteron D-State Probability and Energy Dependent NN Interactions*, Phys.Lett. **B203** (1988) 200.

[189] M.Düren, *The HERMES Experiment: From the Design to the First Results*, Habilitation (1995), Univ.Erlangen-Nürnberg, HERMES Internal Note 95-02.

[190] P.Lenisa, private communication (2001). HERMES Internal Note in preparation.

[191] E.Aschenauer, P.Liebig, F.M.Menden, V.Mexner, *Pairs of High p_T Hadrons in the Years 1996-2000*, Hermes Internal Note 01-024.

[192] T.Sjöstrand, *High-Energy Physics Event Generation with PYTHIA 5.7 and JETSET 7.4*, Comp.Phys.Comm **82** (1994) 74.

[193] C.Friberg, *Aspects of QCD and the Photon Structure*, Ph.D.Thesis (2000), Lund University.

[194] C.Friberg, T.Sjöstrand, *Total Cross Sections and Event Properties from Real to Virtual Photons*, JHEP **9** (2000) 10.

[195] A.Donnachie, P.V.Landshoff, *Total Cross-Sections*, Phys.Lett. **B296** (1992) 227.

[196] G.A.Schuler, T.Sjöstrand, *Hadronic Diffractive Cross Sections and the Rise of the Total Cross Section*, Phys.Rev. **D49** (1994) 2257.

[197] H.Fraas, D.Schildknecht, *Vector Meson Dominance and Diffractive Electroproduction of Vector Mesons*, Nucl.Phys. **B14** (1969) 543.

[198] T.Sjöstrand, private communication (2001).

[199] K.Lipka, Ph.D.Thesis, in preparation.

[200] R.Cross,*Structure Functions, the Gluon Density, and PQCD Tests*, hep-ex/9903046.

[201] M.Botje, *A QCD Analysis of HERA and Fixed Target Structure Function Data* Eur.Phys.J. **C14** (2000) 285, DESY-99-038.

M.Botje, *Error Estimates on Parton Density Distributions*, hep-ph/0110123.

[202] D.v.Harrach, W.D.Nowak, J.Soffer, *Theory Meets Experiment for the Determination of* $\Delta G/G$, hep-ph/9712207, DESY 97-232.

[203] The COMPASS Collaboration, COMPASS Reconstruction Code (CoRe), Version 0.3.0.1.

[204] M.C.Simani, private communication (2001).

Acknowledgments

I would like to thank Prof.Kay Königsmann for giving me the opportunity to work for my thesis at HERMES/DESY in Hamburg and at the University of Freiburg. I have profited from his constant support and maximum freedom a supervisor can grant his student in combination with appealing and challenging topics to master.

This work would have been impossible without the continuous feedback of my two exemplary supervisors: Jürgen Franz and Armand Simon. They were always there to answer questions or avoid stupidities and directed me onto the right path when solving problems. I have profited from their professionalism, rationality, and collegiality combined with friendship at the right time and place.

I am indebted to Marc Beckmann and Jürgen Franz who not just proofread this manuscript but also gave instructive feedback which significantly enhanced the quality of this thesis. In this context I have to thank also the members of the high-pt working group: Elke Aschenauer, Patricia Liebing, Katerina Lipka, and Vanessa Mexner. Without their help and feedback it would have been impossible for me to accomplish the thesis within a finite amount of time. Here, I also have to mention Helmut Böttcher who always was available for a discussion on parton distributions and was so kind to give me his parton distribution code even before it was published.

I would like to express my gratitude to Horst Fischer, Fritz-Herbert Heinsius, Ulrich Mück, and Rainer Fastner, who helped from far in Freiburg by organizing Pockels cells, solving hard- and software problems on the alpha machines, arranging computer parts, or by manufacturing customed mountings for exotic Canadian wire chambers. On the Hamburg side, Larry Felawka and Maurice Bouwhuis never hesitated to help solving problems concerning the hermes-machine or the PC-cluster.

I am indebted to Thomas Schmidt who always offered me a place for my sleeping bag; long-term or on short notice, whenever I had to be in Freiburg and had no apartment at hand. I enjoyed his company on ironic working days as well as Ostrich steaks in the Brennessel, Flammkuchen in the Schlappen, or too many Caipirinhas in the Othello Bar. I am also thankful to Marc Niebuhr and Stefan Noster who offered me a place to stay overnight at some occasions as well. Here, I do not want to forget to thank Thomas Elsäßer in Vörstetten, where I had my permanent address for almost four years.

Working in the Freiburg group always was fun whenever Heiko Lacker, Marc Beckmann, or Stephan Brauksiepe were present. The mixture of spoiled political correctness, absolutely senseless ideas, and distractive actions of all kind was just right. Many insane conversations helped us all not to go bananas between surviving Praktikum days and crawling through the laser-green illuminated HERA tunnel at night. Including Thomas Schmidt, Roman Risken, and some Praktikum students we always had fun after hours, no matter if we fought some Federweissen or other Breisgauian beverages. Thankful greetings also go to Ulrike Elschenbroich and Marc Beckmann who always posed reliable and hilarious container-mates in the Blasenkammer, the real-German-oak-walled forge of quality work.

The other Freiburg group members Paolo Sereni, Andreas Grünemaier, Michael Ruh, Christian Schill, and Joachim Seibert were always there for some interesting conversations. I have learned incredible things about the constantly rising HERA tunnel temperature and the unlimited possibilities of modern Lavazza detectors. In Hamburg, working life was fun with Falk Meißner, Matthias Hartig, and Thore Lindemann who offered friendship, ironic insights, and some Bauernweisheiten whenever needed. I am also indebted to Björn Seitz for all these endless Monte Carlo productions he set up for me so I could finish my analysis. Thanks also go to Naomi Makins who always helped me with explanations and valuable suggestions on the fragmentation front.

Things would have been less pleasant without the cordial help from our secretaries crew: Ramona Matthes, Sabine Krohn, Soerne Möller in Hamburg and Angela Göller and Gisela Mössner in Freiburg. I would also like to express my gratitude to Mike Vetterli who gave me some important strategical advice at critical times. Peter Schüler and Norbert Meyners always posed helpful during LPOL operations; either with some profound critics wrapped in sly sayings or by organizing weird equipment or keys. I would also like to thank Wolfgang Scobel for a comment on some historical backgrounds.

I have always enjoyed the good working atmosphere in the Freiburg and the HERMES group. The pasta parties in the early Hamburg days with Jan Visser, Chiara Simani, Erika Garutti, Lara De Nardo, Marc Beckmann, Stephan Brauksiepe, and Ulrike Elschenbroich were unforgettable events involving Spaghetti and Scalls for everybody. I also have to thank my Hamburg friends Götz, Mati, Gesine, Heinz-Jörg, Uschi, Christine, Ansgar, Andi, Jens, Christiane, Claudia, Hannes, Mark, Petra, Ise, Ronald and my siblings Linus, Nina and Sophie who all helped me to gain some distance from time to time by clearing up my 'Tunnelblick'. In am grateful to Viola who was always there for me; in the dark days of my thesis she cushioned my setbacks with her affection. Final thanks go to my parents who have given me roots and wings to accomplish all this. From the first day on, they regularily asked me how many pages I have written already ...